Incoherent Thomson scattering investigations in Hall thruster, planar magnetron and ECR ion source plasmas

Benjamin Vincent

Centre Val de Loire UNIVERSITÉ Spirit of the Loire Valley

UNIVERSITÉ D'ORLÉANS

UNIVERSITE D'ORLEANS

ÉCOLE DOCTORALE ÉNERGIE, MATÉRIAUX, SCIENCES DE LA TERRE ET DE L'UNIVERS

LABORATOIRE : INSTITUT DE COMBUSTION AÉROTHERMIQUE RÉACTIVITÉ ET ENVIRONNEMENT

Thèse présentée par :

Benjamin VINCENT

soutenue le : **17 Décembre 2019**

pour obtenir le grade de : **Docteur de l'Université d'Orléans**

Discipline : **Physique**

Incoherent Thomson scattering investigations in Hall thruster, planar magnetron and ECR ion source plasmas

Thèse dirigée par :

Sedina TSIKATA	Chargée de recherche, ICARE, CNRS, Orléans, France

RAPPORTEURS :

Ivo FURNO	Professeur, Ecole Polytechnique Fédérale de Lausanne, Suisse
Gerard van ROOIJ	Professeur, Eindhoven University of Technology, Pays Bas

JURY :

Ivo FURNO	Professeur, Ecole Polytechnique Fédérale de Lausanne, Suisse
Gerard van ROOIJ	Professeur, Eindhoven University of Technology, Pays Bas
Laurent GARRIGUES	Directeur des recherches, LAPLACE, CNRS, Toulouse, France
Stéphane MAZOUFFRE	Directeur des recherches, ICARE, CNRS, Orléans, France
Tiberiu MINEA	Professeur, LPGP, Univ. Paris XI, CNRS, Orsay, France
Yevgeny RAITSES	Senior Research Physicist, PPPL, Princeton, USA
Jérôme FILS	Research Engineer, GSI/CEA Saclay, Darmstadt, Allemagne

Acknowledgements

Working with great people makes you great; you learn a lot and it also gives you the experience and confidence to move on with your own career.

— *Nas, Askmen Interview*

Contents

List of Symbols

t	Time
t	Light velocity
g	Acceleration of gravity at sea level
k_B	Boltzmann constant
ε_0	Vacuum permittivity
μ_0	Permeability constant
e	Electron charge
m_e	Mass of the electron
n_e	Electron density
T_e	Electron temperature
$v_{e,drift}$	Electron drift velocity
$\vec{E}$	Electric field
$\vec{B}$	Magnetic field
$\vec{k_i}$	Incident wave vector
$\vec{k_s}$	Scattered wave vector
$\vec{k}$	Probed wave vector
L_{obs}	Observation volume length scale
L_{coh}	Coherence length scale of the laser
f_{v_i}	Velocity distribution function along the i-direction
f_v	Velocity distribution function
$f_{\vec{v}}$	Vector velocity distribution function
f_{E_i}	Energy distribution function along the i-direction
f_E	Energy distribution function
S_k	Spectral form factor distribution
R	Reflectance
T	Transmitance
α	Degree of ionization
λ_{De}	Debye length
ω_p	Plasma frequency
n_i	Ion density
ν_{ei}	Electron ion collision frequency
ν_{en}	Electron neutral collision frequency
ν_{eh}	Electron collision frequency with heavy particles
V_d	Discharge voltage
I_d	Discharge current
P	Power
m_{Xe}	Xenon atom mass
m_{Kr}	Krypton atom mass
$\dot{m}_g$	Mass flow of a give gas (g)
η	Thruster efficiency
I_{sp}	Specific impulse

List of Abbreviations

CNRS	Centre National de le Recherche Scientifique
CEA	Commissariat à l'Energie Atomique et aux énergies alternatives
NASA	National Aeronautics and Space Administration
ICARE	Institut de Combustion, Aérothermique, Réactivité et Environnement
LPGP	Laboratoire de Physique des Gaz et des Plasmas
LEDA	Laboratoire dÉtudes et de Développements pour les Accélérateurs
TMP-DS	équipe Théorie et Modélisation des Plasmas - Décharges et Surfaces
JPL	Jet Propulsion Laboratory
THETIS	THomson scattering Experiments for low Temperature Ion Sources
PRAXIS	PRopulsion Analysis eXperiments via Infrared Scattering
NExET	New Experiments in Electric Thrusters
DIVA	Dispositif d'Ionisation de la VApeur
ECRIN	Electron Cyclotron Résonance Ion Négatif
ISCT	ICARE Small customizable Thruster
MIREA	Moscow State Institute of Radio Engineering Electronics and Automation
ITS	Inchoherent Thomson Scattering
CTS	Coherent Thomson Scattering
LIF	Laser Induced Fluorescence
OES	Optical Emission Spectroscopy
LP	Langmuir Probe
THz-TDS	TeraHertz Time-Domain Spectroscopy
CETS	Cavity Enhanced Thomson Scattering
PIC	Particle-In-Cel
UV	UltraViolet
IR	InfraRed
PMT	PhotoMultiplier Tube
CCD	Charge-Coupled Device
GBF	Générateur Basse Fréquences
EIA	Electronic Industries Alliance
FWHM	Full Width at Half Maximum
RMS	Root Mean Square
OD	Optical Density
NA	Numerical aperture
TGS	Triple Grating Spectrometer
VBG	Volume Bragg Grating
VBG-NF	Volume Bragg Grating based Notch Filter
PTR	Photo-Thermo-Reflective
DC	Direct Current

AC	Alternating Current
EEDF	Electron Energy Distribution Function
EVDF	Electron Velocity Distribution Function
IVDF	Ion Velocity Distribution Function
DCMS	Direct Current Magnetron Sputtering
HiPIMS	High Power Impulse Magnetron Sputtering
PVD	Physical Vapor Deposition
IPVD	Ionized Physical Vapor Deposition
RF	Radio Frequency
ECR	Electron Cyclotron Resonance
HT	Hall Thruster
SPT	Stationary plasma thruster
MS	Magnetic Shieldeding
US	Unshielded

List of Figures

List of Tables

Chapter 1

Introduction

"Take care of all your memories"
said my friend, Mick
" For you cannot relive them
And remember when youre out there
Tryin to heal the sick
That you must always
First forgive them "

—*Bob Dylan, Open the Door Homer*

The concept of the plasma state is described in this chapter, as well as the successive diagnostics invented and developed to study and better understand it. The motivations for this thesis are listed and justified before the presentation of the aim and scope of this manuscript.

Contents

1.1 The plasma state

1.1.1 From mythology to science

From time immemorial, humans have always faced manifestations of the plasma state. Observation of natural plasma phenomena caused amazement or fear in our ancestors, who tried to find explanations for

(a) The two sides of the Geissenklösterle ivory plate. It is, to date, the oldest identifiable visualization of an asterism [2].

(b) Reverse of the Babylonian tablet containing the record of the aurora in 567 BCE [6].

(c) Thor's Fight with the Giants (1872) by Mårten Eskil Winge.

Figure 1.1: Examples of historical marks from natural plasma states on human history.

such intriguing and magnificent natural events. Lacking a scientific background, they usually attributed such phenomena to deities.
While the first depiction linked to the observation of a constellation (composed of some celestial plasma objects such as stars and nebulae) is estimated to date from 30000 to 36000 BCE [2] (see Figure 1.1a), it was only after breakthroughs such as the invention of writing, probably developed under the first human civilizations in Egypt and Mesopotamia, that reliable dateable proofs of these observations were recorded. The world's earliest known star map was found in Egypt, dating approximately from 1534 BCE [3]. In this map are represented some well-known constellations. At the time, constellations were already considered as the personification of local deities.
Impressed by and fearful of lightning and thunder, humans also attributed such events to well-known divinities such as Thor (see Figure 1.1c), Zeus, Jupiter, etc. Similarities between their power and history are intriguing. Historians and linguists believe these gods descend from one first god of lightning named Perk^{w}unos [4], who was venerated in the supposed Proto-Indo-European mythology by a population who lived on the Pontic-Caspian steppes around 4000 years BCE [5].
Most aurorae appear in frozen underpopulated regions and the occurrence of such phenomena is rare. The earliest dateable observational proof of such magnificent plasma phenomena come from a Babylonian astronomical text (see Figure 1.1b). This observation was made during the night of March 12 in 567 BCE at Babylon [6]. During this era, aurorae were attributed to either Gods or spirits.

Another common feature of natural plasma phenomena are their proximity to the concept of fire. This leap can be attributed both to the role of lightning in wildfire and the ability of plasma states to emit light in a similar way to fire. This misunderstanding of the difference between plasma and combustion events created a bias of interpretation that followed the first scientist working in plasma physics. Unfortunately, it will take much more time to master the plasma state than it took to master fire.

The first attempts to explain, understand and demystify a natural plasma phenomenon (even if the word "plasma" did not exist at the time) come from the American Benjamin Franklin (portrait in Figure 1.2a). Through the invention of the lightning rod in 1752 [7], humans entered the era of mastering of the plasma state. In his first paper, Benjamin Franklin described the "the wonderful Effect of Points, both in drawing off and throwing off the Electrical Fire". From his experimentation, he discovered the role of the electricity in lightning, but he still did not understand the nature of the plasma state and simply called it electrical fire.
In his lifetime, Benjamin Franklin tried to describe another plasma phenomenon: the aurora borealis. In a paper finished by his grandson in 1779, he gives the following explanation of the aurora borealis:

> May not then the great Quantity of Electricity brought into the Polar Regions by the Clouds

> which are condensd there & fall in Snow, which Electricity would enter the Earth but cannot penetrate the Ice; May it not, I say, as a bottle overchargd, break thro that low Atmosphere and run along in the Vacuum over the Air towards the Equator, diverging as the degrees of Longitude enlarge, strongly visible where densest, and becoming less visible as it more diverges, till it finds a Passage to the Earth in more temperate Climates; or is mingled with their upper Air? [8]

Once more, Benjamin Franklin had good intuition concerning the role of electricity to induce such events. Nevertheless, most of the arguments about the low conductivity of polar regions are incorrect. A correct explanation was not possible at the time due to the lack of knowledge on atmospheric stratification and in particular the presence of the magnetosphere.

In 1875 [9] humans made a significant step forward towards understanding the plasma state (called "radiant matter" at the time) with the first observation of a plasma inside a Crookes Tube by the English physicist William Crookes (portrait in Figure 1.2b). With reproducible experiments available in laboratories, more exhaustive experiments and observation became available.
The English physicist Joseph John Thomson (portrait in Figure 1.2c) studied a reproducible phenomenon observed inside Crookes tubes named cathode rays. From experiments, he proved in 1897 [10] that this phenomenon originated from negatively charged particles much lighter than ions. A few years later, this negatively charged light particle would be called the "electron".

The previous experiments and interpretations allowed the development of the necessary concepts and vocabulary for the description of the behavior of the plasma state constituents. From this scientific background, scientists such as the Norwegian Kristian Olaf Bernhard Birkeland (portrait in Figure 1.2d) were better able to describe the composition of the interplanetary space and beyond:

> According to our manner of looking at the matter, every star in the universe would be seat and field of activity of electric forces of a strength that no one could imagine.
> We have no certain opinion as to how the assumed enormous electric currents with enormous tension are produced, but it is certainly not in accordance with the principles we employ in technics on the earth at the present time. One may well believe, however, that a knowledge in the future of electrotechnics of the heavens would be of great practical value to our electrical engineers.
> It seems to be a natural consequence of our points of view to assume that the whole of space is filled with electrons and flying electric ions of all kinds. We have assumed that each stellar system evolutions throws off electric corpuscles into space. It does not seem unreasonable therefore to think that the greater part of the material masses in the universe is found, not in the solar systems or nebulae, but in "empty" space. [11]

From this hypothesis of electron and ion profusion above the atmosphere, he built the theory of the aurora in 1902. Most of the concepts of its theory remain correct today, but it was not until the year 1967 that validation became possible, with experimental observations from the U.S. Navy satellite 1963-38C dedicated to ionospheric study.

Finally, one of the most important scientists for plasma physics development is certainly the American physicist Irving Langmuir (portrait in Figure 1.2e). In 1924 Irving Langmuir invented a probe that bears his name now [12,13]. The Langmuir probe was the first diagnostic that enabled quantitative experiments inside the plasma medium. The increased knowledge on the plasma state composition led him to ascribe the word "plasma" (inspired by the blood plasma medium) to what used to be called "radiant matter". The word "plasma" better reflects the complexity of the structure and behavior of such a medium; it does not reflect only on its ability to emit light. In an article, Langmuir gives a relatively precise definition of what he called "plasma":

> It seemed that these oscillations must be regarded as compressional electric waves somewhat analogous to sound waves. Except near the electrodes, where there are sheaths containing very few electrons, the ionized gas contains ions and electrons in about equal numbers so that the resultant space charge is very small. We shall use the name plasma to describe this region containing balanced charges of ions and electrons. For purposes of calculation we may consider the plasma to consist of a continuum of positive electricity having a charge density ρ;with free electrons distributed within it, the average electron space charge being ρ. [14]

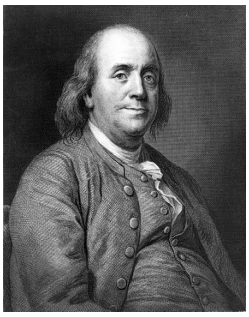

(a) Benjamin Franklin (1706-1790)

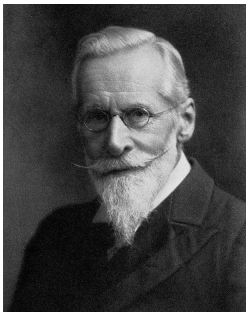

(b) William Crookes (1832-1919)

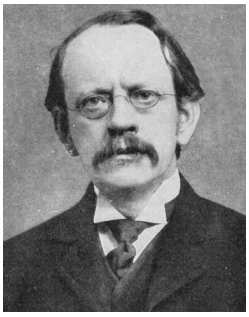

(c) Joseph John Thomson (1856-1940)

(d) Kristian Olaf Bernhard Birkeland (1867-1917)

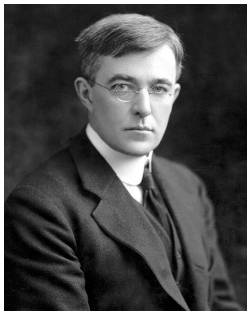

(e) Irving-Langmuir (1881-1957)

Figure 1.2: Some of the remarkable physicists who contributed to the emergence of plasma physics.

From this clear definition, Irving Langmuir settled the key concepts that characterize the plasma states and opened a new branch of physics. He also significantly contributed to the increased diversity of plasma diagnostics and plasma sources that led to progress on the application of the plasma state [15] [16].

1.1.2 Current and future applications

From a better understanding of the plasma state enabled from the discoveries of many pioneers, many applications related to the plasma state arose. Today it is widely used for applications such as welding [17], etching or manufacturing [18] of solar cells for example. Plasma physics also has a long history in ion sources [19], where extracted ions are used daily in particle accelerators to perform experiments. Ions created by a plasma source can also be accelerated to create thrust, an increasing number of satellites only use electric thrusters [20] for orbit transfer, deorbiting or even lunar missions [21]. Spacecraft can also use plasma actuators for reentry control.
Although widely used, some of these technological plasmas are still poorly understood. More intensive research activities in the field may lead to a broader range of usage and higher performances of the associated technologies.

Even more exotic applications of plasma are still under development. By understanding how a plasma discharge catalyzes chemical reactions, specific plasma sources may allow conversion of CO_2 into solar fuels with competitive efficiency levels [22]. The effect of reactive species (generated inside plasmas) on living cells is studied in plasma biomedicine [23]. Finally, a deeper understanding of how instabilities develop inside a plasma could lead to the use of fusion reactions as a cost-effective and almost unlimited way to produce electricity on earth [24].

Improvement of our understanding of the physics of these plasma sources is possible only through complementary theoretical and experimental investigations. Throughout this thesis, we play our part by supplying and discussing reliable experimental results obtained on three different plasma sources.

1.2 The motivations for electron properties characterization

The scope of this thesis mainly focuses on the study of low-temperature and pressure magnetized plasma sources for technological applications. Inside these plasma sources, an applied electric field (DC or AC) generates the plasma inside dedicated plasma reactors while a specific magnetic field topology near the plasma source enhances its operation. Three main arguments motivated the characterization of electron properties.

1.2.1 A key actor for low-temperature plasma physics

The behavior of low-temperature and pressure magnetized plasma sources is governed to a considerable extent by electrons properties. Electrons being much lighter and more mobile than other species, they play a significant role in:

- **Energy transfer:** Kinetic energy gained from an external electric field rises with a quadratic slope with time: t^2/m (where t is the time and m the mass of a given charged particle). The mass ratio between ions and electrons being on the order of 10 000, at short time scales the energy gained by light particles is much higher. Therefore electrons are largely responsible for energy transfer from the electric field towards the plasma; their kinetic energy can quickly reach tens of electronvolt when collisionality is low.

- **Excitation and ionization:** On top of being energetic, the processes of electron impact on neutral are much more efficient at removing or exciting the electrons of atoms than the same process between two neutrals. As a result, ionization and excitation of atoms and molecules from electron collisions is much more efficient in cold non-thermal discharges [25].

- **Energy dissipation:** A small part of the energy transferred to electrons leads to excitation and ionization of the surrounding atoms or neutrals. Most of the remaining energy leaves through heating of the closest plasma source walls. Electron properties have a significant influence on this process.
  One part of the heat load comes from ions accelerated by the sheath voltage, which is usually proportional to electron temperature. The other part comes from the few electrons in the high energy tails of electron velocity distribution function; only this population can work its way up the sheath barrier and directly impact and heat the wall.

Electron properties are thus a crucial parameter in most of the fundamental processes for plasma generation. Knowing their properties allows an estimation of not only both energy transfer efficiency to the plasma and ionization rate, but also one part the heat flux towards the plasma source walls.

1.2.2 Sensitivity to external parameters

In addition to their central role in the plasma properties, electrons are also very sensitive to external parameters such as the magnetic field, wall material, or the gas used for plasma generation.

Self-generated magnetic fields or externally applied magnetic fields modify electron behavior inside the plasma. Indeed, the Lorentz force makes charged particles gyrate around magnetic field lines. Due to the light mass of the electrons, their gyro-radius is much smaller than that of other particles. Even a low-intensity magnetic field can magnetize electrons by making the gyro-radius smaller than the characteristic size of the plasma source. The transition from non-magnetized to magnetized plasma has significant consequences. Magnetized plasmas lead to a modification of electron mobility; the way it is modified depends strongly on the magnetic field configuration.
Crosswise from the electron trajectory, the magnetic field can act as a low energy filter. It filters a range of electron energies and can lead to a separation of the plasma into two regions. If a wall is along the trajectory, plasma-wall interaction can significantly decrease [26] and also contribute to the changes in plasma properties.
Parallel to the electron trajectory, the magnetic field can trap electrons inside a closed trajectory through either the magnetic mirror effect or by creating closed magnetic field lines. The addition of an electric field allows efficient heating of electrons. Such configurations produce highly energetic electrons which quantitatively modify the plasma discharge behavior [27].

The addition of a magnetic field also produces new modes of oscillation of electrons. Waves already present are significantly modified while new types of waves allowed exhibit behavior which depends strongly on their direction of propagation relative to the magnetic field lines [28]. Such waves may contribute to the production of electrons with nonisotropic properties and non-classical electron transport across magnetic field lines.

The nature of the walls facing the plasma can also significantly affect electron properties. Following the impact of an ion or an electron coming from the bulk plasma, walls can emit new electrons. This process is characterized by the secondary electron emission coefficient, which corresponds to the number of secondary electrons emitted for one incident particle. Accelerated by the sheath, secondary electrons can feed a second electron population with temperature sometimes different from the bulk plasma. For high values of the secondary electron emission coefficient, the sheath may transit from a classical Debye sheath to space charge limited sheath. To maintain zero current toward the walls, electron losses towards the walls would increase. The increase in electron losses would have the consequence of decreasing the sheath potential and increasing the wall temperature due to the lower temperature of the secondary electrons emitted. From the modification of the losses toward the wall, the secondary electron emission process would modify the macroscopic properties of the plasma. Moreover, in the presence of a magnetic field, some of the secondary electrons may have an initial velocity vector perpendicular to the magnetic field direction; it would contribute to increased mobility across magnetic field lines through the so-called near-wall conductivity [29].

Because impact ionization of neutral and ions is one of the main paths for electron energy damping, the gas used for the discharge largely affects electron properties. Ionization energies of the gas used are one of the parameters which shape the electron energy distribution function. While in a noble gas plasma electrons with energies up to 24.6 eV are necessary for the first ionization of a neutral at ground state, energies below 5 eV are enough for most of the alkali metal family. For example, if we consider the seeding of metal atoms inside a noble gas-based plasma, this would have the consequence of allowing electrons with low energies to contribute to ionization. Such a process could be induced from the sputtering of a metallic wall, for example, and would lead to a reduction of the electron mean energy and may increase electron density.

1.2.3 Information needed for simulations

As pointed out in Section 1.2.2, electron properties and plasma behavior is strongly dependent on external parameters. Quantitative prediction of plasma behavior can be obtained only through sophisticated numerical simulations. Still, simulations are not self-sufficient; experimental measurements are necessary beforehand and afterward.

Plasma simulations use databases of experimental values of differential cross-section (ionization, charge exchange, moment transfer, etc.), secondary electron emission coefficient, and sputtering yield. Even if quantum mechanics simulations are now able to predict the differential cross-sections of simple systems, experimental values are still needed for either validation or for characterization of complex systems of atoms and molecules. The secondary electron emission coefficient is also a parameter complex to predict because it is an integrated value (a sum over electron, ion, and metastable impact contributions) which is expected to depend on wall purity [30] and microstructure; sophisticated experimental investigations are once more essential to accurately estimate such a parameter or validate the simulated value.

Once simulated, results from simulations are only a representation of reality; they still need to be validated. For validation, it has to be verified that the simulation correctly reproduces phenomena and conditions observed inside the plasma. Because electrons dictate most of the physics inside a low-temperature magnetized plasma, prediction of experimentally-observed electron behavior inside the plasma is a trustworthy indicator for simulation validation.
For example, plasma instabilities are one of the phenomena that depend on electron behavior inside the plasma. Theoretically, sophisticated PIC simulations can simulate some of these instabilities. Experimentally, diagnostics such as coherent Thomson scattering allow measurement of the electron density fluctuation and through this, identification of different waves. Simulations of some of the plasma sources studied in this thesis [31, 32] have already been strengthened through comparison to experimentally-measured instabilities .
Thermal properties of electrons, such as density, temperature, and drift velocity, are other appropriate quantities for validation of simulations. The ability of a plasma simulation to reproduce temporal and

spatial profiles of electron properties measured in parametric studies would tend to validate the reality of the representation made by the simulation. The magnetic field and numerous multiscale instabilities inside the plasma source studied in this thesis are expected to lead to non-Maxwellian energy distribution functions for electrons. For such cases, kinetic models are necessary, and the electron velocity distribution function would be the accurate experimental information for code validation.

1.3 Methods for electron properties characterization

Section 1.2 highlighted the interest of electron properties characterization. Diagnostics methods for electron properties measurement have a long history in plasma physics. Each diagnostic has its domain of application depending on the range of electron properties that can be detected, the scope of validity of the theory used for data analysis and the spatio-temporal resolution accessible. This section performs a brief historical introduction of the main diagnostics used for electron property investigation as well as a description of their characteristics.

1.3.1 Langmuir probes

Invented in 1924 by Langmuir [12], Langmuir probes were the first tools for quantitative plasma (called "radiant matter" at the time) investigations. Since, they have been extensively used to probe various type of plasmas [33–35]. The success of this diagnostic can be attributed to its cheapness and simplicity to implement. In its simplest version, a Langmuir probe is a simple electrostatic probe made of a metallic collector with dimensions determined according to the plasma conditions expected. Langmuir probes are directly inserted inside the plasma and polarized to obtain a current-voltage characteristic at the position probed. From the current-voltage curve, probe theories [13, 36] allow the estimation of electron density, temperature and Electron Energy Distribution Function (EEDF) as well as plasma potential and ion flux.

However, Langmuir probes have several shortcomings which partly cancel out their advantages.
When inserted into a plasma discharge, a Langmuir probe can lead to significant plasma perturbation [37]. At large scale, the current collected by the probe is sometimes not negligible and can temporally modify the discharge mode as well as properties of electrons. At small scales, for plasmas with energetic electrons and ions, significant sputtering of the probe can occur and modify plasma properties around the probe.
As pointed out above, one has to deal with significant sputtering of the probe for plasmas with highly energetic particles. Such a process can rapidly modify the total surface area of the probe during the time of the experiment. In such cases, the estimation of the effective current collection area of the probe is challenging. Fast probe displacements [38] are used to reduce these sputtering issues. Still, Langmuir probes remain poorly-adapted for the most energetic regions of some plasmas.
Available probe theories also have limits in magnetized plasma regions and for high-pressure collisional plasmas [39, 40]. For these plasmas, the required conditions for the application of conventional theories such as an electron mean free path greatly exceeding the sheath radius are sometimes not satisfied or are challenging to achieve.
Finally, plasma properties measured with a Langmuir probe remain an average along various dimensions. One obtains an estimate of electron properties averaged over the various directions the Langmuir probe can collect electrons; this wholly depends on the probe design. The properties estimated are also an average over space, with the resolution limited by the fixed dimension of the active collection area of the current; this uncontrolled surface area depends on the probe size and the Debye screening length associated with the properties of the plasma probed. Lastly, a limited time resolution arises from the time needed for the polarization of the probe over the needed range.

1.3.2 Optical emission spectroscopy

Optical emission spectroscopy (OES) is a passive diagnostic originally used to probe astrophysical plasma [41, 42]. For a simple plasma containing only hydrogen atoms, protons, and electrons, the method is relatively straightforward. After estimation of electron density (with a Langmuir probe for example), the emission line intensities are used to estimate electron temperature and eventually obtain information on deviations of the EEDF from the Maxwellian case.

The development of laboratory plasmas with significantly different physics from astrophysics plasma needed more complex OES theory to be applied [43, 44]. In low-pressure laboratory plasmas, electrons are

frequently out of equilibrium with transient phenomena. Models for estimation of the density of excited states population are needed to compute electron temperatures from emission intensities efficiently. This task is usually complicated as such populations do not necessarily follow a Boltzmann statistic distribution. The use of a collisional radiative model is possible [44], but it requires a complete analysis of the excitation and de-excitation of the metastable levels as well as a highly-accurate knowledge of the associated cross-sections, which are challenging to obtain for some particles. The corona equilibrium model is a relatively simple alternative, but it relies on assumptions regarding the concentration of excited states and the nature of the transitions involved.

One last fundamental limit of OES appears for probing of a plasma source with high electron temperature. Most excitation cross sections are weakly dependent on the electron energies above 20 eV. As a consequence, the estimation of electron temperature from some line intensities ratio has poorer accuracy at high energies [45, 46].

Because it is a passive method, OES is usually non-perturbative. However, OES methods can sometimes be considered as active when a small amount of rare gas must be added to the plasma in order to simplify spectral analysis [47]. This method allows one to focus only on the emission from the Paschen 2p levels and consider a simplified radiative model. This simplification is obtained at the cost of possible perturbations of the plasma, even if these perturbations are expected to be much less significant than if hydrogen, for example, were injected [48].

An attempt to perform temporally resolved OES is possible. A prior estimation of the various transient time scales (de-excitation, excitation, ionization, electron relaxation, etc.) remains necessary to know the lowest time resolution worth considering. Still, the lowest time resolution achievable is often limited by the detector resolution, which is usually the result of a trade-off between spatial, spectral, and temporal resolution.

1.3.3 Interferometry

Interferometry also has a long history as an active plasma diagnostic technique [49,50]. Interferometric methods generally use the dependence of the (complex) refractive index on the density of the plasma. The phase shift between a reference beam and a beam sent through the plasma allow an estimation of the electron density. Although simple in principle, its use only became widespread after the development of the first coherent light source such as the MASER [51, 52]. Coherent microwave light sources eased the achievement of a coherence length large enough to insert the plasma source inside one arm of the interferometer [53–55].

Nowadays, a wide range of coherent light sources are available for interferometry studies; the method sensitivity increases with the wavelength of the light-source (while the associated frequency remains below the plasma frequency). On the other hand, higher spatial resolution is achievable at a lower wavelength. The choice of the light source wavelength is a trade-off between the sensitivity and spatial resolution needed. Another parameter to take into account is the higher probability of perturbing the plasma through simple or multi photo-ionization processes if one wants to work at a low wavelength.
Overall, if the characteristics of the light source used are carefully chosen, interferometry remains a non-invasive, non-perturbative measurement technique for electron density estimation. Interferometry can easily reach a relatively high temporal resolution when the response time of the detector is not a limit. While spatial resolution along the transverse direction can be tuned depending on the light source wavelength, the electron density estimated is an averaged value along the path traveled by the light beam inside the plasma and this constitutes the most important drawback for the diagnostic in many applications.

1.3.4 Terahertz time-domain spectroscopy

Terahertz time-domain spectroscopy (THz-TDS) technique is similar to interferometry. Both rely on the measurement of the absorption and phase delay induced on a microwave traveling through the plasma to estimate electron density and sometimes collision frequency. Contrary to interferometry, which uses a continuous monochromatic microwave, THz-TDS deals with a short pulse of microwave electromagnetic radiation with a broadband spectrum (typically in the 0.1 THz to 40 THz range). Its first application was dedicated to the characterization of electron properties inside semiconductor plasmas [56]; this technique allowed characterization of electron dynamics inside such plasmas with outstanding subpicosecond

resolution [57].
Application of THz-TDS to gaseous plasma is more recent [58]. The lower phase shift induced by low-density plasmas makes its application more challenging. Since this first application, it has been applied to some RF [59] or pulsed [60] plasma sources as an alternative to the commonly used Langmuir probes.

The main advantage of THz-TDS is the higher time resolution obtained in comparison with interferometry; nevertheless, longer measurement times are necessary to compensate for reduced sensitivity. As for interferometry, with this technique, the electron properties estimated are the averaged value along the beam path. The transverse resolution depends on the size of the light beam; it can reach a length scale below a centimeter. The highest resolution is limited either by the diffraction limit of the electromagnetic wave used (wavelengths in the millimeter length scale range and below) or the lowest signal detectable [60, 61].

1.3.5 Thomson scattering

Thomson scattering is the process of elastic scattering of electromagnetic radiation from free charged particles (free electrons for example). Explained for the first time at the beginning of the 20^{th} century by Joseph John Thomson [62, 63], its theory shows that it is usually a simple and straightforward way to probe electron properties [64, 65]. Despite the relatively large probability of Thomson scattering events in comparison to other processes such as Rayleigh scattering, the few scattering particles inside laboratory plasmas have made its detection challenging.

The first observation of Thomson scattering events observed dates back to 1958 with the detection of the backscattering Thomson signal from free electrons of the ionospheric plasma [66–68]. For these experiments, the scattering volume probed was large enough to compensate for the low plasma density. The electromagnetic wave emitted by the powerful radar pulses, backscattered by the numerous scattering particles encountered inside the large scattering volume, was large enough for detection. Due to the broad altitude range probed, properties of scattering electrons covered a broad range. As a result, extensive theoretical work was performed to explain the unexpected spectra of the backscattered light observed [69].

The application of Thomson scattering diagnostics to laboratory plasma sources required technological breakthroughs. Because the plasma size and density of such sources are relatively small, the number of scattering particles inside the probed volume is usually low. Increasing the scattered signal would require increasing the intensity of the incoming electromagnetic wave to levels not available with contemporary light sources.
To separate the Thomson scattering signal from the intense optical emission signal from laboratory plasma, it was necessary to await the discovery and demonstration of the possibility to generate energetic pulses of light with the Q-switch ruby laser [70] in 1962. Coupled with the already well tried and tested technology of the PhotoMultiplier Tube (PMT) [71], detection of Thomson scattering signals were now feasible inside laboratory plasma sources.

The high instantaneous power available after the discovery of Q-switch lasers led to the first implementation of Thomson scattering for laboratory plasma investigations. The first result obtained on a magnetically focused electron beam [72] proved the principle of the diagnostic. During the years that followed the use of Thomson scattering was extended to other plasma sources such as theta-pinch plasmas [73] and arc plasmas [74]. Work by theorists also continued on the ways to extract pieces of information from the Thomson spectra shapes [75], in particular for relativistic electrons and in the coherent regime.

The most popular application of Thomson scattering remains that of Peacock et al. [76]. At the time, a competitive environment reigned with a race toward nuclear fusion mastery through plasma machines. When the Soviet delegation announced in 1965 that their Tokamak machine was producing electron temperatures up to 1 keV (at least ten times that of any other machine), many scientists remained skeptical. The main arguments of the opposition criticized the indirect method based on the measurement of magnetic properties of the plasma for electron temperature estimation. To put an end to the controversy, the Kurchatov Institute in Moscow decided to invite the team from the Culham laboratory led by N. Peacock to employ a Thomson scattering diagnostic on their Tokamak. The UK team was well-known and respected for their expertise on Thomson scattering on plasma discharges [74, 77]. The success of the campaign in proving the claimed temperature of the plasma strengthened the role of the tokamak as a leading configuration for plasma confinement in fusion plasma research and the popularity of the Thomson scattering diagnostic for investigation of such plasmas.

The increased availability of pulsed lasers and intensified detectors led to the extension of the Thomson scattering diagnostic to a larger range of plasma sources [78–83].
The success of this technique relies on its numerous advantages. Firstly, this diagnostic is non-invasive if the laser intensity remains below some limits depending on the plasma conditions [84] [85]. Inside the scattering regime probing individual electron properties (incoherent regime) estimation of electron density, temperature and drift velocity from the spectrum of the scattered light is straightforward. Under certain hypotheses and with a finer analysis of the Thomson spectrum shape, extraction of the EEDF is possible from the spectral shape derivative. Finally, spatial resolution in the millimeter scale and temporal resolution only limited by the incoming pulse duration (usually in the tens of nanoseconds) are easily achievable. The drawbacks of Thomson scattering are due to the low signal levels available for detection; the signal is spectrally close to a relatively intense peak of intensity at the wavelength of the incoming light. This intense peak is due to both reflections on surfaces near the probe volume and Rayleigh scattering on neutrals and ions. For plasmas with a low electron density and temperature, the redistribution of the peak can significantly deform the Thomson spectrum. In these cases, it is necessary to spectrally filter the parasitic light with methods that often reduce the sensitivity of the diagnostic [64].

1.4 Aim and scope of this thesis

In recent years the range of application of low-temperature plasma source has significantly grown [86]. For devices operated at atmospheric pressure, the large plasma density has eased the use of Thomson diagnostics for their characterization; in the low density of low-pressure plasma sources, characterization has been more challenging. This thesis started from this analysis of a lack of reliable diagnostics to probe electron properties for a selection low-temperature and pressure magnetized plasma sources. Beyond simple characterization of electron properties, it was established previously that a complete physical understanding of such sources (including the role of instabilities and self-organization) could be advanced through the development of an ITS diagnostic.

1.4.1 Investigations on magnetized plasma sources for simulation validation

The study of Hall thruster, planar magnetron, and ECR ion source plasmas is the main focus of this thesis. These sources belong to the subgroup of magnetized plasma sources. It means that they share the common feature of using a magnetic field to trap electrons along the field lines. By doing so, the residence time of electrons increases, and the ionization of the surrounding gas is more efficient. As a result, these plasma sources generate plasmas with a high degree of ionization and relatively energetic electrons. While these are interesting characteristics for their applications, such characteristics participate in the complexity of the associated physics.

These plasmas sources expected to be out of thermal equilibrium at certains positions are better simulated using fully kinetic 3D models. Such computationally time-intensive simulations are still under development. For the moment, simulations can predict discharges regimes [87], spontaneous organization of plasma structures [31] or the possible contribution of instabilities in electron heating mechanism [88]. However, device design through modeling of the full spatial and temporal scales of the sources is not possible for the moment. Time-dependent features, spatial complexity, and anisotropy of these plasmas may generate large-scale self-organization such as spokes and contribute to the increased plasma complexity. The complexity of contemporary simulations and understanding of the role plasma turbulence still has to increase to enable simulation of the entire plasma sources.

The growth potential of accurate modeling and methods for source development depends on the availability of a reliable diagnostic for investigation of electron properties inside a given plasma source. This shared assessment to improve the understanding of the physics of different plasma sources led to a collaboration between three laboratories for the development of a reliable diagnostic. Each of the three laboratories involved in the collaboration contributed their expertise on one of the plasma sources (Hall thruster, planar magnetron, and ECR ion source) and financial support for the diagnostic development.

At the ICARE laboratory of the CNRS, investigations on the Hall thruster technology were carried out. The development of the ITS diagnostic and its specific application in the thruster context was envisaged as a complementary development to enrich plasma turbulence measurements achieved using the coherent Thomson scattering diagnostic (PRAXIS) [89] .
Planar magnetron investigations were carried out at the LPGP laboratory of the CNRS. The TMP-DS

team is equipped with numerous vacuum chambers for experimental investigations as well as various models for plasma simulations [90].
Investigations of the ECR ion source took place at the LEDA laboratory of the CEA Saclay, specializing in the design of ion sources for particle accelerators and the development beam diagnostics [91, 92].

1.4.2 Design of a new Thomson scattering diagnostic

As shown in Section 1.3, in the incoherent regime, Thomson scattering is the only diagnostic method which enables the measurement of electron density, temperature, and drift velocity at the same time without significant plasma perturbation. The temporal and spatial resolution of this diagnostic has the other advantage of being high enough to resolve some temporal dynamics and gradient sizes inside the plasma discharge. Because we expect electrons out of Maxwellian equilibrium inside the sources studied, the ability to extract the EVDF from the Thomson spectrum shape is an important diagnostic property.

From the previously presented arguments, Thomson scattering stands out from the other diagnostics for efficient characterization of the plasma sources mentioned above. Still, the development of the required diagnostic remained challenging; the diagnostic needed to be sensitive enough to probe electron densities down to the $1 \times 10^{15}\,\mathrm{m}^{-3}$ to $1 \times 10^{17}\,\mathrm{m}^{-3}$ range. Until now, few Thomson scattering diagnostics have been able to report measurement of densities down to this range. When such sensitivities were realized, it involved cumbersome diagnostic design hardly transportable from one laboratory to another for multiple implementations on various plasma sources.

Recent advances in some of the critical technologies used for Thomson scattering diagnostics were used to overcome the previously-mentioned difficulties. While an improvement in laser design and light filter technologies allowed space-saving on the diagnostic, efficient light detectors permitted sensitive light detection while remaining flexible to the range of plasma parameters expected.

1.5 Content of the thesis

An introduction to the theory of Thomson scattering and the connection between the scattering spectrum and plasma properties is presented in Chapter 2. This chapter also discusses the limits of application of the technique; in particular, it highlights the necessary hypotheses for signal interpretation.

A description of the diagnostic design, as well as justifications of technological choices, is the topic of Chapter 3. This chapter also describes the method for calibration and estimation of the electron properties of the plasma probed. It ends with an assessment of the limits of the diagnostic due to plasma perturbation or distortion of the scattered signal.

The chapters which follow discuss chronologically the results of the investigations performed on the various plasma sources. Chapter 4 deals with the study of planar magnetron discharges in both DCMS and HiPIMS mode. It discusses the axial profiles and temporal profile of the estimated electron properties obtained under various discharge conditions. Chapter 5 deals with the implementation of the Thomson scattering diagnostic on an ECR ion source. Finally, Chapter 6 focuses on the investigations performed on Hall thruster discharge with various magnetic field intensities, configurations and discharge conditions.

Chapter 2

Basic principles of Thomson scattering

> By dint of being confined to application, one would lose sight of the principles, and when one had entirely forgotten the principles one would follow the methods derived from them badly; one would no longer be able to invent new ones, and one would employ without intelligence and without art the erudite procedures that one would no longer understand.
>
> —*Alexis de Tocqueville, Democracy in America*

A historical introduction of Thomson scattering was presented in Chapter 1, it reminded the necessity to get each tiny discovery into the perspective of its potential. In this chapter, a discussion on Thomson scattering theory is realized in light of our contemporary knowledge.

Contents

2.1 Light scattering

Light scattering is the physical process in which the direction of propagation and energy of an electromagnetic wave is modified from the scattering on particles (atoms, molecules, etc.). The entanglement between the scattered radiation properties and the scattering particles properties allowed the development of probing techniques. Estimation of meaningful information on the scattering particles is possible if the incident light properties are well known, and the scattered light properties correctly analyzed.

To ease the following discussions we consider that the incident light consists of a steady and monochromatic (photons having all the same energy) light. We suppose that the light is perfectly collimated and linearly polarized so that the electromagnetic wave associated with the light intensity is expressed as

$$\boxed{\vec{E}_i(\vec{r},t) = \vec{E}_{i0}\cos(\vec{k}_i \cdot \vec{r} - \omega_i t + \Phi_0)} \tag{2.1}$$

$\vec{E}_{i0}$ indicate both the electric field intensity and the polarization direction (see Figure 2.1), $\vec{k}_i$ is the wave vector of the incident light and ω_i is its frequency, $\vec{r}$ is the vector between the position of the source and the position where the electric field is estimated; finally Φ_0 is the initial phase of the electric field at t =0 s. Unless otherwise specified, light intensities (noted I) will refer to the surface power density of the electromagnetic wave crossing a surface with a unit normal vector collinear to $\vec{k}_i$ (i.e. along the direction of energy propagation), for $\vec{E}_i(\vec{r},t)$ it can be expressed as $I_i = n|E_{i0}|^2/2c\mu_0$.

If we consider the intensity of an incident light beam I_i on scattering particles, only a small fraction I_s of it will be scattered. The scattered intensity is expressed as

$$I_s = n_s L I_i \sigma_s \tag{2.2}$$

where n_s is the volumetric density of scattering particles and L the length of light beam considered. When $n_s L = 1$ (i.e., one scattering particle per meter squared), the coefficient of proportionality between the incident and scattered intensities is called the scattering cross-section, usually noted σ_s for a given scattering regime. From a general point of view, σ_s gives an evaluation of the efficiency of the force that dictates the interaction between the scattered and scattering particles. In that sense, σ_s is tied to each pair of scattered-scattering particles. For light scattering, the scattering cross-section indicates how sensitive the scattering particles are to forces generated by the electromagnetic fields; other scattering processes may involve interactions such as Coulombic, magnetic, gravitational, contact, and so on.
The analysis of the directional distribution of the scattered light is even more characteristic of a scattering process. In the case of a light scattered in the direction of $\vec{e}_s$, the normed unit vector collinear to k_s (see Figure fig:scattering-config), the directional distribution of intensity may depend on the direction of $\vec{e}_s$ with respect to the direction of propagation and the polarization of the incident light. From a parameterization such as that presented in Figure 2.1, the scattering cross-section can be differentiated with respect to the θ and φ variables at a distance r=1 m from the source (i.e., over the solid angle sphere). The differential scattering cross-section obtained gives the probability that the incident light is scattered and deviated through a differential solid angle of $d\Omega$. Mathematically this can be written as:

$$\frac{dI_s}{d\Omega}(\vec{e}_s) = n_s L I_i \frac{d\sigma_s}{d\Omega}(\vec{e}_s) \tag{2.3}$$

For simple scattering processes, it is possible to predict the differential scattering cross-section theoretically. However, for scattering processes with complex scattering particles, experimental investigations are vital for efficient characterization.

While scattered intensity values and their spatial distribution strongly depend on the kind of interaction involved, the spectral distribution of the scattered light also offers a wealth of information on the scattering particle properties. Depending on the incident photon energy the scattering process can be divided into two categories: elastic and inelastic scattering.
Elastic scattering happens when the energy of the incident photon is much lower than any internal energy level of the scattering particles. In this case, the scattering process only affects the scattered photon energy, and modification of the scattered photon energy distribution (or scattered light spectrum) is only due to the Doppler effect induced by the velocities of the scattering particles (thermal or drift components).
When the scattering particle's kinetic energy or internal energy change induced by the incoming photons is no longer negligible, scattering becomes inelastic. At the cost of scattering particle perturbation, inelastic scattering makes the scattered photon energy distribution a bearer of information related to intrinsic properties of the scattering particles (mass, rotational levels, vibrational levels, ...). These pieces of information remain entangled with the Doppler broadening and shift induced by the movement of the scattered particles; this makes the scattered spectra analysis even more complex. Besides, because the dynamic and macroscopic properties of the scattered particles may change, the transition towards inelastic scattering can sometimes cause a change in the differential scattering cross-section.

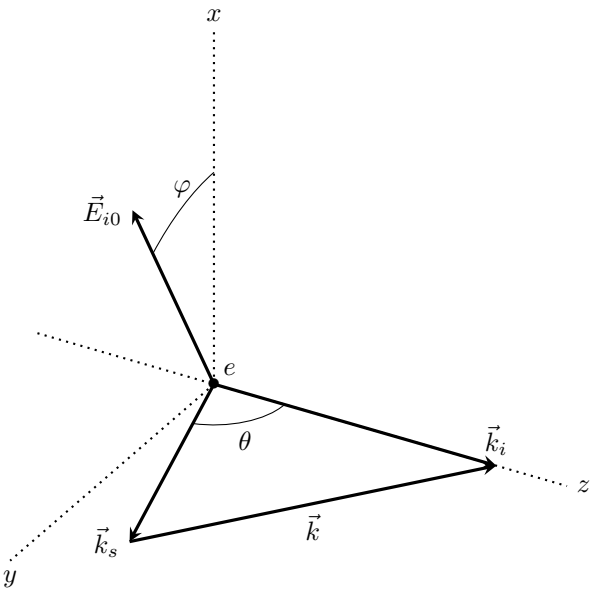

Figure 2.1: Parametrization of the scattering configuration, inside an orthonormal referential linked to an electron (refered as e). By convention $\vec{k}_i$ is defined along the z-axis, the y-axis is chosen so that all scattering wave vectors ($\vec{k}_i$, $\vec{k}_s$ and $\vec{k} = \vec{k}_i - \vec{k}_s$) belong to the (yez) scattering plane. θ indicate the angle between the direction of observation (collinear to $\vec{k}_s$) and the direction of propagation of the laser (collinear to $\vec{k}_i$). φ gives the angle between the normal vector of the scattering plane and the polarization vector $\vec{E}_{i0}$.

The remarks mentioned above show that a scattered photon spectrum contains information on the properties of the scattered particles. The introduction of a distribution function called the spectral form factor and noted $S_k(\omega_s)$ allows the separation of the spectral shape of the spectrum from its intensity. The scattered intensity equation can be differentiated further with respect to the scattered wave frequency (or energy) so that the scattering equation becomes

$$\boxed{\frac{dI_s}{d\Omega d\omega_s}(\vec{e}_s, \omega_s) = n_s L I_i \frac{d\sigma_s}{d\Omega}(\vec{e}_s) S_k(\omega_s)} \tag{2.4}$$

As the spectral form factor is a distribution function, $S_k(\omega_s)d\omega_s$ gives the probability that the scattered photon is found at the frequency ω_s inside an interval $d\omega_s$, and we have $\int_{-\infty}^{+\infty} S_k(\omega_s)d\omega_s = 1$ so that the total probability is equal to one. The subscript k refers to the fact that the form factor shape is characteristic of the dynamics of the scattering particles only along the direction $\vec{k}$ presented in Figure 2.1. Section 2.3 provides a clear demonstration for this.

2.2 Prerequisite for elastic light scattering on free electrons

As pointed out in Chapter 1, this thesis focus on the study of Thomson scattering on free electrons inside the plasma. Thomson scattering corresponds to a scattering regime where charged particles elastically scatter photons. In this thesis, the charged particles of interest will be an electron, from now on and unless otherwise stated, and discussions of Thomson scattering will always refer to the scattering process on free electrons. From a larger-scale approach, Thomson scattering is the low energy limit of a broader inelastic scattering regime named Compton scattering. The transition between both regimes happens when the incident photon energy is sufficiently low to not affect the scattering particle energy levels. Because we will focus more specifically on Thomson scattering on the electrons, the incident photon energy below which the simplified theory of elastic scattering (i.e., Thomson scattering) is relevant can be estimated. At the time of the writing of this manuscript, the contemporary physics theory considers electrons as fundamental point particles with a given charge and no spatial extent, with their translational

kinetic energy the only energy that can be modified. While the photon energy remains at least two orders of magnitude below the electron energy, single-photon scattering event are expected to induce negligible energy changes on the electron. Considering an electron at rest (E_0=511 keV), the elastic-inelastic scattering transition would happen for an incident photon energy of ≈5 keV (i.e. wavelength of ≈240 pm), corresponding to soft X-rays photons. This condition fixes the first fundamental upper limit of usable photon energy for Thomson scattering investigation on an electron.

The plasma properties themselves fix the lower limit of usable photon energy for probing of free-electron inside plasmas. One fundamental frequency named the plasma frequency indicates the natural dynamics of an electron inside the plasma medium. For cold electrons, it depends only on the electron density (n_e) and is expressed as

$$\omega_p = \sqrt{\frac{n_e e^2}{m_e \varepsilon_0}} \tag{2.5}$$

where m_e and e are the electron mass and charge respectively, and ε_0 is the vacuum permittivity. In the presence of an electric field (from an electromagnetic wave for example), separation of positive ions and negative electrons will occur. $2\pi/\omega_p$ gives an order of magnitude of the time needed for the electrons to react in order to screen the applied electric field.
For low frequency events, the electromagnetic wave penetrates the plasma up to a characteristic diffusion depth $\delta = \sqrt{2\rho/\omega\mu_0}$ (with ω the frequency of the incident wave, ρ the plasma resistivity and μ_0 the permeability). However, at a macroscopic scale, the electromagnetic wave is reflected, as if the associated photon did not have enough energy to go through the plasma.
At frequencies higher than the plasma frequency (ω_p), the electron dynamics are too slow to screen the electric field perturbation and the wave can propagate through the plasma medium with negligible attenuation. The plasma frequency sets the limit of reflection of the plasma. The electron densities inside the plasma sources studied in this thesis being below $1 \times 10^{19}\,\mathrm{m}^{-3}$; this sets the lower limit of photon energy needed to propagate to ≈0.1 meV (i.e., a wavelength of ≈10 mm).

The rest of the chapter deals with the use of Thomson scattering to probe electron properties inside low-density plasmas. Because of the scope of this study, the Thomson scattering phenomenon theory will be described under the hypothesis that the energy of incident photons goes from ≈0.1 meV to ≈5 keV (i.e., wavelength from ≈240 pm to ≈10 mm). Chapter 3 will deal with the more restrictive limitations due to technological constraints and light-induced plasma perturbations as well.

2.3 From an individual Thomson scattering process

To start simply, we will focus on the scattering processes with only one electron at a fixed position along the path of a light beam of one meter square in diameter. Under this single scattering hypothesis the coefficient $n_s L$ is equal to 1 inside Equation 2.2, Equation 2.3 and Equation 2.4.

2.3.1 Electron radiation inside a dynamic electric field

Inside the range of incident photon energies introduced in Section 2.2, free electrons inside the plasma will be able to feel the associated electromagnetic field without a quantitative modification of its kinetic energy. If we continue with the single electron approach, Thomson scattering is a scattering event generated by the interaction between an electromagnetic field and an unbounded electron through the Lorentz force.

For convenience, the problem is solved in the reference frame of the laboratory, corresponding to the (x_0,y_0,z_0) coordinates in Figure 2.2. The light source and observer are fixed relative to it while the electron may move. The velocity of the electron inside the laboratory basis is considered low enough ($v_e/c \ll 1$) that relativistic effects and the contribution of the magnetic field to the Lorentz force are negligible. When no other forces act on the electron, the equation of motion simplifies to

$$\frac{d\vec{v}_e}{dt}(t) = -\frac{e\vec{E}_i(\vec{R}_e(t), t)}{m_e} \tag{2.6}$$

$\vec{R}_e(t)$ is the position of the electron at a time t in the laboratory frame. $\vec{E}_i(\vec{R}_e(t), t)$ is the monochromatic electric field introduced in Equation 2.1 estimated at the position of the electron; any electromagnetic radiation with a spectrum inside the interval defined on the previous section could be considered.

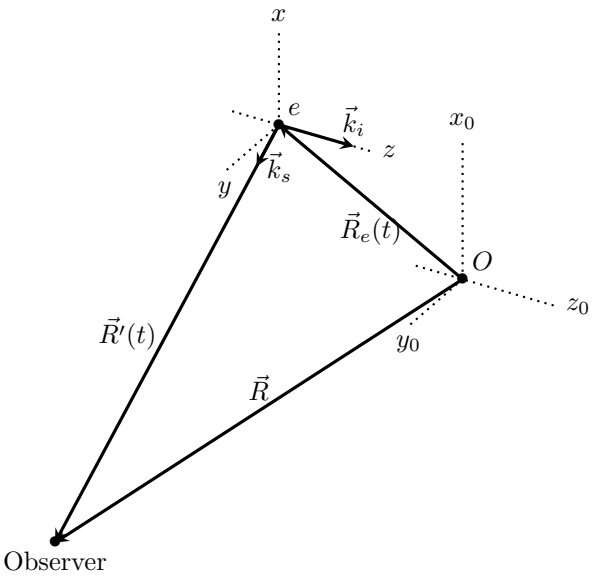

Figure 2.2: Definition of the position vector of respectively the electron $\vec{R}_e(t)$ and observer $\vec{R}$ inside the reference frame linked to the experiment. $\vec{R}'(t')$ is the position vector of the observer inside the reference frame linked to the electron.

The periodic acceleration of the electron from the applied electric field generates its own electric field that can be detected by an observer at a distance $R'(t)$ from it. The electric field sensed by the observer at a time t is related to the dynamics and position of the electron at a retarded time t' (i.e., when it was emitted). Considering the parametrization of Figure 2.2,the retarded time is given by

$$t' = t - R'(t')/c \tag{2.7}$$

The demonstration for the electromagnetic field created by an accelerated electron (non-relativistic) at a distance $R'(t')$ is made in reference [93], the corresponding electric and magnetic field can be written as

$$\begin{cases} \vec{E}_s(\vec{R},t) & = \frac{e}{4\pi\varepsilon_0}\left(\frac{\vec{e}_s-\vec{\beta}_e(t')}{(1-\vec{\beta}_e(t')\cdot\vec{e}_s)R'(t')^2}\right) + \frac{e}{4\pi\varepsilon_0 c}\left(\frac{\vec{e}_s\times((\vec{e}_s-\vec{\beta}_e(t'))\times\dot{\vec{\beta}}_e(t'))}{(1-\vec{\beta}_e(t')\cdot\vec{e}_s)^3R'(t')}\right) \\ \vec{B}_s(\vec{R},t) & = \frac{n}{c}\left(\vec{e}_s\times\vec{E}_s(\vec{R},t)\right) \end{cases} \tag{2.8}$$

with $\vec{e}_s$ representing the unit vector collinear to $\vec{k}_s$, c the speed of light, $\vec{\beta}_e(t')$ is the $\vec{v}_e(t')$ to c ratio and $\dot{\vec{\beta}}_e(t')$ its derivative with respect to the retarded time. The refractive index of the medium, referred to as n, is considered equal to 1 for the rest of the study (valid for the low density of the plasma of our study). The scattered electric field $\vec{E}_s(\vec{R},t)$ is composed of two terms. The first term is named the "velocity field" as it depends only the electron velocity; its decreasing law in $R'(t')^{-2}$ is characteristic of a static electric field. The second term is named the "acceleration field" as it depends on the electron velocity and acceleration; its decreasing law in $R'(t')^{-1}$ and the electric field vector remaining perpendicular to $\vec{e}_s$ are characteristic of a radiated electromagnetic wave.

2.3.2 Intensity of the electromagnetic wave scattered

Some hypotheses related to the experimental conditions lead to the simplification of the expressions for the amplitude and polarization of the scattered wave.

(i) When using Thomson scattering as a diagnostic, the observer/detector is positioned relatively far from the scattering volume in comparison to the distance traveled by the electron during the scattering process. The far field approximation can be performed so that the "velocity field" can be neglected. If the coordinate systems (x,y,z) and (x_0,y_0,z_0) are chosen sufficiently close, the

intensities of the wave at the distances $R'(t')$ and R from the electron are expected to be almost identical (this is not true for the wave phase).

(ii) Because the electron is supposed non-relativistic, the norm of the vector $\vec{\beta}_e(t')$ is much lower than unity.

Under these hypotheses and by expanding the expression of $\dot{\vec{\beta}}_e(t')$, Equation 2.8 reduces to

$$\vec{E}_s(\vec{R},t) = \frac{e^2}{4\pi\varepsilon_0 m_e c^2}\frac{\vec{e}_s \times (\vec{e}_s \times \vec{E}_{i0})}{R}\cos(\vec{k}_i \cdot \vec{R}_e(t') - \omega_i t' + \Phi_0) \tag{2.9}$$

The power density scattered is characterized by the Poynting vector of the wave, defined as

$$\vec{S}_s(\vec{R},t) = \frac{\vec{E}_s(\vec{R},t) \times \vec{B}_s(\vec{R},t)}{\mu_0} \tag{2.10}$$

where $\vec{B}_s(\vec{R},t)$ is the magnetic field wave that can be expressed as a function of $\vec{E}_s(\vec{R},t)$ using Equation 2.8.

The projection of $\vec{S}_s(\vec{R},t)$ on the unit normal vector of a surface gives the intensity I_s of the wave through it. Because in our case the electromagnetic field is emitted by a point source (the electron), the non-collimated power density transported by the Poynting vector decreases with a R^{-2} law. To obtain the typical equation of spatial distribution of the scattered intensity presented in Equation 2.3, the Poynting vector has to be estimated on the differential surface of the sphere of unity radius (i.e., on the solid angle sphere with $\vec{R} = \vec{e}_s$) and projected along the corresponding unit normal vector (i.e., along $\vec{e}_s$). Finally, because most of detectors are not sensitive to the fast oscillation of the light intensity, only a time average can be considered so that the spatial distribution of the scattered intensity is expressed as

$$\frac{dI_s}{d\Omega}(\vec{e}_s) = \overline{\frac{\vec{E}_s(\vec{e}_s,t) \times (\vec{e}_s \times \vec{E}_s(\vec{e}_s,t))}{c\mu_0}} \cdot \vec{e}_s \tag{2.11}$$

Using the cross product identity $\vec{a} \times (\vec{b} \times \vec{a}) = (\vec{a} \cdot \vec{a})\vec{b} - (\vec{a} \cdot \vec{b})\vec{b}$ and knowing that $\vec{E}_s(\vec{R},t)$ and $\vec{e}_s$ are perpendicular lead to the following simplifications

$$\begin{aligned}\frac{dI_s}{d\Omega}(\vec{e}_s) &= \overline{\frac{\vec{E}_s(\vec{e}_s,t) \cdot \vec{E}_s(\vec{e}_s,t)}{c\mu_0}} \\ &= \frac{1}{c\mu_0}\left(\frac{e^2}{4\pi\varepsilon_0 m_e c^2}\right)^2 \underbrace{|\vec{e}_s \times (\vec{e}_s \times \vec{E}_{i0})|^2}_{(1-\sin^2\theta\sin^2\varphi)|\vec{E}_{i0}|^2} \underbrace{\overline{\cos^2(\vec{k}_i \cdot \vec{R}_e(t') - \omega_i t' + \Phi_0)}}_{1/2}\end{aligned} \tag{2.12}$$

The calculation of the cross product in the (x,y,z) coordinate system is straightforward. By recognizing the incident intensity $I_i = (1/2c\mu_0)|\vec{E}_{i0}|^2$, the typical scattering equation is obtained

$$\frac{dI_s}{d\Omega}(\vec{e}_s) = I_i\left(\frac{e^2}{4\pi\varepsilon_0 m_e c^2}\right)^2 (1 - \sin^2\theta\sin^2\varphi) \tag{2.13}$$

By identification with Equation 2.3 the coefficient of proportionality between both intensities is the differential scattering cross section. From a corpuscular point of view, if the photon is considered as a point, the associated surface/cross section can be attributed to the projected surface of an electron. From the estimation of this equivalent surface can be derived the classical electron radius

$$\boxed{r_e = \frac{e^2}{4\pi\varepsilon_0 m_e c^2} \approx 2.82 \times 10^{-15}\,\mathrm{m}} \tag{2.14}$$

According to our contemporary understanding, the electron is a point particle with a point charge; such a distance gives only an order of magnitude of the length scale at which an electromagnetic field and an electron can interact. The Thomson differential scattering cross section now depends on only one characteristic length and on the scattering configuration parameters. It can be expressed as

$$\boxed{\frac{d\sigma_T}{d\Omega}(\vec{e}_s) = r_e^2(1 - \sin^2\theta\sin^2\varphi)} \tag{2.15}$$

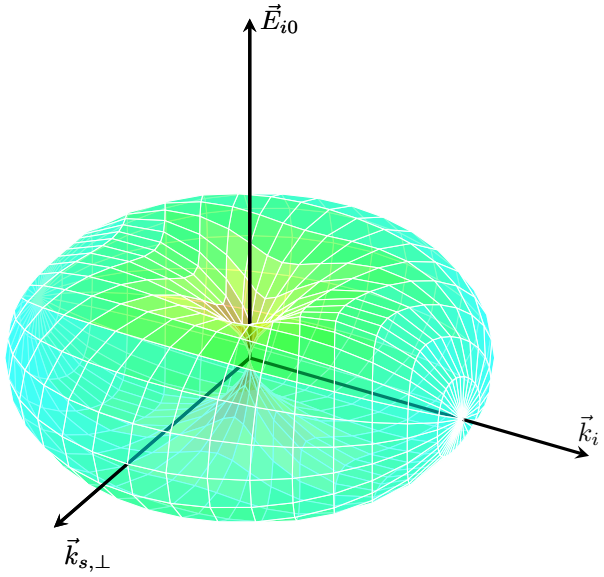

Figure 2.3: Spatial distribution of the differential scattering cross section for Thomson scattering inside the ($\vec{E}_{i0}$,$\vec{k}_{s,\perp}$,$\vec{k}_i$) reference frame linked to the electron.

Fortunately, theoretical calculation of the Thomson scattering differential cross-section in our conditions is relatively straightforward and leads to a simple theoretical expression; it is sufficiently rare to highlight it. The shape of the differential cross-section of Thomson scattering (under all the assumptions performed) shown in Figure 2.3 depends on the direction of the scattered wave vector $\vec{k}_s$ inside the basis linked to the electron and with directions fixed by the incident light polarization vector $\vec{E}_{i0}$ and wave vector $\vec{k}_i$ as well as the perpendicular scattering wave vector $\vec{k}_{s,\perp}$ (special case when $\vec{k}_s$ is perpendicular to both $\vec{E}_{i0}$ and $\vec{k}_i$). In Figure 2.3 the distance of the plotted surface from the origin gives the relative intensity of the differential cross-section. A color gradient is used to help the visualization. Inside the plane created by $\vec{k}_i$ and $\vec{k}_{s,\perp}$ the differential cross-section of Thomson scattering is maximum and goes from r_e^2 to 0 as the $\vec{k}_i$ direction becomes closer to $\vec{E}_{i0}$. Finally, its value is invariant for rotation around $\vec{E}_{i0}$ and central symmetry around the basis origin (relativistic electrons would break this symmetry).

2.3.3 Phase of the electromagnetic wave scattered

The phase of the electromagnetic wave scattered contains implicit information relative to the electron position and dynamics, at the time of the scattering event. As shown in Equation 2.9 it can be expressed as

$$\Phi(t') = \vec{k}_i \cdot \vec{R}_e(t') - \omega_i t' + \Phi_0 \tag{2.16}$$

A clearer view about the entangled information is obtained through a step by step expansion of its constitutive terms.

(i) Inside the the retarded time expression, $R'(t')$ can be expanded as $R'(t') = \sqrt{(\vec{R} - \vec{R}_e(t'))^2} = R\sqrt{1 - (2\vec{R} \cdot \vec{R}_e(t') + R_e^2)/R^2}$. A first order expansion of the square root gives

$$R'(t') \approx R - \vec{e}_s \cdot \vec{R}_e(t') \tag{2.17}$$

(ii) If no collision happens during the scattering process, such that the electron dynamics do not change significantly, $\vec{R}_e(t')$ can be approximated by its Taylor expansion to the first order

$$\vec{R}_e(t') \approx \vec{R}_e(0) + \vec{v}_e t' \tag{2.18}$$

with $\vec{R}_e(0)$ the position of the electron at t'=0 s and $\vec{v}_e$ the electron velocity at $t = t'$ considered constant (the argument (t') of this variable will be omitted for the rest of the discussions).

(iii) Substituting Equation 2.18 inside Equation 2.17 and then inside Equation 2.7 gives

$$t' = t - \frac{R - \vec{e}_s \cdot (\vec{R}_e(0) + \vec{v}_e t')}{c} \tag{2.19}$$

once t' is isolated on one side of the equation, we obtain

$$t' = \left(t - \frac{R}{c} + \frac{\vec{e}_s \cdot \vec{R}_e(0)}{c}\right)\left(1 - \frac{\vec{e}_s \cdot \vec{v}_e}{c}\right)^{-1} \tag{2.20}$$

To start, the Equation 2.18 can be substituted inside the phase of the scattered electromagnetic wave

$$\Phi(t') = \vec{k}_i \cdot \vec{R}_e(0) + (\vec{k}_i \cdot \vec{v}_e - \omega_i)t' + \Phi_0 \tag{2.21}$$

Using the formula $c\vec{k}_i = \omega_i \vec{e}_i$ with $\vec{e}_i$ the unit vector collinear to $\vec{k}_i$ and from the substitution of the expression of t', the expression of the phase becomes

$$\begin{aligned}\Phi(t) &= \vec{k}_i \cdot \vec{R}_e(0) - \omega_i \left(1 - \frac{\vec{e}_i \cdot \vec{v}_e}{c}\right)\left(t - \frac{R}{c} + \frac{\vec{e}_s \cdot \vec{R}_e(0)}{c}\right)\left(1 - \frac{\vec{e}_s \cdot \vec{v}_e}{c}\right)^{-1} + \Phi_0 \\ &= \vec{k}_i \cdot \vec{R}_e(0) - \omega_i t \frac{c - \vec{e}_i \cdot \vec{v}_e}{c - \vec{e}_s \cdot \vec{v}_e} + k_i R \frac{c - \vec{e}_i \cdot \vec{v}_e}{c - \vec{e}_s \cdot \vec{v}_e} - k_i \vec{e}_s \cdot \vec{R}_e(0) \frac{c - \vec{e}_i \cdot \vec{v}_e}{c - \vec{e}_s \cdot \vec{v}_e} + \Phi_0\end{aligned} \tag{2.22}$$

The typical phase terms of the scattered electromagnetic wave Doppler shifted are now visible. The associated frequency and wave vector are respectively $\omega_s = \omega_i(c - \vec{e}_i \cdot \vec{v}_e)/(c - \vec{e}_s \cdot \vec{v}_e)$ and $\vec{k}_s = k_i(c - \vec{e}_i \cdot \vec{v}_e)/(c - \vec{e}_s \cdot \vec{v}_e)\vec{e}_s$. With these new notations, the scattered electromagnetic field can finally be expressed as

$$\boxed{\vec{E}_s(\vec{R}, t) = \frac{r_e}{R} \cos\left(k_s R - \omega_s t + (\vec{k}_i - \vec{k}_s) \cdot \vec{R}_e(0) + \Phi_0\right)\left(\vec{e}_s \times (\vec{e}_s \times \vec{E}_{i0})\right)} \tag{2.23}$$

with $\vec{e}_s \times (\vec{e}_s \times \vec{E}_{i0}) = (\vec{e}_s \cdot \vec{E}_{i0})\vec{e}_s - \vec{E}_{i0}$

From the expression of ω_s, it is clear that the frequency shift ($\Delta\omega$) between the scattered and incident wave frequency is the result of two Doppler effects. A first Doppler effect happens at the "absorption" with an apparent velocity $\vec{e}_i \cdot \vec{v}_e$ and a second at the "emission" with an apparent velocity $\vec{e}_s \cdot \vec{v}_e$. The associated shift can be derived from the definition of ω_s

$$\omega_s \left(1 - \frac{\vec{e}_s \cdot \vec{v}_e}{c}\right) = \omega_i \left(1 - \frac{\vec{e}_i \cdot \vec{v}_e}{c}\right) \tag{2.24}$$

Isolating the frequency difference and using the formula $c\vec{k}_{i/s} = n\omega_{i/s}\vec{e}_{i/s}$ gives

$$\Delta\omega = \omega_i - \omega_s = (\vec{k}_i - \vec{k}s) \cdot \vec{v}_e \tag{2.25}$$

If the probed wave vector is defined according to the representation in Figure 2.1

$$\boxed{\vec{k} = \vec{k}_i - \vec{k}s} \tag{2.26}$$

The previous equation becomes

$$\boxed{\Delta\omega = \vec{k} \cdot \vec{v}_e} \tag{2.27}$$

This equation illustrates the fact that the two Doppler effect processes are similar to one Doppler effect process induced by the velocity component of the electron along the probed direction defined by $\vec{k}$ (named probed wave vector). Spectral analysis of the scattered light allows an estimation of the electron dynamics along $\vec{k}$ at the time of the scattering event. This point highlights the directional sensitivity of Thomson based diagnostic and the importance of wisely choosing a scattering configuration in order to make the probe wave vector collinear to one of the characteristic directions of the plasma studied.

When looking at a Thomson spectrum as a function of the wavelength with the probe wave vector convention chosen (i.e., $\vec{k} = \vec{k}_i - \vec{k}_s$), a positive wavelength shift (wavelength shifted at a higher value) will correspond to an electron velocity in the same way as the probed wave vector. This convention

is in the opposite direction of the commonly used conventions attributing a positive frequency shift to an electron velocity in the same direction as the probed wave vector. This convention has no influence on the norm of the probed wave vector, for elastic scattering (i.e., $k_i \approx k_s$). It can be expressed as $k = \sqrt{k_i^2 + k_s^2 - 2k_i k_s)} \approx 2k_i sin(\theta/2)$. While the direction of $\vec{k}$ gives the directional sensitivity of the scattering configuration, its norm gives the absolute sensitivity of the Doppler effect. Indeed, because $|\Delta\omega| = 2\sin(\theta/2)/c$ the relative spectral broadening is directly linked to k through the $\sin(\theta/2)$ coefficient. As a consequence, a back-scattering configuration (θ 180°) is the most Doppler shift sensitive configuration while the forward-scattering configuration is insensitive to the Doppler effect.

2.4 Toward collective Thomson scattering effects

As mentioned in Section 1.4.2, the diagnostic developed in this thesis only focuses on the incoherent regime of Thomson scattering. Still, it is useful to correctly explain the origin of the differentiation between incoherent and coherent scattering regimes. In this section, the scattered intensity in both regimes is derived to show the distinction between both regimes. It allows a description of the relevant parameters fixing the regime transition as well as the specificity of each regime. The derivation of the scattered light spectrum for both regimes would be another way to introduce this regime distinction. Such an approach would require more calculations without bringing fundamental insights. The discussion will therefore focus only on the scattered light spectrum in the incoherent regime.

Due to the low differential scattering cross section, all Thomson scattering based diagnostics measure the intensity from the scattering of a light beam on large number of electron (N_e) positioned inside an observation volume (V). The electromagnetic radiation of all these oscillating dipole will add up so that some interference patterns may appears inside the scattered intensity. Using the equations shown on Section 2.3, the total electric field scattered $\vec{E}_s(\vec{R}, t)$ can be expressed as a continuous summation of individual electric fields scattered over the observation volume positions, weighted by the electron density distribution at the positions considered

$$\begin{aligned}\vec{E}_s(\vec{R}, t) &= \int\limits_{\vec{R}_e \in V} n_e(\vec{R}_e, t')\vec{E}_s(\vec{R}, \vec{R}_e, t) d^3\vec{R}_e \\ &= \int\limits_{\vec{R}_e \in V} n_e(\vec{R}_e, t')\frac{r_e}{R}\cos\Phi(\vec{R}, \vec{R}_e, t)\left(\vec{e}_s \times (\vec{e}_s \times \vec{E}_{i0})\right) d^3\vec{R}_e\end{aligned} \tag{2.28}$$

where $n_e(\vec{R}_e, t')$ is the electron density at the position $\vec{R}_e$ at the time of the scattering event (t') and its integral over the observation volume is equal to $N_e(t')$. The hypothesis $\vec{R}(\vec{R}_e) \approx R\vec{e}_s$ is performed for all electrons inside the detection volume. It is valid for sizes of the observation volume small in comparison with the distance of observation (usually true experimentally). This hypothesis implies that all scattered waves measured did propagate the same way once emitted by the scattering particle (i.e., observer at "infinite distance"). The scattered wave properties are fixed at the time of the scattering event. These properties depend only on the position and dynamics of the electron at this time. Finally it must be highlighted that contrary to the single scattering theory presented in Section 2.3, multiple scattering theory must account for the electron position as a variable as the phase shift induced by the various electron positions is significant. For both single and multiple scattering events, the electron velocity has no effect on the scattered wave intensity (which is not the case for relativistic electrons). Its effects on the scattered waves frequency will be discussed in Section 2.5.

The total differential intensity scattered on the direction $\vec{e}_s$ can be expressed as

$$\frac{dI_s}{d\Omega}(\vec{e}_s, t) = \frac{1}{c\mu_0}\overline{\int\limits_{\vec{i}\in V}\int\limits_{\vec{j}\in V} n_e(\vec{i}, t')n_e(\vec{j}, t')\left(\vec{E}_s(\vec{e}_s, \vec{i}, t)\cdot\vec{E}_s(\vec{e}_s, \vec{j}, t)\right) d^3\vec{i}d^3\vec{j}} \tag{2.29}$$

where $\vec{u}$ and $\vec{j}$ are the two independent mute variables of integration corresponding to electron positions($\vec{R}_e(t')$). A joint distribution function $n_e^2(\vec{u}, \vec{j}, t') = n_e(\vec{j}, t')n_e(\vec{u}, t')$ can be defined. For observation of the scattered power over long periods, the electron density inside the observed volume may change; contrary to the single scattering events described in Section 2.3, these time variations have to be included for a realistic description of a scattering intensity from multiple electrons. The time-averaged operator previously

introduced for estimation of the intensity is more a low frequency filter with a cutoff frequency on the order of the acquisition frequency of the detector.

The differential scattered intensity can be separated into two contributions. On one side the contribution from the power created by the superposition of electromagnetic fields from the same position (from isolated individual electrons) can be identified and corresponds to the case when $\vec{i} = \vec{j}$. The number of occurrences of these events corresponds to the conditional occurrence of coming across the scattered electric field from an electron around the position $\vec{i}$, knowing that the previous occurrence also came from the position around $\vec{j} = \vec{i}$. Mathematically this translates to the following distribution

$$n_e(\vec{i}|\vec{j} = \vec{i}, t') = \frac{n_e^2(\vec{i}, \vec{j}, t')}{n_e(\vec{j}, t')} = n_e(\vec{i}, t') \tag{2.30}$$

The integrals of the power scattered over the remaining electron pairs corresponds to the intensity created by superposition of scattered electromagnetic fields from two electrons at different positions. The probability density of occurrence of these events follows the same distribution ($n_e^2(\vec{i}, \vec{j}, t')$), but only the pairs of positions with $\vec{i} \neq \vec{j}$ are considered. From this division of the domain of integration, the scattered power can be separated in the sum of two terms, and using the linearity of the time average operator, the differential scattered power becomes

$$\frac{dI_s}{d\Omega}(\vec{e}_s, t) = \frac{1}{c\mu_0}\left(\int_{\vec{i}\in V} \overline{n_e(\vec{i}, t')|\vec{E}_s(\vec{e}_s, \vec{i}, t)|^2 d^3\vec{i}} + \overline{\int_{\vec{i}\in V}\int_{\vec{j}\in V\setminus\vec{i}} n_e^2(\vec{i}, \vec{j}, t')\left(\vec{E}_s(\vec{e}_s, \vec{i}, t)\cdot\vec{E}_s(\vec{e}_s, \vec{j}, t)\right) d^3\vec{i}d^3\vec{j}}\right) \tag{2.31}$$

If the expression of the scattered electric field from each electron is developed, the incident intensity and differential cross section of Thomson scattering appears and the expression simplifies to

$$\frac{dI_s}{d\Omega}(\vec{e}_s, t) = 2\frac{I_i}{|\vec{e}_s|^2}\frac{d\sigma_T}{d\Omega}(\vec{e}_s)\left(\int_{\vec{i}\in V} \frac{n_e(\vec{i}, t')}{2} d^3\vec{i} + \overline{\int_{\vec{i}\in V}\int_{\vec{j}\in V\setminus\vec{i}} n_e^2(\vec{i}, \vec{j}, t')\cos\Phi(\vec{e}_s, \vec{i}, t)\cos\Phi(\vec{e}_s, \vec{j}, t) d^3\vec{i}d^3\vec{j}}\right) \tag{2.32}$$

The $1/|\vec{e}_s|^2$ term is not simplified in order to preserve the equation homogeneity. For readability, it is omitted for the rest of the discussion. As said previously, the integral of $n_e(\vec{i}, t')$ over the scattering volume (V_{obs}) gives $N_e(t')$, the number of electrons inside the scattering volume at the time of the scattering event. Finally, the product of cosines function can be linearized. Only the phase difference term may suppress the time dependence related to the wave frequency and lead to a non zero time average value (considering the cutoff frequency of the detector). The simplified expression can be written as

$$\frac{dI_s}{d\Omega}(\vec{e}_s, t) = I_i\frac{d\sigma_T}{d\Omega}(\vec{e}_s)\left(N_e(t') + \overline{\int_{\vec{i}\in V}\int_{\vec{j}\in V\setminus\vec{i}} n_e^2(\vec{i}, \vec{j}, t')\cos\left(\Phi(\vec{e}_s, \vec{i}, t) - \Phi(\vec{e}_s, \vec{j}, t)\right) d^3\vec{i}d^3\vec{j}}\right) \tag{2.33}$$

For readability, the remaining continuous sum over $\cos(\Phi(t'_n) - \Phi(t'_m))$ can be replaced by its statistical mean multiplied by the number of electrons pairs inside the interval of integration ($N_e(t)(N_e(t) - 1)$). From this last simplification is obtained the typical interference formula

$$\boxed{\frac{dI_s}{d\Omega}(\vec{e}_s, t) = N_e(t')I_i\frac{d\sigma_T}{d\Omega}(\vec{e}_s)\left(\underbrace{1}_{\text{incoherent term}} + \underbrace{\overline{(N_e(t') - 1)\langle\cos\left(\Phi(\vec{e}_s, \vec{i}, t) - \Phi(\vec{e}_s, \vec{j}, t)\right)\rangle_{\vec{i}\neq\vec{j}}}}_{\text{coherent term}}\right)} \tag{2.34}$$

This equation highlights the importance of the electron position $\vec{R}_e$ (referred to through the mute variable $\vec{i}$ and $\vec{j}$ in the formulas above). It is its variation from an electron to another that will induce most of the phase shifts and may generate coherent scattering phenomena.

2.4.1 Coherent Thomson Scattering

At first glance, there is no reason for electromagnetic waves scattered by electrons located at different positions and with probably a different microscopic dynamic to be scattered coherently. Restrictive experimental conditions for such a coherence phenomenon to take place are required. This section focuses on the necessary conditions for this event to happen as well as the associated scattered intensity.

Coherent Thomson Scattering (CTS) happens when the statistical mean $\langle \cos\Big(\Phi(\vec{e}_s,\vec{i},t)-\Phi(\vec{e}_s,\vec{j},t)\Big)\rangle_{\vec{i}\neq\vec{j}}$ has non-zero values. As it rises with a N_e^2 law, the contribution from coherent scattering to the total scattered intensity can rapidly become significant. We can notice that for highly destructive interference, when $\langle \cos\Big(\Phi(\vec{e}_s,\vec{i},t)-\Phi(\vec{e}_s,\vec{j},t)\Big)\rangle_{\vec{i}\neq\vec{j}}=-1$ for example, the scattered Thomson intensity becomes strongly negative. This means that most of the intensity is scattered in the coherent regime and propagates along the opposite direction of the incoherently scattered intensity. In the coherent regime, the intensity scattered depends on the orientation of the probed wave vector and consequently the direction of the scattering wave vector.

For discussion on the scattering intensity in the coherent regime, it is more convenient use the Equation 2.33 forms with the incoherent term included inside the integral sum so that the scattered power can be expressed as

$$\frac{dI_s}{d\Omega}(\vec{e}_s,t)=I_i\frac{d\sigma_T}{d\Omega}(\vec{e}_s)\overline{\int_{\vec{i}\in V}\int_{\vec{j}\in V} n_e^2(\vec{i},\vec{j},t')\cos\Big(\Phi(\vec{e}_s,\vec{i},t)-\Phi(\vec{e}_s,\vec{j},t)\Big)\,d^3\vec{i}d^3\vec{j}} \tag{2.35}$$

Developing the retarded time expression and using Equation 2.17 inside the expression of the phase of the scattered wave given in Equation 2.16 leads to the expression

$$\Phi(\vec{R},\vec{R}_e,t)=k_i(\vec{e}_i-\vec{e}_s)\cdot\vec{R}_e(t')+k_iR-\omega_it+\Phi_0 \tag{2.36}$$

Under the elastic scattering hypothesis $k_i\approx k_s$ for all scattering electrons so that the probe wave vector can be identified. Using the mute variables of integration, the phase difference at the position $\vec{R}=\vec{e}_s$ becomes

$$\Phi(\vec{e}_s,\vec{i},t)-\Phi(\vec{e}_s,\vec{j},t)=\vec{k}\cdot(\vec{i}-\vec{j})+\Delta\Phi_0 \tag{2.37}$$

Contrary to single scattering events, in the multiple scattering regimes, both the scattered spectrum and intensity significantly depend on the probe wave vector characteristics. In single scattering event, the probe wave vector characteristics only affected the wave through the $\vec{k}\cdot\vec{v}_e$ dot product that induced the frequency shift and the $\vec{k}\cdot\vec{R}_e(0)$ dot product that induced a phase shift. Similar to a butterfly effect, it is all these small relative phase shifts that induce a macroscopic effect on the scattered intensity in the coherent regime.

From these first steps in the calculation development, a discussion on the conditions for coherent Thomson scattering to happen is possible. As mentioned previously, only the term with a phase difference inside the cosine function can lead to non-zero coherent term, but it is not sufficient. The phase difference still has to be non-erratic for at least some of the scattered wave pairs so that the time average does not cancel out. For this, two necessary but not sufficient conditions of coherence have to be respected:

- **Light source coherence:** The first necessary condition relies on the coherence of the light source. For the scattered radiation to have a chance of being coherent, all the scattering electrons inside the observation volume have to feel incident electromagnetic waves that are coherent. As shown in Figure 2.4, this criterion will depend on both the coherence length of the light source (L_{coh}) and the typical dimension of the observation volume (L_{obs}) equal to $V_{obs}^{1/3}$ for the spherical observation volume presented in Figure 2.4). For coherent scattering to happen, the ordering of distances $\boxed{L_{obs}\ll L_{coh}}$ is the first criterion which needs to be respected. As shown in Figure 2.4), if this ordering is not respected, the volume observed can be filled with incoherent wave packets represented

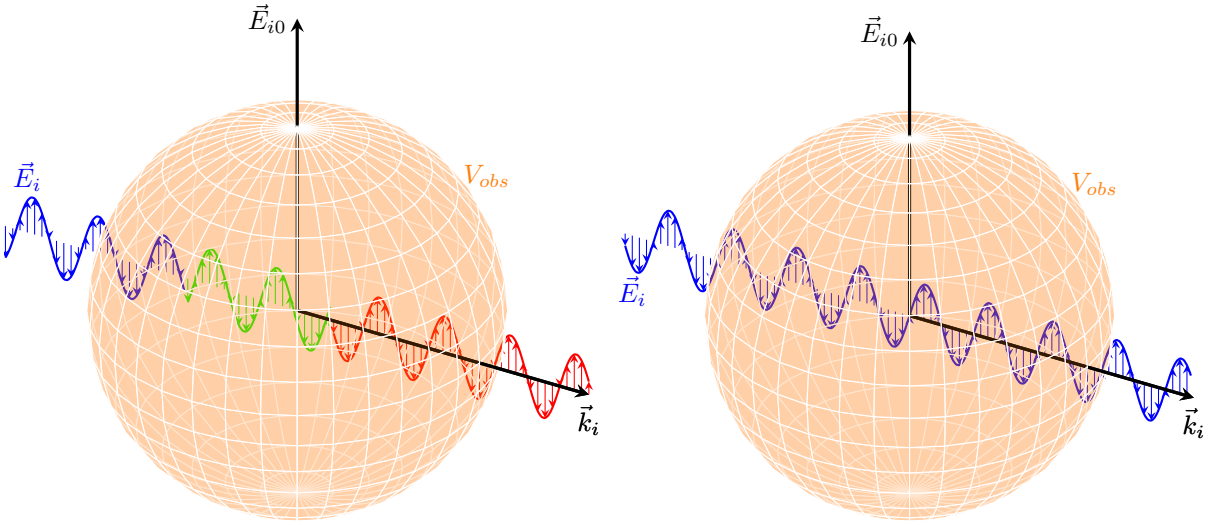

Figure 2.4: Illustration of the electric field at a time t near the scattering volume observed. When the coherence length is lower than the observation volume length scale, several incoherent wave packets can fill the volume (a). When the coherence length is higher, one wave packet fills the entire volume (b).

with various colors. All electrons will feel the coherent electric field from one wave-packet when the ordering is respected.

When the light source is a continuous laser, the light source coherence criteria is usually highly respected. This may not be the case for a pulsed laser, particularly for short pulse durations. For laser pulses of duration τ, the higher limit for coherence length is simply $L_{coh} \approx \tau c$. The inequality between observation and coherence length gives the criteria $\tau \gg (1/3)L_{obs} \times 10^{-8}$ for the pulse duration. As an example, for typical observation volumes on the centimeter scale, the pulse duration must be higher than approximately 20 ps.

- **Plasma coherence:**

  From here we assume a sufficiently coherent light source so that $\Delta\Phi = \Phi_{s0}$ with Φ_{s0} a constant. In this case, the coherence of the scattered intensity only depends on the distribution of the scattering particles relative to the probe wave vector. Under this hypothesis, the function $\cos\left(\Phi(\vec{e}_s, \vec{i}, t) - \Phi(\vec{e}_s, \vec{j}, t)\right)$ is plotted for two scattering configurations in Figure 2.5, with yellow corresponding to a positive values and blue to negative values. Spatial frequency, as well as the direction of the associated pattern, are characterized respectively by the norm and direction of the scattering wave vector $\vec{k}$. Changes in the phase Φ_{s0} would only generate a spatial shift of the pattern along the direction of $\vec{k}$.

  In Figure 2.5 are also represented two electromagnetic waves associated with the incident light and the scattered light (considered coherent with the incident beam all over the observation volume). The pattern shown is equivalent to the interference pattern generated by the interference of these two light beams over the observation volume. This duality relies on the time-reversal invariant property of light. The coherently scattered beam comes from the same scattering particle position distribution as the positions of coherent interference between the scattered beam propagating in the opposite direction and the incident beam that generated the scattering signal.

  From these observations, it is clear that the most favorable situation for coherent scattering would correspond to the case when the electron density distribution is concentrated only where the plotted pattern is maximal. In this case we would have $n_e^2(\vec{\xi}, t') = N_e(t')^2\delta(\vec{\xi} - 2m\pi\vec{k}/k^2)$ with $\vec{\xi} = \vec{i} - \vec{j}$ with $m \in \mathbb{Z}$. For such an electron density distribution, the scattered wave scattered in the $\vec{k}_s$ direction would be directly proportional to $N_e(t')^2$, I_i and the differential cross section for Thomson scattering.

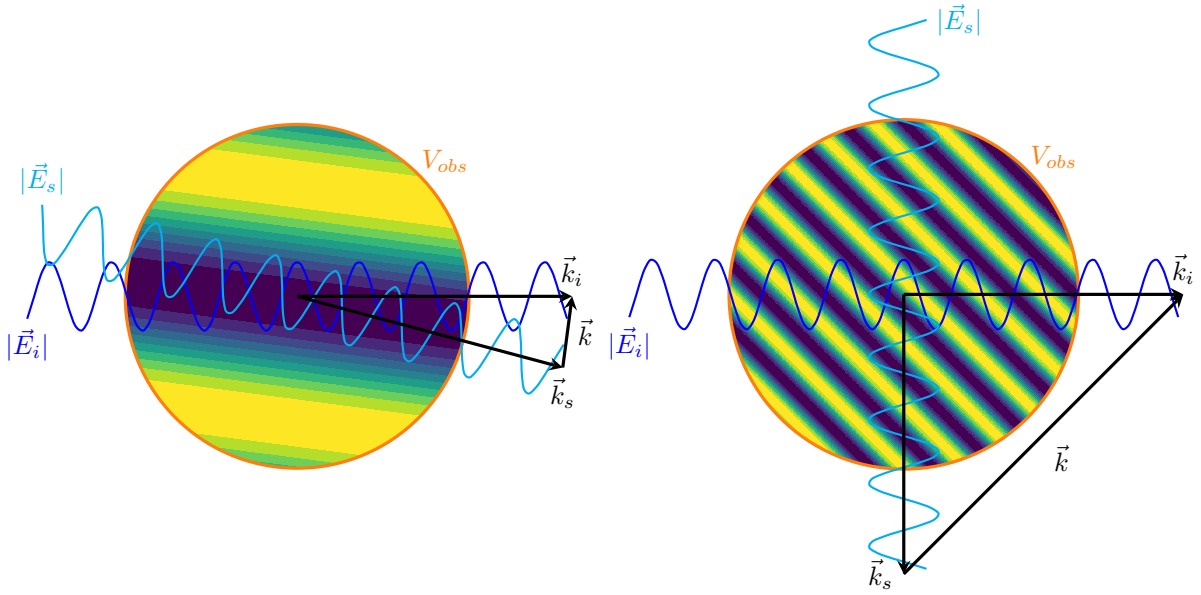

(a) (b)

Figure 2.5: Pattern of the $\cos\Big(\Phi(\vec{e}_s,\vec{i},t)-\Phi(\vec{e}_s,\vec{j},t)\Big)$ function over the observation volume (V_{obs}) for two scattering configurations. A scattering configuration with θ=15° is shown on the left (a) and a configuration with θ=90° is shown on the right (b).

In practice, due to Coulomb repulsion force, the probability for a large quantity of electrons to be concentrated inside a fixed small volume would be extremely low. Such a configuration would generate a strong electric field which would tend to destroy spatial confinements rapidly. For the plasma state of matter, the coulomb force between oppositely charged particles rearranges particles distribution so that screening of charge separation happens. However, thermal agitations of particles tend to destroy such a screening effect. A characteristic length scale, named the Debye length, characterizes the typical distance at which screening of the electric field takes place. It gives the radius of the sphere (called the Debye sphere and represented in Figure 2.6 under the notation V_{De}), centered around a charge disparity, where the corresponding surface density of the electric potential becomes equal to the thermal energy of charged particles. Considering a single ion and electron population, this length scale is expressed as

$$\lambda_{De}=\left(\frac{e^2 n_e/\varepsilon_0}{k_B T_e}+\frac{z e^2 n_i/\varepsilon_0}{k_B T_i}\right)^{-1/2} \tag{2.38}$$

where n_e and n_i are the electron and ion density and T_e and T_i their respective temperatures. z is the charge state of the considered ion population.

Consequently, the electron population distribution would be able to follow the patterns of the interference pattern of the $\cos\Big(\Phi(\vec{e}_s,\vec{i},t)-\Phi(\vec{e}_s,\vec{j},t)\Big)$ function only if the ordering of distances $\boxed{\lambda_{De}\ll 2\pi/k}$ is respected ($2\pi/k$ is usually called the probed wavelength). This fixes the second criterion for glsCTS to happen.

Under the previously described conditions, coherent scattering may happen so that the coherent term of Equation 2.34 would be non-zero. Using the change of variable $\vec{i}=\vec{\xi}+\vec{j}$ and expanding the joint distribution function inside Equation 2.35, the scattered intensity distribution can be expressed as

$$\frac{dI_s}{d\Omega}(\vec{e}_s,t)=I_i\frac{d\sigma_T}{d\Omega}(\vec{e}_s)\overline{\int_{\vec{\xi}\in V}\int_{\vec{j}\in V} n_e(\vec{j},t')n_e(\vec{j}+\vec{\xi},t')\cos(\vec{k}\cdot\vec{\xi}+\Phi_{s0})d^3\vec{j}d^3\vec{\xi}} \tag{2.39}$$

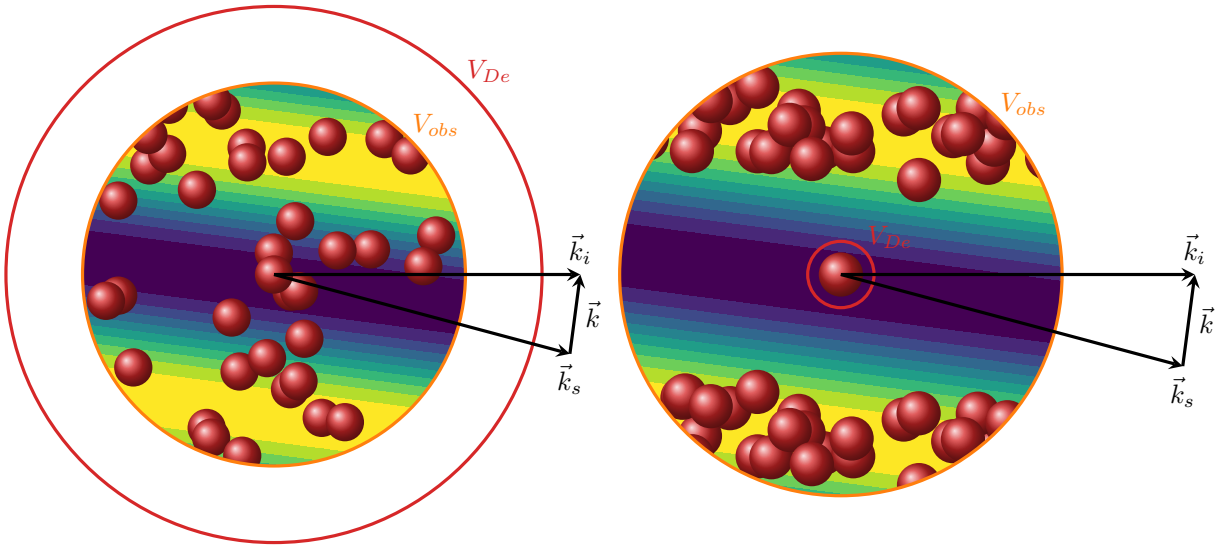

(a) (b)

Figure 2.6: Superposition of the pattern of the $\cos\Big(\Phi(\vec{e}_s,\vec{i},t)-\Phi(\vec{e}_s,\vec{j},t)\Big)$ function with possible distributions of electrons (red spheres not to scale) inside the observation volume (V_{obs}) when $\lambda_{De} \gg 2\pi/k$ (a) and when $\lambda_{De} \ll 2\pi/k$ (b).

From here,the first integral over $\vec{j}$ corresponds to the cross-autocorrelation product of the density distribution $(n_e \star n_e)(\vec{\xi},t')$. Expanding the cosine function, Fourier sine and cosine transforms of this cross-autocorrelation product are recognized so that using the property of the Fourier transform of a cross-correlation we obtain

$$\frac{dI_s}{d\Omega}(\vec{e}_s,t) = I_i \frac{d\sigma_T}{d\Omega}(\vec{e}_s)\overline{\Big((\hat{n}_e^c(\vec{k},t'))^2\cos\Phi_{s0} - (\hat{n}_e^s(\vec{k},t'))^2\sin\Phi_{s0}\Big)} \tag{2.40}$$

where $\hat{n}_e^c(\vec{k},t')$ and $\hat{n}_e^s(\vec{k},t')$ are the sine and cosine spatial transforms of the electron density distribution along the direction $\vec{k}$. The Fourier transform was recognized under the hypothesis of a sufficiently large scattering volume compared to probed wavelength $2\pi/\vec{k}$. In practice it may not be the case so that, as the temporal variation of an electrical signals observed over a finite temporal window (rectangular, Hanning, etc.), the Fourier transform would be the result of the convolution of the Fourier Transform of the window with the true Fourier transform of electron density fluctuations. Consequently the peaked signal from "monochromatic" electron oscillations would be naturally broadened due to the limited size of the observation volume. To neglect the peak broadening effect induced by this convolution, the ordering of distance $\boxed{2\pi/k \ll L_{obs}}$ has to be respected.

With the same comparison with the temporal analysis of electric signals, the analogy to a case when the acquisition rate is too low (aliasing of the spectrum) is possible. For this, one could imagine the case of the investigation of relatively high spatial frequencies inside a low-density plasma. For such a case, aliasing issues may happen if scattering electrons are not numerous enough, i.e., if the ordering $\boxed{1/\sqrt[3]{n_e} \ll 2\pi/k}$ is not respected. However, it is highly probable that such an ordering is respected if the CTS orderings are respected.

Finally, as shown in Equation 2.40 the intensity scattered is proportional to the time variations of the scattering electron position fluctuations along the direction and at length scales characterized by the probed wave vector $\vec{k}$. The intensity in the coherent Thomson scattering regime is not directly related to the absolute electron density. At best, an estimation of mean square density fluctuation rate is possible. Because electron dynamics can be extremely fast, the limitation on the upper limit of the scattered intensity fluctuations frequency usually depends on the cutoff frequency of detection equipment used to analyze the scattered intensity.

In practice, as described in [94] for the CTS diagnostic named PRAXIS, the time variations of the scattered intensity are used to obtain information on electron dynamics inside plasma sources. To obtain

a maximum of information on electron properties, the cutoff frequency and detector sensitivity have to be as high as possible. For example, for the PRAXIS diagnostic, a high-intensity continuous laser coupled with heterodyne techniques is used to generate the scattering signal and spectrally isolate it from sources of noise. The modulated scattered signal detected with a highly sensitive diode cooled with liquid nitrogen is then digitized with a high acquisition rate card (50 MHz for the cited example) and filtered in order to reconstruct the sine and cosine Fourier transform components of the scattered intensity. From this signal information on plasma oscillations at various length scale and along different directions can be deduced.

2.4.2 Incoherent Thomson Scattering

Incoherent Thomson scattering (ITS) happens when either the distance ordering $L_{obs} \ll L_{coh}$ or $\lambda_{De} \ll 2\pi/k$ are not respected. Under these conditions, the length scale probed is below the Debye length so that the phase differences between the waves scattered by the electrons inside the observation volume is random. As a result, the intensity and spectrum of the light scattered is simply the weighted sum from the contribution of the scattering electrons inside the observation volume.

2.4.2.1 Intensity of the light scattered

For the intensity scattered, the Equation 2.34 can be considered with the coherent term equal to zero so that the scattered intensity is expressed as

$$\frac{dI_s}{d\Omega}(\vec{e}_s, t) = N_e(t')I_i\frac{d\sigma_T}{d\Omega}(\vec{e}_s) \tag{2.41}$$

Contrary to the coherent regime, scattering intensity in the incoherent regime only rises proportionally to the absolute value of electron number $N_e(t')$. This translates to a much less intense signal scattered. The scattered light has to be intensely generated inside a small temporal window so that highly sensitive gated detectors may allow the associated signal to be distinguished from the noise. Experimentally, an energetic pulsed laser such as Q-switch laser is used to generate a sufficiently intense scattering signal. Such techniques do not allow temporally resolved analysis of the scattering particle number; the scattered signal can be detected only through integration over the complete laser pulse duration. If the signal-to-noise ratio is not sufficiently high, accumulation over multiple laser pulses may help the analysis of the scattered intensity so that the mean scattering particle number may be estimated.

By identification with Equation 2.4, the relation $N_e/|\vec{e}_s|^2 = n_e L$ could be deduced (the $|\vec{e}_s|^2$ coefficient has been omitted until now). This would correspond to a theoretical case where spatial limitations of the scattering configuration are not taken into account. Experimentally, a quantitative analysis of the Thomson scattering signal needs a calibration measurement procedure from Raman scattering on a known scattering population density (see Chapter 3). The calibration coefficient relies information on the observation volume dimension and losses through the analysis procedure; from it, estimation the electron density is feasible.

Contrary to the coherent regime, the scattered intensity in the coherent regime does not depend on the scattering wave vector characteristics. The scattered intensity has the same dependency on the scattering configuration as the differential cross-section of Thomson scattering; it depends only on the relative direction of observation ($\vec{k}_s$) with respect to the polarization vector ($\vec{E}_{i0}$). As a result, it does not depend on the orientation of $\vec{k}_s$ and $\vec{k}$ or on rotation around $\vec{E}_{i0}$. Nevertheless, even in the incoherent regime, the spectrum of the scattered intensity does depend on the orientation of $\vec{k}_s$ and $\vec{k}$.

2.4.2.2 Spectrum of the light scattered

As it has been shown in last section, from the Thomson scattering intensity, absolute electron density or density fluctuations at larger scale than Debye length can be estimated in the incoherent and coherent regime respectively. To use Thomson scattering for an estimation of thermal properties of electrons, an analysis of the spectrum associated with this intensity is required. It is in the incoherent regime that estimation of thermal properties is the most straightforward. To obtain the link between thermal properties of the scattering electrons and the scattered intensity spectrum from Thomson scattering, the Equation 2.41 has to be differentiated with respect to the electron velocity. From this differentiation we obtain

$$\frac{dI_s}{d\Omega}(\vec{e}_s, \vec{v}) = n_e L I_i \frac{d\sigma_T}{d\Omega}(\vec{e}_s) f_{\vec{v}}(\vec{v}) d^3\vec{v} \tag{2.42}$$

with $f_{\vec{v}}(\vec{v})$ the electron vector velocity distribution function, its integral over all possible positions inside the velocity space equals unity while the $f_{\vec{v}}(\vec{v})d^3\vec{v}$ coefficient gives the probability of finding an electron inside a volume $d^3\vec{v}$ of the velocity space.

As shown in Section 2.3.3 the frequency shift of the scattered wave depends only on the velocity distribution of the scattering electrons along the direction collinear to $\vec{k}$; as a result, all electrons with the same projection over the probe wave vector will induce the same Doppler shift. Under the hypothesis of a velocity distribution inside the plane perpendicular to the vector $\vec{k}$ independent of the value of the velocity along this vector, the electron vector velocity distribution function can be written as the product of two separate electron velocity distribution functions so that $f_{\vec{v}}(\vec{v}) = f_{v_k}(v_k)f_{\vec{v}_\perp}(\vec{v}_\perp)$. $f_{v_k}(v_k)$ is the one-dimensional velocity distribution function along the probed wave vector (with $v_k \in [-c; c]$) and $f_{\vec{v}_\perp}(\vec{v}_\perp)$ is the two-dimensional vector velocity distribution function inside the plane perpendicular to $\vec{k}$. The spectral distribution of the scattered wave will be the same for all values of electron velocity projection along the $\vec{v}_\perp$ directions. After integration over all accessible $\vec{v}_\perp$ and because $f_{\vec{v}_\perp}(\vec{v}_\perp)$ is also normed, we obtain

$$\frac{dI_s}{d\Omega}(\vec{e}_s, v_k) = n_e L I_i \frac{d\sigma_T}{d\Omega}(\vec{e}_s) f_{v_k}(v_k) dv_k \tag{2.43}$$

Because $\omega_i - \omega_s = kv_k$, after a change of variable the previous expression can be expressed with respect to the frequency of the scattered wave so that

$$\frac{dI_s}{d\Omega d\omega_s}(\vec{e}_s, \omega_s) = n_e L I_i \frac{d\sigma_T}{d\Omega}(\vec{e}_s) \frac{f_{v_k}(v_k = (\omega_i - \omega_s)/k)}{k} \tag{2.44}$$

From here we recognize the spectral form factor introduced inside Equation 2.4. It is apparent that the spectral form factor of the scattered intensity directly reflects the one-dimensional electron velocity distribution function along the probed wave vector through the relation $S_k(\omega_s) = f_{v_k}(v_k = (\omega_i - \omega_s)/k)/k$.

It is necessary to highlight that the result obtained requires the hypothesis of an electron following a vector velocity distribution function whose dependency along the $\vec{v_\perp}$ directions does not depend on the value of v_k. For example, an isotropic electron vector velocity distribution function does respect this hypothesis. Nevertheless, the hypothesis may also include cases where the one-dimensional electron drift velocity along the probe direction is either shifted due to a drift velocity or follows a distribution different from the other two directions. This observation shows that contrary to the intensity scattered, the spectrum scattered may depend on the orientation of $\vec{k}$ and on a rotation of $\vec{k}_s$ around the laser polarization vector E_{i0}.

The spectral form factor for electrons at thermal equilibrium may be written. If elastic collisions such electron-electron collisions are the main process driving the system toward equilibrium, electrons are expected to follow an isotropic Maxwell-Boltzmann velocity distribution function. Under these assumptions, the spectral form factor is proportional to the one-dimensional Maxwell-Boltzmann electron velocity distribution function along the probed direction and can be expressed as

$$S_k(\omega_s) = \sqrt{\frac{m_e}{2\pi k_B T_e k^2}} \exp\left(-\frac{m_e(\omega_i - \omega_s - kv_{e,drift})^2}{2k_B T_e k^2}\right) \tag{2.45}$$

where T_e is the electron temperature along the probed direction, and $v_{e,drift}$ the macroscopic drift velocity of the electron population at thermal equilibrium along the same direction. Because all the other parameters are fixed for a specific scattering configuration, from the fitting of the spectral form factor, electron properties can be estimated. T_e is estimated from the amplitude or standard deviation of the Gaussian distribution (with a normed integral) while $v_{e,drift}$ is estimated by the spectral shift of the mean of the distribution with respect to the laser frequency.

For the moment, we have only dealt with the simplified case of thermalized electrons. As shown previously, under a few hypotheses, the spectral form factor is sensitive to the one-dimensional wave vector. The analysis of the spectral form factor can detect deviations of electron behavior from thermal equilibrium and may be used to asses the three-dimensional electron distribution functions as described in the next section.

2.5 From the electron distribution functions to the incoherent Thomson spectrum

2.5.1 Origins of the link between the spectral form factor and the electron distribution functions

The demonstration of the link between the spectral form factor and the electron distribution functions can be found in other works [64,65,95]. The present demonstration sets notation conventions used in this manuscript and describes the hypotheses needed for each derivation procedure.

2.5.1.1 The one-dimensional electron velocity distribution function

In the last section, the hypothesis of independence of electron velocity along the probed direction from other directions was used to decompose and simplify integration of the vector velocity distribution function over perpendicular directions in the velocity space. This simplification allowed the derivation of the spectral form factor from the one-dimensional electron velocity distribution function in case of thermal equilibrium. This derivation showed the link between both distributions through the following formula

$$\boxed{f_{v_k}\left(v_k = \frac{\omega_i - \omega_s}{k}\right) = kS_k(\omega_s)} \tag{2.46}$$

This relation requires only a hypothesis based on the independence of the one-dimensional electron velocity distribution function along the probe wave vector from the other directions.

NB: we have the identity $f_{E_k}(E_k)dE_k = f_{v_k}(v_k)dv_k$ with $E_k = m_e v_k^2/2$ the kinetic energy along the probed direction. The differentiation $dv_k = dE_k/(m_e v_k)$ injected inside the previous equation allows the estimation of the link between the spectral form factor and the one dimensional energy distribution function that is expressed as

$$\boxed{f_{E_k}\left(E_k = \frac{m_e}{2}\left(\frac{\omega_i - \omega_s}{k}\right)^2\right) = \frac{k^2}{m_e(\omega_i - \omega_s)}S_k(\omega_s)} \tag{2.47}$$

2.5.1.2 The three-dimensional electron vector velocity distribution function

With the previous method, the link with the electron vector velocity distribution functions is lost. From a stronger hypothesis of an isotropic electron vector velocity distribution function, the link can be preserved. In this case the dependence of the distribution with the direction is lost and only the dependence with the absolute velocity remains and we can write $f_{\vec{v}}(\vec{v}) = f_{\vec{v}}(v)$ (with $v \in [0; c]$). The integration over transverse velocities $d^2\vec{v}_\perp$ is simplified after two changes of variables:

- firstly by switching to polar coordinates inside the transverse plane (see Figure 2.7), after a first integration around $\vec{v}_k$ that does not affect the absolute velocity v, we obtain $d^2\vec{v}_\perp = 2\pi v_\perp dv_\perp$ with $v_\perp \in [0; c]$.
- then using the identity $v = \sqrt{v_k^2 + v_\perp^2}$ with $vdv = v_\perp dv_\perp$ we finally obtain $d^2\vec{v}_\perp = 2\pi v dv$ with $v \in [v_k; c]$

From these changes of variables we obtain

$$\frac{dI_s}{d\Omega}(\vec{e}_s, v_k) = n_e L I_i \frac{d\sigma_T}{d\Omega}(\vec{e}_s) dv_k \int_{v_k}^{c} f_{\vec{v}}(v) 2\pi v dv \tag{2.48}$$

Using the relation between v_k and ω_s the spectral form factor can be identified and expressed as

$$S_k(\omega_s) = -\frac{1}{k} \int_{(\omega_i - \omega_s)/k}^{c} f_{\vec{v}}(v) 2\pi v dv \tag{2.49}$$

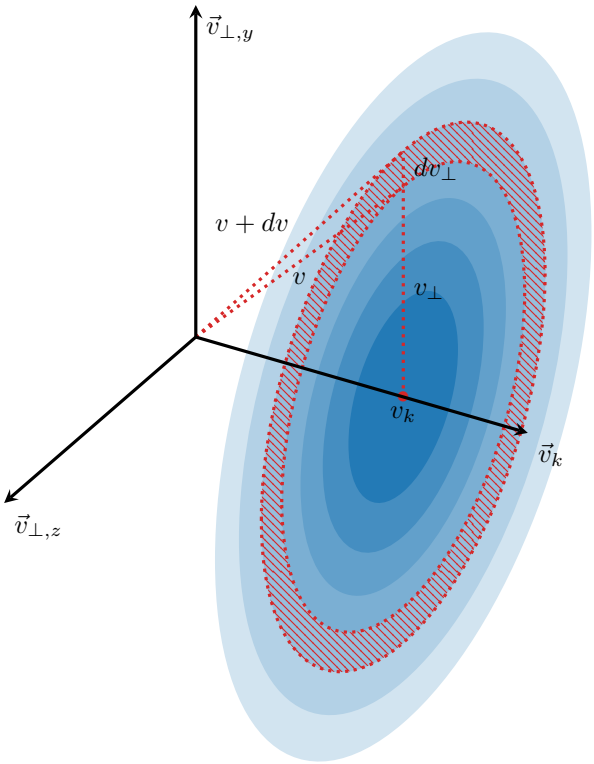

Figure 2.7: Illustration of an isotropic vector velocity distribution function (plotted with concentric discs in blue) estimated at a given velocity along the $\vec{v}_k$ direction. The distribution is unchanged over differential concentric rings represented by a dashed pattern in red.

To obtain a simpler relation between both distribution functions, a derivative with respect to $(\omega_i - \omega_s)/k$ is necessary. From this derivation and few rearrangements we obtain the relation

$$\boxed{f_{\vec{v}}\left(v = \frac{\omega_i - \omega_s}{k}\right) = -\frac{k^3}{2\pi(\omega_i - \omega_s)}\frac{dS_k}{d\omega_s}(\omega_s)} \tag{2.50}$$

with a hypothesis of an isotropic electron vector velocity distribution function.

2.5.1.3 The electron velocity distribution function

The electron velocity distribution function, also abbreviated EVDF and noted $f_v(v)$, implies by definition the isotropic hypothesis made previously. The coefficient $f_v(v)dv$ gives the probability for the norm of the electron velocity to range between v and $v + dv$. From the identity $f_v(v)dv = f_{\vec{v}}(\vec{v})d^3\vec{v}$ and because $d^3\vec{v} = 4\pi v^2 dv$ a simple relation between the two distributions is obtained: $f_v(v) = 4\pi v^2 f_{\vec{v}}(\vec{v})$. By injecting this into Equation 2.50, the following formula for EVDF estimation is obtained:

$$\boxed{f_v\left(v = \frac{\omega_i - \omega_s}{k}\right) = -2k(\omega_i - \omega_s)\frac{dS_k}{d\omega_s}(\omega_s)} \tag{2.51}$$

2.5.1.4 The electron energy distribution function

The electron energy distribution function will be abbreviated as EEDF and noted $f_E(E)$. Similarly to the EVDF case, we suppose that electron energy is redistributed equally inside the three degrees of freedom for electron translation. From the identity $f_E(E)dE = f_v(v)dv$ and because $dv = dE/(m_e v)$, a simple relation between the two distributions is obtained: $f_E(E)dE = f_v(v)dE/(m_e v)$. By injecting this

inside Equation 2.51, the following formula for EEDF estimation is obtained:

$$\boxed{f_E\left(E=\frac{m_e}{2}\left(\frac{\omega_i-\omega_s}{k}\right)^2\right)=-2\frac{k^2}{m_e}\frac{dS_k}{d\omega_s}(\omega_s)} \tag{2.52}$$

2.5.2 Examples for relevant electron distribution functions

Inside this section, the relations of Section 2.5 are used to derive the shape of the spectral form factor for a selection of commonly encountered electron distributions inside plasmas discharges; other examples can be found elsewhere [75]. For all the example below, we consider an electron with isotropic behavior. To simplify the comparison inside Table 2.1, we consider an identical standard deviation (noted σ) for all the one dimensional electron velocity distribution functions along the probed direction. The three distributions functions discussed are:

- **The Maxwell-Boltzmann distribution:** As previously mentioned, the Maxwell-Boltzmann distribution corresponds to the distribution expected for electrons at thermal equilibrium. Usually encountered inside plasmas with a high degree of ionization, this distribution is obtained from the Boltzmann equation when elastic collisions between electrons are the main path for the energy exchange. Under these conditions, the consideration of a constant collision frequency (ν) is valid, and the shape of the associated EEDF predicts a slow decrease of the density inside the high energy tail.

- **The Bi-Maxwell-Boltzmann distribution:** Inside plasmas with a high degree of ionization but with two distinct electron populations, Bi-Maxwell-Boltzmann distributions may better describe electron behavior. The presence of two populations of electrons may appear at the boundary between two different plasmas. The presence of two processes with highly different efficiency (sheath acceleration and ECR resonance, for example) for electron energization may also lead to such distributions. For this distribution, other coefficients appear such as the density ratio and the temperature ratio between the two populations.

- **The Druyvesteyn distribution:** The Druyvesteyn distribution was introduced to better describe plasmas where the degree of ionization is low. For such plasmas, the high energy tail electrons contribute to elastic and inelastic collision with neutrals. This behavior is modeled by considering a constant mean free path (l) so that the electron collision frequency rises linearly with the electron velocity (v) (through the relation $\nu = v/l$). From this hypothesis, electrons with high energy have less time to gain energy from the electric field between consecutive collisions. This non-constant collision frequency affects the high energy tail in the EEDF; the density inside the high energy tail is lower than in the case of an equivalent Maxwell-Boltzmann distribution.

Distribution function	Maxwell	Bi-Maxwell	Druyvesteyn
$f_{v_k}(v_k)$	$\frac{1}{\sqrt{2\pi}}\frac{1}{\sigma}\exp\left(-\frac{1}{2}\left(\frac{v_k}{\sigma}\right)^2\right)$	$\frac{1}{\sqrt{2\pi}}\left[\eta_c\frac{1}{\sigma_c}\exp\left(-\frac{1}{2}\left(\frac{v_k}{\sigma_c}\right)^2\right)+\eta_h\frac{1}{\sigma_h}\exp\left(-\frac{1}{2}\left(\frac{v_k}{\sigma_h}\right)^2\right)\right]$	$\beta\frac{1}{\sigma}\operatorname{erfc}\left(\alpha\left(\frac{v_k}{\sigma}\right)^2\right)$
$f_v(v)$	$\sqrt{\frac{2}{\pi}}\frac{v^2}{\sigma^3}\exp\left(-\frac{1}{2}\left(\frac{v}{\sigma}\right)^2\right)$	$\sqrt{\frac{2}{\pi}}\left[\eta_c\frac{v^2}{\sigma_c^3}\exp\left(-\frac{1}{2}\left(\frac{v}{\sigma_c}\right)^2\right)+\eta_h\frac{v^2}{\sigma_h^3}\exp\left(-\frac{1}{2}\left(\frac{v}{\sigma_h}\right)^2\right)\right]$	$8\alpha\beta\frac{1}{\sqrt{\pi}}\frac{v^2}{\sigma^3}\exp\left(-\alpha^2\left(\frac{v}{\sigma}\right)^4\right)$
$f_{\vec{v}}(\vec{v})$	$\left(\frac{1}{2\pi}\right)^{3/2}\frac{1}{\sigma^3}\exp\left(-\frac{1}{2}\left(\frac{\lVert\vec{v}\rVert}{\sigma}\right)^2\right)$	$\left(\frac{1}{2\pi}\right)^{3/2}\left[\eta_c\frac{1}{\sigma_c^3}\exp\left(-\frac{1}{2}\left(\frac{\lVert\vec{v}\rVert}{\sigma_c}\right)^2\right)+\eta_h\frac{1}{\sigma_h^3}\exp\left(-\frac{1}{2}\left(\frac{\lVert\vec{v}\rVert}{\sigma_h}\right)^2\right)\right]$	$\beta^3\frac{1}{\sigma^3}\operatorname{erfc}\left(\alpha\left(\frac{\lVert\vec{v}\rVert}{\sigma}\right)^2\right)$
$f_E(E)$	$\frac{2}{\sqrt{\pi}}\sqrt{\frac{E}{(m_e\sigma^2)^3}}\exp\left(-\frac{E}{m_e\sigma^2}\right)$	$\frac{2}{\sqrt{\pi}}\left[\eta_c\sqrt{\frac{E}{(m_e\sigma_c^2)^3}}\exp\left(-\frac{E}{m_e\sigma_c^2}\right)+\eta_h\sqrt{\frac{E}{(m_e\sigma_h^2)^3}}\exp\left(-\frac{E}{m_e\sigma_h^2}\right)\right]$	$8\alpha\beta\sqrt{\frac{2}{\pi}}\sqrt{\frac{E}{(m_e\sigma^2)^3}}\exp\left(-4\alpha^2\left(\frac{E}{m_e\sigma^2}\right)^2\right)$
$S_k(\omega_s)$	$\frac{1}{\sqrt{2\pi}}\frac{1}{k\sigma}\exp\left(-\frac{1}{2}\left(\frac{\omega_i-\omega_s}{k\sigma}\right)^2\right)$	$\frac{1}{\sqrt{2\pi}}\left[\eta_c\frac{1}{k\sigma_c}\exp\left(-\frac{1}{2}\left(\frac{\omega_i-\omega_s}{k\sigma_c}\right)^2\right)+\eta_h\frac{1}{k\sigma_h}\exp\left(-\frac{1}{2}\left(\frac{\omega_i-\omega_s}{k\sigma_h}\right)^2\right)\right]$	$\beta\frac{1}{k\sigma}\operatorname{erfc}\left(\alpha\left(\frac{\omega_i-\omega_s}{k\sigma}\right)^2\right)$

Table 2.1: Comparison of the various distribution functions for electrons following a Maxwell-Boltzmann distribution, a Bi-Maxwell Boltzmann and a Druyvesteyn distribution velocity distribution function. The σ constant is fixed as the standard deviation of the one dimensional velocity distribution functions ($f_{v_k}(v_k)$). η_c and η_h are introduced for the Bi-Maxwell-Boltzmann distribution and give the proportion of cold and hot electron densities respectively with respect to the total electron density. The standard deviations σ_c and σ_h depend on the temperatures of the two electron populations and respect the equality $\sigma=\sqrt{\eta_c\sigma_c^2+\eta_h\sigma_h^2}$. For the Druyvesteyn distribution, the parameters $\alpha=\Gamma(5/4)/3\Gamma(3/4)$ and $\beta=(1/2)\sqrt{\pi}\Gamma(5/4)/3\Gamma(3/4)^3$ as well as the complementary error function erfc were introduced (with Γ the gamma function).

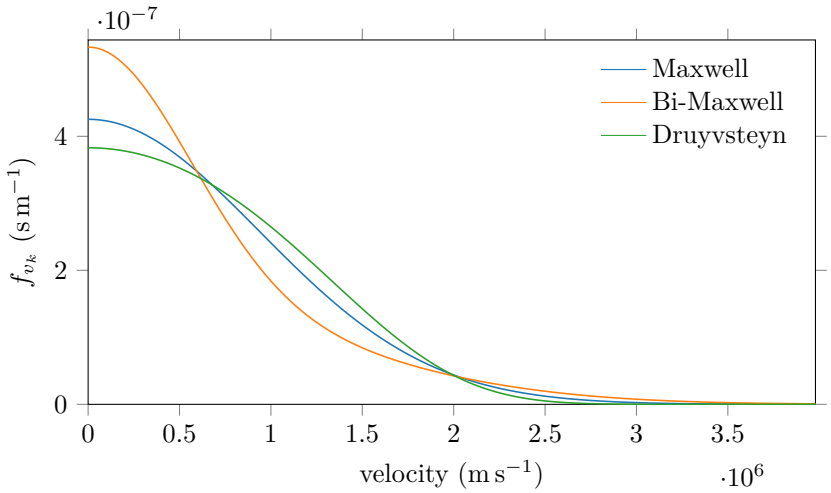

Figure 2.8: One dimensional electron velocity distribution functions in the case of a Maxwell-Boltzmann, a Bi-Maxwell-Boltzmann and a Druyvesteyn distribution. The following parameter values are chosen for the plot: σ=9.38 $\times$ 10^6 m s^{-1}, $\eta_c = \eta_h$=0.5 and $T_{e,h}/T_{e,c}$=5.

For the Maxwell-Boltzmann case, the standard deviation of the one-dimensional velocity distribution function is by definition connected to the electron temperature through the relation $T_e = m_e\sigma^2/k_B$. The other distributions are associated with electrons out of thermal equilibrium so that a thorough approach would forbid any definition of electron temperatures. Fundamentally, the standard deviation maintains the same physical meaning for any distribution. In this thesis, we will sometimes use the standard deviation of a non-Maxwellian distribution as a means of electron temperature estimation; this allows easier comparisons with other results.

Using the formulae of Table 2.1, estimation of the shape of the distribution functions for the selected distribution function cases is possible. For example, Figure 2.8 shows the one-dimensional electron velocity distribution function for the three previously listed distribution functions. Even if the three distributions are normed and characterized by an identical standard deviation, their shapes sharply diverge. This would have a quantitative impact on the macroscopic transport coefficients estimated from each distribution. This observation highlights both the advantage of sensitivity to the electron distribution function and the different meaning of a given "temperature" for electron populations out of thermal equilibrium.

The EVDF and EEDF corresponding to the previously introduced one-dimensional electron velocity distribution functions are shown in Figure 2.9 and Figure 2.10 respectively. For all the plots a fixed electron temperature of 5 eV is chosen, corresponding to a standard deviation for the one-dimensional velocity distribution functions of approximately $\sigma\approx$9.38 $\times$ 10^6 m s^{-1}. For the Bi-Maxwell-Boltzmann distribution, the curve shown corresponds to an example with the two electron populations having an equal density ($\eta_c = \eta_h$=0.5) and a temperature ratio $T_{e,h}/T_{e,c}$=5 (the identity $T_e = \sqrt{T_{e,c}^2 + T_{e,h}^2}$ is respected).

Finally, Figure 2.11 shows the spectral form factor of the Thomson intensity scattered for the selected electron distribution functions. The curves shown correspond to a spectrum obtained with a frequency of the incident light of ω_i=3.54 $\times$ 10^{15} rad s^{-1} and a scattering configuration angle θ=90°. Justifications for these choices will be explained in Chapter 3.

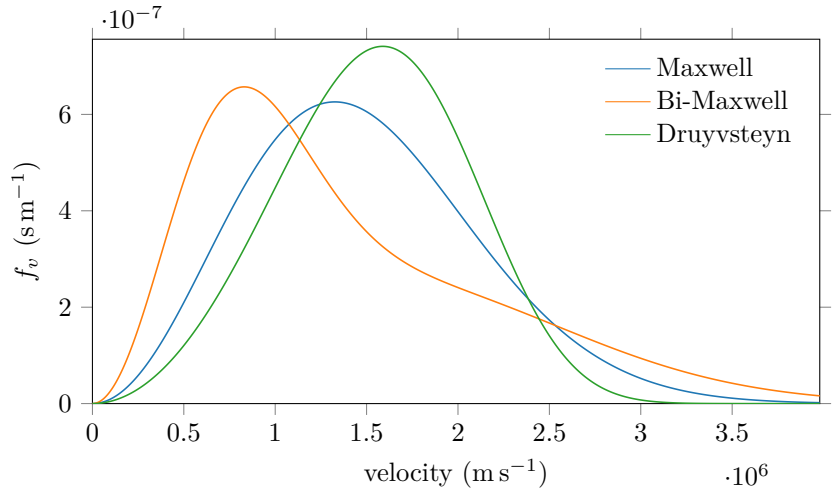

Figure 2.9: EVDF in the case of a Maxwell-Boltzmann, a Bi-Maxwell-Boltzmann and a Druyvesteyn distribution. The following parameter values are chosen for the plot: σ=9.38 $\times$ 10^6 m s^{-1}, $\eta_c = \eta_h$=0.5 and $T_{e,h}/T_{e,c}$=5.

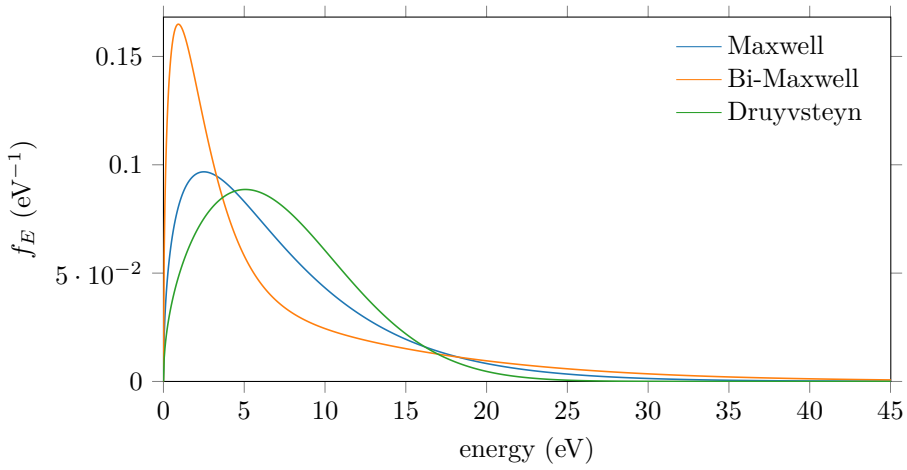

Figure 2.10: EEDF in the case of a Maxwell-Boltzmann, a Bi-Maxwell-Boltzmann and a Druyvesteyn distribution. The following parameter values are chosen for the plot: σ=9.38 $\times$ 10^6 m s^{-1}, $\eta_c = \eta_h$=0.5 and $T_{e,h}/T_{e,c}$=5.

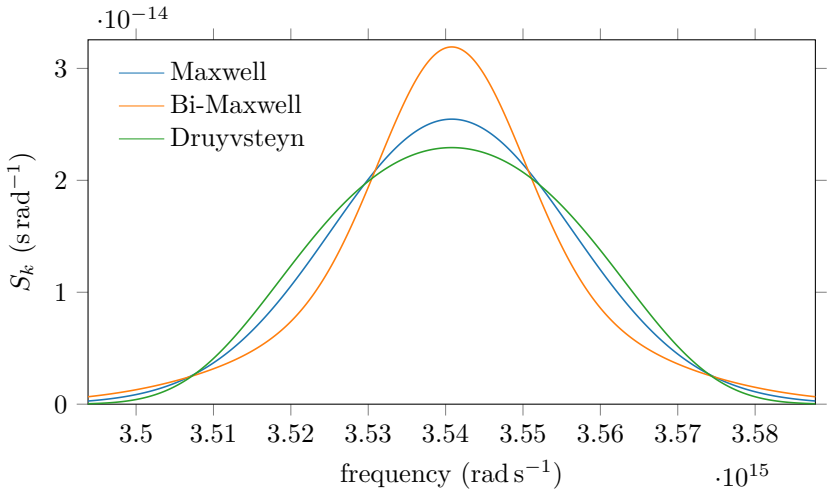

Figure 2.11: Spectral form factor of the scattered light in the case of an electron following a Maxwell-Boltzmann, a Bi-Maxwell-Boltzmann and a Druyvesteyn distribution. The following parameter values are chosen for the plot: σ=9.38 $\times$ 10^6 m s^{-1}, $\eta_c = \eta_h$=0.5, $T_{e,h}/T_{e,c}$=5, ω_i=3.54 $\times$ 10^{15} rad s^{-1} and θ=90°.

Chapter 3

The THETIS diagnostic

> Technological progress has merely provided us with the most efficient means for going backwards.
>
> — *Aldous Huxley, Tomorrow and Tomorrow and Tomorrow*

To a certain extent, it is understandable to be skeptical about the benefit of some contemporary technologies. Technological progress has led to an improvement in our standard of living, but also contributed to applications such as weapons development or mass surveillance. Breakthroughs that allow us to advance our understanding of the universe may be compatible with scientific ethics. In experimental science, new technologies provide the opportunity to build on and improve upon existing methods.

This chapter presents the recently developed incoherent Thomson scattering diagnostic which was the focus of this thesis. Its basic principles are old, but its capabilities take an advantage of a combination of newer and existing technologies. Motivations for equipement choices and the inherent limits are described.

Contents

3.1 The THETIS diagnostic spirit

The first step of this thesis focused on the design and preliminary implementation of the new incoherent Thomson scattering (ITS) platform known as *THomson scattering Experiments for low-Temperature Ion Sources* (THETIS) [96].

As mentioned in its name, the THETIS diagnostic was intended for multiple implementations on several low-temperature ion sources. Its development occurred in the context of a collaboration between the ICARE and LPGP laboratories of the CNRS and CEA Saclay, initiated in 2015. The specific diagnostic applications envisaged required that the diagnostic be relatively lightweight and compact for flexible implementation.

Moreover, the THETIS diagnostic was intended to be applied inside plasma sources with low electron density. While remaining compact, it had to reach a sensitivity level equivalent to the highest ever reached for a similar diagnostic. It was determined that room for achieving such diagnostic sensitivity would rely on increasing the signal level reaching the detector, through improvement of two parts of the diagnostic:

- **The transmission branch:** This corresponds to the optical path followed by the incident beam used to generate the Thomson scattering signal. Improving this branch would mean an increase of light intensity inside the observation volume. This can be achieved by either reducing the optical losses inside the branch (already low) or by increasing the power of the light source.
- **The detection branch:** This corresponds to the optical path followed by the scattering light collected; it includes the imaging, transport, filtering, dispersion and detection procedures. Improving this branch would mean a decrease of the optical losses insides the branch, through, for example, a minimization of the optical elements and an improvement of their transmission efficiency.

Because an increased power of the light source would increase the bulk of the platform and might induce plasma perturbations (see Section 3.5), the THETIS diagnostic design followed the path aiming at the minimization of losses inside the detection branch. As it will be shown in Section 3.2, the path based on the improvement of the detection branch has the advantage of being synergetic with the size reduction of the diagnostic.

3.2 The THETIS diagnostic design

As previously mentioned, the THETIS diagnostic can be divided into two branches. Figure 3.1 shows an illustration of the THETIS diagnostic implemented on a vacuum vessel named NExET (a detailed description is made in Section 6.2.1) for preliminary investigation on an hollow cathode discharge. In this figure, the dark green light corresponds to the laser beam inside the transmission beam while a light green color depicts the scattered light. The description below focuses on the last version of both branches obtained at the end of this thesis. Some optics were changed during the thesis, in particular, the increased size of a light filter led to a new design of the notch filter chamber.

3.2.1 Transmission branch

3.2.1.1 Light source

The transmission branch starts with the diagnostic light source; a Quantel Nd:YAG laser (Q-Smart 850) frequency-doubled for operation at approximately 532 nm (with a FWHM<20 pm, a pulse width of 5 ns, a repetition rate of 10 Hz, a nominal pulse power of 430 mJ, and a beam diameter at the exit of the laser cavity of 9 mm). The laser model was chosen for its compactness (required in a setup to be implemented on several sources), high pulse power and stability. The choice of the laser wavelength and pulse duration were also made to ensure measurement in the incoherent regime with the parameters of the plasmas investigated.

As will be shown in the next sections, the observation volume length scale ($Ł_{obs}$) is on the millimeter length scale. Considering that all photons inside each pulse of light are coherent, the coherence length of laser (L_{coh}) is on the meter length scale and respects the ordering $L_{obs} \ll L_{coh}$ needed for coherent scattering to happen.

For the plasma coherence, the lowest Debye length inside the plasma sources probed could be obtained

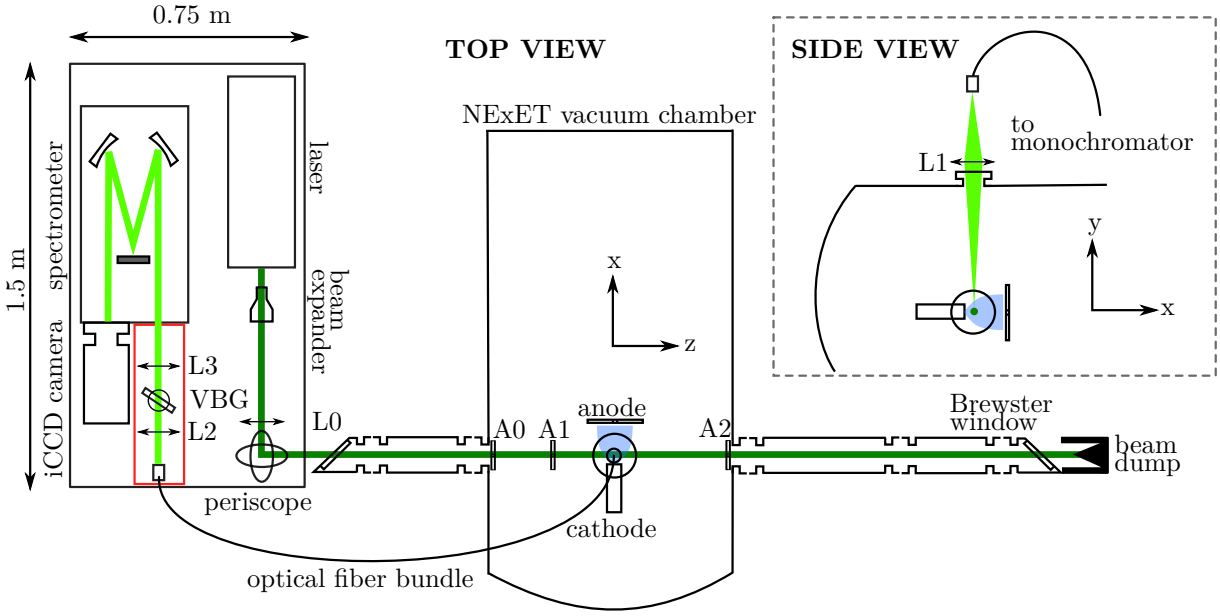

Figure 3.1: View of the THETIS ITS bench setup (not to scale). Two views are shown: a top view of the bench and laser beam trajectory (in dark green) and a side view, showing the collection of scattered light (in light green) at the top of the vacuum vessel. L0, L1, L2, and L3 indicate lenses; A0, A1, and A2 indicate apertures; VBG indicates the volume Bragg grating notch filter used for Rayleigh and stray-light suppression. The plasma volume of a cathode discharge is shown in blue

with a maximum electron density ($n_e \approx 1 \times 10^{19}\,\mathrm{m}^{-3}$ for example) and a minimum temperature ($T_e \approx 1\,\mathrm{eV}$ for example); under these conditions the Debye length would remain above the micrometer length scale ($\lambda_{De} \approx 1.7 \times 10^{-6}\,\mathrm{m}$). The scattering configuration with the observation direction characterized by the angle θ=90° (partially justified by the simplicity of implementation in various vacuum chambers) lead to a length scale probed ten times smaller than the Debye length ($2\pi/k \approx 3.8 \times 10^{-7}\,\mathrm{m}$). In the "worst case scenario" for the plasma conditions, and with the scattering configuration and laser wavelength chosen, the ordering $\lambda_{De} \ll 2\pi/k$ will be never respected. From this observation, we expect the scattered signal to be only composed of the incoherent term of the Thomson scattering intensity (see Equation 2.34).

The choice of laser wavelength was also motivated for technological reasons. The availability of highly efficient detectors (quantum efficiency up to 50 %) and optics with high transmission at 532 nm made the use of the fundamental frequency of the laser (at 1064 nm) less attractive. Even if a lower parasitic signal from Rayleigh scattering is induced at 1064 nm (due to the cross-section varying as λ^{-4}), the low efficiency of detectors at this wavelength would make the diagnostic less efficient, and the higher wavelength would reduce the margin for the transition toward the coherent regime.

3.2.1.2 Transport optics

The transmission branch is composed of several optics used to shape the light beam and reduce the amount of parasitic reflections of the laser beam near the observation volume.

The laser beam is first sent to a beam expander which increases the diameter by a factor of 3 (reducing the beam divergence by the same factor for better focusing efficiency). This beam expander is composed of fused silica lenses, coated for a maximum reflectance R of 0.25 % at 532 nm. The exiting beam is then transmitted to a fused silica lens L0 (50 mm diameter, focal length 2000 mm, R<0.25 % at 532 nm) for focusing inside the observation volume of the plasma. A periscope assembly, using fused silica mirrors coated for a reflectance R>99.6 % at 532 nm, are used to transmit light to the observation volume.

The beam entering the vacuum chamber is polarized in the (xy) plane, with >80 % of the incident optical power along the x-direction. The vacuum chamber is equipped with custom fused silica Brewster windows (100 mm minor diameter) aligned for optimal transmission of the laser polarization along the x-direction. This leads to a minimization of parasitic reflections. Brewster windows are mounted at

the end of aluminum tubes (total lengths 0.8 m for the left side and 1.3 m for the right side in the current implementation). The use of long tubes ensures that reflections at the Brewster window surfaces have a low probability of reaching the measurement volume; this configuration also increases the time of flight of occasional reflected beams, potentially allowing partial temporal filtering with sufficiently narrow detection gate.

As seen in Figure 3.1, several apertures have been set up between the entering laser beam, starting at the vessel wall and up to the plasma volume, with a last aperture at the second vessel wall. These elements, identified by A0, A1, and A2 in Figure 3.1, are intended to further minimize the propagation probability of stray-light toward the observation volume (originating from reflections on optical components such as Brewster windows). The apertures are constructed from thin aluminum sheets and diaphragms with matte black coatings. In the center of the plasma volume, the measured beam waist is about 0.3 mm. After traversing the plasma, the beam is sent to a beam dump with a large acceptance aperture (66 mm diameter) which provides multiple internal reflections, limiting the return of dumped light to the plasma. When possible, a viewing dump made of anodized aluminum is placed on the surface behind the observation volume.

3.2.2 Detection branch

From the arguments of Section 3.1, the main motivation of the detection branch design is the recovery of the maximum number of photons by limiting optics losses as much as possible (for example, by reducing the number of mirrors and lenses required to recover the scattered radiation). The easy implementation of the diagnostic on various plasma sources is the second motivation.

3.2.2.1 Light sources

The light source of the detection branch is the light emitted by the observation volume over the aperture of the first lens. Some of the photons of this light source come from Thomson scattering light, but the majority of the light has other origins. These other light sources and may be an issue for analysis of the signal of interest; for this reason, we used the term "stray-light" to define it.

Stray-light sources can be divided into several categories depending on their characteristics:

- Stray-light from laser reflections on surfaces close to the observation volume generates stray-light spectrally close to the Thomson signal but with a much lower spectral width (given by the spectrometer resolution in our case). The probability for reflection is high and is directly proportional to the laser intensity, resulting in a signal from this source of stray-light several orders of magnitude higher than the Thomson scattering signal. Due to the low temperature of neutrals and ions, stray-light from Rayleigh scattering on heavy particles has the same characteristics as reflection. Both of these stray-light sources are intensively emitted during the laser pulse and spectrally entangled to the Thomson scattering signal.

- Stray-light from plasma emission is another source of light emitted through the detection branch during the whole duration of the plasma discharge. The intensity and spectral shape of plasma emission may depend on the plasma conditions themselves but for the plasma studied, the spectrum will always be composed of a series of relatively sharp emission lines that may overlap the Thomson scattering spectrum.

- Stray-light from fluorescence may happen when the observation volume is close to fluorescent materials. This light intensity is usually relatively weak but it covers a large spectral range at wavelengths higher than the incident wavelength.

3.2.2.2 Transport optics

The transmission of the light toward the optical table for its filtering and analysis can be divided into three main parts:

- A lens that collects the light emitted by the observation volume is placed perpendicular to the incident beamline, in the y-direction, as seen in Figure 3.1. Here, a 100 mm diameter fused silica, plano-convex lens L1 of 200 mm of focal length (coated for R<0.25 % at 532 nm) and placed at the

top port of the vacuum vessel is used to recover the radiation and focus it onto the entrance of a fiber bundle. For the condition associated with cathode investigations, the distance between L1 and the center of the plasma is 520 mm; the lens and fiber bundle end are separated by 325 mm (the side view image of Figure 3.1 is not to scale). This gives an image magnification factor of 0.625.

- A custom fiber bundle is used to relay light collected from the scattering volume to a spectrometer. This fiber bundle is composed of 45 fused silica fibers (NA=0.22 ± 0.02) of diameter 300 µm, stacked in a 15×3 matrix on the entrance and a 45×1 matrix at the other end. The use of fiber arrays to transport the scattered light has been performed by other authors, for example, in [97]. This method of light collection has some advantages. It is possible to maximize the collection of the scattered light while still providing an easily adjustable spatial resolution of the observation region (obtained by changing the number of collecting fibers). The stacking used for collection (15×3) allows for easy recovery of the scattered light and is robust to misalignment, while the 45×1 configuration at the spectrometer end allows for measurement within a narrow spectrometer slit (for example 300 µm if the magnification of the notch filter chamber is 1). The fiber bundle also simplifies the mounting of the detection branch. All of these advantages are important for a diagnostic specifically designed for ready installation on a variety of vacuum chambers and plasma sources. The only drawbacks of light transport with a fiber bundle are the slight increase of losses due to reflection losses when light is injected inside the fiber and the loss of 7 % of the photons during the propagation along the 15 m long fiber used.

  Light from the scattering volume is focused onto a reduced number of fibers by the lens L1. Taking into account the system magnification and the number of fibers imaged (5×3 matrix), the maximum area which can be viewed in the plane (zx) has dimensions of 2.4 mm × 1.4 mm. However, the actual scattering length viewed along x is set by the laser beam waist (0.3 mm). Assuming a scattering length along y also set by the dimensions of the laser beam waist, the plasma scattering volume from which the Thomson signal is recorded has dimensions of $0.216\,\mathrm{mm}^3$ (0.3 mm × 2.4 mm × 0.3 mm). The signal from all 15 imaged fibers is summed to compose the scattered spectrum.

- A notch filter chamber is placed at the exit of the fiber bundle. Firstly, it collimates the light emitted by the bundle with an aspheric lens of 125 mm of focal length and 50 mm of diameter (at the last update of the optical bench). After a filtering procedure described in the next section, the light is focused toward the slit of the spectrometer with a lens of 300 mm of focal length and 50 mm of diameter to fit the numerical aperture of the spectrometer.

3.2.2.3 Filtering optics

Once on the optical table, the detected light has to be filtered before the analysis of the entangled Thomson scattering signal. Because stray-light sources from laser reflections and Rayleigh scattering are intense and spectrally close to the signal of interest, a filtering procedure is imperative before analysis of Thomson scattering signal from low-temperature plasmas sources. Several already applied techniques for stray-light filtering at the wavelength of the laser light source (532 nm) were considered during the diagnostic design phase:

- Triple Grating Spectrometer (TGS) is the most commonly used techniques for filtering of stray-light from reflections and stray-light [64, 98]. This technique uses the first grating to disperse light. For spectral filtering, a mask is positioned inside the spectrum to stop the light rays inside a desired spectral range. Light dispersion is then canceled with a second grating to focus it inside an intermediate slit. Light entering the last slit is finally dispersed with a third grating before detection.

  This type of architecture filter light with a sharp spectral profile of rejection (FWHM<1 nm) and an efficient attenuation at the rejected wavelength (OD>5). However, the numerous optics and gratings used for filtering results in transmission efficiency of the diagnostic usually below 15 % (even with holographic gratings and adapted optical coatings). Another direct consequence of the complexity is the increased size and mass of the diagnostic; this would make the transportation of such a diagnostic complicated.

- Gas cells are other techniques less commonly used [99–101]. These techniques rely on the absorption properties of some vapor-phase species (e.g, I_2, Hg, K, Rb) [102], sometimes diluted in another gas. A gas cell is simply positioned along the path of the light inside the detection branch and the gas species used will absorb photons with an energy matching the electronic transition. Through control of the gas pressure and temperature inside the cell, absorption profiles can be shaped to a certain extent to fit the required performance.

  The simplicity of this technique (no optics needed) makes it attractive. Nevertheless, the method can be applied only for a restricted range of stray-light wavelengths where absorption is strong enough. Saturation of the electron transitions used for absorption by a strong stray-light level may be an issue and would require a longer gas cell. Finally, because the electronic structure of the atoms or molecules inside the vapor phase is usually complex, electronic transitions that may significantly absorb light are numerous. For example, an iodine cell is expected to be well adapted for attenuation of stray-light from reflections and Rayleigh scattering generated by intense pulses of Nd:YAG Q-switch lasers frequency-doubled to 532 nm, yet the numerous other absorption rays around 532 nm would, for example, distort the Thomson spectrum and make its analysis challenging. This technique may be interesting in the case of a plasma with very low electron temperature (i.e., with a Thomson spectrum spanning a sharp spectral range).

- Conventional notch filters are frequently used for Thomson scattering diagnostics. They are particularly useful for extraction of spectral parts of the large spectral distribution encountered in fusion devices such as Tokamak [103]. The rejection bandwidth of such notch filter types remains relatively large (typically FWHM>10 nm). The broad spectral range of attenuation makes these types of notch filters inappropriate for low-temperature plasma investigations. Both stray-light and Thomson contributions would be systemically filtered.

  Conventional notch filters are based on the deposition of several thin films of dielectric coatings on a glass substrate. The alternation of two dielectric coatings with different refractive indices creates a rectangular oscillation of the refractive index for which some wavelengths may respect the Bragg conditions and be reflected (dielectric mirror and anti-reflection coating use the same principle). The reflectivity efficiency rises with both the optical index contrast of consecutive layers and the number of modulation cycles; on the other side, the increased contrast enlarges the spectral rejection bandwidth. In practice, stable deposition of dielectric layers over large thicknesses is challenging (around 100 modulations at maximum). To overcome this weakness, large optical index contrasts are used to reach sufficiently large attenuation (or reflection if it is used as a mirror). Large attenuation levels are reached at the cost of the larger spectral bandwidth (typically FWHM>10 nm) which makes this technique inadequate to our application.

- The Volume Bragg Grating-based Notch Filter (VBG-NF) technology is based on a modulation of the optical index recorded inside a transparent material. Similarly to dielectric layers-based notch filter, the VBG-NF can efficiently reject stray-light, but with a much lower spectral and angular rejection bandwidth. Before this thesis, such a filter had never been applied in a Thomson scattering diagnostic, but its efficiency was already proven through its use in Raman scattering diagnostics [104–106], which face similar filtering challenges to Thomson scattering.

  The VBG-NF technology, commercialized less than 10 years ago [104], uses a weak modulation of the optical index inside the bulk of a Photo-Thermo-Reflective (PTR) glass [107, 108]. The optical index modulation is obtained from the exposure of the PTR glass to a periodic interference pattern created by a UV laser. This exposure induces a modification of the distribution of ions inside the glass that once heated above 500 °C will precipitate into micro-crystals responsible for optical index modulation. From the control of the exposure duration and intensity of the interference pattern, the contrast of optical index modulation is finely tuned in order obtain a rejection bandwidth a sharp as possible (FWHM below the nanometer length scale for wavelength in the visible range). To compensate for the reduced reflectivity, the optical index inside VBG-NF is modulated over more than 1000 cycles without any issue of layer stability so that high rejection efficiency is also achieved (typically OD>3). The only drawback of such technology is its sharp spectral rejection range that results in a small acceptance angle.

Because of the unique features of VBG-NF, THETIS uses this type of optical element for filtering. Figure 3.2 illustrates plots of some quantitative specifications of the VBG-NF supplied by OptiGrate,

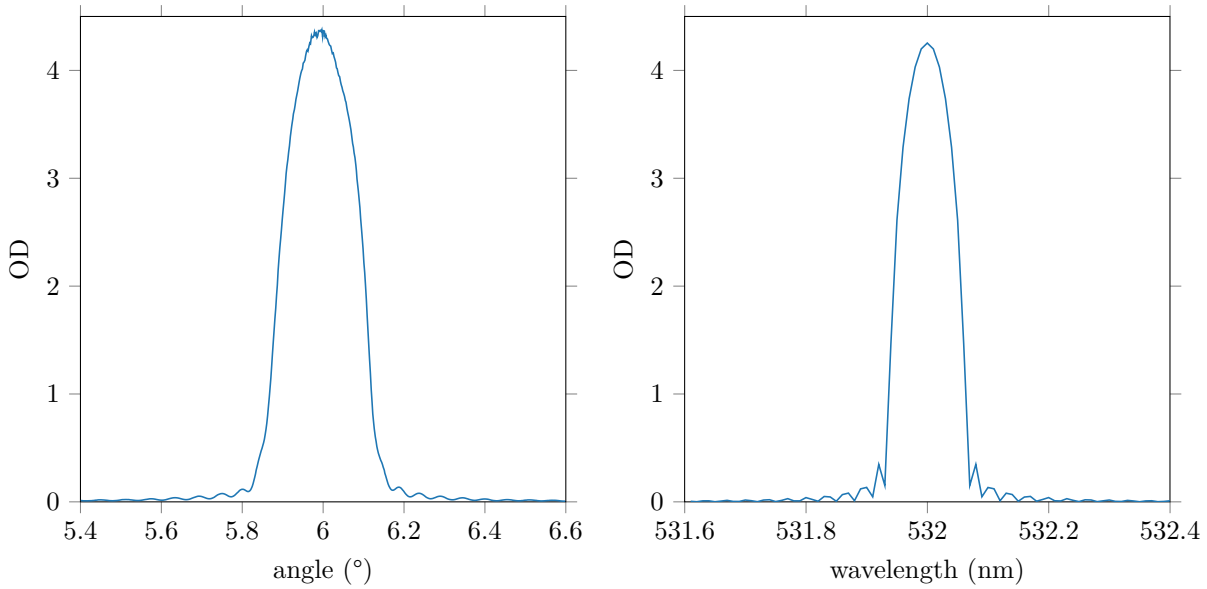

Figure 3.2: Optical density (OD) of the volume Bragg grating notch filter as a function of incident (a) angle and (b) wavelength (courtesy: OptiGrate).

the company that manufactured the VBG-NF used in this thesis (similar technologies are developed by other companies [109]).

Figure 3.2a shows the sensitivity of the grating attenuation to the alignment angle (which is referenced with respect to a perpendicular incidence angle at 0°). The acceptance angle of this profile is approximately 0.3°; this shows that maximizing the attenuation requires limiting the beam divergence below this value. In practice, this collimation is guaranteed by a notch-box positioned upstream of the spectral dispersion step. As shown in Figure 3.1, the VBG-NF is positioned between the lenses L2 and L3 of the notch filter chamber (previously described) whose characteristics were chosen to fit the accepted light divergence of the filter and spectrometer respectively. The high angular selectivity of the VBG-NF requires fine-tuning of the incidence angle; this is done with a micrometric rotation stage on which the filter is mounted.

Once the light beam is correctly collimated and tuned at the desired incidence angle, the VBG-NF has high spectral filtering capabilities. Figure 3.2b shows attenuation as a function of wavelength for the filter optimized for 532 nm wavelength rejection, it illustrates the sharp filtering with a FWHM of only 0.2 nm and a maximum optical density of 4. Outside the narrow bandstop, the transmission efficiency exceeds 96 % so that the light spectrum outside this spectrum is neither distorted nor attenuated.

The THETIS setup was first limited to the use of a VBG-NF with a clear aperture of 11 mm × 11 mm (only Chapter 4 is concerned with this element). The filter was later updated to a VBG-NF with a clear aperture of 25 mm × 25 mm (with investigation of Chapter 5 and Chapter 6 realized after the update); a comparison of the two filter dimensions is shown in Figure 3.3. This update allowed improvement of the transmission efficiency of the detection branch by allowing better recovery of light rays originally falling outside the filter dimensions. These losses were simply due to the large focal length needed for a sharp enough collimation before transmission of light through the VBG-NF. Typically, the required distance for collimation rises with both a lower acceptance angle of the VBG-NF and an increased size of the fiber bundle. In the ideal case, the size of the VBG-NF should fit the area of the collimated beam that increases with both the collimation distance and the numerical aperture of the fiber bundle used.

The compactness of our setup can be largely attributed to the replacement of the commonly used TGS by a single grating spectrometer (described in the next section) paired with a VBG-NF. Our optical bench has dimensions of only 1.5 m × 0.75 m; a typical triple grating spectrometer alone would occupy a similar area.

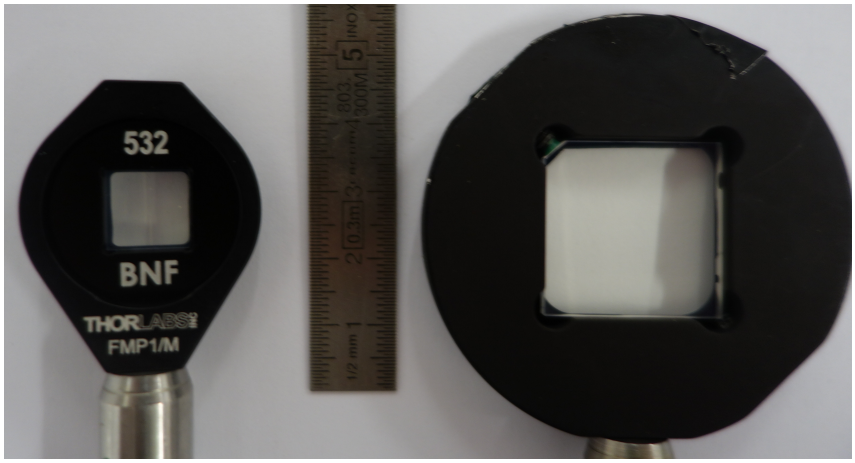

Figure 3.3: Picture of the 11 mm × 11 mm (left) and 25 mm × 25 mm (right) VBG-NF used for filtering of stray-light from laser reflection and Rayleigh scattering on neutrals and ions.

3.2.2.4 Dispersion optics

The THETIS setup uses a single spectrometer. The spectrometer (a Princeton Instruments Acton SP-2750, f/9.7) is fitted with silver-coated mirrors (reflectivity in the visible spectrum range >98 %). It uses one of two turret-mounted gratings: a ruled grating with 600 lines mm^{-1} (grating efficiency of approximately 70 % average over P and S plane polarizations), or a blazed holographic grating with 2400 lines mm^{-1} (grating efficiency of approximately 60 % average over P and S plane polarizations). The spectrometer is controlled using the Princeton Instruments LightField program, which allows for the change of grating. These gratings allow us to select between covering the spectral width expected at high temperatures (tens of eV) and providing adequate wavelength resolution at low electron temperatures (a few eV).

Over the size of the detector, the spectrometer provides a full wavelength coverage, determined at 532 nm, of 5.1 nm and 28.6 nm, respectively, for the 2400 lines mm^{-1} and 600 lines mm^{-1} grating. The wavelength coverage can be expressed in terms of a corresponding electron velocity and energy coverage as

$$v = c\frac{\lambda - \lambda_i}{2\lambda_i \sin(\theta/2)} \tag{3.1}$$

and

$$E = \frac{1}{2} m_e v^2 \tag{3.2}$$

where v is an equivalent velocity (based on a spectral half-shift) and E is the corresponding energy associated with this velocity. m_e, λ_i and θ are the electron mass, incident laser wavelength and scattering angle, respectively. These expressions give a v of 1×10^6 m s^{-1} and 5.7×10^6 m s^{-1} for the 2400 lines mm^{-1} and 600 lines mm^{-1} gratings, respectively. The corresponding energy coverage (half-spectrum) is 2.94 eV and 92.3 eV, respectively.

With the minimum slit width of the spectrometer (highest resolution), the narrowest signal has a FWHM corresponding to 3 pixels wide. This corresponds to a maximum resolution of 0.09 nm for the 600 lines mm^{-1} grating and 0.018 nm for the 2400 lines mm^{-1} grating.

3.2.2.5 Detection camera

The detector is a Princeton Instruments ICCD PI-MAX 4-1024f camera, triggered using the laser Q-switch signal. Its Gen II (RB Fast Gate) intensifier has a quantum efficiency of 10 % at 532 nm (a Gen III intensifier could reach efficiency up to 50 % at the same wavelength). The front-illuminated CCD dimensions are 13.3 mm × 13.3 mm (with pixels of size 13 µm × 13 µm).

The camera is controlled with the same Princeton Instruments LightField program, which allows for the choice of acquisition parameters (such as triggering, detector gain, gating duration, number of

accumulations, pixel binning) and the storing of the acquired spectra. The easy modification of all these parameters simplifies the adaptation of the diagnostic to a large range of signal intensities expected.

Gated operation of the camera is applied with a temporal window usually between 10 ns and 15 ns; this allows attenuation of the light outside the gating period up to OD6. The use of such detectors with short intensification periods contributes to the attenuation of light at 532 nm by limiting the collection of stray-light from optics far from the observation volume. The continuous contribution of light from plasma emission is also efficiently reduced by observation with a low duty cycle of this contribution (acquisition at 10 Hz frequency) and attenuation outside the 10 ns gate.

To increase the signal-to-noise ratio, we perform signal acquisition on binned macro-pixels. Binning along the spatial direction (along the length of the slit) is chosen so that the macro-pixel height fits the height of the slit illuminated by the fiber bundle. This pixel binning removes the possibility of spatial resolution but was necessary given the low level of to measure. Along the spectral direction, the size of the pixel binning chosen depends on the slit width and the signal intensity expected.

Still, we expect few photons from Thomson scattering detected per laser pulse. To reconstruct the spectrum we perform signal averaging of the signal detected at each laser shot over 6000 accumulations. This accumulation method is more efficient than *on-CCD accumulation*, because, for our particular acquisition conditions (a large number of bins, a low laser repetition rate and a low camera readout noise), the dark current noise in the case of *on-CCD accumulation* between two laser pulses would be larger than twice the read noise.

3.3 Experimental procedures for diagnostic calibration

The use of any ITS diagnostic requires appropriate calibration procedures.

To start, we routinely perform spectral calibration of the spectrometer with calibration lamps to know the wavelength of the signal measured with both spectrometer gratings. This calibration is necessary for estimation of electron temperature and drift velocity; it is quite a common procedure that will not be detailed here.

Then, the calibration of the intrinsic light redistribution of the spectrometer is realized through the measurement of the instrument function of the apparatus. This calibration is obtained from the acquisition of the signal of a monochromatic and isolated light beam. An accurate instrument function is needed for a more precise estimation of all the electron properties.

Finally, intensity calibration is necessary for estimation of the transmission efficiency of the detection branch. Typically it uses either Rayleigh scattering or Raman scattering and is necessary for estimation of the absolute electron density.

3.3.1 Instrument function determination

The estimation of the instrument function of the diagnostic, performed after the spectral calibration, is realized with the same acquisition parameters and configuration as those to be used for the intensity calibration and Thomson measurement (i.e., the same spectrometer slit width, diffraction grating, pixel binning, intensification, and number of accumulations).

The instrument function is determined according to the following procedure. The vacuum vessel is pumped down to its lowest pressure to remove residual gas (which could contribute to Raman or Rayleigh scattering) and the laser beam is sent across the vessel to provide an artificially-large level of stray-light at 532 nm (for example, by allowing the beam to graze a reflective object). This signal is collected by the detection branch with no VBG-NF mounted. A similar measurement is then made with the laser off, for the same duration; this acquisition constitutes the background noise. The instrument profile is determined from the difference between these two spectra.

Before using it for data analysis, the instrument function profile is normalized such that $\Sigma I(\lambda)\delta\lambda = 1$, where $I(\lambda)$ is the intensity (in photo-detector counts) and $\delta\lambda$ is the spectral width associated with each pixel. This normalized instrument function will be later convoluted with the theoretical calibration spectra to account for the actual redistribution of light intensity at one given wavelength over the surrounding pixels. Such redistribution is the consequence of the specific features of the detection branch. With the experimental conditions used for Thomson signal measurement (pixel binning and large slit width), the spectral width of the monochromatic light is negligible in comparison to the instrument function width. It

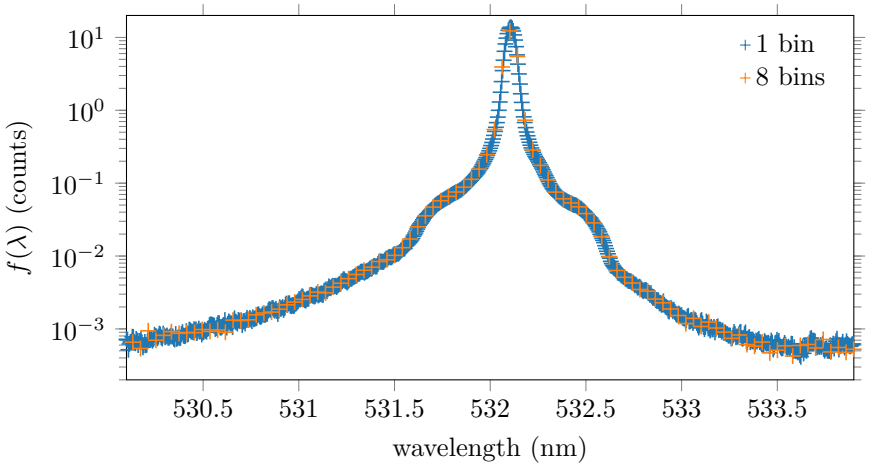

Figure 3.4: Instrument function profile for the THETIS diagnostic obtained using the 2400 lines mm^{-1} grating with a 300 µm spectrometer slit width. The instrument function obtained without horizontal wavelength binning and with binning over eight horizontal pixels are shown with blue "+" symbols and yellow "x" symbols respectively.

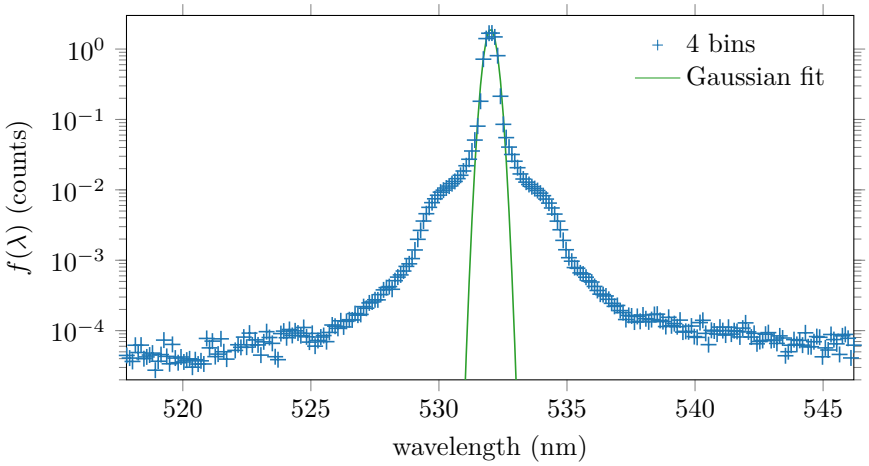

Figure 3.5: Instrument function profile for the THETIS diagnostic obtained using the 600 lines mm^{-1} grating with a 300 µm spectrometer slit width. The "+" symbols in blue correspond to experimental data while the green line shows the Gaussian best fit of the profile.

is therefore considered that it does not affect the signal measured (convolution with a Dirac distribution) so that it corresponds directly to the instrument function. This redistribution is assumed to be constant over the spectral interval probed. For data analysis, the function associated with the linear interpolation of the instrument function measured at 532 nm will be used to simulate the spectral broadening of all rays inside the spectral range covered by the CCD.

Figure 3.4 shows the normalized instrument functions determined with the 2400 lines mm^{-1} and for an experimental slit width of 300 µm. The plot shows the comparison between two cases: in the absence of horizontal pixel binning, and with binning over eight horizontal pixels. With no binning, the FWHM of the instrument function peak is 0.06 nm; with binning over eight pixels, the instrument function FWHM is 0.08 nm. This comparison shows that a pixel binning that preserves at least 3 macro-pixels inside the FWHM of the profile without binning will not affect quantitatively the spectral resolution. The motivation for a high pixel binning is the increase of the signal-to-noise ratio through the reduction of the read noise per unit surface of a pixel. Depending on the plasma density, binning over fewer pixels was used in this work.

Figure 3.5 shows with blue "+" symbols, the normalized instrument function determined with the

600 lines mm^{-1}, a slit width of 300 µm, and a spectral binning over eight pixels. The green line represents the Gaussian best fit of the instrument function. This plot shows that an analytic function rapidly diverges from the experimental function. To take into account the wider redistribution profile of the detection branch, we systematically use the interpolated function of the experimental instrument function for a more relevant data analysis, the interpolation fixed the intensity of light redistribution outside the spectral width measured to 0.

3.3.2 Intensity calibration

Rayleigh or Raman scattering are commonly used for the calibration of Thomson scattering diagnostics. Both scattering regimes correspond to the scattering of an electromagnetic field on atoms or molecules generated from the appearance of an oscillating dipole; the nature of energy re-emission determines the type of scattering. For atoms or molecules at rest, if the energy re-emission happens at the same frequency as the incident radiation, the scattering is of the (elastic) Rayleigh type. On the other hand, if the electric field causes a change of the vibrational or rotational state of the molecule, scattering is of the (inelastic) Raman type. Resonance Raman scattering is associated with changes in the electronic state of the molecule. In Raman scattering, the molecule may emit photons of lower energy than the incident photon, in which case the corresponding emission lines (known as Stokes lines) are at wavelengths higher than the incident wavelength. On the other hand, the molecule, if previously in an excited state, may emit photons of higher energies than the incident photons, resulting in spectral emission lines (known as anti-Stokes lines) at shorter wavelengths than the incident radiation.

For Rayleigh calibration, used for example in [110, 111], the Rayleigh scattered signal and the diagnostic stray-light are superposed at the initial laser wavelength. A certain degree of care is required in the use of Rayleigh signals for calibration. Since the detector response is not usually perfectly linear with light intensity (a feature we have observed in our case, with deviations increasing at very high light intensities), there is a risk of inaccuracy when high amplitude Rayleigh spectra are used to calibrate the weaker Thomson scattered radiation (particularly if acquisition parameters are changed). It is also worth noting that for our particular setup, even at pressures which are expected to give Rayleigh scattering peak amplitudes similar to those of the Thomson scattering signal, the stray-light contribution still dominates at 532 nm and this would render our calibrations using this method unreliable. Lastly, the Rayleigh calibration and Thomson spectrum setups differ slightly in their optical components (obtaining the Rayleigh spectrum requires the removal of the VBG-NF used to attenuate light at the incident wavelength); such differences between the setups must be taken into account for correct calibration and add another source of uncertainty to the measurement.

We have opted to use Raman scattering for calibration. The Raman calibration procedure, used for example in [79, 99, 112, 113], relies on fitting to rotational emission lines which are shifted with respect to the laser wavelength. This method is expected to allow better estimation of the calibration coefficient as experimental conditions of the detection branch for measurement of Raman and Thomson scattering are identical. In particular, to work over the same amplitude dynamic on the detector, we use Raman signals measured at pressures which give spectra of comparable amplitudes to the Thomson scattering spectra.

3.3.2.1 Raman spectrum acquisition procedure

The following procedure is used to obtain a typical Raman spectrum used for calibration in this work.

The previously pumped vacuum vessel is filled with dinitrogen to a known pressure (1000 Pa for all the calibrations in this thesis) and the Bragg volume grating is initially misaligned to allow the detection of a large Rayleigh signal. This Rayleigh signal is used simply for preliminary alignment of the detection branch, ensuring the correct positioning of the optical fiber used to collect light. Once this alignment is completed, the Bragg grating is realigned to minimize the light peak at 532 nm.

Signal acquisition is performed with the laser beam (repetition frequency 10 Hz) traversing the vessel for 10 min (6000 camera acquisitions for one Raman spectrum), followed by a noise spectrum acquisition with the laser off. This latter signal is subtracted from the first. Typically, the use of hardware binning of 4 or 8 pixels on the horizontal axis (wavelength direction) improves the signal-to-noise ratio by a maximum value of respectively 4 or 8 compared to the unbinned case. For all Thomson and Raman acquisitions, the camera counts the charges on the CCD at each laser pulse and averages this over 6000 laser pulses. The summation known as *on-CCD accumulation* was not used in this work.

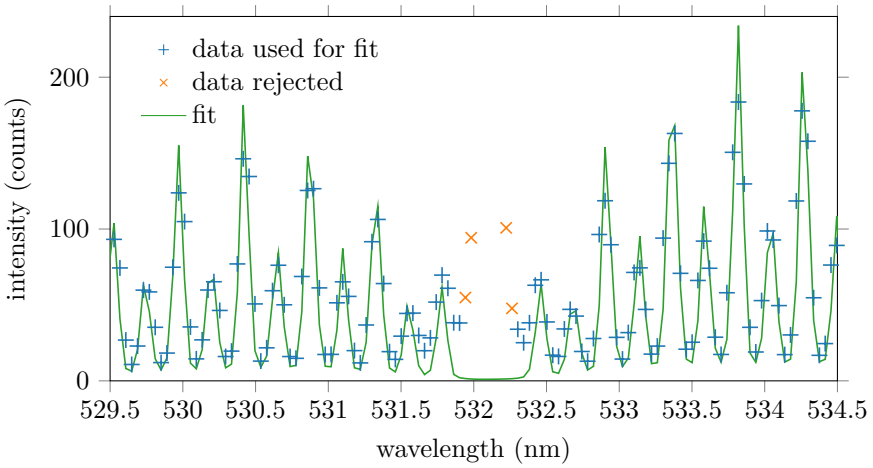

Figure 3.6: Example of a Raman scattering spectrum used for calibration, obtained with dinitrogen at 1000 Pa, the 2400 lines mm^{-1} grating and a spectrometer slit width of 300 µm. From the experimental data represented with "+" and "x" symbols, the central part corresponding to the yellow "x" symbols is excluded for the estimation of the best fit drawn with a green line.

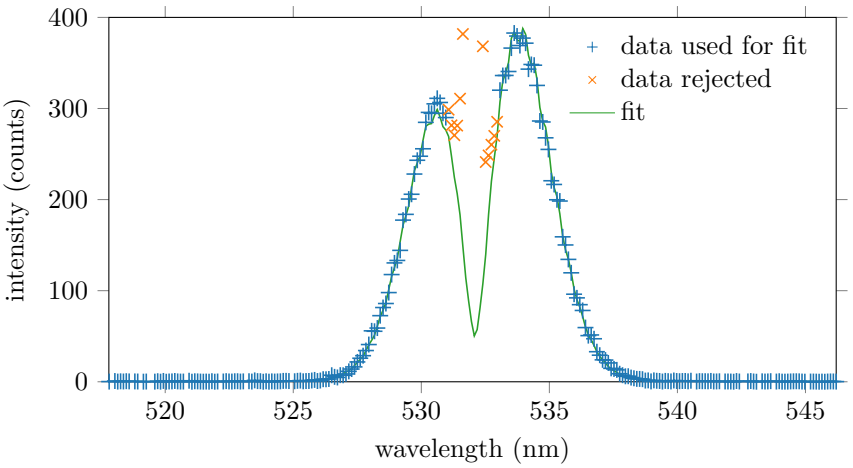

Figure 3.7: Example of a Raman scattering spectrum used for calibration, obtained with dinitrogen at 1000 Pa, the 600 lines mm^{-1} grating and a spectrometer slit width of 300 µm. From the experimental data represented with "+" and "x" symbols, the central part corresponding to yellow "x" symbols is excluded for the estimation of the best fit drawn with a green line.

Examples of two Raman spectra obtained are shown in Figure 3.6 and Figure 3.7. These figures show the experimental points acquired (blue and orange symbols) as well as the best fit function (green line). The parameters of this function were obtained after the fitting procedure described in Section 3.3.2.3). The blue "+" symbols indicate data points taken into account for fitting. The orange "x" symbols correspond to the data points around the laser wavelength which are excluded for the fitting procedure. At this proximity from the laser, the signal may be affected by both the VBG-NF filtering spectral range and redistribution of light from the remaining stray-light peak.

The spectral width of data rejection is fixed depending on the width of the instrument function ($f(\lambda)$) whose acquisition procedure is described in Section 3.3.1. The interval for data rejection is centered on the stray-light peak and its width is set to three times the FWHM of instrument function. With this restriction, the distortion from redistribution remains over two orders of magnitude lower than the amplitude of the remaining stray-light peak. Such a criterion will be sufficient for all the Thomson spectra acquired as the remaining stray-light peaks do not exceed two orders of magnitude above the Thomson scattering signal in intensity.

These figures, showing Raman spectra, illustrate the performance of the VBG-NF. It allows a significant attenuation the light at 532 nm while permitting the Stokes transitions (wavelengths above 532 nm) and anti-Stokes transitions (wavelengths below 532 nm) close to the laser wavelength to be fully resolvable. Without the notch filter, the Raman peaks would be blurred by the redistribution of the strong stray-light peak around 532 nm.

We have performed similar Raman spectrum measurements over a range of pressures (50 to 1000 Pa) and verified that with the same value of fit parameters applied to all spectra, superposition of the experimental and theoretical curves scales only with the pressure. This validates the linearity of our detection in this dynamic range and thus, the use of such spectra in calibrations.

3.3.2.2 Raman spectrum intensity distribution

The spectral peaks visible in Figure 3.6 correspond to transitions from one rotational state to another. The first rotational states are characterized by their rotational quantum number J (with $J \in \mathbb{N}$) and their state energy $E_J = J(J+1)B$, with B the rotational constant equal to 2.48×10^{-4} eV for N_2 [114]. Only J to $J \pm 2$ transitions are authorized due to symmetry selection rules. The expected wavelengths and line powers associated with these transitions can be predicted using an analytical expression developed in detail in other works, such as in [115]. Here we summarize only a few useful forms.

The wavelengths of the different Raman peaks associated with these transitions are given by

$$\lambda_{J\to J\pm2} = \lambda_i \pm \frac{\lambda_i^2}{hc}(4J + 2 \pm 4) \tag{3.3}$$

with the minus ("-" symbol) representing Stokes transitions leading to scattered wavelengths at larger wavelengths than the initial laser wavelength (λ_i), and the plus ("+" symbol) for anti-Stokes transitions leading to shorter scattered wavelengths.

The distribution of the scattered Raman powers over the various wavelengths follows the law given by

$$\frac{dI_R}{d\Omega}(T, \lambda, \vec{e}_s) = n_g I_i L \sum_{J,J'} \frac{n_J(T)}{n_g} \frac{d\sigma_{R,J\to J'}}{d\Omega}(\vec{e}_s)\delta(\lambda - \lambda_{J\to J'}) \tag{3.4}$$

where $\delta(\lambda - \lambda_{J\to J'})$ is the Dirac distribution. n_g is the gas density, I_i the incident laser power and L the length of the scattering volume. $\frac{d\sigma_{R,J\to J'}}{d\Omega}(\vec{e}_s)$ is the differential cross-section for a Raman transition $J \to J'$ and n_J represents the density of an initial rotational state J. Equation 3.4 neglects natural line broadening, Doppler broadening and pressure broadening. The measured Raman peak widths will be set by the instrument function redistribution (determined by the instrument function) which has the most significant contribution.

In Equation 3.4, $\frac{d\sigma_{R,J\leftarrow J'}}{d\Omega}(\vec{e}_s)$ is dependent on the direction of observation, for the direction of observation used with the THETIS diagnostic (perpendicular to both the wave vector of the incident beam and its polarization vector and noted $\vec{e}_{s,\perp}$). The differential cross section of each level can be simplified through the expression

$$\frac{d\sigma_{J\to J'}}{d\Omega}(\vec{e}_{s,\perp}) = (1+\rho)\gamma^2 \frac{32\pi^4}{45\varepsilon_0^2} \frac{b_{J\to J'}}{\lambda^4_{J\to J'}} \tag{3.5}$$

where ρ is the depolarization ratio of the molecule's Raman band (equal to 3/4 for N_2 under Placzeks polarizability approximation) and γ the anisotropy of the molecular polarisability tensor (for N_2, the interpolation of γ^2 using the values from [114] gives a value of $0.505 \times 10^{-48}\,\mathrm{cm}^{-6}$). Similar to Rayleigh scattering, the scattering cross section of Raman scattering decreases with the fourth inverse power of scattered wavelength $\lambda_{J\to J'}$ associated with a given transition. Finally, the Placzek-Teller coefficients are the last weighting parameters that determine the value of the cross-section for Raman scattering from a given rotational transition. They are expressed as [114]

$$b_{J\to J\pm2} = \frac{3(2J+1\pm1)(2J+1\pm3)}{8(2J+1)(2J+1\pm2)} \tag{3.6}$$

This equation shows that although the difference of the Placzek-Teller coefficients between Stoke $(J-2)$ and anti-Stoke $(J+2)$ transitions may be significant for low J values, it weakens at higher values. This term is the main source for the weak asymmetry of the Raman spectra measured.

The term n_J of Equation 3.4 respects Maxwell-Boltzmann statistics and gives the population density for each energy level. Figure 3.7 shows a Raman spectrum obtained with a grating of 600 lines mm^{-1} which is not sufficiently dispersive for individual transition peak resolution; for large shifts from the incident wavelength (once Placzek-Teller coefficients are almost constant), the envelopes of Stokes and anti-Stokes scattered intensities are a direct image of the Boltzmann statistic, for rotational states. The statistic of these states is expressed as

$$n_J(T) = n_g Q^{-1} g_J (2J+1) \exp\left(-\frac{E_J}{k_B T}\right) \tag{3.7}$$

The partition sum term Q is similar to a normalization coefficient (in order to have $\sum n_J = n_g$) and can be approximated as $Q \approx (2I+1)^2 k_B T/2B$, with T the gas temperature. B is the rotational constant for the lowest vibrational level (for N_2 molecules, B=2.48 $\times$ 10^{-4} eV) and I the nuclear-spin quantum number (for N_2 molecules, I=1). Finally, the statistical weighting factor g_J depends on the parity of the energy levels; for N_2 diatomic molecules, it is 6 for even values of J and 3 for odd values [114].

3.3.2.3 Raman spectrum fitting procedure

The theoretical expression for Raman scattering intensity expressed in Equation 3.4 does not perfectly match the measured intensity. To express the actual measured Raman signal S_R, certain effects have to be taken into account:

(i) The observation of light is through a limited solid angle $\Delta\Omega$.

(ii) The transmission τ of the system is much lower than 1. It represents the fraction of scattered light which is detected after the total optical losses associated with the detection branch and detector conversion efficiency.

(iii) The radiation is redistributed due to the instrument function $f(\lambda)$.

(iv) The discrete nature of the measured signal (due to recording by individual pixels) discretizes the signal. The scattered power on each pixel comes from the integral of the power spectral density over the associated spectral width.

Taking these features into account, the measured Raman scattering spectrum may be written as

$$S_R(c_1, T, \lambda) = n_g c_1 I_i \delta\lambda \sum_{J,J'} \frac{n_J(T)}{n_g} \frac{d\sigma_{J\to J'}}{d\Omega}(\vec{e}_{s,\perp}) f(\lambda - \lambda_{J\to J'}) \tag{3.8}$$

where $\delta\lambda$ is the wavelength step associated with one pixel. This function is fitted to the experimental data using a least-squares fitting algorithm to extract the optimized constants, $c_1 = \tau L \Delta\Omega$, and T. The values of the gas density n_g, laser intensity I_i and wavelength step $\delta\lambda$ are known and are entered directly into Equation 3.8. The c_1 coefficient is composed from various parameters linked to the scattering volume dimensions and transmission efficiency. No variation of these quantities is expected from the Raman calibration to the end of Thomson scattering investigations.

We note that our data analysis involves the fitting of the Raman profile, however, some other authors opt for calibration using the area under the Raman profile. This approach is valid and is equivalent if the spectral rejection range is narrow enough to not exclude the Raman lines close to the incident wavelength.

3.4 Procedures for Thomson scattering investigations

3.4.1 Procedure for Thomson spectrum acquisition

The acquisition of one Thomson spectrum implies several records depending on the plasma source probed. All records are performed with the same acquisition parameters as for Raman scattering acquisitions. In particular, all acquisitions of this thesis are realized through an averaging over 6000 laser pulses (corresponding to acquisitions over 10 min due to the 10 Hz repetition rate of the laser).

To start, we make a record—A with both the plasma and laser on. From this record we detect the signal from Thomson scattering, plasma emission and camera noise (dark current and read noise) and other sources of light that may have to be taken into account. For plasmas with a sufficiently large

Thomson scattering signal in the spectral range probed, a simple subtraction of a record—B with only the electronic noise (plasma and laser off) is enough.

In practice, plasma emission is not always negligible in comparison to the Thomson scattering signal inside the spectral range probed (despite the camera gating used to attenuate the emission contribution). To remove it, if the plasma discharge is stable enough (which is not perfectly the case in Chapter 6) a record—C with the plasma on and laser off is realized. The Thomson signal is then isolated from the plasma emission signal after the subtraction of the record C from the record A.

For some cases, when surfaces near the observation volume are close to fluorescent materials, the Thomson spectrum is also distorted from the fluorescence emission. To remove this contribution, a record—D is realized with the plasma off (but with the same gas injection flow) and the laser on. From the record subtraction D-B, the signal from fluorescence and the remaining stray-light are isolated. The Thomson signal is finally isolated from the complete subtraction (A-C)-(D-B).

The "+" and "x" in Figure 3.8 show an example of the signal obtained from Thomson scattering. We acquired this spectrum from a cathode discharge 3.3 mm from its orifice. The discharge was sustained under a xenon flow of $1.6\,\mathrm{mg\,s^{-1}}$ and a discharge current of 16 A. With this plasma source and at these discharge conditions, the parasitic signal was sufficiently low so that simply the subtraction A-C was enough to isolate the Thomson signal with an acceptable signal-to-noise ratio.

3.4.2 Procedure for estimation of electron density, temperature and drift velocity

3.4.2.1 Thomson spectrum intensity distribution

For convenience, the formula for the total Thomson scattered spectrum power, demonstrated in Chapter 2, can be expressed as a function of wavelength of the scattered light, leading to the following equation:

$$\frac{dI_T}{d\Omega}(n_e, \Delta\lambda_g, \lambda_0, \lambda, \vec{e}_s) = n_e I_i L \frac{d\sigma_T}{d\Omega}(\vec{e}_s) \frac{1}{\Delta\lambda_g\sqrt{2\pi}} \exp\left(-\frac{(\lambda-\lambda_0)^2}{2\Delta\lambda_g^2}\right) d\lambda \tag{3.9}$$

where n_e is the averaged electron density inside the observation volume. $\frac{d\sigma_T}{d\Omega}(\vec{e}_s)$ is the Thomson scattering differential cross-section, along the observation direction $\vec{e}_{s,\perp}$ of the THETIS diagnostic. In this case, it is r_e^2. The last term is the spectral form factor of the scattered intensity for a Maxwell-Boltzmann distribution of electron velocity. The shape of this Gaussian form factor is characterized by its standard deviation ($\Delta\lambda_g$) and central wavelength (λ_0).

It is worth mentioning that the transition from a spectral form factor of the scattered intensity depending on the light frequency to its wavelength involves some hypotheses. From the parameter introduced in Equation 2.45 the wavelength notation gives $\lambda_i = 2\pi c/\omega_i$ for the incident wavelength, $\lambda = 2\pi c/\omega_s$ for the scattered wavelength, and $\lambda_0 = \lambda_i/(1 - 2\sin(\theta/2)(v_{e,drift}/c))$ for the central wavelength of the Gaussian distribution shifted by the electron drift velocity of the probed electrons. With the introduction of the wavelength notation, the difference of the inverses of λ_0 and λ appears in the spectral form factor. For wavelength shifts negligible in comparison to the absolute values of the incident wavelength, the approximation $\Delta\omega \approx -2\pi c\Delta\lambda/\lambda^2$ obtained from linearization is relevant. For example, for a spectral shift of 10 nm from a central wavelength of 532 nm, this hypothesis gives a relative error below 2 %. The maximum spectral shifts expected inside the plasma sources of this thesis are at the limit of validity of this approximation. We derived Equation 3.9 under this hypothesis, leading to the following expression for the standard deviation of the Gaussian spectrum

$$\Delta\lambda_g = \frac{k\lambda_i^2}{2\pi c}\sqrt{\frac{k_B T_e}{m_e c^2}} \tag{3.10}$$

The simple expression of the wavelength shift induced by electron velocity also requires the non-relativistic electron velocity hypothesis (already considered in Chapter 2). Indeed, a simplified expression of $\lambda_0 - \lambda_i$ is obtained only after a Taylor expansion of the expression of λ_0 so that $\lambda_0 - \lambda_i \approx 2\sin(\theta/2)\lambda_i(v_{e,drift}/c)$.

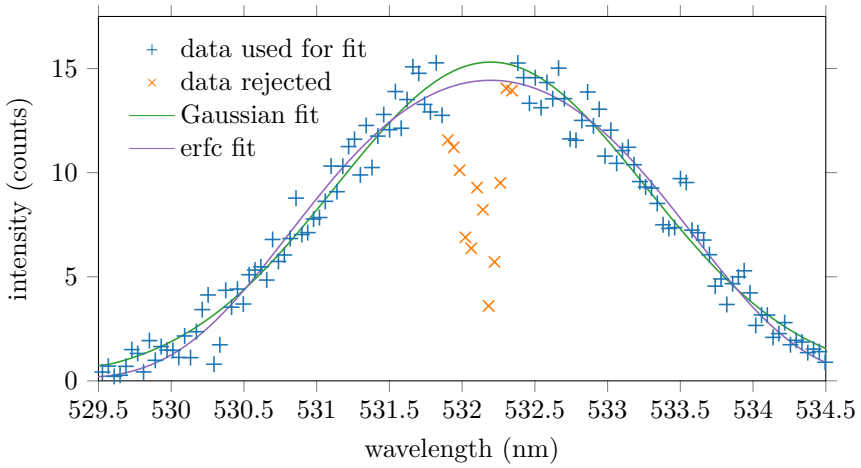

Figure 3.8: Example of a Thomson scattering spectrum obtained with the 2400 lines mm^{-1} grating and a spectrometer slit width of 300 µm. From the experimental data indicated with "+" symbols the best Gaussian and erfc fit functions are estimated.

3.4.2.2 Thomson spectrum fitting

Due to the same consideration as for Raman scattering, the expression of the signal measured from Thomson scattering (S_T) is given by

$$\boxed{S_T(n_e, \Delta\lambda_g, \lambda_0, \lambda) = n_e c_1 I_i L \delta\lambda \frac{d\sigma_T}{d\Omega}(\vec{e}_{s,\perp}) \int_{-\infty}^{+\infty} \frac{1}{\Delta\lambda_g} \exp(-\frac{(u-\lambda_0)^2}{2\Delta\lambda_g^2}) f(\lambda - u) du} \tag{3.11}$$

This analytic form contains the parameter c_1 estimated from the Raman calibration. The laser intensity I_i is re-measured and is treated as an input term in Equation 3.11 in order to account for possible variations in its value between the Raman and Thomson measurements. The term $\delta\lambda$ is also entered directly and depends on both the number of pixels binning on the CCD and the dispersion of the grating used.

Given the extended solid angle collected, the scattering cross-section for Thomson scattering is not constant over the solid angle surface. For the implementation presented in this thesis, the half-angle of the collection remains below 8°. Even for this "worst case scenario", the relative variations of the cross-section are below 2 % at maximum. This remains acceptable and the maximum value is considered for the data analysis procedure.

The fit of the analytic function to the experimental Thomson spectrum gives the estimated values of n_e, $\Delta\lambda_g$ and λ_0. The fit parameter gives the electron density directly, however, for the other electron properties, the derivation is less straightforward.

The electron temperature T_e is proportional to the square of Gaussian spectrum standard deviation $\Delta\lambda_g$ (relevent under the assumption of a Maxwellian-Boltzman EVDF). T_e is obtained from the Equation 3.10 through the following formula

$$\boxed{T_e = \frac{m_e c^2}{4k_B} \left(\frac{\Delta\lambda_g}{\lambda_i \sin(\theta/2)} \right)^2} \tag{3.12}$$

where k_B is Boltzmanns constant, c the light speed in a vacuum and θ the scattering angle (90° in our case).

λ_0 provides an absolute measurement of the wavelength shift associated with the global electron drift; in the absence of a significant global electron velocity, $\lambda_0 \approx \lambda_i$. When the electron drift velocity is significant enough, it is derived from the formula

$$\boxed{v_{e,drift} = c \frac{\lambda_0 - \lambda_i}{2\lambda_i \sin(\theta/2)}} \tag{3.13}$$

Figure 3.8 shows an example of the signal obtained from a Thomson scattering record subtraction at 1.3 mm from the orifice of a cathode discharge sustained under a xenon flow of $1.6\,\mathrm{mg\,s^{-1}}$ and a discharge current of 16 A. From this spectrum, dominated by the Thomson scattering signal, the spectral range centered on the laser wavelength is rejected over a width equal to three times the FWHM of the instrument function obtained with similar acquisition conditions. This rejection range corresponds to the "x" yellow symbols. The data shown with "+" blue symbols are used to fit the theoretical functions. A Gaussian and an erfc function are used for the fitting of the spectrum; as shown in Section 2.5.2, it corresponds to the spectral form factor expected in case of electron following a Maxwell-Boltzmann EVDF or a Druyvesteyn EVDF. From the fitting procedure, plasma parameters are obtained; the Gaussian fit gives n_e=$(3.2 \pm 0.3) \times 10^{17}\,\mathrm{m^{-3}}$, T_e=$(1.02 \pm 0.09)\,\mathrm{eV}$, and $v_{e,drift}$=$(-6000 \pm 5000)\,\mathrm{m\,s^{-1}}$ while the erfc fit gives n_e=$(3.1 \pm 0.2) \times 10^{17}\,\mathrm{m^{-3}}$, T_e=$(0.87 \pm 0.07)\,\mathrm{eV}$; and $v_{e,drift}$=$(-6000 \pm 5000)\,\mathrm{m\,s^{-1}}$. For both fitting procedures, the estimations of electron density and drift velocity (both below the diagnostic sensitivity) are almost identical. The difference of approximately 17 % between the two methods for electron temperature estimation - obtained from the standard deviation of the spectral form factor - is likely due to the impact of the density of the highly energetic electrons. Both fits of the theoretical curves are optimized over the scattering signal from the high-density low energy electrons (i.e., the relatively large signal at small wavelength shift), the low intensity of the pixels at large spectral shift have a reduced influence on the estimated fit parameters. However, the high energetic tails of a Gaussian distribution decrease slower than for a Druyvesteyn distribution and the density extrapolated inside these tails contributes to a higher standard deviation estimated for the Gaussian distribution (even if the "bulk standard deviation" is the same). This observation explains the higher electron temperature obtained with a Gaussian distribution and highlights the necessity to consider electrons at thermal equilibrium in order to introduce the notion of electron temperature.

3.4.2.3 Uncertainties estimation

The uncertainties associated with the measurement of n_e, T_e, and $v_{e,drift}$ are due to a number of factors. The laser power (RMS value) has been continuously monitored and fluctuates by a maximum value of 1 % over the 10 min acquisition. We have specifically chosen a capacitive diaphragm pressure gauge (Inficon CDG025D, temperature compensated) with high precision in the range of pressures at which we perform our Raman calibrations. The precision of this gauge in the range of 0.13 to 1330 Pa is 0.2 %. There is an uncertainty due to the quality of the Gaussian fit to the experimental data and this is computed by extracting the covariance matrix after the fitting procedure. This uncertainty depends on the signal-to-noise ratio and can be significant for low-amplitude scattered signals. The largest source of uncertainty for large-amplitude scattered signals remains the uncertainty in the value of the Raman cross-sections used for fitting; this is 8 % [114]. The final uncertainties on the estimated properties of the electrons are calculated from the quadratic sum of the propagation of the uncertainties of the previously mentioned contributions.

3.4.3 Thomson spectrum processing for distribution functions estimation

The type of function used for the fitting of a Thomson scattering spectrum relies on an assumption on the exact shape of the electron distribution functions. As shown in Section 3.4.2.2, the consideration of various spectral form factors for the Thomson spectrum fitting quantitatively affects the electron temperature estimated. Using the formula introduced in Section 2.5, the electron distribution function over the probe spectral range is calculable with fewer hypotheses on the electron distribution functions.

The estimation of electron distribution functions is particularly useful for non-Maxwellian distributions that cannot be characterized with few parameters such as temperature and drift velocity. Instead, the EVDF or EEDF provide more complete information on the spread in electron velocities. Non-Maxwellian distributions may arise, for example, due to particle heating by plasma turbulence (producing high-energy tails of the distribution functions), the existence of high energy particle beams, or energy loss processes (resulting in truncated distribution functions). The observation of such deviation through Thomson scattering analysis has been initiated in certain studies [116, 117]. In this section, we describe a less-commonly used method [95] for the estimation of the EVDF and EEDF and highlight its advantages.

With the method presented, the first step of data processing for estimation of both EVDF and EEDF relies on the estimation of the derivation of the spectral form factor of the Thomson spectrum. To

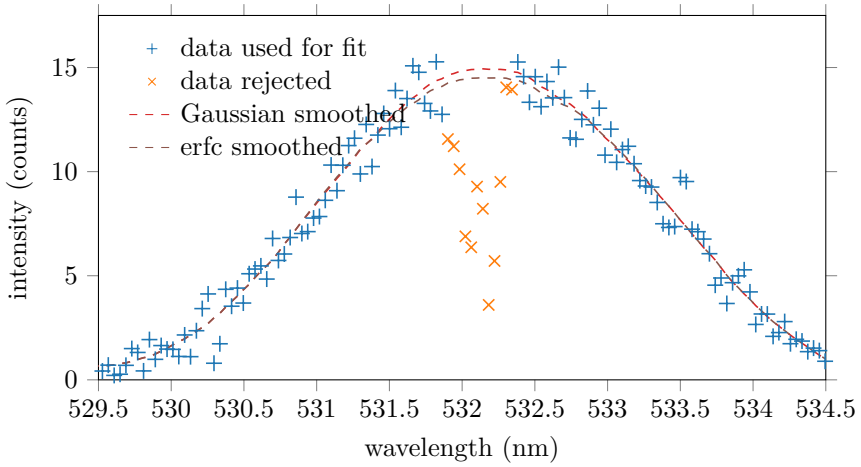

Figure 3.9: Example of the same Thomson scattering spectrum as Figure 3.8 with the analytic functions obtained from a smoothing procedure when Gaussian (red dashed line) and erfc (brown dashed line) fitting functions are considered.

minimize distortion of the derivative due to noise fluctuations, the Thomson spectrum is first smoothed in order to obtain an analytic function. The smoothed function is then analytically derived.

Figure 3.9 shows, with dashed lines, the smoothed functions obtained from the Thomson spectrum measured. To minimize distortion of the smoothed functions at the edges of the data range, the entire spectrum is smoothed at the same time. The rejected range of data is replaced with the values obtained from the fitting procedure. For the smoothing procedure, we used a SavitzkyGolay algorithm [118]. The outputs of this algorithm are either the smoothed functions (shown in Figure 3.9) or the corresponding first-order derivatives.

3.4.3.1 Thomson spectrum processing for EVDF derivation

For estimation of the velocity abscissa of the EVDF, we used the spectral shift from the laser wavelength, with velocity values obtained from the Equation 3.1. Similar to Equation 2.51, the non-normalized EVDF along the observation wave vector direction is obtained from the scattering spectrum derivative with the following expression

$$f_v(v) \propto -(\lambda - \lambda_0)\frac{dI}{d\lambda} \tag{3.14}$$

where $dI/d\lambda$ is the derivative of the Thomson-scattered spectral intensity $I(\lambda)$ with respect to λ obtained from the SavitzkyGolay algorithm and $\lambda - \lambda_i$ is the spectral shift from the center of the Thomson spectrum distribution. Here, we use this spectral shift rather than the shift from the incident laser wavelength $(\lambda - \lambda_i)$ used in Equation 3.1 because it artificially suppresses the non-symmetric shape of the Thomson spectrum. In this way, the formulas used to derive the electron distribution functions are expected to be more accurate because the hypothesis used for their derivation is probably better respected (i.e., an isotropic behavior of electrons).

The EVDFs shown in Figure 3.10 are normalized. For normalization, the non-normalized theoretical EVDFs are divided by their integral over the velocity range probed. In Figure 3.10 the solid lines correspond to the theoretical EVDF estimated from the theoretical fitting function, the green line corresponds to the distribution obtained under the hypothesis of Maxwell-Boltzmann EVDF, and the purple line corresponds to the case of a Druyvesteyn EVDF. The dashed lines correspond to the experimental EVDF estimated for the smoothing and derivation of the Thomson spectrum under the hypothesis of Maxwell-Boltzmann (red dashed line) and Druyvesteyn distributions (brown dashed line). For normalization and to ease comparison, the experimental EVDFs are multiplied by a coefficient in order to have the same maximum as the EVDF obtained under the Maxwell-Boltzmann hypothesis. In theory, the EVDF is defined only for positive velocities (the distribution is supposed symmetric with respect to 0). In our case we also show the EVDF for negative velocities because it is a way to test the isotropic behavior of electrons.

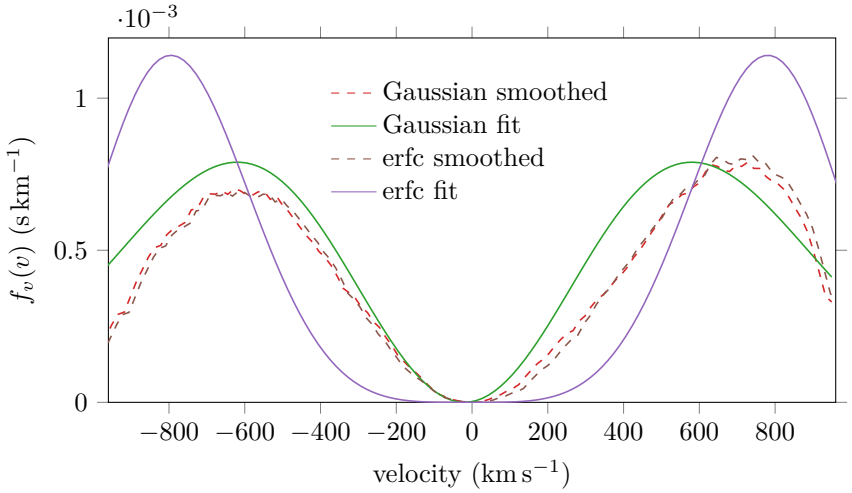

Figure 3.10: EVDFs obtained from a Thomson scattering spectrum. The solid lines correspond to the theoretical EVDFs obtained from the fitting functions shown in Figure 3.8 (green line for Maxwell-Boltzmann distribution and purple line for Druyvesteyn distribution). The dashed lines correspond to the experimental EVDFs obtained from the smoothing functions shown in Figure 3.9 (red dashed line for Maxwell-Boltzmann distribution and brown dashed line for Druyvesteyn distribution).

Both experimental EVDFs shown in Figure 3.10 are almost identical but clear deviations from theoretical distribution are visible. The deviations are clearly not identical for negative and positive values of electron velocity. For negative values of electron velocity, the deviation remains close to the EVDF expected at thermal equilibrium; for positive values, the experimental EVDF becomes even closer to the distribution expected for Druyvesteyn distribution. Even if these deviations are weak, they were observed for multiple distances close to the cathode orifice and were interpreted as a small misalignment of the observation volume with respect to the cathode discharge axis.

3.4.3.2 Thomson spectrum processing for EEDF derivation

Similar to the EVDF, the spread in electron energies may be estimated from the shift from the incident wavelength using Equation 3.2. The non-normalized EEDF ($f_E(E)$) can be obtained from the scattering spectrum derivative with the following expression

$$f_E(E) \propto -\operatorname{sgn}(\lambda - \lambda_0)\frac{dI}{d\lambda} \tag{3.15}$$

where sgn represents the sign function, which equals -1 for negative values of $\lambda - \lambda_0$ and 1 for positive values. Contrary to the EVDF, the derivative of Thomson spectrum is not multiplied by the values of spectral shift. As a result, for large spectral shifts, where the signal-to-noise becomes low, the EEDF will not be amplified by a coefficient which rises with the spectral shift.

Figure 3.11 shows the EEDF obtained with presented method. The experimental EEDF obtained from the smoothing procedure deviates from the theoretical shapes in the same way as for the EVDF.

Figure3.12 shows another way to identify deviation of the theoretical EEDF from the case at thermal equilibrium. Indeed, the natural logarithm of the measured intensity versus the energy calculated from the spectral shift gives a linearly decreasing slope at thermal equilibrium. Such a representation is frequently used in the literature. However, a comparison between Figure3.11 and Figure3.12 shows that this method is sensitive only to large deviations from thermal equilibrium. Such a representation is also applicable only for deviation from thermal equilibrium. For deviation from a Druyvesteyn distribution, the logarithm of the intensity should be represented with respect to the square of the energy. This representation makes the identification of a transition between two types of distributions less easy to identify and less sensitive, compared to the representation based on the derivation of the true distribution functions from the Thomson spectrum.

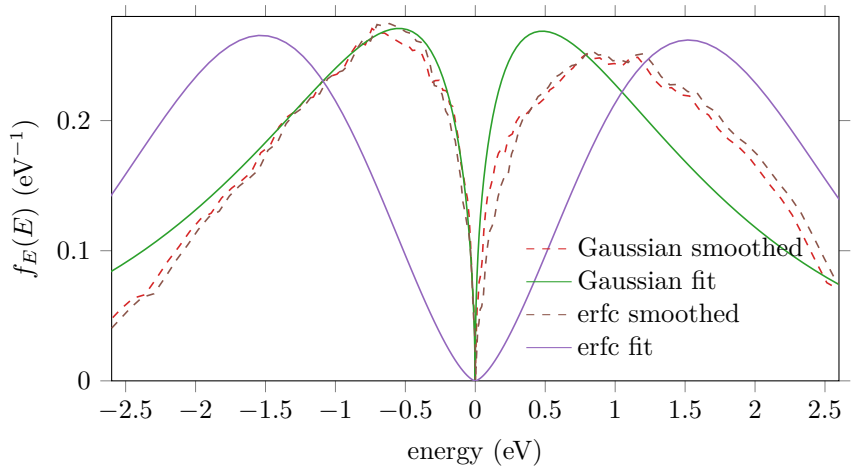

Figure 3.11: EEDFs obtained from a Thomson scattering spectrum. The solid lines correspond to the theoretical EEDFs obtained from the fitting functions shown in Figure 3.8 (green line for Maxwell-Boltzmann distribution and purple line for Druyvesteyn distribution). The dashed lines correspond to the experimental EEDFs obtained from the smoothing functions shown in Figure 3.9 (red dashed line for Maxwell-Boltzmann distribution and brown dashed line for Druyvesteyn distribution).

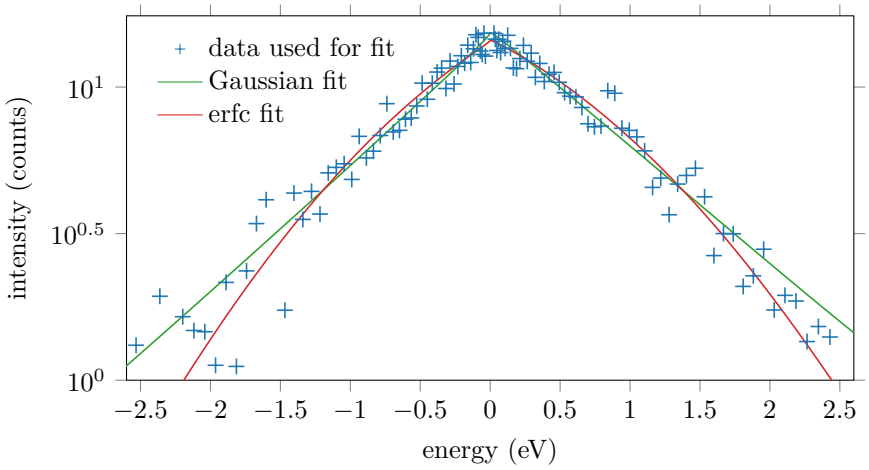

Figure 3.12: Representation of the logarithm of the Thomson scattering intensity as a function of the energy of the corresponding scattering electron (i.e., square of the spectral shift). The "+" symbols represent experimental data and the green and red lines correspond to the fitting functions for Gaussian and Druyvesteyn EVDFs, respectively.

3.5 Light-induced plasma perturbation

Depending on both the plasma conditions and the characteristics of the laser used to induce Thomson scattering, the properties of the electron probed can be modified by the laser by various processes.

3.5.1 Inverse Bremsstrahlung heating

Inverse Bremsstrahlung is the process of absorption of a photon by an electron during its collision with a heavy charged particle (where the collision with a heavy particle is necessary for momentum conservation). In a plasma illuminated by a laser, this process may happen when an electron collides with ions or atomic nuclei and may lead to heating of many electrons positioned along the path of the laser beam.

Taking into account both electron-ion and electron-neutral collisions, Carbone and Nijdam [84, 98]

derived the critical laser fluence (laser energy divided by the beam size) below which the increase of electron temperature remains below a critical value. The corresponding critical fluence is expressed as

$$F_{crit} = 6\pi^2 \frac{\varepsilon_0 m_e c^3 k_B T_e}{\nu_{eh} e^2 \lambda_i^2} \xi \tag{3.16}$$

where m_e is the electron mass, ε_0 the vacuum permittivity, c the speed of light in vacuum, and k_B is Boltzmanns constant. The electronic charge is denoted by e and the laser wavelength by λ_i. ξ is defined as an arbitrary acceptable ratio of temperature perturbation δT_e to the electron temperature T_e. The laser fluence is the external key parameter in the heating process whereas the total collision frequency of the electron with the heavy species (ν_{eh}) is the main internal plasma quantity that determines the efficiency of this process. ν_{eh} is the sum of the electron-ion collision frequency ν_{ei} and the electron-neutral collision frequency ν_{en}.

Using the general expression given by Froula [65], in the case of relatively cold singly-charged ions, the electron-ion and electron-neutral collision frequencies are expressed as

$$\begin{cases} \nu_{ei} \approx \dfrac{n_i}{3} \left(\dfrac{e^2}{m_e \varepsilon_0} \right) \left(\dfrac{m_e}{2\pi k_B T_e} \right)^{3/2} \ln \Lambda \approx \dfrac{\nu_{ee}}{2} \\ \nu_{en} \approx \dfrac{8}{3} n_n r_n^2 \sqrt{\dfrac{2\pi k_B T_e}{m_e}} \end{cases} \tag{3.17}$$

where Λ is the Coulomb logarithm which can be expressed as $\Lambda \approx \frac{12\pi\varepsilon_0 k_B T_e}{e^2} \sqrt{\frac{\varepsilon_0 k_B T_e}{e^2 n_e}}$. In these forms n_i, n_e and n_n are the ion, electron and neutral densities, respectively. r_n is the effective radius of the neutral. As a reminder, the relation between electron-ion and electron-electron collision frequency (ν_{ee}) is given.

To apply these forms, we use a "worst case scenario" which would give the lowest value of F_{crit} applicable to our plasma. To do so we assume a lower limit on T_e of 1 eV, an upper limit on n_e and n_i of $10^{19}\,\mathrm{m}^{-3}$, an upper limit of $1 \times 10^{21}\,\mathrm{m}^{-3}$ for n_n (the order of magnitude for a pressure of approximately 10 Pa at ambient temperature), and an upper limit of 200 pm for the neutral radius (corresponding to the xenon radius, the heaviest noble gas used). This gives a value of Λ of 4500. The corresponding value of ν_{ei} is $2.5 \times 10^8\,\mathrm{s}^{-1}$ and the value of ν_{en} is $1.1 \times 10^8\,\mathrm{s}^{-1}$, giving a value of ν_{eh} of $3.6 \times 10^8\,\mathrm{s}^{-1}$.

For Equation 3.16, we assign an acceptable value of ξ of 1 %. Substituting the other parameters (maintaining T_e of 1 eV and using the calculated value of ν_{eh}), we obtain a value of F_{crit} of $7.9 \times 10^6\,\mathrm{J\,m}^{-2}$. For our experiment, with a peak value of laser pulse energy of 430 mJ and a beam diameter in the observation region of 0.3 mm, we obtain a fluence F_{exp} of $6.1 \times 10^6\,\mathrm{J\,m}^{-2}$. This experimental value of F_{exp} remains below the threshold value F_{crit} for disturbing the plasma, even in the "worst case scenario".

Electron heating from the laser fluence fixes an upper limit of electron density that can be investigated with the THETIS diagnostic. It proves the futility of a strategy which significantly increases the laser energy for investigation of these plasma sources. Considering the range of electron temperatures and neutral densities expected inside the plasma sources probed, perturbation would become significant if electron density reaches $10^{20}\,\mathrm{m}^{-3}$.

The above perturbation criterion is derived under the hypothesis of no energy transfer from the scattering volume to the rest of the plasma volume. Energy transfer would lower the temperature increase and lead to higher critical fluency. On the other hand, a hot point inside the profile of the laser beam may lead to higher fluence than the critical value, inducing local heating even if the perturbation criterion averaged over the beam profile is respected.

3.5.2 Ponderomotive acceleration

Ponderomotive acceleration is the acceleration process induced by the force of the same name. The ponderomotive force is a non-linear force that affects charged particles in the presence of a strong electromagnetic field with fast variation in space (i.e., spatial profile with sharp edges). During its acceleration by the electric field, the charged particle will see a variation of the electric field within one period of the wave, resulting in a net acceleration - averaged over one wave period - directed toward regions with a lower electric field.

As recently shown theoretically [85] and in simulations [119] by Shneider et Powis, ponderomotive forces on electrons can result in density perturbations for a low temperature, low density plasma and may

affect the accuracy of electron density estimation from Thomson scattering measurement. The relative decrease of electron density inside the observation volume is given by

$$\frac{|\delta n_e|}{n_e} \approx \frac{e^2 \lambda_i^2 I_i}{4\pi^2 \bar{e} m_e c^3 \varepsilon_0 k_B T_e \left(1 + \frac{r_L^2}{2\lambda_{De}^2}\right)} \tag{3.18}$$

where I_i is the laser intensity used ($1.2 \times 10^{15}\,\mathrm{W\,m^{-2}}$ near the beam waist), $\bar{e}$ is Eulers constant, λ_i is the laser radiation wavelength, r_L is the beam waist radius and λ_{De} the Debye length.

When $\lambda_{De} \ll r_L$, the perturbation criterion becomes independent of electron temperature but varies with the inverse of the electron density. To check the largest possible density perturbation in our case, we have to consider the "worst case scenario" that corresponds to the lowest electron density and lowest electron temperature; values below respectively $10^{15}\,\mathrm{m^{-3}}$ and 1 eV are not expected inside the plasma sources investigated inside this thesis. This combination gives 2.5×10^{-4} m for λ_{De}, while with the laser and optics used, r_L is approximately 1.5×10^{-4} m. The corresponding relative density perturbation obtained from Equation 3.18 is 0.2 %. Even considering this worst case, the density perturbation is negligible.

For high values of T_e and n_e, the relative perturbation by ponderomotive acceleration is negligible. Nevertheless, this criterion fixes the lower electron density limit that can be probed with the THETIS diagnostic without significant perturbation of the plasma. Typically, due to this criterion, it would not be reasonable to investigate plasma sources with electron density below $10^{15}\,\mathrm{m^{-3}}$ and electron temperature around 1 eV. This observation further justifies the path followed for the development of the THETIS diagnostic. To extend the range of applicability of a Thomson scattering diagnostic toward low electron density, the laser power cannot be increased indefinitely; instead, it is wiser to increase the camera sensitivities and decrease losses inside the detection branch.

It has to be highlighted that the derivation of the electron density perturbation in Equation 3.18 requires the hypothesis of a Gaussian beam profile. A non-Gaussian beam may possess sharper edges (i.e., a higher gradient of the intensity profile) and would induce electron density perturbation for lower laser intensities.

3.5.3 Photo-ionization and Photo-detachment

Photo-ionization is the process of detachment of an electron from a neutral atom or an ion if the energy of an incoming photon is higher than the corresponding ionization energy. For the laser used, the photon energy associated with a photon with a wavelength of 532 nm is 2.33 eV. For the plasma sources investigated, the first ionization energy of the noble gas neutral or ion used to sustain the discharge is much higher; only multi-photon ionization can lead to ionization. The cross-section for multi-photon processes being much lower, this process is extremely rare and is not susceptible to quantitatively perturbing the plasma.

However, the presence of neutrals or ions metasbables would increase the probability of photo-ionization, even from one photon with energy as low as 2.33 eV. The issue of photo-ionization of metastable atoms has been examined for a xenon microwave plasma by Yamamoto and colleagues [120]. In their work, a threshold incident laser intensity of $1.2 \times 10^{15}\,\mathrm{W\,m^{-2}}$ was established empirically for photo-ionization of xenon metastables. The value we obtain for our incident intensity is also $1.2 \times 10^{15}\,\mathrm{W\,m^{-2}}$. However, we have no means of knowing whether the two plasmas are truly comparable, and the proportion of metastables present is unknown for both plasmas. Still, with the laser intensity used, this criterion suggests that the perturbation remains within acceptable limits.

Similar to photo-ionization, photo-detachment is a process of detachment of an electron from a negatively charged ion. The photon energy needed for this process is significantly smaller; a photon energy of 2.33 eV can be enough for many negative ions. That is why, for electronegative plasmas, it would be necessary to reduce the laser fluence to avoid photo-detachment of electrons. Reducing the laser energy to prevent a quantitative perturbation from photo-detachment would result in fewer scattered photons for the scattered spectrum, raising the detection limit above $10^{16}\,\mathrm{m^{-3}}$ (unless this is compensated for, for example, by increasing the number of laser shots or the detection sensitivity). However, the gases used to sustain the plasma discharges investigated in this thesis are weakly electronegative and the electron temperature will be relatively high. These experimental conditions make the probability of production of electronegative ions small. For these reasons, perturbation from photo-detachment will not be considered in this thesis.

3.6 Scattering signal perturbation

The derivation of the Thomson scattering signal performed in Chapter 2 did not take into account the influence of the magnetic field, the influence of intense electric field, or the finite time of interaction between the electron and the electric field. For the range of plasmas probed, even without consideration of plasma perturbation, these parameters can modify the scattering process and consequently the shape of the Thomson spectrum expected.

3.6.1 Finite transit time effect

Due to the large mobility of electrons and to the small volume of observation, many electrons will not remain inside the observation volume during the entire time of the laser pulse. The reduced time of observation induces an increase of the spread in wavelength of the wave analyzed. This spread in wavelength ($\Delta\lambda_{FT}$) relative to the standard deviation of the Thomson spectrum ($\Delta\lambda_g$) can be expressed as [65]

$$\frac{\Delta\lambda_{FT}}{\Delta\lambda_g} \approx \frac{v\lambda_i}{v_{th}L_{obs}} \tag{3.19}$$

where v the velocity of a given electron, $v_{th} = \sqrt{2k_BT_e/m_e}$ the thermal velocity of electrons, λ_i the laser wavelength and L_{obs} the lowest size of the observation volume.

With the THETIS diagnostic, the observation volume radius remains a least two orders of magnitude above the laser wavelength. Even if electrons with velocity ten times higher than the maximum expected thermal velocity are considered, the spread of wavelength due to the finite transit time effect is negligible.

3.6.2 Electron magnetization effects

3.6.2.1 Faraday rotation

In the presence of a magnetic field, the dynamics of electrons under the interaction with an electromagnetic wave is different for left-hand and right-hand polarization. It results in an optical index depending on the polarization and the possibility to rotate the polarization vector of a wave through the so-called Faraday effect. For thin plasmas, the rotation angle (ψ) can be derived theoretically, for a constant magnetic field, and is expressed as

$$\psi = \frac{n_e e^3 \lambda_i^2}{8\pi^2 \varepsilon_0 m_e^2 c^3} Bl \tag{3.20}$$

where B is the magnetic field and l the distance traveled by the electromagnetic wave inside the plasma.

The direct consequence of Faraday rotation is the modification of the scattering configuration so that the angle φ introduced in Figure 2.1 is no longer zero. This modification leads to a decrease of the cross-section for Thomson scattering. For the THETIS diagnostic, the "worst case scenario" would correspond to an electron density of $10^{19}\,\mathrm{m}^{-3}$, a magnetic field of 0.2 T and a maximum distance of 10 cm. For these conditions, the polarization of light would rotate approximately $8 \times 10^{-7\circ}$ and would lead to a negligible modification of the scattering configuration.

3.6.2.2 Helical electron trajectories

In presence of a magnetic field inside the plasma, the incident electromagnetic wave of the laser may interfere with the plasma. In particular, if the frequency of the laser is on the order of the electron cyclotron frequency ($\omega_{c,e} = eB/m_e$), a resonance phenomenon appears with significant modifications of the cross-section for Thomson scattering [121, 122]. For electromagnetic waves in the visible range, this criterion would require a magnetic field on the order 2×10^4 T that is susceptible to be encountered only inside celestial objects such as neutron stars.

Even with no interference between the magnetized plasma and the incident wave, the helical trajectory of a magnetized electron is enough to modify the spectral form factor of the Thomson scattering spectrum. This new characteristic of electron trajectories leads to a modulation of the Thomson spectrum at the electron cyclotron frequency [63]. The intensity of the modulation depends strongly on the relative direction between the probed wave vector ($\vec{k}$) and the magnetic field direction ($\vec{B}$). For a magnetic field

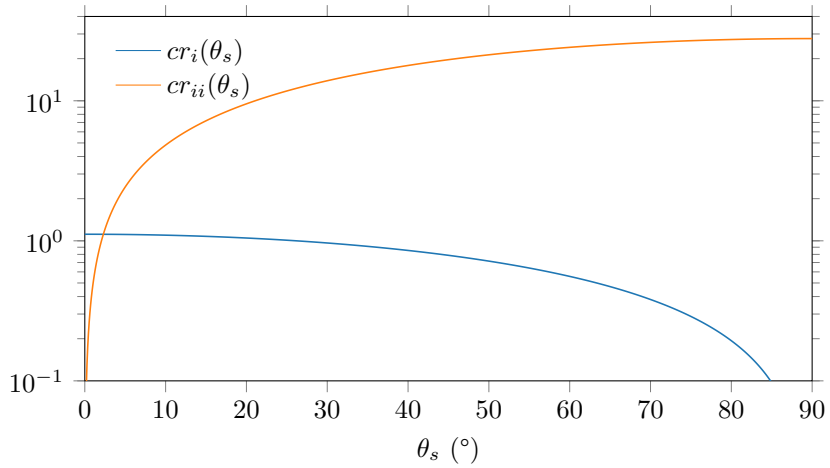

Figure 3.13: Representation of the criterion necessary for detection of Thomson spectrum modulation for various value of the θ_s angles. The "best case scenario" were considered for the choice of the input parameters of the functions.

aligned with the probed wave vector, modulation is maximum; the lowest level of modulation is obtained for perpendicular directions.

For the magnetized plasma sources studied and the scattering configurations used for our investigations, the theory indicates that such modulations are present in the spectrum of the scattered photons. However, the experimental observation of these modulations requires two conditions [65].

(i) To be observable, the spectrum modulation width has to be lower than the Thomson spectrum spectral width. This criterion translates to the inequality

$$cr_i(\theta_s) = \frac{8\pi c}{\lambda_i \omega_{c,e}} \left(\frac{v_{th}}{c}\right)^2 \sin(\theta/2)\cos\theta_s < 1 \tag{3.21}$$

where θ_s is a new introduced parameter corresponding to the angle between the direction of the magnetic field and the scattering wave vector ($\vec{k}_s$). For the scattering configuration used with the THETIS diagnostic, this criterion will be respected if the scattering wave vector is perpendicular to the magnetic field.

(ii) Because the light is collected over a extended solid angle, the direction of the probed wave vector fluctuates over a non-negligible amplitude. In order to resolve the modulation on the Thomson spectrum, despite the average over all the probed wave vector directions, the following criterion has to be respected

$$cr_{ii}(\theta_s) = \frac{2\pi}{\lambda_i \omega_{c,e}} v_{th} \sin\theta_s \Delta\theta_s < 1 \tag{3.22}$$

where $\Delta\theta_s$ is the range of variation of the θ_s angle. $\Delta\theta_s$ is approximately equal to the variation of the scattering angle (θ) for the various directions of scattering light collected by the collection lens (L1). This second criterion will be respected if the scattering wave vector is aligned with the magnetic field.

In order to observe the spectrum modulation, both criteria presented above have to be respected. To ease the identification of the range of θ_s angles for which the criteria may be respected, Figure 3.13 shows the dependence of the functions cr_i and cr_{ii} for θ_s varying from 0° to 90°. For the plot of these functions, the "best case scenario" was considered, corresponding to the lowest electron temperature and the highest magnetic field. For the plasma sources investigated, the electron temperature remained above 1 eV, and at the positions investigated the magnetic field did not exceed 0.2 T.

From Figure 3.13, it is clear that the cr_i and cr_{ii} functions never respect the criteria (<1) for identical values of the θ_s angle. As a result, we expect that modulation of the Thomson spectrum will not be visible for the plasma sources probed. However, we did not consider the magnetic field that may be created by the plasma itself. This contribution may result in a higher magnetic field intensity and a reduced value of the criteria needed for the observation of these modulations.

Among all the investigations of this thesis, it is during the investigation on the planar magnetron that the required criteria were the closest to being respected (plasma source presented in Chapter 4). However, the alignment angle with the magnetic field (θ_s=45°) did not allow the observation of the modulation of the scattered spectrum. Positioned on the axis of the magnetron with the scattering wave vector aligned along the axial direction of the magnetron, it may be possible to detect these modulations. The analysis of these modulations would provide an innovative method for non-intrusive investigations of the magnetic field intensity inside the plasma.

3.6.3 Non-linear and relativistic effects

The calculations in Chapter 2 considered plasma with a priori no relativistic electrons. However, if a sufficiently intense laser beam is used, the corresponding strong electric field can accelerate the free electrons to high speeds. Typically when light intensities approach $10^{22}\,\mathrm{W\,m^{-2}}$, the electric field of the wave accelerates the electron at velocities close to the speed of light while the magnetic field curves electron trajectories in figure-eight patterns. The consequence of this non-linear scattering effect is the emission of another wave at half the incident wavelength and a different spatial distribution of the scattered light [123].

The non-linear Thomson scattering regime may be grouped with the linear regime of Thomson scattering on a relativistic electron. As shown by Glenzer et al. [65], at first order, Thomson scattering on relativistic electron exhibits only a small shift toward lower wavelengths (due to the relativistic Doppler effect). Even at higher order, no harmonic peaks appear in the relativistic regime. The difference between the two regimes relies on the non-negligible role of the magnetic field for the non-linear Thomson scattering regime.

Both the laser intensity and the electron temperature inside the plasma sources probed are too weak to induce such exotic modifications of the scattering signal.

Chapter 4

Incoherent Thomson scattering investigation in the planar magnetron discharge

> The test of all knowledge is experiment. Experiment is the sole judge of scientific "truth".
>
> — *Richard Philips Feynman, Atoms in Motion*

In the last chapter, the theory and motivations behind the Thomson scattering diagnostic developed were presented. In this chapter, we present the results from the first implementation of the THETIS diagnostic on a magnetized plasma: a planar magnetron discharge. In particular, the capabilities of the diagnostic are investigated with spatial and temporal explorations. These investigations are realized in order to compare the dependence of electron properties on the discharge regime, more precisely, the difference between low power (DCMS) and high power (HiPIMS) regimes. Such measurements also provide information relevant to ongoing studies of $\vec{E} \times \vec{B}$ physics, of key interest to the ICARE and the LPGP teams involved.

Contents

4.1 Introduction

Introduced by J.S. Chapin in 1974 [124,125], a planar magnetron is a plasma source used for material deposition and etching applications. Unlike chemical vapor deposition techniques, plasma-based depo-

sition and sputtering techniques are not limited to materials with a low melting point. The interest of planar magnetrons in comparison to other plasma sources is that they offer the possibility to sustain the plasma discharge even with a low pressure of input gas (Ar, Ne, for example). The operating pressure achieved in this device was at least one order of magnitude below the pressure used with previous techniques. Sputtering at low pressure is motivated by the higher deposition rates and better quality of the coating achieved, which is explained by the reduced collision rate of the sputtered atoms with the atoms of the neutral gas. However, this lower collisionality leads to a decrease of the electron impact ionization probability which makes the sustainability of plasma discharge more difficult at low pressure.

The architecture and principle of operation of a planar magnetron are shown in Figure 4.1. The discharge is sustained between a disc cathode and a concentric circular anode called the guard ring. In the range of pressure used for planar magnetron discharge (0.1 Pa to 10 Pa), the electron mean free path is higher than the source characteristic length. Along the path between the cathode and the anode, the probability of collision of an electron with a neutral is extremely low. In order to keep the electron impact ionization probability high enough to sustain the plasma discharge, the path length of an electron is extended with a magnetic barrier. Typically, the magnetic field is generated with permanent magnets or coils placed beneath a target material disc used as an anode. The radial magnetic field in front of the target is strong enough to magnetize electrons accelerated by the electric field of the sheath. Once magnetized, electrons are trapped in an azimuthal $\vec{E} \times \vec{B}$ closed drift, which leads to an increase of the probability of collisions with a neutral. If an atom from the neutral gas is ionized by impact ionization, for example, the ion is affected by the electric field of the extended pre-sheath and is accelerated toward the target. The collision of the ion with the target sputters atoms or ions from it; after diffusion downstream, the sputtered particle can deposit on a substrate, for example.

The design of the planar magnetron drastically increases ionization efficiency while maintaining a simple architecture. However, the physics of such discharges is complex and needs sophisticated codes for a reliable simulation of the plasma behavior. For example, multi-scale behavior and phenomena such as instabilities leading to plasma non-uniformity and anomalous transport [126, 127] contribute to the complexity of the physics. Finally, the nature of the discharge regime is also expected to be able to drastically impact the physics of the discharge.

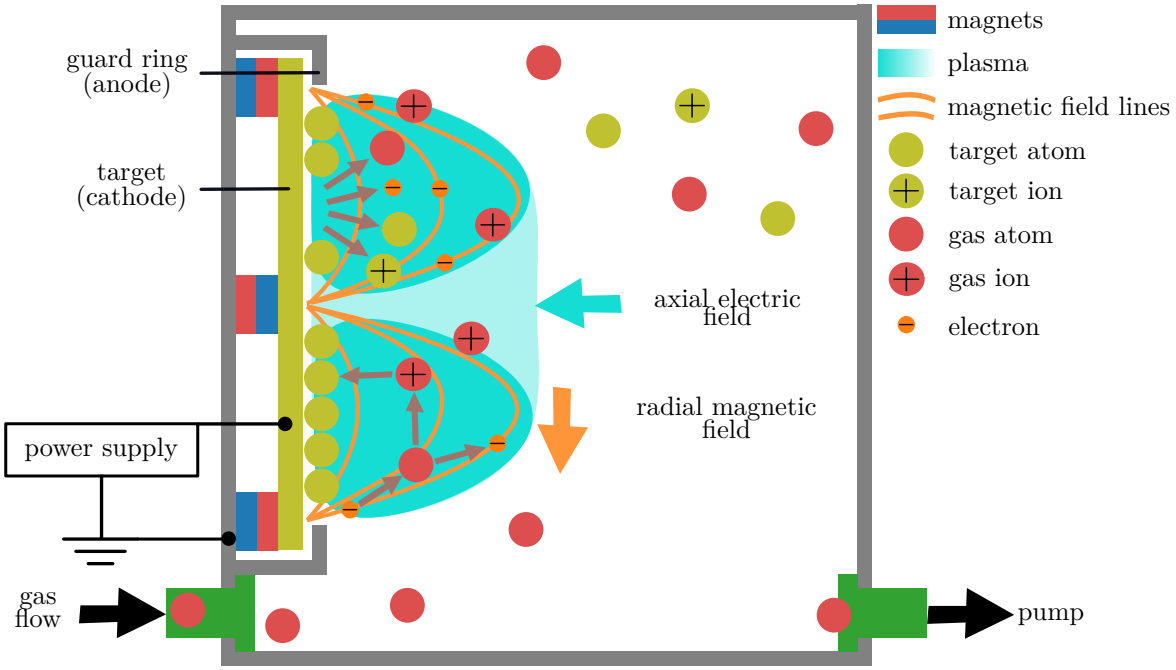

Figure 4.1: Architecture and principle of operation of a planar magnetron discharge.

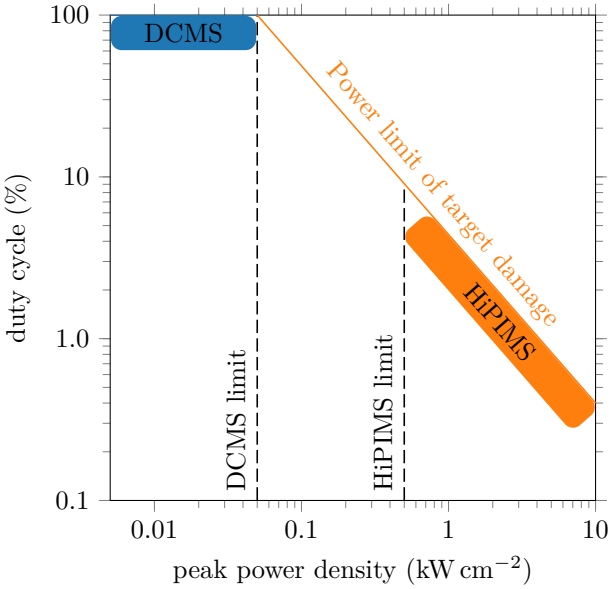

Figure 4.2: Position of the DCMS and HiPIMS regimes for a planar magnetron discharge in duty cycle versus peak power density diagram.

4.1.1 Discharge regimes of the planar magnetron

4.1.1.1 DCMS regime

The Direct Current Magnetron Sputtering (DCMS) regime was the first historically used regime for planar magnetron discharge. This regime is characterized by DC power applied to the target (see Figure 4.2). The thermal load induced by the impact of ions can lead to melting of the target disc. This fixes a limit on the power density applicable at the target, and even with a heat exchanger to cool the target, it is difficult to apply DC power density above 500 kW cm^{-2}.

The low power applied to the discharge creates a plasma with a relatively low density. Due to this lower plasma density, very few atoms sputtered from the target are ionized. The sputtered atoms simply drift towards the substrate for deposition and are insensitive to the internal electric field of the plasma discharge; the associated deposition regime is called Physical Vapor Deposition (PVD). Typically, the PVD regime allows a high deposition rate but the quality of the deposition on the substrate is sensitive to the shadowing effect [128].

4.1.1.2 HiPIMS regime

Triggered by constant progress in power transistor technologies, pulsed magnetron regimes emerged. In recent years, it has led to High Power Impulse Magnetron Sputtering (HiPIMS) regime. This discharge regime is characterized by peak power density above 500 W cm^{-2} [129] and a low duty cycle which avoids the target damage threshold (see Figure 4.2). The high instantaneous power generates much higher plasma density such that a significant fraction of the sputtered atoms are ionized. HiPIMS regimes opened the way to Ionized Physical Vapor Deposition (IPVD) regimes. With HiPIMS, the energy and direction of the sputtered ions can be controlled through an electric field near the substrate, allowing microstructure tuning [130] and better film quality. In particular, HiPIMS regime allows deposition on complex surfaces without the shadowing effect [128] but the deposition rate is significantly reduced.

4.1.2 Previous work on electron property investigation

To improve the understanding of the physics underlying planar magnetron discharges and to validate computer simulations under development, gaining knowledge of electron properties is a key goal.

Estimation electron properties from Langmuir probe techniques has been performed in both DC [131] and HiPIMS [132] regimes. However, results from Langmuir probes must be assessed with consideration

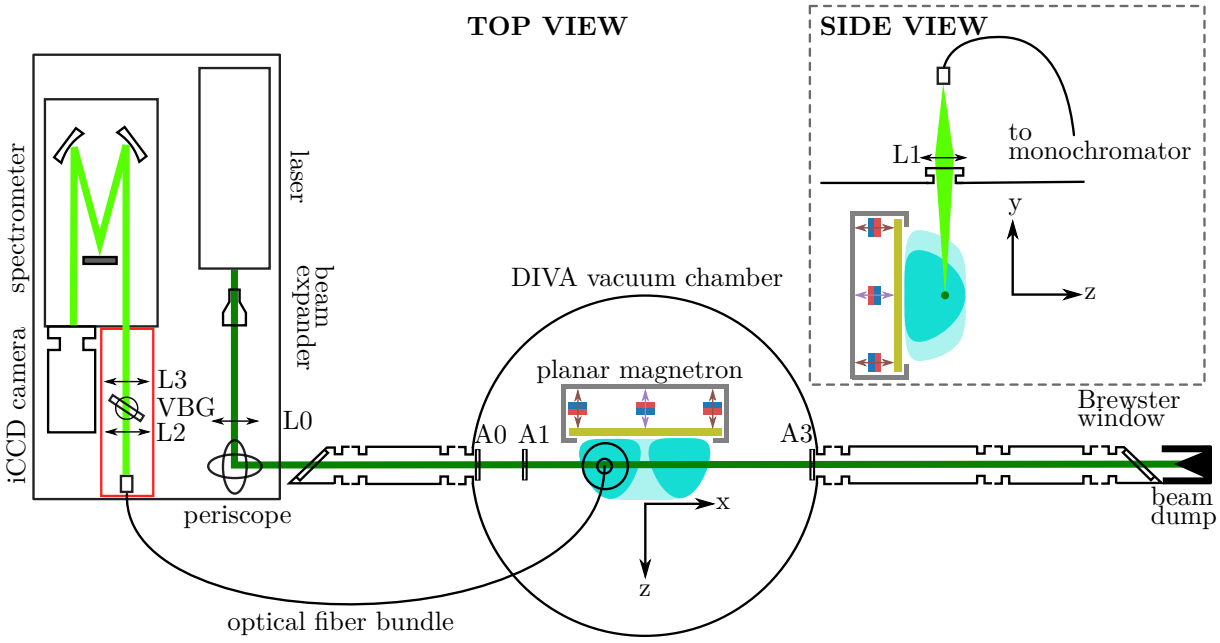

Figure 4.3: Setup of the diagnostic THETIS on the DIVA planar magnetron vacuum chamber in Orsay. The top view corresponds to the view in the plane created by the polarization vector (horizontal polarization) and the laser wave vector. The side view corresponds to a view in the plane created by the polarization vector and the scattering wave vector. The light beam on the transmission branch used to induce the Thomson scattering signal corresponds to the dark green line. Light on the detection branch containing the Thomson scattering signal to be analyzed is represented with a light green line.

of the numerous shortcomings of this diagnostic in such discharges. The absence of reliable theory for magnetized electrons with expected anisotropic and/or non-Maxwellian EVDF and the possibility of probe contamination or perturbation of the plasma may contribute to underestimated measurement uncertainties.

The recent implementation of THz spectroscopy to measure electron density in magnetron discharge in HiPIMS regime [60] should be highlighted. It is a non-perturbative Langmuir probe alternative, but it is limited to electron density measurement.

Soon after our first implementations on a planar magnetron [133], other teams successfully implemented a Thomson scattering diagnostic for investigation of electron properties inside a HiPIMS discharge and comparison with results from Langmuir probe diagnostics [134, 135].

4.2 Experimental setup

4.2.1 Test facility and plasma source

All experiments were performed in the DIVA (Dispositif d'Ionisation de la VApeur) vacuum chamber of the LPGP laboratory (CNRS, Paris XI University) in Orsay. It is a cylindrical vacuum chamber (height 43 cm and diameter 55 cm). As shown in Figure 4.3, long tubes ended by Brewster windows were mounted on the sides of the vessel for the implementation of the THETIS diagnostic. The picture shown in Figure 4.4 shows the layout of the THETIS diagnostic implemented on the DIVA vacuum chamber. This chamber is equipped with a primary pump and a turbo-molecular pump. The pumping assembly reaches a residual pressure around 5×10^{-4} Pa when no gas is injected. The injection of gas is realized with a mass-flow meter. A chosen pressure inside the vacuum chamber is fixed by adjusting both the injected gas flow and the pumping speed. The latter adjustment is realized with a controlled butterfly valve located between the vacuum chamber and the turbo-molecular pump.

The plasma source is a VTech circular magnetron from Gencoa, equipped with a Ti (99.9 %) target

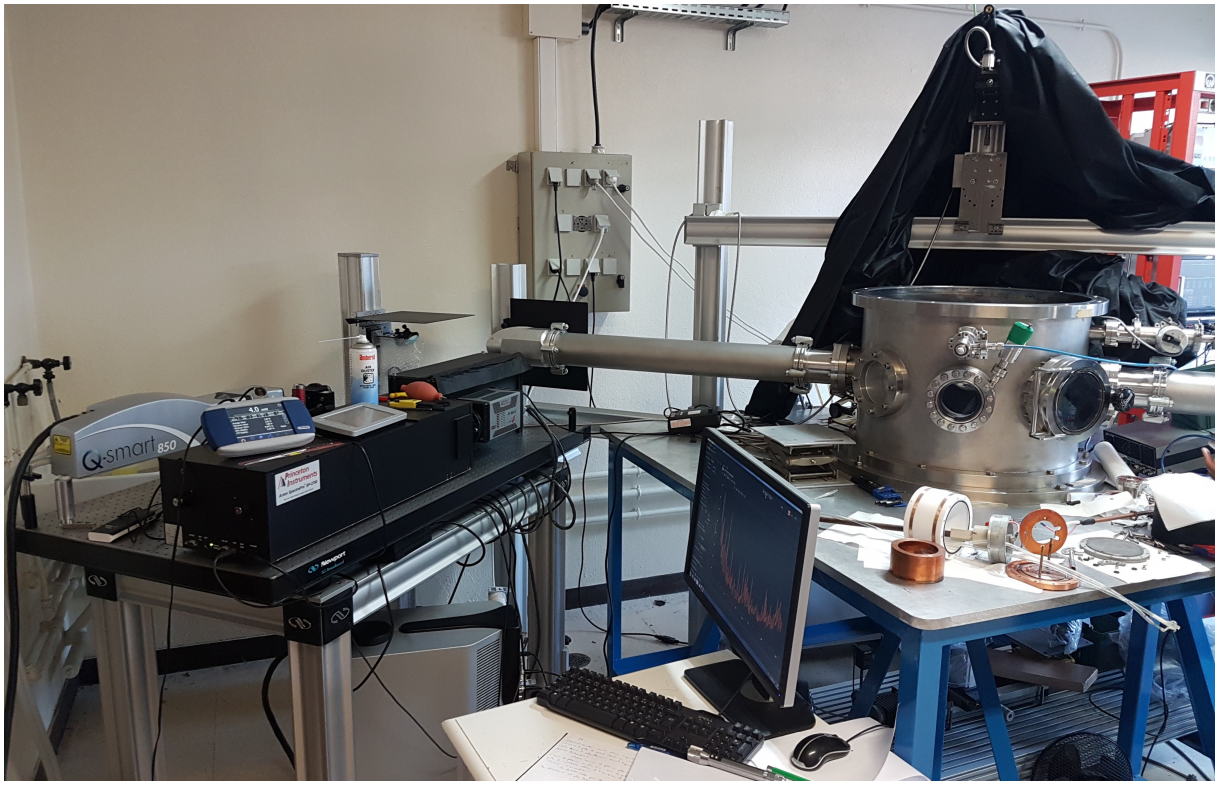

Figure 4.4: Picture of the DIVA vacuum chamber (right side of the picture) with the THETIS diagnostic implemented on it (left side of the picture).

100 mm in diameter (surface of 7850 mm^2). The magnets placed behind the target create a magnetic field mainly in the radial direction near the target surface and above the region etched by the plasma created, often referred to as the "race track". As shown in Figure 4.5, at this position the magnetic field is directed toward the outer diameter. The magnetic field intensity, as well as its shape, can be tuned by independently displacing the outer and inner ring of magnets with a translation system controlled by micrometer screws. In Figure 4.3 the available displacements of the inner and outer ring of magnets are shown with purple and brown arrows respectively. As a convention, the position of the central magnet is indicated with the letter C followed by a number ranging from 0 (when the magnets are at the closest to the target) and 10 (for the opposite limit of magnet displacement). The same convention is used for the external ring, but the letter E is used instead of C. For example, it is with the configuration C0E0 that the highest magnetic field near the target is achieved. Thermal loads on both the target and the magnets are minimized using water cooling near the target. Finally, the entire assembly is mounted on movable bellows for easy axial millimeter-scale displacement.

Figure 4.5 shows the topography of the magnetic field intensity for various configurations. Streamlines indicate the orientation of the magnetic field vector. Only the configurations C0E0, C5E5, C10E10, C10E0, and C0E10 are shown, as the work of this thesis focuses only on investigations with these configurations. The magnetic field was measured with a Lake Shore 425 Gauss meter (Lake Shore Cryotronics, Westerville, OH, USA) equipped with a Hall probe. The topographies presented in Figure 4.5 were measured with a resolution of 5 mm over the presented range, except for the radial component of the magnetic field for which z=11 mm was the closest distance that could be probed. Below this distance, the radial component was interpolated. All the topographies shown correspond to the weakly unbalanced configuration, with C10E0 the most unbalanced (the magnetic null point seems to be farther than z=70 mm). The "balanced" configuration refers to one in which the inner and outer magnets have the same field strengths; the "unbalanced" configuration refers to differing field strengths for the inner and outer magnets. Among all these configurations, the C0E0 was the most frequently used, with all the axial investigations performed above the race track (at a radial distance of approximately 20 mm from the target axis). For this reason, the topography of the intensity of the gradient of the magnetic field

intensity is shown in Figure 4.6 for this configuration. The streamlines indicate the orientation of the gradient vector.

To obtain the values of the magnetic field gradient, we applied a SavitzkyGolay filter to the magnetic field topographies presented in 4.5. The application of the filter along both the radial and axial directions gives the component of the gradient along the radial and axial directions, respectively. Because we expect no variations of the magnetic field along the azimuthal direction, the radial and axial components are enough to compute the gradient intensity. The lack of values for the radial component of the magnetic field below z=11 mm required the use of interpolated values down to z=0 mm, leading to an underestimated gradient close to the target.

Before turning on the plasma discharge, the vacuum chamber is pumped down to the minimal pressure for degassing. The gas injection and pumping speed are then adjusted to reach a stable pressure between 1 Pa and 10 Pa with the desired gas to sustain the discharge. Once the steady pressure is achieved, the plasma discharge is ignited by a potential difference between the cathode and the guard ring. In DCMS regime, we used a factory-made DC power supply (SR1.5-R-1500 from Technix) to ignite and sustain the discharge. In the HiPIMS regime, a home-made pulse power supply was used for the generation of the current pulses. Triggering of the current pulses was synchronized with the Q-switch signal output of the THETIS laser fixed at 10 Hz. A delay was added between the Q-switch output and the power supply with a Stanford Research Systems DG645 digital delay generator. This delay enables probing of the ITS signal at various times inside the temporal profile of the current pulse. The delay generator was also used to shape the temporal width of the voltages pulses (60 µs for most of the investigations of this thesis).

Visualization of the discharge current and voltage were performed on a Teledyne LeCroy - HDO6104A oscilloscope. The voltage and current were measured with a LeCroy - PPE4KV voltage probe and a LeCroy - CP150 current probe, respectively. The observation of the current profile allows an estimation of the delay for plasma ignition.

4.2.2 THETIS diagnostic

A full description of the THETIS diagnostic design and the procedure for Thomson spectrum acquisition were made in Chapter 3. This section focuses only on specificities related to its implementation for planar magnetron investigations.

For most of the investigations, the sources of stray-light were weak and the plasma emission remained reproducible. The Thomson spectrum could be isolated by a simple subtraction between the record with the laser and plasma on (record—A) and the records with only the plasma on (record—B). However, for some discharge conditions (usually when the repetition frequency was low), the delay for plasma ignition significantly varied from one pulse to another (a plasma ignition "jitter" due to the power supply or the low residual electron density making ignition more difficult). In these cases, data was not considered exploitable with the 6000 accumulations typically used. In these particular cases, fluctuations prevented a fine temporal resolution at the beginning of the current pulse. No such issues were encountered for the moment when the plasma discharge was turned off, where the current decrease was highly reproducible.

The scattering volume was imaged onto the 3×5 fiber bundle with a 200 mm focal length lens (diameter of 100 mm) with a $2f$ configuration. With this configuration (lens magnification of 1), the scattering volume can be approximated by a cylinder of 0.3 µm diameter (transverse size of the laser beam) and 1.5 mm long (limited by the fiber bundle length). Electron properties obtained from Thomson scattering measurements correspond to an averaged value over this volume.

As shown in Figure 4.7, the scattering volume observed was positioned above the race track of the magnetron, 20 mm from its axis of revolution. The axial position from the cathode was varied by moving the magnetron with the movable bellows to vary its distance from the fixed laser beam. The closest position probed was limited by the guard ring positioned 8 mm from the target. The closest relevant Thomson scattering signals measured with a reasonable level of stray-light were obtained 1 mm from the guard ring (i.e., 9 mm from the target). However, for distances below 8.6 mm from the guard ring, the solid angle for the light collection was reduced. To compensate for this, the acquired signal was multiplied by a coefficient for normalization, calculated from the scattering geometry at each axial position. The maximum distance was limited by either the detection threshold of the diagnostic or the dynamic of displacement of the translation plate.

The scattering configuration is also presented in Figure 4.7. In the observation volume, the laser is linearly polarized along the z-direction (see Figure 4.3). The scattering wave vector is perpendicular to

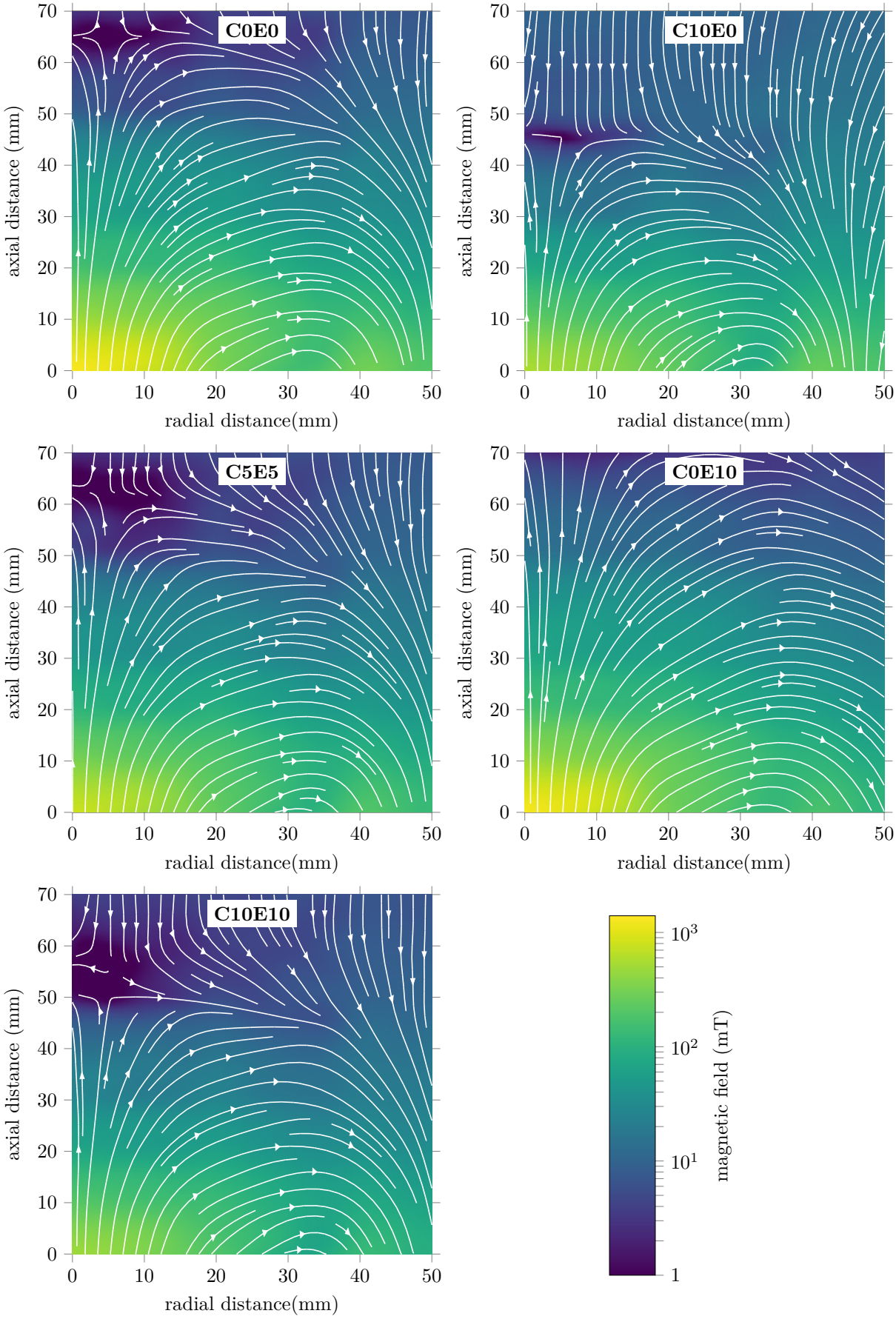

Figure 4.5: Topography of the magnetic field intensity for various magnetic configurations. The orientation of the magnetic field vector is shown with the streamlines.

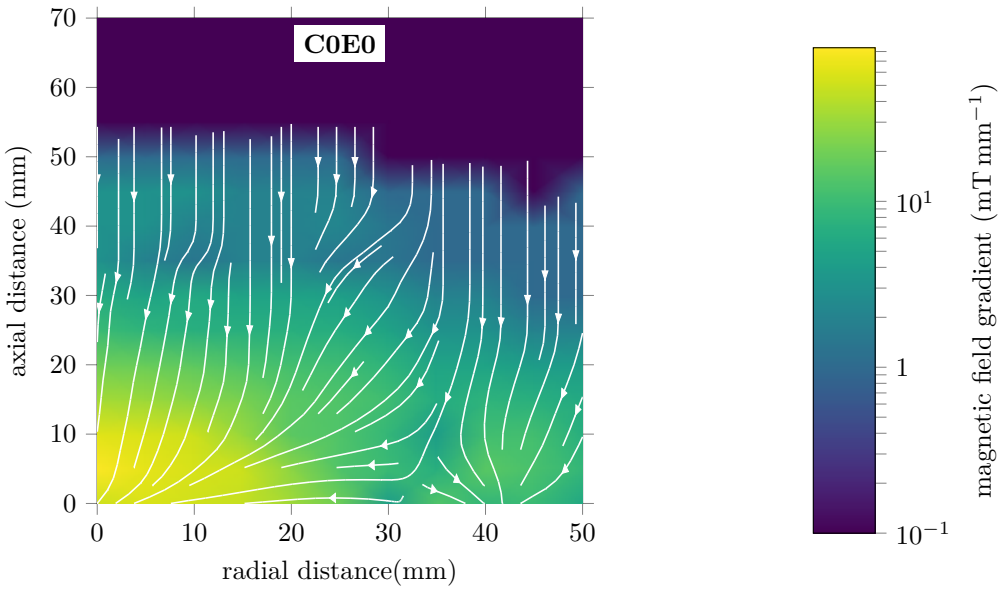

Figure 4.6: Topography of the norm of the gradient of the magnetic field intensity for the C0E0 magnetic configuration. The streamlines give an indication on the orientation of the gradient.

both the laser polarization direction and the wave vector of the incident laser. Due to this scattering configuration, the direction of the probed wave vector ($\vec{k}$), along which electron properties are probed, is inclined by 45° with respect to the incident wave vector direction. With the laser passing in the horizontal plane of symmetry of the magnetron, electron properties along both the azimuthal and radial directions are probed with equal weighting.

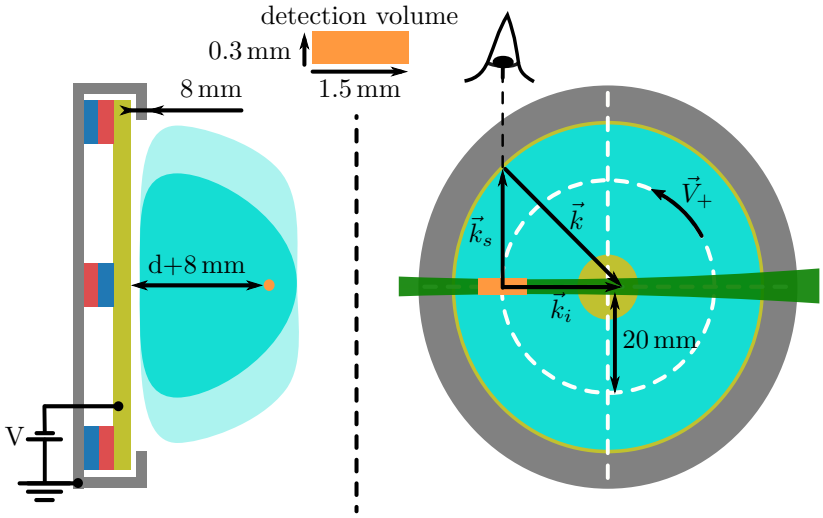

Figure 4.7: Scattering configuration used for the measurements of electron properties. $\vec{k}_i$, $\vec{k}_s$ and $\vec{k}$ correspond, respectively, to the laser wave vector, the scattering wave vector and the probed wave vector. The observation volume in orange is approximately 0.3 mm diameter and 1.5 mm long, placed on the magnetron race track (20 mm from the magnetron axis). The closest axial distance probed was limited by the guard ring positioned 8 mm from the target.

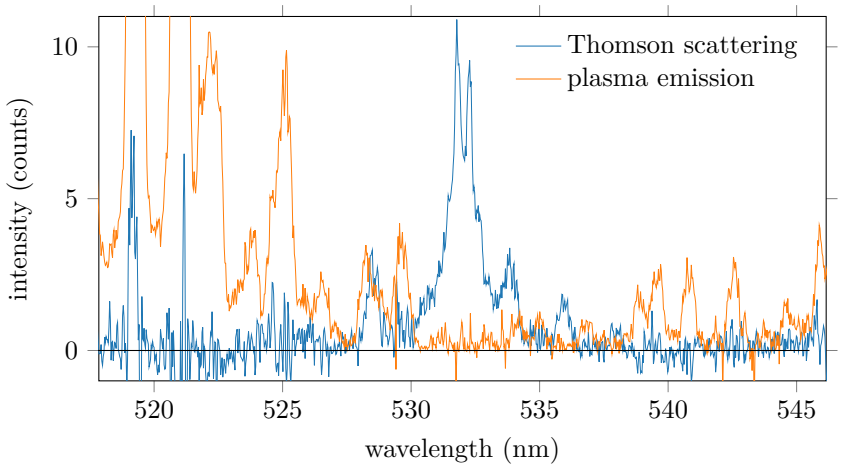

Figure 4.8: Example of the signal obtained from the Thomson scattering and plasma emission records 5 mm from the guard ring, with the 600 lines mm^{-1} grating. The discharge was sustained with a current of 0.8 A and a voltage of 296 V for an Ar pressure of 1 Pa.

4.3 Results in the DCMS regime

The first measurements were performed with the magnetron discharge in the DCMS regime with the C0E0 magnetic field configuration. These tests are simplified because no acquisition synchronization is needed. The low electron density expected also provides an opportunity to test the sensitivity of the diagnostic.

4.3.1 With Ar gas

Because Ar is commonly used for planar magnetron discharges, the first investigation was performed with this gas. The Ar pressure was set at 1 Pa and the discharge was sustained with a current of 0.8 A and a discharge voltage of 296 V.

Figure 4.8 shows an example of the signal obtained from a Thomson scattering record (i.e., the difference between the record with the laser and plasma on minus the record with only the plasma on) without any pixel binning along the spectral direction. The two peaks near 532 nm are residual lines from filtering of the stray-light peak from Rayleigh scattering and reflections. Without the VBG-NF these peaks would be more than three orders of magnitude higher. The slow decrease toward zero on either side of this peak cannot be explained only from the redistribution of light characterized by the instrument function. These slowly decreasing wings on either side of the peak may be attributed to the contribution from Thomson scattering. However, the presence of unexpected parasitic peaks makes the fitting of the spectrum impossible. These many peaks can hardly be explained from Thomson scattering contribution. An exploration at various distances from the guard rings showed that the intensity of the peaks at approximately 528.5 nm, 534 nm and 536 nm did not vary. On the other hand, the peaks visible near 519 nm and 521 nm disappeared at larger axial distances from the guard ring.

The signal from plasma emission measured during the same gating period of the camera (10 ns) as for Thomson scattering acquisition is shown in Figure 4.8. All the emission lines of this spectrum are characteristic of the titanium neutral atom emission spectrum. Two very intense peaks are visible at 519.3 nm and 521 nm, with intensities of, respectively, 80 counts and 100 counts at 5 mm from the guard ring. The intensity of the emission spectrum was observed to decrease at higher distances. From these observations, we supposed that the peaks still visible on the Thomson spectrum near 519 nm and 521 nm arise from a weak variation of the plasma emission intensity between the acquisitions of the various records. Even a small variation of amplitude of the intense emission lines can quantitatively affect the weak signal from Thomson scattering.

The presence of lines at 528.5 nm, 534 nm and 536 nm inside the Thomson signal cannot be attributed to imperfect subtraction of plasma emission lines. Figure 4.9 shows the signal obtained with the same conditions as Figure 4.8 but recorded with a more dispersive grating. Despite the low signal-to-noise

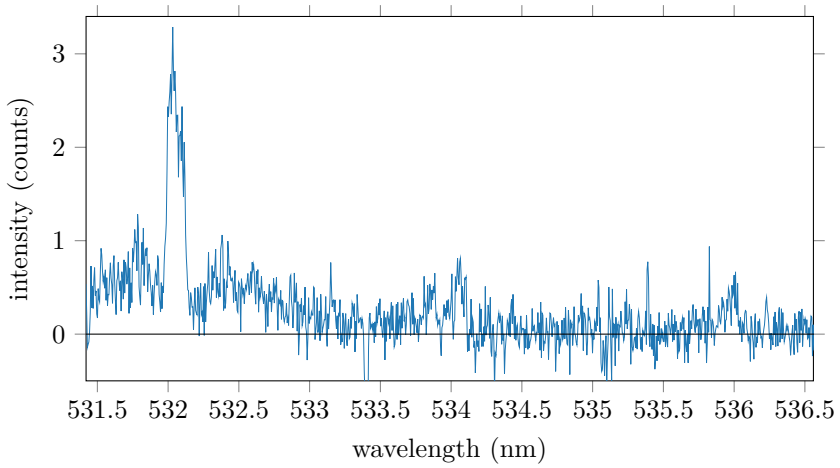

Figure 4.9: Example of the signal obtained from the Thomson scattering records with the same experimental conditions as Figure 4.8 but with the 2400 lines mm^{-1} grating.

Source	Target	Gas	P (Pa)	J_c (A m^{-2})	U_d (V)	$B_{r,rt}$ (mT)
presented work	Ti	He	10	127	210	238
Sheridan et al. (1989)	Cu	He	11	290	300	245

Table 4.1: Comparison of the experimental conditions used in this work with those of a previous article investigating of electron properties inside a direct current planar magnetron discharge sustained under a background pressure of helium.

ratio, the peaks at 534 nm and 536 nm are still discernible and seem to remain relatively sharp. Based on previous observations, we believe that these lines would come from Raman scattering on molecules sputtered from the titanium target. The spectral shifts of the peaks at 528.5 nm and 536 nm fit well with already observed Raman peaks at approximately 144 cm^{-1} (corresponding to a wavelength shift of 4.1 nm at 532 nm) from scattering on the anatase phase of titanium dioxide (characteristic of a triply-degenerated (E_g) vibrational mode). The lack of Raman investigations in the anatase phase down to very low phase shifts prevent a discussion on the peak we observed at 534 nm. The shift of this E_g band seems to vary weakly with the crystalline structure [136] or nanocrystal size [137]. We speculate that the peaks observed come from Raman scattering on anatase nanocrystals of various sizes in suspension inside the chamber. This hypothesis requires oxidation of the titanium, which may have happened over the surface of the target while it was exposed in the open air.

4.3.2 With He gas

During the previous investigation with argon, the sputtered titanium atom or molecules complexified the analysis of Thomson scattering records. In this section, helium is used to sustain the plasma discharge in order to minimize the density of sputter elements. The much weaker mass of helium ions significantly decreases the target sputtering efficiency. By using helium, we should be able to focus on the study of a plasma composed of only neutral gas atoms and ions.

The magnetron discharge was sustained under a steady pressure of 10 Pa and a discharge current of 1 A. Under these conditions the discharge voltage was 210 V.
These experimental conditions were chosen in order to be similar to available experimental results obtained with Langmuir probes by Sheridan et al. [131, 138]. A comparison of experimental conditions is made in Table 4.1. The main differences in the experimental conditions are in the lower mean discharge current density (J_c) and discharge voltage (U_d) used in our study. The difference of target material is expected to have a minor influence on discharge properties due to the low sputtering of the target expected with He atoms. The plasma pressure (P) and the radial component of the magnetic field on the surface of the

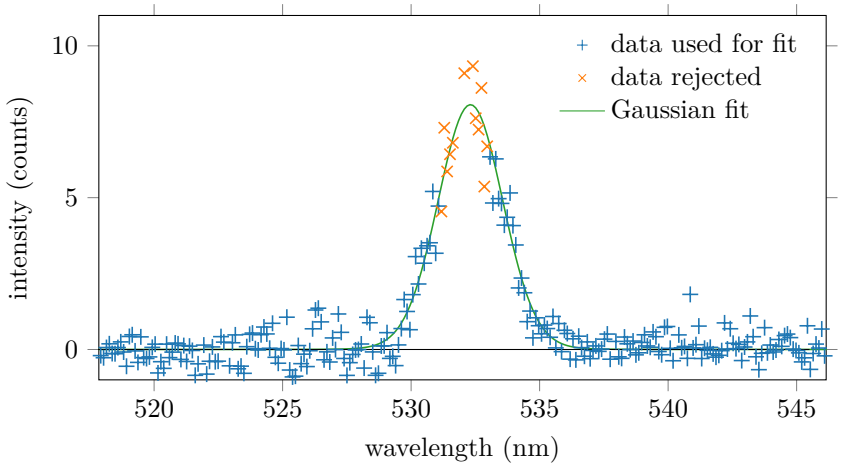

Figure 4.10: Thomson spectrum measured 5 mm from the guard ring with a plasma discharge sustained with a DC current of 1 A, a voltage of 210 V and a helium pressure of 10 Pa. The Gaussian fit gives an electron density and temperature of respectively $(2.8 \pm 0.2) \times 10^{16}\,\mathrm{m}^{-3}$ and $(1.3 \pm 0.1)\,\mathrm{eV}$.

race track ($B_{r,rt}$) can be considered as identical.

As shown in Figure 4.10, at the same distance from the guard ring and with a similar discharge power, the Thomson scattering signal is much clearer when helium rather than argon gas is used to sustain the discharge. The four pixel-binning along the spectral direction allowed an increase of the signal-to-noise ratio for data analysis. After the rejection of the spectral range associated with redistribution of the stray-light from Rayleigh scattering and reflections remaining after filtering with the VBG-NF, a Gaussian fit is applied to the data. For example, the fit parameters obtained from the data presented in Figure 4.10 give an electron density and temperature of respectively $(2.8 \pm 0.2) \times 10^{16}\,\mathrm{m}^{-3}$ and $(1.3 \pm 0.1)\,\mathrm{eV}$.

An axial investigation of Thomson scattering was performed by moving the magnetron with respect to the laser beam. From the analysis of the Thomson spectrum, an axial profile of electron density and temperature were extracted. The results are plotted in Figure 4.11 for distances ranging from 1 mm (when stray-light from reflection on the guard ring become significant, i.e., $I_{SL}/I_{Thomson,max} \gtrsim 200$)) and 50 mm (when the signal-to-noise ratio becomes too low for relevant data analysis, i.e., $I_{Thomson,max}/\sigma_{noise} \lesssim 3$).

An electron density in the $2 \times 10^{16}\,\mathrm{m}^{-3}$ range with an almost monotonic decrease with distance is observed. The maximum electron density can be used to estimate the maximum ionization degree inside the plasma. We considered a homogeneous distribution of neutrals plus ion density inside the vacuum chamber and a temperature near the ambient temperature ($T_i = T_n \approx 300\,\mathrm{K}$). Under these hypotheses we obtain $n_n + n_i \approx 2.4 \times 10^{21}\,\mathrm{m}^{-3}$ using the ideal gas law. These values are consistent with an ionization degree of $\alpha \approx 0.002\,\%$, confirming the low ionization degree in DCMS discharges.

Electron temperature slowly decreases from 1.6 eV to 1.2 eV until an apparent increase for distances above 30 mm, however, this increase remains almost inside the error bars of our results. The peaked electron temperature observed at 20 mm is due simply to a technical issue (a stall of the Peltier module for the acquisition camera CCD cooling, which led to a significant increase of the noise signal at this point and consequently a distorted Thomson spectrum).

With the electron density and temperature estimated, a rough estimate of electron collision frequency is possible. Considering a helium radius of approximately 10^{-10} m and using Equation 3.17 gives $\nu_{ei} \approx 7 \times 10^5\,\mathrm{s}^{-1}$ and $\nu_{en} \approx 2 \times 10^8\,\mathrm{s}^{-1}$. Despite an electron-electron collision frequency twice as high as ν_{ei}, collisions with neutrals remain the main process for electron energy dissipation in the DCMS regime.

Our results can be compared with those of Sheridan et al. [131]. While Sheridan et al. observed an electron density in the range of $2 \times 10^{16}\,\mathrm{m}^{-3}$ at maximum, we observed a maximum around $4 \times 10^{16}\,\mathrm{m}^{-3}$. Considering differences of experimental conditions presented in Table 4.1, this difference remains acceptable.

However, Langmuir probes indicated the presence of a two-temperature electron population, which was not visible with our ITS diagnostic. The ratio between the "hot" (approximately 7.6 eV) and "cold" (approximately 0.5 eV) electron densities was observed to be high close to the target and low once outside the magnetic trap. The disagreement with our results may arise from several reasons. The small difference

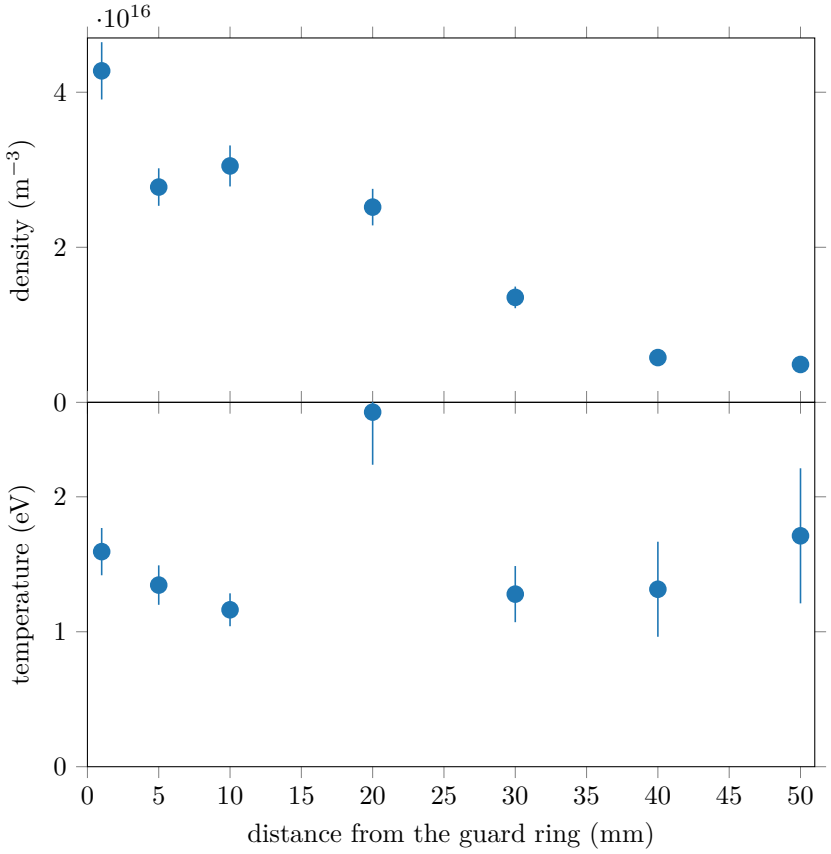

Figure 4.11: Axial profile of electron density and temperature obtained in the DCMS regime. The discharge current, voltage and pressure were respectively 1 A, 210 V and 10 Pa.

between our experimental conditions and those of Sheridan could be responsible for creating a different discharge regime. Moreover, if there were a second electron population with much higher temperature (≈10 eV) and similar density the actual sensitivity of our diagnostic may prevent its detection due to the higher spectral intensity dilution. However, in case of a two-electron population, we should have observed, with the THETIS diagnostic, a decrease in the density of cold electrons near the target (at this position the plasma is dominated by hot electrons, according to Sheridan's observations); we do not observe this. Finally, the discrepancy could also be explained by the lack of reliable theory to analyze Langmuir probe signals in a magnetized plasma - the second electron population may be an artifact linked to the behavior of magnetized electrons.

4.4 Results in HiPIMS regime

Investigations in the HiPIMS regime followed the investigations in DCMS. These studies are facilitated by the higher electron density. However, discharge regimes with high repeatability are required to obtain a trustworthy averaging during the 10 min of acquisition.

4.4.1 With He gas

For the HiPIMS regime with helium, measurements were performed with a pulse width of 60 µs, a 10 Hz repetition rate and with the C0E0 magnetic field configuration. The discharge was sustained under a steady pressure of 10 Pa and the peak discharge current value was kept at (200.0 ± 0.2) A. Under these conditions the maximum discharge voltage was 1260 V.

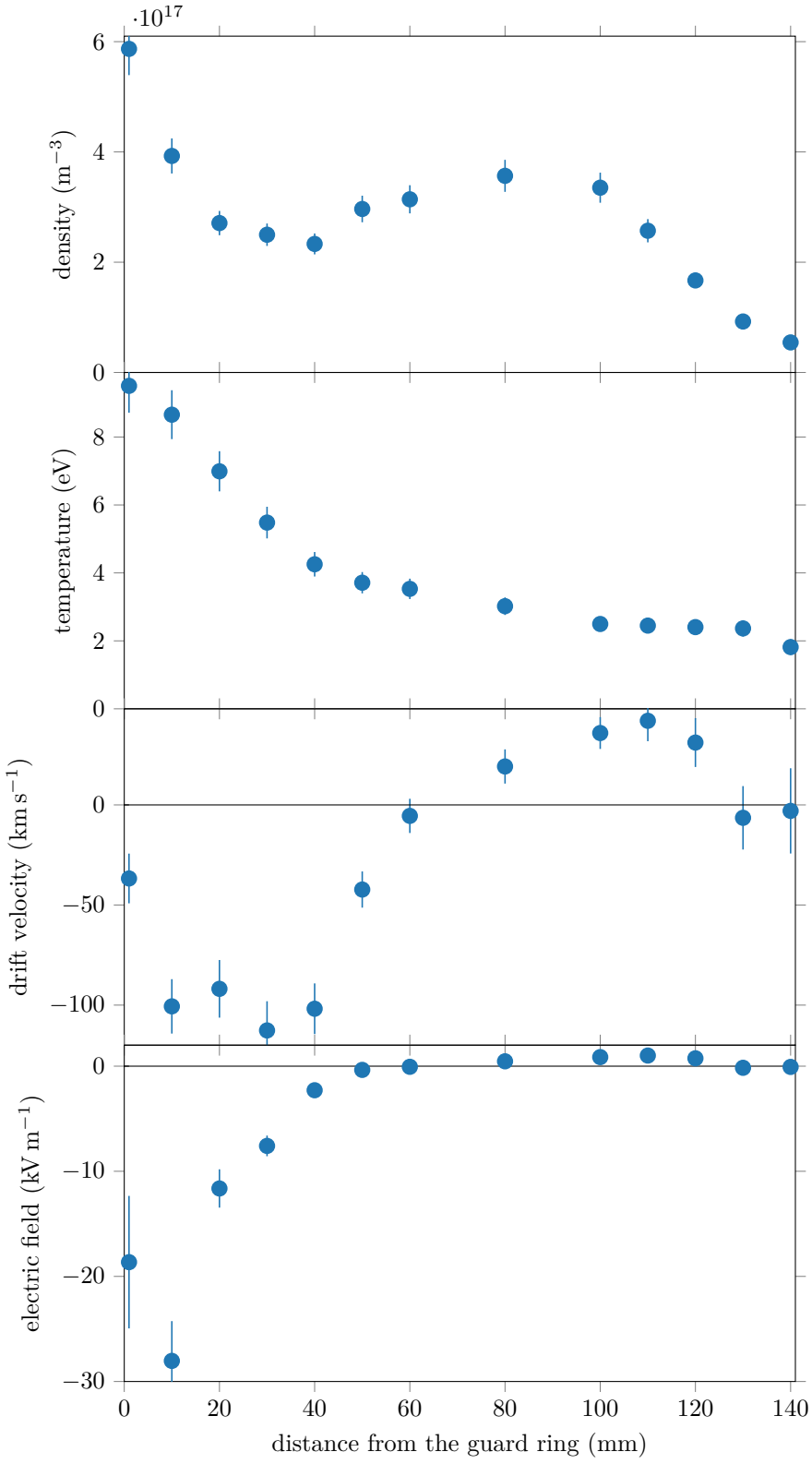

Figure 4.12: Axial profile of electron density, temperature and drift velocity obtained at the end of a 60 µs current pulse in the HiPIMS regime. The discharge was operated with He at pressure 10 Pa, peak discharge current (200.0 ± 0.2) A and peak discharge voltage 1260 V. The axial profile of the axial electric field was deduced from the values of electron temperature and drift velocity measured.

4.4.1.1 Axial exploration for various magnetic field configurations

Similar to DCMS regime investigations, electron properties were measured at various distances from the guard ring in the HiPIMS regime. The axial profiles obtained from investigations at the end of the HiPIMS current pulse are shown in Figure 4.12.

As expected, due to the high current density compared to what was used in DCMS regimes, the electron density in HiPIMS is significantly higher. The relatively high scattered signal enabled measurement up to distances of 140 mm from the guard ring. Despite an increase of two orders of magnitude in current density, electron density increased only one order of magnitude. A non-monotonic variation of electron density is observed with two local maxima, one localized close to the target and another one as far away as 80 mm.

Electron temperature in the HiPIMS regime is also significantly higher than in DCMS regime. It reaches values as high as 10 eV close to the guard ring. Electron temperature progressively decreases with the distance from the target, but it remains as high as 2 eV even at 140 mm from the guard ring. Such a high electron temperature supports the hypothesis previously made regarding very low sputtering of the target with helium. Indeed, in the absence of Ti atoms (first ionization energy of 6.8 eV), there are few energy dissipation mechanisms for the electron population until they reach sufficiently high energy to ionize He atoms (first ionization energy of 24.6 eV). Because the sputtering yield is much lower in the DCMS regime [139], the Ti atom density was certainly higher in the DCMS plasma. With their lower first ionization energy, Ti atoms would certainly have absorbed energy from energetic electrons. This would explain the much lower electron temperatures measured in the DCMS case.

The increased electron temperature observed in the present case shows that paths for electron energy dissipation from collisions with the walls or other particles (ionization, excitation, etc.) are reduced in HiPIMS regimes. An increased fraction of the discharge power is used to heat electrons to higher characteristic energy. The reduced fraction of available power for ionization results in a moderate increase of electron density. A higher electron density increase would have been expected with unchanged electron energy losses from DCMS to HiPIMS regime.

In the HiPIMS regime, electron drift velocities above $44\,\mathrm{km\,s^{-1}}$ are large enough to be measured. This lowest limit corresponds the drift velocity associated with the spectral width of one bin of 4 pixels with the 600 lines mm grating. Larger limits may be obtained with a larger slit width and noisier data. In theory, the drift velocity measured corresponds to a 45° projection of both radial and azimuthal velocity. To ease the interpretation we assumed that the radial drift velocity is negligible compared to the azimuthal drift velocity. For data analysis, the convention setting the velocity along with the anticlockwise direction as positive (collinear to the $\vec{V}_+$ and $\vec{k}$ direction in Figure 4.7) was adopted.

A negative electron drift velocity of at least $100\,\mathrm{km\,s^{-1}}$ is observed close to the cathode ($141\,\mathrm{km\,s^{-1}}$ if the 45° projection is taken into account). This negative drift velocity corresponds to an electron drift anti-collinear to the $\vec{V}_+$ vector. Knowing that the magnetic field is directed toward the external pole, this negative value is expected with an electric field directed toward the target. The electron drift velocity then progressively increases with the distance until it reaches zero at 60 mm from the guard ring, and becomes positive downstream of this position. The direction change of electron drift depending on the distance from the target was already deduced from electrostatic probe measurements in the HiPIMS regime [140, 141]. Such velocity gradients are known to be a source of instabilities which may create localized ionization zones [142, 143] and could explain the increase of electron density observed for distances greater than 40 mm from the guard ring.

The electron drift velocity can be used to extract information about the axial projection of the electric field inside the plasma. The $E \times B$ drift is usually the main source of electron drift velocity in a magnetron discharge. However, for a precise estimation, we have to assess the order of magnitude of other contributions.

With a planar magnetron discharge, if temporally averaged behaviors are considered, we expect no azimuthal component and dependence of the magnetic field. At the radial positions probed, we consider only the axial and radial variations of the magnetic field, which is simply expressed as $\vec{B}(r_0, z) = B_r(r_0, z)\vec{e}_r + B_z(r_0, z)\vec{e}_z$, where $B_r(r_0, z)$ and $B_z(r_0, z)$ are the radial and axial components of the magnetic field estimated at the radial position probe (r_0=20 mm). On the other hand, we also suppose that the electric field is mainly along the axial direction and if we consider only its axial and radial variations, it can be expressed as $\vec{E} \approx \vec{E}(z) = E_z(r_0, z)\vec{e_z}$.

The sources of electron drift velocity along the probed wave vector direction are the electric field drift

$\vec{V}_{E\times B}$, the polarization drift $\vec{V}_P$, the magnetic field curvature $\vec{V}_{DC}$ and gradient $\vec{V}_{DG}$ drifts, and higher order contributions due to electron pressure anisotropy. As a first order approximation, we will make the hypothesis of a steady electric field so that the polarization drift can be neglected. To simplify the analysis we also make the hypothesis of isotropic electron pressure so that the anisotropy drift can be neglected. This last assumption may become less relevant near the magnetron cathode or in Hall thruster discharges where large anisotropies of electron properties are expected [144]. If we also consider that the magnetic pressure is higher than the electron pressure (true for most of the positions investigated), the azimuthal electron drift velocity may be expressed with the following expression

$$\vec{V}_\perp = \frac{\vec{E}\times\vec{B}}{B^2} + \frac{2v_\parallel^2 + v_c^2}{2\omega_{c,e}}\frac{\vec{\nabla}(B)\times\vec{B}}{B^2} \tag{4.1}$$

The first term of Equation 4.1 corresponds to the well known $E\times B$ drift while the second groups magnetic field curvature and gradient drifts. $v_\parallel$ corresponds to the velocity parallel to the magnetic field, v_c is the electron cyclotron velocity and $\omega_{c,e}$ is the electron cyclotron frequency.
The $E\times B$ contribution is only along the azimuthal direction due the hypothesis of electric field only along the axial direction and the absence of an azimuthal magnetic field. Under these assumptions, we simply have $\vec{V}_{E\times B} = \frac{E_z B_r}{B^2}\vec{e}_\theta$.
To estimate the second term we will assume that electrons respect the energy equipartition theorem along their three degrees of freedom, such that we have $\frac{1}{4}m_e v_c^2 = \frac{1}{2}m_e v_\perp^2 = \frac{1}{2}k_B T_e$. Magnetic field intensity and magnetic field gradient along the axial and radial direction are extracted from Figure 4.6. Because the magnetic field does not have a component and variation along the azimuthal direction, the cross product between the gradient of the magnetic field intensity and the magnetic field vector gives a contribution only along the azimuthal direction. From these approximations, the expression of the drift velocity from magnetic field curvature and gradient simplify to $\vec{V}_{DC} + \vec{V}_{DG} \approx \frac{k_B T_e}{eB^3}(B_r\frac{dB}{dz} - B_z\frac{dB}{dr})\vec{e}_\theta$.
Under these assumptions the axial electric field can be estimated from the electron temperature and drift velocity estimated from incoherent Thomson scattering spectra. Taking into account the $\pi/2$ projection of the azimuthal drift velocity estimated, the electric field can be calculated through the following formula

$$E_z = \sqrt{2}v_{drift,e}\frac{B^2}{B_r} - \frac{k_B T_e}{eB}\left(\frac{dB}{dz} - \frac{B_z}{B_r}\frac{dB}{dr}\right) \tag{4.2}$$

At 1 mm from the guard ring, the electron drift velocity is significantly negative. At this position, despite high electron temperature ($T_e \approx$10 eV), its multiplication (in eV units) with the weak $\frac{1}{B^3}(B_z\frac{dB}{dr} - B_r\frac{dB}{dz})\approx 8\,\mathrm{m^{-1}\,T^{-1}}$ coefficient leads to a negligible drift velocity contribution directed in the positive direction ($||\vec{V}_{DG} + \vec{V}_{DC}||\approx 80\,\mathrm{m\,s^{-1}}$). To reach the highly negative drift velocity observed, the $E\times B$ contribution has to be negative. Balancing the electron drift velocity enables an estimation of the axial electric field at the probed position. As shown in Figure 4.12, an electric field of approximately $-19\,\mathrm{kV\,m^{-1}}$ at 1 mm from the guard ring is obtained with this method and remains as high as $-8\,\mathrm{kV\,m^{-1}}$ even 30 mm from the guard ring. These large values of the axial electric field are higher than the order of magnitude previously deduced from plasma potential measurement with emissive probes [140, 141, 145]. This discrepancy may be explained by the higher magnetic field used during our measurement. PIC models [146] suggest that the pre-sheath width increases for higher magnetic field intensities. With the C0E0 configuration used, we may probe the end of this thick pre-sheath with the ITS diagnostic. Perturbation of the plasma induced by emissive probes may be another explanation for this discrepancy.
For distances from 10 mm to 60 mm from the guard ring, the electron temperature remains relatively large (above 3.5 eV), while the coefficient $\frac{1}{B^3}(B_z\frac{dB}{dr} - B_r\frac{dB}{dz})$ becomes significant and varies from approximately $-6000\,\mathrm{m^{-1}\,T^{-1}}$ to $2000\,\mathrm{m^{-1}\,T^{-1}}$. At maximum, the magnetic curvature and gradient drift can reach approximately 10 % of the total velocity measured. For the 10 mm to 40 mm range, taking into account the curvature and gradient contribution leads to an even more negative electric field estimated than if only the $E\times B$ contribution is taken into account. From 40 mm to 60 mm the same contribution tends to shift the estimated electric field towards positive values.

For distances above 60 mm, the contribution from gradient and curvature drift becomes negligible. The calculated electric field profile directly reflects the variation of the electron drift velocity, with a weighting related to the magnetic field intensity. This is why between 60 mm and 80 mm the electric field direction reverses, like the electron drift, and reaches a positive value that increases up to $1\,\mathrm{kV\,m^{-1}}$ at 110 mm from the guard ring. Such a change in the electric field sign depending on the axial distance

was already predicted from experiments [147] and models [148]. Experimentally, the observation of a change of spoke rotation direction while the structure moves more downstream from the target suggested electric field reversal [147]. A bulk plasma model also observed an electric field reversal in the vicinity of the ionization region, in the so-called extended pre-sheath [148]. This reversal is predicted to be more pronounced for high resistivity perpendicular to the field line. The conditions for voltage reversal may be respected with the relatively high magnetic field of the C0E0 configuration (see Section 4.4.2.1) and the low density obtained within the helium discharge we investigated.

4.4.1.2 Temporal exploration

In the HiPIMS regime, the measurement of the temporal profile of electron properties was performed by tuning the delay between the laser Q-switch signal and the pulser switch using the Stanford Research Systems DG645 digital delay generator. The temporal origin (t = 0) was set at the end of the current pulse, such that the pulse occurs between [−60 µs; 0 µs]. Positive time values correspond to the afterglow region. At ignition, the time for plasma (i.e., the appearance of a current) oscillated in a relatively large range, between −57 µs and −49 µs before the end of the current pulse. In contrast, at the end of the −60 µs pulse, the discharge switched off immediately with a reproducible exponential decrease of the discharge current. This stability of the switch-off time is the reason for the choice of this time as a reference. Figure 4.13 shows a plot of the temporal profile of electron properties performed at 1 mm and 60 mm from the guard ring and for various times from the end of the current pulse.

At 1 mm from the guard ring, electron density follows the discharge current profile shown in Figure 4.14. The only discrepancy at the beginning of the pulse, where a peak of density is observed, may be due to fluctuations in the mean delay time for ignition between the various acquisitions. After a sharp increase at ignition, electron density reaches a plateau at $6 \times 10^{17}\,\mathrm{m}^{-3}$ and decreases exponentially with a characteristic time of 10 µs after the end of the pulse (against 3 µs for the discharge current).
At 60 mm from the guard ring, electron density variations are smoothed and the maximum of density is lower (near $3 \times 10^{17}\,\mathrm{m}^{-3}$). In the afterglow, the characteristic time of the decreasing exponential is much higher than at 1 mm and seems to stabilize around $2 \times 10^{16}\,\mathrm{m}^{-3}$.

The electron temperature at 1 mm and 60 mm from the guard ring increases linearly until it reaches, respectively, 9.5 eV and 3.5 eV at the end of the pulse. This linear increase suggests that energy dissipation processes weaken with time or that the plasma is increasingly supplied with hot electrons. This trend is expected to change (at least a saturation should appear) when the electron temperature gets closer to the first ionization energy of helium if longer pulses were used. In the afterglow, electron temperature exponentially decreases with similar characteristic times as electron density.

At both positions, the probed electron drift velocity remains negative, close to $\approx -40\,\mathrm{km\,s}^{-1}$, for the entire duration of the pulse. It suggests that the electric field does not vary significantly during the pulse.
At 1 mm from the guard ring, during the pulse, electron drift velocity remains near $40\,\mathrm{km\,s}^{-1}$, below the value expected from only magnetic curvature and gradient contributions. After the pulse, the electron drift velocity displays a kink up to $50\,\mathrm{km\,s}^{-1}$ during approximately 5 µs before going back to its previous value. This kink could be explained by a positive overshoot of the voltage while it goes back to zero after the pulse. After this kink, electron drift velocity reaches a steady value around $-50\,\mathrm{km\,s}^{-1}$.
At 60 mm from the guard ring, electron drift velocity is also negative during the pulse but the absolute value is lower than that expected from only curvature and gradient contributions. After the pulse, electron drift velocity goes also to positive values, but permanently and with a gradual increase.

With the same method presented for the axial exploration, the axial electric field was calculated from the electron temperature and drift velocity estimated from Thomson spectra.
At 1 mm from the guard ring, the contribution from curvature and gradient drift is negligible, which makes the temporal profile of the electric field proportional to the electron drift velocity profile. During the pulse, the negative electric field of approximately $-15\,\mathrm{kV\,m}^{-1}$(directed toward the target) is the main source for the azimuthal drift of electrons in the negative direction. At the end of the pulse, the overshoot of voltage seems to temporally reverse the electric field (directed outwards) before it suddenly goes back to a negative value afterward.
As seen with the axial profile, at 60 mm from the guard ring, the curvature and gradient drift becomes negligible. Again, the electric field is negative and have almost the same trends as the electron drift velocity (not visible with the scale of Figure 4.13). The values of electric field calculated at the end of the pulse are consistent with the value obtained at this position during the axial exploration. After the

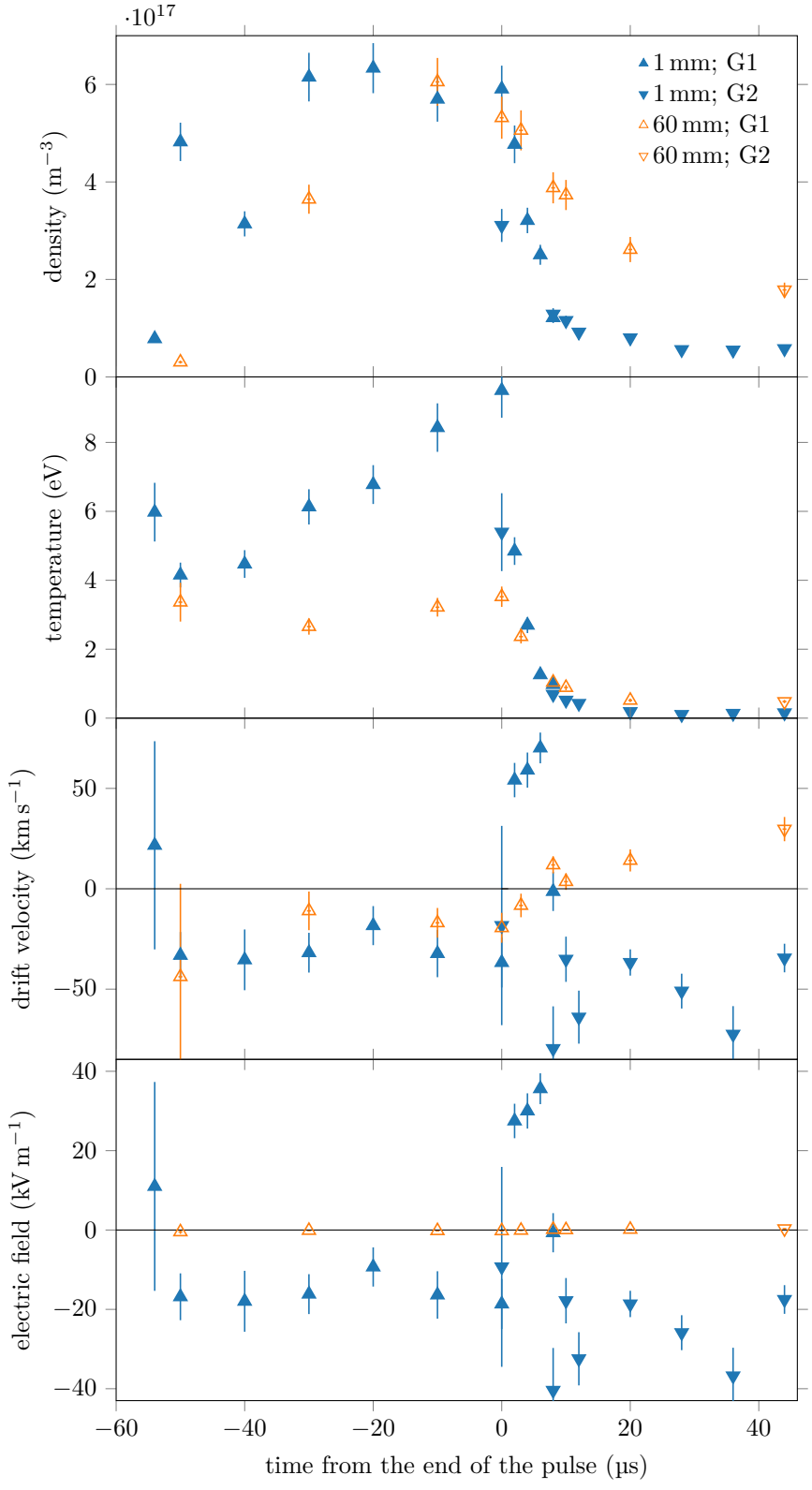

Figure 4.13: Temporal profile of electron density, temperature and drift velocity obtained at 1 mm and 60 mm from the guard ring. The 600 lines mm^{-1} grating (G1) was used to probe high electron temperature positions while the highly dispersive 2400 lines mm^{-1} grating (G2) was used in the case of low electron temperatures. The temporal profile of the axial electric field was calculated with the values of electron temperature and drift velocity estimated from the Thomson spectrum.

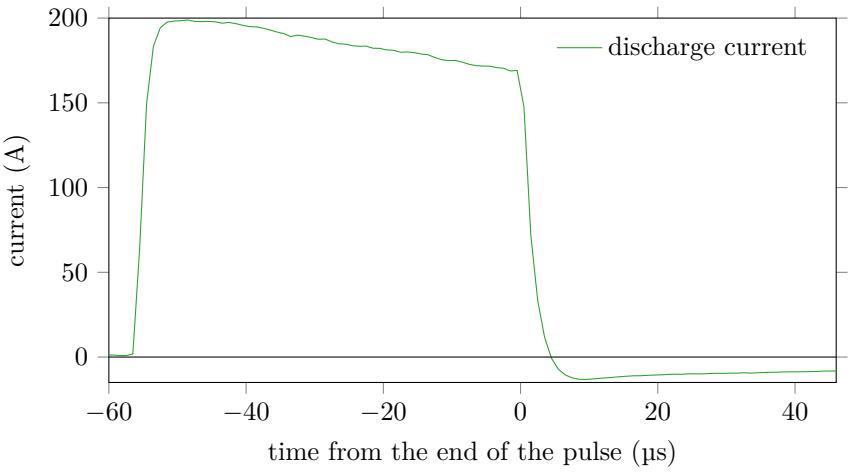

Figure 4.14: Temporal profile of the discharge current measured with the current probe obtained under the same conditions as Figure 4.13.

end of the pulse, no jump of the electric field is visible as was observed at 1 mm. In the afterglow, the electric field changes sign, like the electron drift, and reaches a maximum value of $300\,\mathrm{V\,m^{-1}}$, 44 µs after the end of the pulse.

4.4.1.3 Discharge mode discussion

A discharge classification suggested by Brenning et al. [87] identified two main types of magnetron discharges depending on the sputtering process. In the first type of discharge, named type A, it is mainly through the recycling process of sputtered ions that new particles are accelerated toward the target (and may lead to sputtering); this process is called self sputtering. With the other type of discharge, named type B, its is mainly the recycling and ionization of the surrounding gas (injected through the flow-meter) that particles are accelerated toward the target for sputtering.

A deeper characterization of the sputtering process inside the discharge we investigated is needed to determine definitively which type of discharge we dealt with. However, Ti targets are known to have low self-sputtering yield and He atoms being light, we do not expect a sufficiently high density of sputtered ions for self sputtering process. These experimental parameters strongly suggest that we dealt with a type B plasma discharge, i.e., a gas recycling discharge.

Above a critical current introduced by Huo et al. [149], both type A and type B discharges change behavior. For the type A discharge, above this critical current, the discharge current reaches a plateau and is dominated by self sputtering recycling with little sheath energization and secondary emission contribution to the discharge current. With the type B discharge, the discharge current remains dominated by gas recycling power but becomes unstable. The decreased stability is coupled to an increase in sheath energization of secondary electrons which increases the secondary electron emission contribution to the discharge current.

With the experimental conditions used for investigation of the HiPIMS regime with He gas, the 200 A discharge current used to sustain the discharge was above the critical current (estimated at approximately 130 A). In the preceding discussions, we have noted the large jitter in the pulse initiation time with respect to the applied trigger, which may be linked to characteristics of the power supply used. However, one further contribution to the jitter may be our operation above the critical current for a type B discharge. Operation in this regime may also account for the abnormally high electron temperature observed.

Still, we only estimated an average electron temperature over the radial and azimuthal directions. Because the direction of the sheath electric field is mainly axial, we expect the electron temperature to be higher along this direction. Exploration of electron properties along the axial direction would be needed in order to solve the origin of the linear temporal increase of electron temperature 1 mm from the guard ring. The linear increase with time may derive from a more efficient redistribution of electron energy as the plasma density increases downstream from the target and allows more numerous collisions. Another explanation would be based on an increase in sheath energization while the discharge develops.

Similar to what we have done in the DCMS regime, we may estimate the maximum ionization degree of the plasma in this regime. Under similar hypotheses, we obtain an ionization degree $\alpha \approx 0.03\,\%$ at maximum. The corresponding values of electron-ion and electron-neutral collision frequencies are respectively $1 \times 10^8\,\mathrm{s}^{-1}$ and $1 \times 10^6\,\mathrm{s}^{-1}$. Collisions are still dominated by neutrals due to the increased electron temperature and the neutral pressure remaining high.

4.4.1.4 Deviations from thermal equilibrium

Because the signal-to-noise ratio was high in HiPIMS regime, it was possible to smooth the Thomson scattering spectra measured to extract their derivatives. The spectrum derivatives allowed computation of the corresponding EVDF with the method presented in Section 3.4.3.1.

Figure 4.16 shows the EVDF computed from the Thomson spectra shown in Figure 4.15, which were obtained at 30 mm and 110 mm from the guard ring, and at the end of the HiPIMS pulse. The choice was made to show the EVDF at these distances because these positions are ones where the electron drift velocities are extreme. In the figures presented, the green line ("from fit") corresponds to the theoretical EVDF associated with the Gaussian fit of the Thomson spectrum, derived under the Maxwell-Boltzmann hypothesis. The red line ("from smoothing") corresponds to the experimental EVDF extracted from the shape of the Thomson spectrum.
30 mm from the guard ring, on the side corresponding to positive electron velocities, both theoretical and experimental EVDFs are in good agreement. The weak discrepancy in the wings may come from the derivation procedure of the Thomson spectrum for large spectral shifts. In the Thomson spectrum wings, the signal-to-noise ratio is low and leads to an even noisier derivative. For EVDF derivation, this noisy part of the derivative is amplified by the $\lambda - \lambda_0$ coefficient, leading to unreliable values of the EVDF for large velocities. The amplification of the noise is less significant with the EEDF, however, the scale associated with low electron velocity is shrunk. With an EEDF, the shift of the center of the distribution would not be as clear as with the EVDF presented. For the side corresponding to negative electron velocities, a quantitative deviation from the Maxwell-Boltzmann EVDF is visible, with a clear high-velocity tail. The discrepancy on this side is systematic for distances below 60 mm from the guard ring (and at the end of the HiPIMS pulse). This range of positions corresponds to the positions where a significant negative electron drift velocity is measured (see Figure 4.12).
At 110 mm from the guard ring, the best agreement between the theoretical and experimental EVDF is obtained on the side corresponding to negative electron velocities. The agreement is less perfect than in the 30 mm case; the EVDF obtained from the smoothing procedure seems to tend toward a Druyvesteyn EVDF. This Druyvesteyn-like EVDF distribution may be explained by the reduced degree of ionization leading to more inelastic collisions for highly energetic electrons. The larger discrepancy is observed in the part of positive electron velocity portion, with again, a high-velocity tail. The correlation between the electron drift velocity direction and the side of the EVDF is distorted, suggesting that the electron drift velocity direction may break the symmetry of the EVDF in two ways:

- The center of the EVDF shifts in the direction of the drift velocity. This phenomenon is clearly visible in Figure 4.16. It was also visible in Figure 4.15 with a global shift of Thomson spectrum between the two positions.
- A high-velocity tail appears on the side of the EVDF corresponding to the drift velocity direction. This high-velocity tail may arise from the acceleration of highly energetic secondary electrons along the azimuthal drift direction.

These observations prove that in such magnetized plasma sources, non-Maxwellian electron behavior can be observed with the Thomson scattering diagnostic. This discrepancy can be deduced from weak distortions of Thomson spectra which are not immediately visible on inspection of the Thomson spectra alone. More significant distortions are expected closer to the magnetron target or in Hall thruster sources. These strong distortions might place in doubt the hypothesis of spherically symmetric EVDFs used for their derivation from the Thomson spectra [95].

4.4.2 With Ar gas

It is well known that the deposition rate in HiPIMS regime is lower than in the DCMS regime [150,151]. The time-varying nature of the plasma properties in HiPIMS suggested that we should find distances

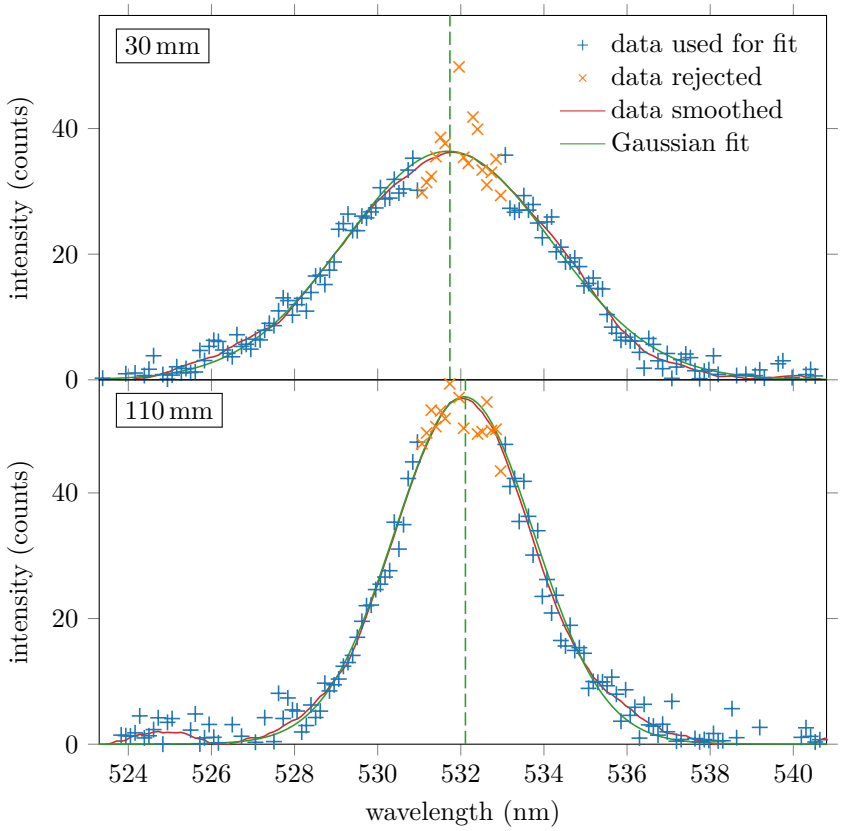

Figure 4.15: Thomson spectra at 30 mm (top) and 110 mm (bottom) from the guard ring. The Gaussian fit applied to estimate electron properties is shown with a green line, the vertical dashed line in green indicates the center of the fit. The smoothed function used to derive the EVDF shown in Figure 4.16 is indicated with a red line.

and/or times where the Thomson spectrum is not distorted from Raman scattering on sputtered particles as in DCMS regime.

As shown in Figure 4.17, in HiPIMS regime with argon gas, the Thomson signal is not affected by emission peaks as in the DCMS regime. However, for this high signal-to-noise ratio Thomson spectrum, parasitic peaks with equivalent intensity as in DCMS regime would hardly be visible; the strong Thomson intensity may hide them. Still, for all investigations shown in this section, the peaks seen in the DCMS regime were not observed. We speculate that in the HiPIMS regime, the molecules that could be sputtered (TiO_2 for example) would be split by the high density and temperature of the electron inside the plasma. The higher ionization of the sputtered neutrals is a characteristic feature of HiPIMS regime [152, 153].

The absence of Thomson spectrum distortion, even with the higher density and similar temperature levels encountered in DCMS regime, strengthen our belief that the no laser-induced perturbation of the plasma happened in both regimes. As described in Section3.5.1, if a constant electron temperature is considered, the critical laser fluence for inverse Bremsstrahlung should decrease at higher density. If laser perturbation from plasma absorption did happen in DCMS, it should be more intense in HiPIMS regime, close to the target at least.

4.4.2.1 Axial exploration

Figure 4.18 shows the electron density and temperature obtained from axial explorations at the end of a HiPIMS pulse, from the analysis of Thomson spectra with the 600 lines mm^{-1} grating. During the measurement, an argon flow guaranteed a background pressure of 1 Pa to sustain the discharge. We realized axial explorations with the various magnetic configurations presented in Figure 4.5. With all the magnetic field configurations, the discharge repetition rate and the maximum discharge current were fixed to 10 Hz and 80 A, respectively. The discharge voltage was the adjustment parameter, with its

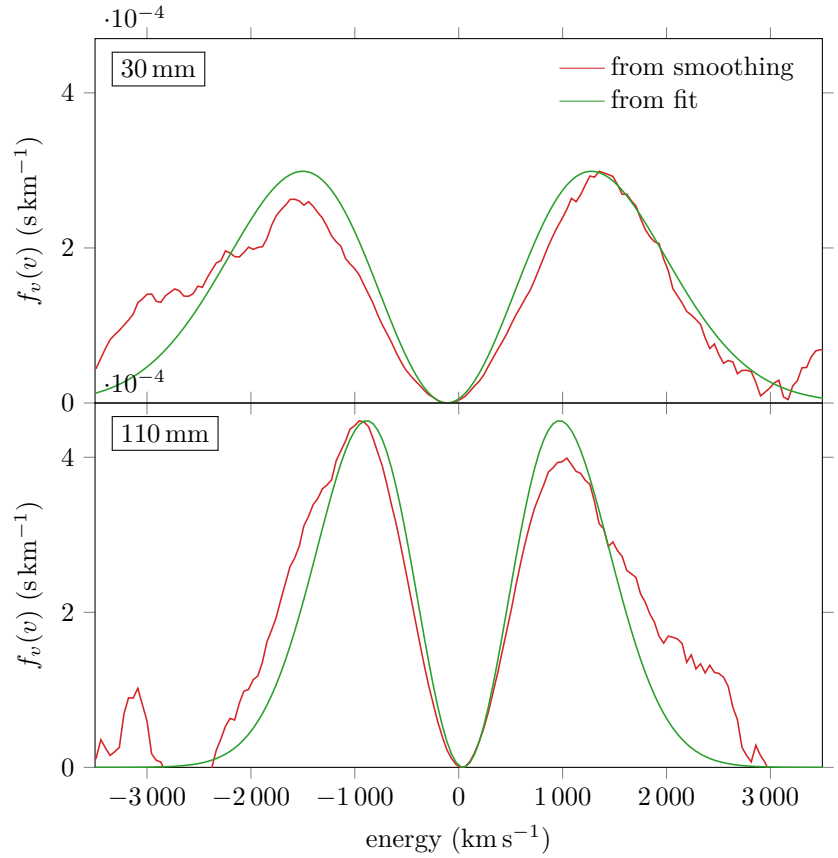

Figure 4.16: EVDF at 30 mm (top) and 110 mm (bottom) from the guard ring. Two estimations of the EVDF are shown: one extracted from the Gaussian fit applied to the Thomson scattering spectra (green line) and the other from the smoothed shape of the Thomson spectrum (red line).

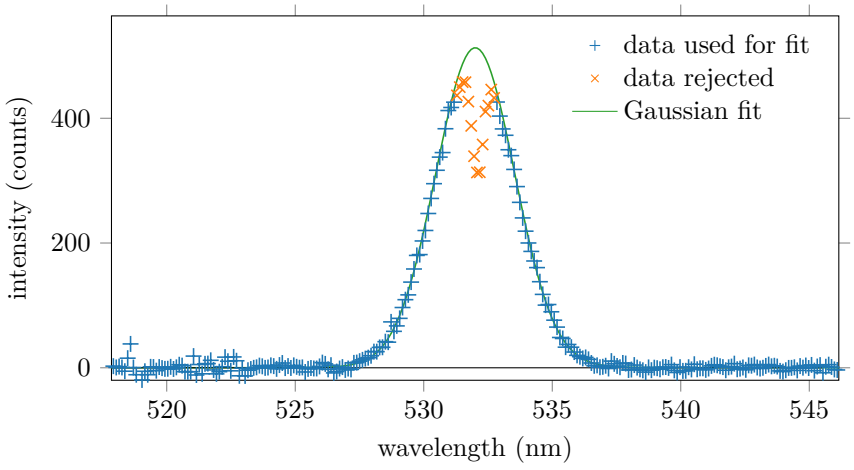

Figure 4.17: Example of a Thomson spectrum and its corresponding fit obtained with the 600 lines mm^{-1} grating, at the end of a HiPIMS current pulse, and at 3 mm from the guard ring. The argon pressure was fixed to 1 Pa and the discharge current and voltage profiles are shown in Figure 4.19 for the C10E10 configuration. The Gaussian fit gives n_e=$(2.2 \pm 0.2) \times 10^{18}$ m^{-3}, T_e=(2.0 ± 0.2) eV and $v_{e,drift}$=(-19 ± 3) km s^{-1}.

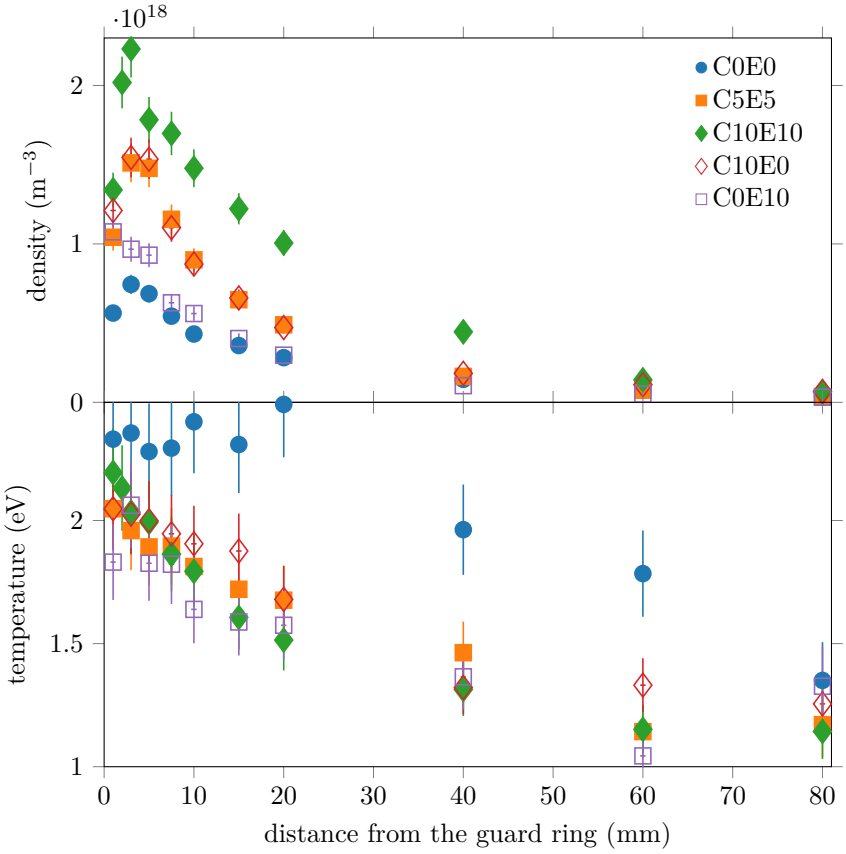

Figure 4.18: Axial profiles obtained from investigations at the end of the HiPIMS pulses (10 Hz repetition rate) with argon gas to sustain the discharge and for various magnetic field configurations. Figure 4.19 shows an example of the associated current and voltage temporal profiles.

Magnetic configuration	U_d (V)	w_I (µs)	σ_{w_I} (µs)
C0E0	813	48	3
C5E5	857	36	7
C10E10	920	39	6
C10E0	857	35	7
C0E10	846	38	9

Table 4.2: Comparison of the discharge voltage (U_d), the FWHM of the temporal profile of the discharge current (w_I) and its standard deviation (σ_{w_I}) for the various magnetic field topographies investigated.

value varied in order to keep the current constant. The magnetic field topography also affected the FWHM of the temporal profile of the discharge current (noted w_I). As with the studies with helium, we fixed the width of the voltage gate to 60 µs. Figure 4.19 illustrates these variations of the temporal profile of both the discharge current and voltage. The exact shape and time of the current rise exhibited large fluctuations between two pulses, quantified by the standard deviation of w_I, noted σ_{w_I}. Table 4.2 summarizes the values of the parameters affected by the magnetic field topographies.

As shown in Figure 4.18, when the discharge current is maintained constant, the electron density profile decreases monotonically for an increased magnetic field. This ordering of plasma density correlates with trends observed by quartz crystal micro-balance (QCM) measurements on the same planar magnetron [154]. These QCM explorations focused on positions above the center of the target (r =0 mm), and for

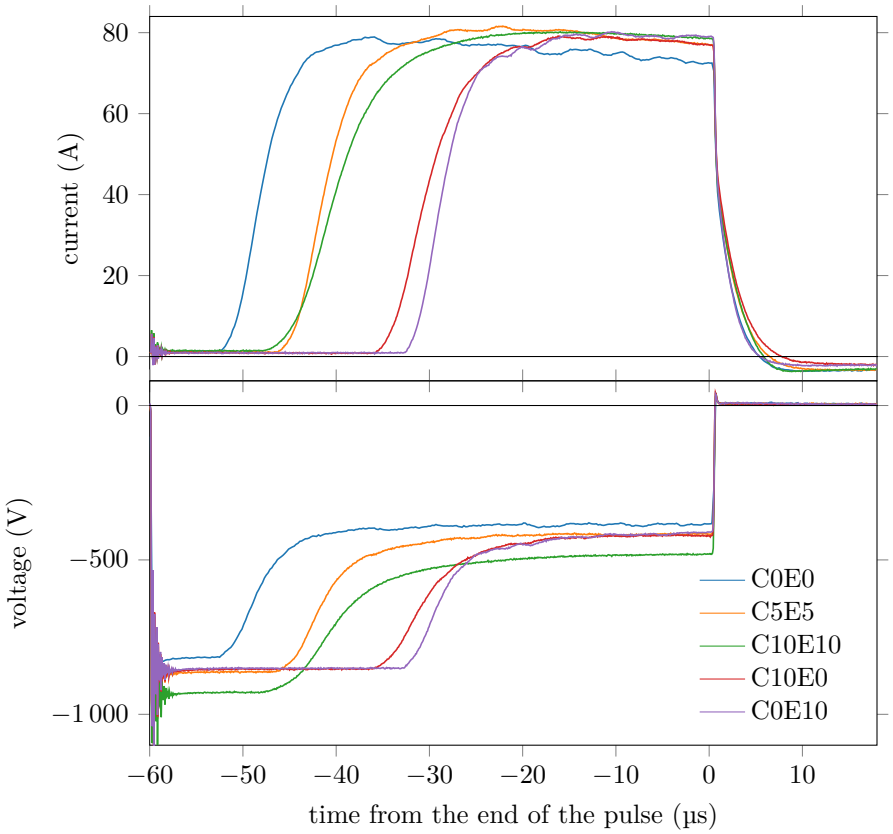

Figure 4.19: Temporal profile of the discharge current (first row) and voltage (second row) of the HiPIMS discharge for the magnetic field configurations presented in Figure 4.5. The maximum discharge current was kept constant by tuning the value of the applied electric field.

various magnetic field topographies at a fixed current. These explorations also showed an increase of the Ti ionized flux fraction (70 mm downstream from the target center) for a decreasing magnetic field intensity. The different trends observed at 30 mm from the target may arise from large variations of plasma properties with respect to the radial position at small axial distances. The rise of the back attraction probability of the sputtered species is expected to be the main parameter governing the decreased ion density at larger magnetic field [155, 156].

The axial profile of electron temperature, shown in Figure 4.18, doe not depend significantly on magnetic field intensity. Typically, it decreases from 2 eV near the target to approximately 1.2 eV at 80 mm from the guard ring. Only the configuration with the highest magnetic field (C0E0) leads to another behavior. With the C0E0 configuration, electron temperature stays at a steady value from the guard ring up to 20 mm from it, then decreases linearly. This higher temperature may be explained by better confinement of electrons, leading to fewer losses. The reduced plasma density obtained with this configuration may also decrease the sputtering rate, leading to fewer Ti atoms and consequently fewer paths for electron energy losses through ionization.

The highest degree of ionization obtained with the magnetron discharge is achieved with the C10E10 configuration, where it reaches a maximum $\alpha \approx 0.9\,\%$. For this configuration the electron-ion and electron-neutral collisions are respectively $2.5 \times 10^7\,\mathrm{s}^{-1}$ and $1.8 \times 10^7\,\mathrm{s}^{-1}$. This rough estimate indicates that indeed, in HiPIMS regimes with Ar gas, the plasma can be considered as fully ionized, and Coulomb collisions become the dominant process for the transfer of electron energy.

4.4.2.2 Temporal exploration

The 10 Hz acquisition frequency used up to this point eased synchronization of the discharge with the laser. However, it corresponds to a discharge condition with large peak power, low average power (usually below 100 W) and low duty cycle (approximately $6 \times 10^{-2}\,\%$). These conditions correspond to

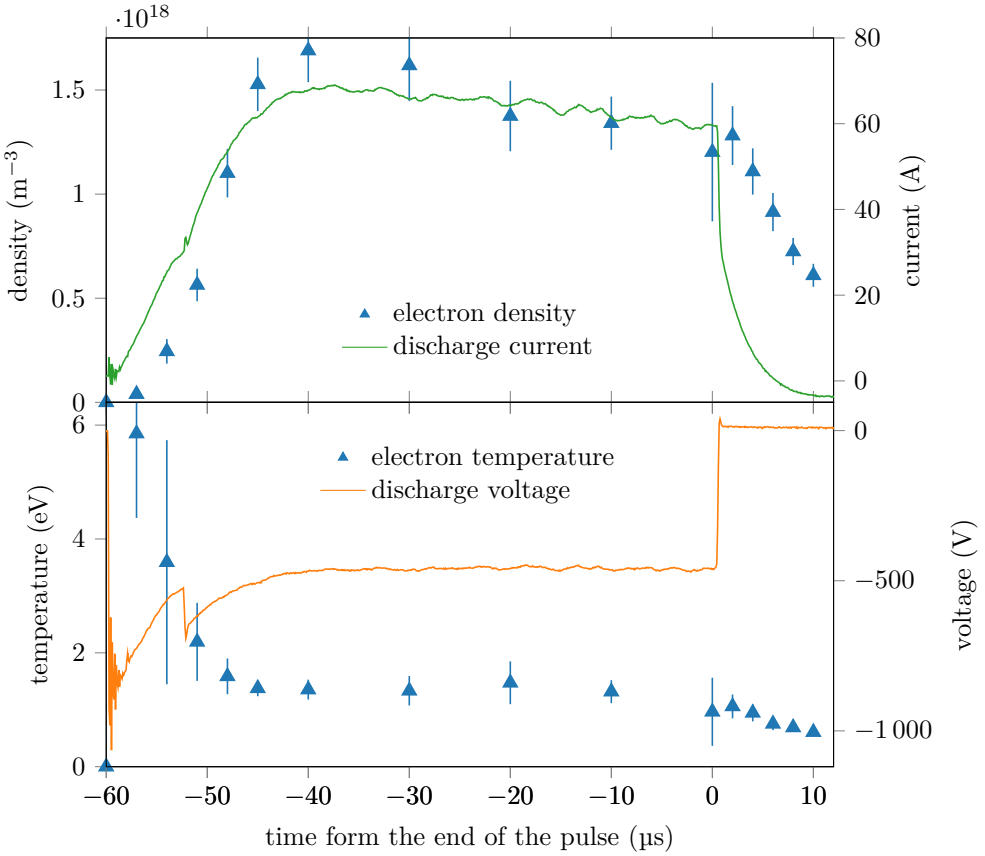

Figure 4.20: Temporal profile of electron density (first row) and temperature (second row) estimated from Thomson scattering spectra. The temporal profile of the discharge current is superposed on the density profile while the discharge voltage is shown superposed on the electron temperature profile.

a regime in the lower right area in the diagram of Figure 4.2. This low duty cycle leads to a low residual plasma density before the next plasma ignition. Without a high enough electron density, the delay for plasma ignition is less stable. In order to work at a higher duty cycle and average power, we set the digital delay generator to produce ten pulses (lasting 60 µs) at 100 Hz for each triggering signal from the laser (at 10 Hz). This shortened the delay for plasma ignition and reduced its standard deviation.

For the temporal investigation presented, we used the C0E0 configuration and a discharge current of 80 A peak to peak. We investigated only one position above the race track (r=20 mm) at 5 mm downstream from the guard ring. With these discharge conditions the FWHM of the discharge current profile was 52.8 µs with a standard deviation of 0.8 µs. With identical discharge parameters but at 10 Hz of repetition rate, we had t_d=48 µs and σ_{t_d}=3 µs (see Table 4.2).

Figure 4.20 shows the electron densities and electron temperatures estimated at different instants within the HiPIMS pulse. The absolute electron density closely follows the form of the current profile while the discharge is on. It rises nearly two orders of magnitude from the plasma ignition to the peak current ($3.93 \times 10^{16}\,\mathrm{m}^{-3}$ at -57 s to $1.68 \times 10^{18}\,\mathrm{m}^{-3}$ at -40 s). After the peak current is attained, the density first decreases at a faster rate than the current during the pulse, and then at a slower rate than the current in the afterglow phase. The long time-constant observed for the density decrease in the afterglow region is compatible with the presence of a long-lived residual plasma near the target. For high pulse repetition rates, the presence of such a plasma facilitates the ignition of subsequent pulses and accounts for the lower delay of ignition observed with the 100 Hz repetition rate, in comparison to the 10 Hz case. The easier ignition seems to lead to a more dense plasma. For similar plasma conditions, the electron density reached only $7 \times 10^{18}\,\mathrm{m}^{-3}$ at 10 Hz, compared to $1.7 \times 10^{18}\,\mathrm{m}^{-3}$ at 100 Hz. The electron density decay with time in the afterglow region (2 µs and beyond) is exponential (consistent with a diffusive process). The time constant for this decay is 10.5 µs and bears some similarity to observations made by Seo and colleagues in their probe measurements in the afterglow of a direct current magnetron

discharge [157].

The corresponding electron temperatures for the different instants in the pulse are shown in the second row of Figure 4.20. Here, the highest values of electron temperature are observed at the start of the pulse with a peak around 6 eV. The electron temperature quickly drops from its peak value and remains mostly around 3 eV during the pulse. The large error bars of the values near the pulse ignition reflect the low electron densities encountered at the discharge onset. The uncertainty for these positions in the pulse arises mainly due to the quality of the fit. The electron temperature profile closely follows the applied voltage variation (orange line in the second row of Figure 4.20). The few first electrons may be expected to almost instantaneously gain energy on the initial application of the voltage while Coulomb collisions remain low. After reaching an overshoot value around $-1000\,\mathrm{V}$ at $-60\,\mathrm{s}$ (the beginning of the pulse), the discharge voltage increases until it reaches a flat profile which is established around $-500\,\mathrm{V}$ from $-40\,\mathrm{us}$ to $0\,\mathrm{us}$ from the end of the pulse. This flat voltage profile is correlated with a steady-state temporal profile for the electron temperature. The voltage drops to $0\,\mathrm{V}$ at $0\,\mathrm{s}$, but the decrease of the electron temperatures in the afterglow plasma is more gradual. Processes such as collisions between the electrons and ambient argon atoms ($\nu_{en}{\approx}1.5 \times 10^7\,\mathrm{s}^{-1}$) and between ions and electrons ($\nu_{ei}{\approx}2.9\,\mathrm{s}^{-1}$) will contribute to the electron temperature decrease, but as with the electron density, our measurements in the afterglow phase reflect features of a diffusing plasma.

The trend observed in Figure 4.20, of an initial peak in electron temperature followed by saturation over the pulse duration, is similar to observations made by other authors using ionization region model simulations for more peaked current profiles [148, 158, 159]. The decay of the electron temperature is in line with recent 2D PIC results simulating HiPIMS pulses [90], showing higher electron temperatures at the beginning of the pulse, followed by a plateau in temperature when the current becomes constant. The trends observed for the plasma density are also in line with the numerical 2D PIC simulation results [90] showing an increase in plasma density by two orders of magnitude from the initial state ($10^{16}\,\mathrm{m}^{-3}$) to a maximum reached at the beginning of the current plateau (a few $10^{18}\,\mathrm{m}^{-3}$).

For the same instants shown in Figure 4.20, the electron drift velocities in the direction of the probed wave vector were estimated from the Thomson spectrum. In these measurements, the observed wave vector has been positioned such that measurements have contributions from azimuthal and radial electron motion. Small positive drift velocities, below the estimated resolution of $44\,\mathrm{km\,s}^{-1}$, were observed. The absence of significant variations of the drift velocities may be expected from the steady-state low electric field which is established for much of the pulse inside the bulk of the plasma. More significant values of drift velocity would be expected closer to the target. Contrary to the case presented in Section 4.4.1, it seems that most of the potential drop is located inside a thin sheath near the target, and is therefore not accessible to measurements because of the lower limit for axial explorations set by the guard ring.

4.5 Conclusion

In this chapter we presented the results from the first implementation of the THETIS diagnostic on a low pressure magnetizd plasma source. These studies illustrates the high sensitivity and adaptability of the diagnostic.

Investigation on a planar magnetron discharge in the DCMS regime with argon gas faced difficulties related to the presence of parasitic peaks inside the acquired spectrum. A more in-depth study is needed to determine the origins of these parasitic peaks. Using helium gas led to much cleaner Thomson spectra and demonstrated the sensitivity of the diagnostic down to the $10^{16}\,\mathrm{m}^{-3}$ range (with the $11\,\mathrm{mm} \times 11\,\mathrm{mm}$ VBG-NF).

From the study of the HiPIMS regime, we confirmed the much higher plasma density obtained in this regime. The higher signal-to-noise ratio allowed a reliable estimation of the electron drift velocity from Thomson spectra. Axial and temporal explorations with He were used to demonstrate the possibility of extracting the electric field inside the plasma from the electron properties estimated from the Thomson spectrum and after a complete measurement of the magnetic field topography.

In the HiPIMS regime with Ar gas, spectra were not affected by the parasitic peaks observed in DCMS. Axial exploration with this gas was used to determine the influence of the magnetic field intensity. It seems that the magnetic field intensity mainly affects the electron density. This exploration showed an electron density increase when the magnetic field intensity was reduced. Working with HiPIMS pulses at a higher repetition frequency than that one used with He led to better pulse-to-pulse stability of

the discharge and higher density. This higher stability allowed the demonstration of the capability of the diagnostic for time-resolved measurements of electron properties with a resolution of few tens of nanoseconds, even during the beginning of the current pulse.

Chapter 5

Incoherent Thomson scattering investigations in an ECR ion source

> Even as a boy, I observed that one man alone by giving these impulses at the right instant was able to ring a bell so large that when four, or even six, men seized the rope and tried to stop it they were lifted from the ground, all of them together being unable to counterbalance the momentum which a single man, by properly-timed pulls, had given it.
>
> — *Galileo Galilei, Dialogues Concerning Two New Sciences*

In this chapter, we present the results from the implementation of THETIS on a plasma source based on electron cyclotron resonance. The goal of this campaign was to demonstrate the applicability of the THETIS to diagnostic to such investigations and gain insights into a source relevant for accelerators developed by CEA Saclay. Synchronization with the discharge allowed time-resolved measurements when RF pulses were used to ignite the discharge. The type of gas used to sustain the discharge and the operating pressure on electron properties were modified in order to study their influence on the electron properties. Challenges encountered due to the plasma source design are described.

Contents

5.1 Introduction

Resonance is a physical phenomenon encountered in almost all fields of science. It is encountered, for example, in mechanical structures, electric circuits, and optical cavities. All systems analytically described by equations of second order and above can exhibit at least one natural frequency. The spectral shape

of resonances is an efficient means for systems characterization and illustrates its ability to efficiently concentrate energy inside a limited spectral range.

Humans needed many years to master resonances; at first, these phenomena were merely understood or worse, were the cause of tragic events such as the collapse of bridges. The Electron Cyclotron Resonance (ECR) is no exception to this rule. The natural helical trajectory of electrons at a frequency which depends on the magnetic field comes naturally out of Maxwell's equations. Still, it was not until 1970 that the first application to plasma generation [160, 161] was made. Oddly, the use of ECR resonance happened decades after the mastering of nuclear [162] and electronic [163] spin resonances for estimation of their quantum spin number.

ECR ion sources are plasma sources that use RF waves at the same frequency as the frequency of the electron cyclotron trajectory for electron heating. For non-relativistic electrons, this frequency is called the electron cyclotron frequency ($\omega_{c,e}$) and is given by

$$\omega_{c,e} = \frac{eB}{m_e} \tag{5.1}$$

with e the elementary charge, B the magnetic field and m_e the electron mass.

For a given frequency of the RF wave injected (ω_{RF}), the electric field of the wave is in phase with the electron trajectory if a surface where $B = m_e\omega_{RF}/e$ exists. Over this surface, the energy of the wave is efficiently transmitted to the electron. While electrons gain energy, their velocity increases but the Larmor radius rises linearly such that the period of one revolution remains unchanged. This is why this heating process is not selective on the particle energy and would have no other limits than relativistic effects for electrons staying over a resonance surface.

In practice, the residence time of electron over the resonance surface is low due to the spatial inhomogeneities of the magnetic field as well as the large mobility of electrons. This is why ω_{RF} is usually chosen so that the magnetic field needed for resonance corresponds to an intensity for which most electrons will be magnetized. The most frequently used RF frequency is inside an ISM band [164] at 2.45 GHz. The magnetic field needed to match resonance at this frequency is 87.5 mT. With this magnetic field intensity, the Larmor radius of electrons with temperature up to the kilo-electronvolt range remains on the millimeter scale and electrons would be magnetized for most ECR ion source sizes. Under these conditions electrons follow the magnetic field lines and using the magnetic mirror effect, they can be trapped inside a reduced volume. This magnetic field topology allows the adjustment of the total residence time of electron over a resonance surface, and consequently, the efficiency of the stochastic heating. It is a way to temper or increase the electron temperature depending on the ionization energy needed to produce the ion species desired.

Because ECR ion sources do not require any mechanical elements inside the plasma and allow one of the most efficient ways for electron heating, it is a process widely used for plasma generation. These plasma sources, with few wearing parts, allows a long time of operation without failure. This specificity is a key advantage for applications where ions are produced to be injected into particle accelerators [165] or accelerated to propel spacecraft [166, 167]. With an optimized design of the magnetic bottle, electrons can be trapped for a sufficiently high duration that some reach energies in the kilo-electronvolt range. For this reason, ECR heating is used in ion sources producing heavy ions with unrivaled charge states [165] which are injected in particle accelerators for high-energy nuclear physics studies. Because of the high electron temperature achieved in these magnetic bottles, this design is still considered for controlled fusion applications [168, 169].

5.2 Experimental setup

5.2.1 Context

The Thomson scattering investigation of this chapter was realized on the ECR ion source known as ECRIN (Electron Cyclotron Résonance Ion Négatif) of the CEA Saclay. This ion source was originally designed to provide H^- ions for particle accelerators. Because the regular properties of ECR ion sources (i.e., density and temperature) are not favorable for negative ion production, negative ion production was achieved on this source by separating the plasma chamber (i.e., equivalent to the purple volume in Figure 5.1) into two parts with a biased grid [170, 171].

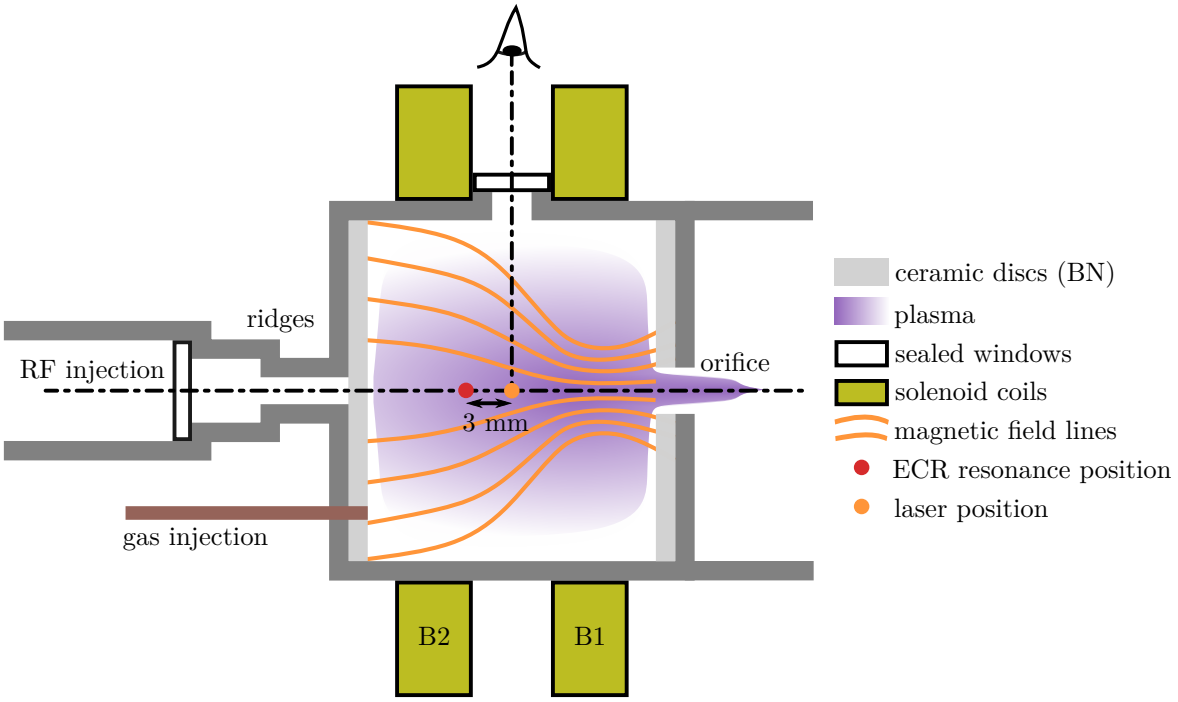

Figure 5.1: Architecture of the ECR plasma chamber. The relative distance between the laser beam and the resonance position is indicated for the configuration with (I_{B1}=64 A; U_{B1}=14.2 V) and (I_{B2}=68 A; U_{B2}=14.8 V).

In the upstream part of the chamber (on the left in Figure 5.1), on the side of the RF and gas injection, the ECR resonance takes place and generated hot electrons for ionization. The magnetic bottle opens in the upstream direction on a boron nitride (BN) ceramic disc; this material was chosen for its high secondary electron emission coefficient for energetic incident electrons [172, 173]. With this magnetic configuration, the electron does not remain for a long time over the resonance surface and as such the temperature remains relatively low. The few energetic electrons that may be produced drift toward the target because the magnetic field intensity is lower in this direction (as shown in Figure 5.2). From the collision with the target, one energetic electron will generate, on average, more than one cold electron. This secondary electron emission process contributes to an increased density of "cold electrons" [174]. A similar BN disc is positioned on the downstream side of the plasma chamber, but a hole 9 mm in diameter is drilled on its center for the extraction of particles.

The biased grid isolates the downstream part of the vacuum chamber from energetic electrons and screens most of the electric field of the RF. Inside this area of the plasma, the probability of negative ion production through dissociative attachment is higher. The H^- ions, as well as electrons, may be accelerated by an extraction electrode positioned a few millimeters downstream from the orifice shown in Figure 5.1. The remaining electrons are then filtered out by specific electrodes.

In its first version, the ECRIN vacuum chamber was a rectangular cuboid with a fixed length of 200 mm and the magnetic field was generated with two solenoids that surround the plasma chamber (similar to Figure 5.1) so that the resonant iso-magnetic surface cross their symmetry axis. An upgrade of the plasma source led to a new design based on a cylindrical plasma chamber made of copper with an internal diameter of 90 mm and adjustable length from 105 mm to 195 mm. Four equally distributed openings around the cylinder surface of the main ring (105 mm long) were added for diagnostic instrumentation. For the second version of the ECRIN plasma source, a permanent magnet multipolar structure in a Halbach geometry was designed in order to generate the magnetic field. With this magnet configuration, the ECR zone was located off-axis, at a radius of approximately 33 mm.

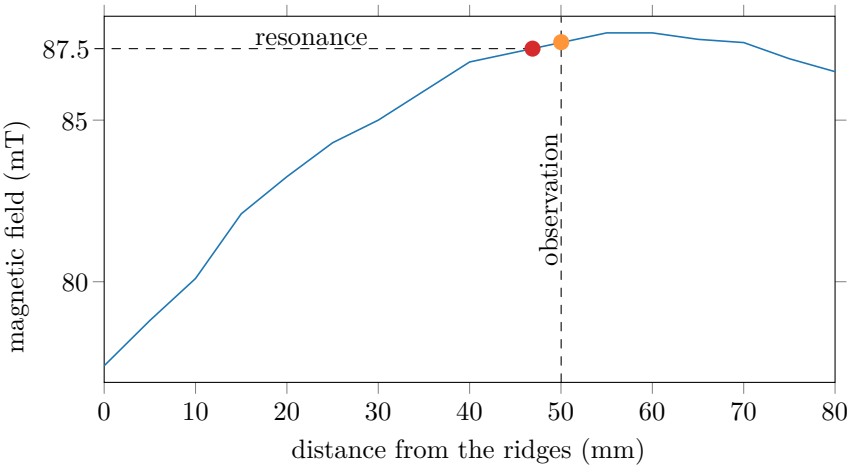

Figure 5.2: Axial profile of the magnetic field intensity along the axis of the plasma chamber for the configuration with (I_{B1}=64 A; U_{B1}=14.2 V) and (I_{B2}=68 A; U_{B2}=14.8 V).

5.2.2 Test facility and plasma source studied

Thomson investigations were realized with the second version of the ECRIN vacuum chamber. As shown in Figure 5.1 and Figure 5.3, two openings are used to pass the laser beam through the plasma chamber, with a third opening is used for the observation of the scattering light. For the investigations presented, we focused on the plasma chamber with the shortest length (105 mm) and a diameter of 90 mm.

As shown in Figure 5.3, the magnetic field was generated by two solenoïds placed around the vacuum chamber. This method of field generation corresponds to the method used for the first version of the ECRIN ion source. With this configuration, the ECR surface crosses the symmetry axis of the plasma chamber, with the position of this intersection point adjusted by tuning the current passing inside the solenoids. Hereafter, the position of the ECR resonance surface will be described by referencing the position of its intersection with the vacuum chamber axis. More efficient coupling is expected when the ECR surface is close to the position of RF injection.

The RF power is generated with a magnetron from Sairem (SP2) which delivers microwaves at 2.45 GHz with a mean power up to 1.2 kW in DC or pulsed mode. In pulsed mode, the shape of the applied pulse was defined with a GBF from Tektronix (AFG3021C) and transmitted to the microwave generator through a coaxial cable. The generated RF wave is transmitted to the vacuum chamber with an assembly of several RF guides respecting the Electronic Industries Alliance (EIA) standards (WR284 flanges are used). The RF wave first passes through two automatic stub-tuners which optimize the RF power coupled to the plasma chamber through the minimization of the reflected power. At the end of the waveguide, before the entrance in the vacuum chamber, ridges are used to focus the RF power near the axis of the plasma chamber. In this way the RF power can be maximized over the ECR surface if it is positioned near this injection point.

With the THETIS diagnostic, only one position can be probed. We were limited by the number of optical access points available for transmission of both the laser beam and the scattered light. Due to these constraints, the observation volume was located on the axis of the vacuum chamber, 50 mm downstream from the BN disc separating the plasma chamber and the ridges. For this reason, we decided to set the resonance position close to the observation volume. As shown in Figure 5.1, the solenoid configuration with (I_{B1}=64 A; U_{B1}=14.2 V) and (I_{B2}=68 A; U_{B2}=14.8 V lead to a magnetic field configuration for which the resonance surface is 3 mm upstream from the observation volume (i.e., 47 mm downstream from the ridges). The axial profile of the magnetic field intensity (supposing that the magnetic field is purely axial) along the chamber axis is shown in Figure 5.2 for the chosen magnetic configuration. The same configuration was maintained during the entire experimental campaign. A plasma chamber with a variable position of the ridges, similarly to what has been used elsewhere [172], would be an interesting upgrade for future investigations at various distances from the RF injection point.

The implementation of the THETIS diagnostic on the ECRIN ion source for time-resolved measurements required synchronization of the various systems. In pulsed mode, both the RF and laser pulses

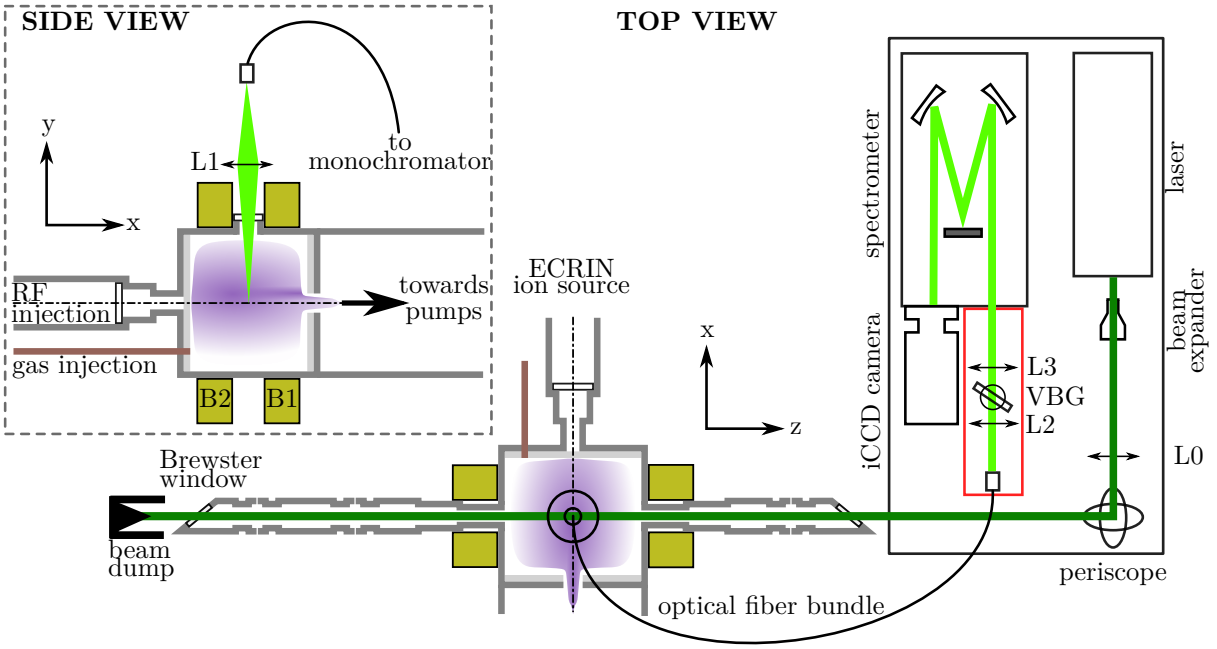

Figure 5.3: Overview of the diagnostic THETIS installed on the ECRIN ion source. The top view corresponds to the view in the plane created by the polarization vector (horizontal polarization in the observation volume) and the laser wave vector. The side view corresponds to a view in the plane created by the polarization vector and the scattering wave vector. The light beam on the transmission branch used to induce the Thomson scattering signal corresponds to the dark green line. Light on the detection branch containing the Thomson scattering signal to analyze is represented with a light green line.

were repeated with a 10 Hz repetition frequency. Both the microwave generator and the laser were synchronized with the 10 Hz clock of the GBF from Tektronix (AFG3021C). A delay generator from Stanford Research Systems (DG645) was inserted between the GBF and the laser, allowing ITS measurements at various times within the pulses delivered by the microwave generator. The various synchronization signals, as well as an image of the reflected power delivered by the stub-tuners, were visualized on a Teledyne LeCroy HDO6104A oscilloscope. This visualization eased the positioning of the time of observation as well as the verification of the discharge stability through the observation of the temporal profile of the RF power reflected.

Before operation, the plasma chamber was pumped through the 9 mm orifice. The assembly of a primary and a turbo-molecular pump allowed a pumping down to 5×10^{-4} Pa for degassing. A mass flow controller from MKS instruments (DM-20-A) was used to inject a mass flow of the working gas near the ridges. H_2 was the gas nominally used for this plasma source, however, investigations with He and Ar were realized. The ion source design did not allow the measurement of the pressure directly inside the plasma chamber. The mass flow rate was tuned in order to reach a given pressure (P_0) measured inside the part of the vacuum chamber located downstream of the orifice. The pressure inside the plasma chamber (P_{plasma}) was estimated with the following formula

$$P_{plasma} = P_0 + \frac{\dot{m}_g}{AC_g} \tag{5.2}$$

where $\dot{m}_g$ is the mass flow rate of gas injected (in Pa m^3 s^{-1} [175]), A the area of the orifice of the plasma chamber (in m^2) and C_g the surface density of the conductance of an orifice (in m s^{-1}). Table 5.1 shows an estimation of the surface density of the conductance of an orifice for the various gases used at ambient temperature (293 K).

In the configuration used for the Thomson scattering investigations, no electrodes were positioned after the orifice for the extraction of the charged particles. The plasma simply expanded from the plasma chamber to the downstream region due to the gradient of pressure and temperature. When the ion source

Gas	H_2	He	Ar
C_g ($m\,s^{-1}$)	440	311	98.5

Table 5.1: Surface density of the pumping conductance of an orifice for various gases used in these investigations (estimated at 293 K).

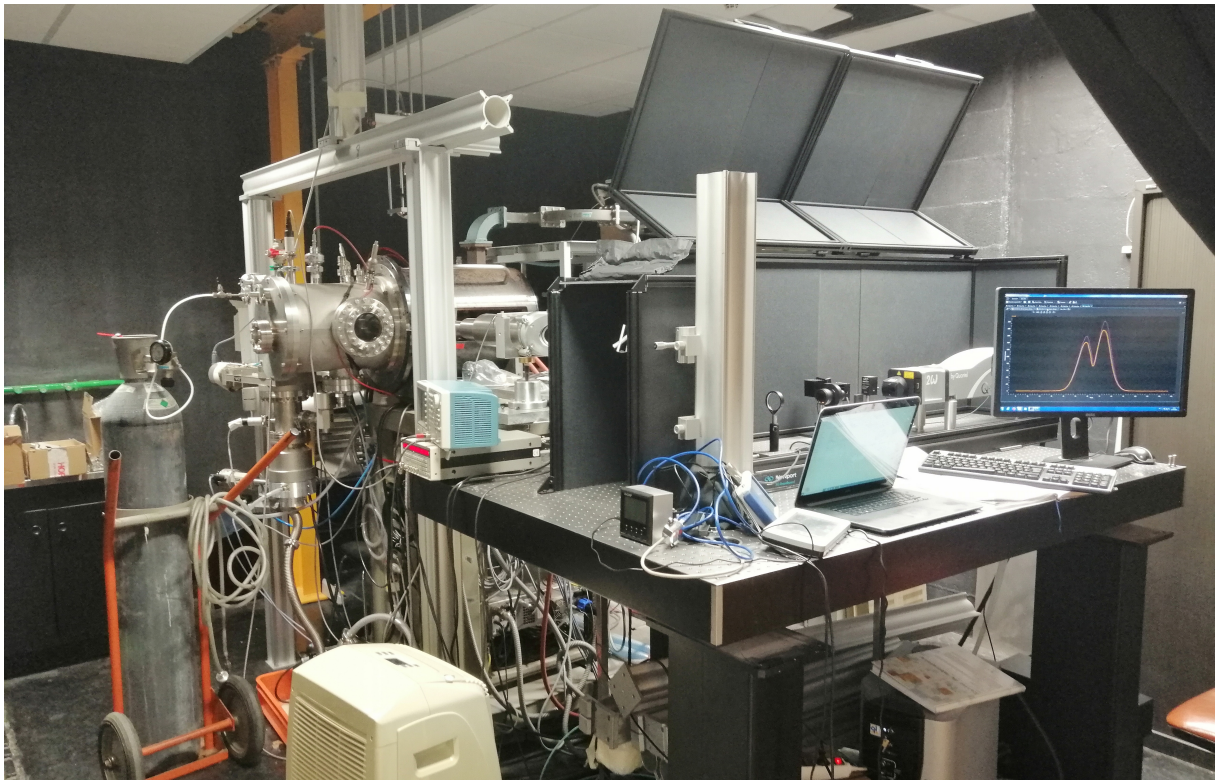

Figure 5.4: Picture of the THETIS diagnostic (right part) implemented on the ECRIN ion source (left part).

is operated in the extraction regime, the capacitance of the orifice may be higher due to the electrostatic acceleration of charged particles through the orifice. This phenomenon may explain the lower optimal pressure (measured in the downstream part of the vacuum chamber) required for optimal operation of the plasma discharge.

5.2.3 THETIS diagnostic

A full description of the THETIS diagnostic design and the procedure for Thomson spectrum acquisition were made in Chapter 3. This section focuses only on the specificities related to its implementation on the ECRIN ion source. A picture of the implementation of the THETIS diagnostic on the ECRIN ion source is shown in Figure 5.4.

The scattering volume, placed at the center of the plasma chamber, was imaged on the 3×5 bundle of fibers using a lens of 100 mm focal length (diameter 100 mm). This collection lens was placed approximately 410 mm from the observation volume, leading to a magnification of 0.32 mm. As shown in Figure 5.5, with this configuration, the probed volume corresponds to a cylinder 3 mm in diameter and 4.7 mm in length. Due to the scattering configuration, electron properties along the radial direction are probed.

It is with the implementation of the THETIS diagnostic on the ECRIN ion source that the mitigation of stray-light sources was the most challenging. The intensity and spectral shape of the various sources

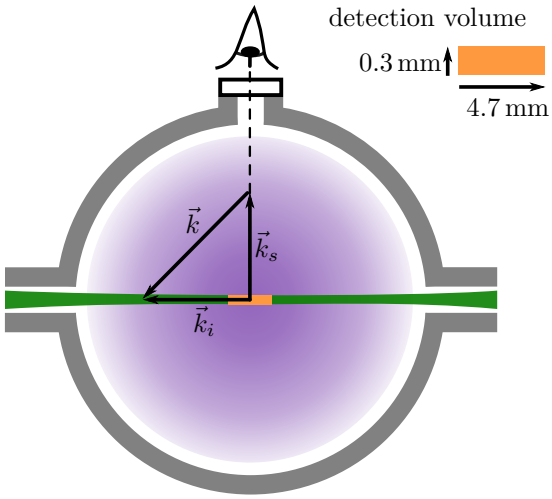

Figure 5.5: Scattering configuration used for the measurements of electron properties. $\vec{k_i}$, $\vec{k_s}$ and $\vec{k}$ correspond, respectively, to the laser wave vector, the scattering wave vector and the probed wave vector. The observation volume in orange is approximately 0.3 mm diameter and 4.7 mm long and placed on the center of the plasma chamber.

of stray-light are shown in Figure 5.6. These spectra were obtained in the middle of the RF pulse, after 6000 exposures with a one-pixel binning along the spectral direction of the CCD. The spectrometer turret scanned wavelengths from 400 nm to 700 nm with the 2400 lines mm^{-1} grating. As for all acquisitions performed in this chapter, the spectra were recorded with a 1 mm slit width.

For the ECR investigation, the stray-light from Rayleigh scattering was low due to the low operating pressure inside the vacuum chamber. However, the small size of the plasma chamber and the presence of metallic surfaces (mainly copper) near the observation volume contributed to a high level of stray-light from reflections. This translates to a stray-light level at 532 nm that remained on the order of 1000 counts despite the use of the VBG-NF. To minimize this contribution, we initially placed a layer of anodized aluminum over the wall of the plasma chamber with apertures in order to allow propagation of both the laser and scattered light. This significantly reduced the level of stray-light but led to a less stable plasma and a faster soiling rate of the window used for Thomson scattering collection. This method was later abandoned, and it was necessary to deal with the relatively large stray-light signal at 532 nm differently. Acquisitions with only the laser turned on were regularly performed (depending on the soiling rate of the windows) in order to subtract this contribution from the records used for Thomson acquisition (record—A).

As shown in Figure 5.6, when only the laser was turned on, a broadband signal for wavelengths larger than 532 nm was also observed. We interpreted it as a fluoresence signal induced by our probing laser on the large ceramic disc positioned on each side of the plasma chamber. The low intensity from this contribution is constant and was subtracted at the same time as the remaining stray-light from Rayleigh scattering and reflections.

The green line in Figure 5.6 shows the typical signal distribution obtained from only plasma emission. It is characterized by strong emission lines corresponding to the electronic transition of the gas used and a broadband low-intensity plateau. In all the investigation of this thesis, the spectral positions of the plasma emission lines were far enough from the Thomson spectrum that only the broadband contribution overlapped the Thomson spectrum. Similar to the other sources of stray-light, the signal from plasma emission was estimated from separate records (made with only the plasma on) and subtracted from the Thomson records to isolate the signal from Thomson scattering.

5.2.4 Experimental method for discharge condition choices

As mentioned previously, the magnetic configuration was chosen so that the position of the ECR resonance was close to the observation volume (3 mm upstream). The standard configuration with the resonance position a few millimeters downstream of the RF injection did not allow the observation of a

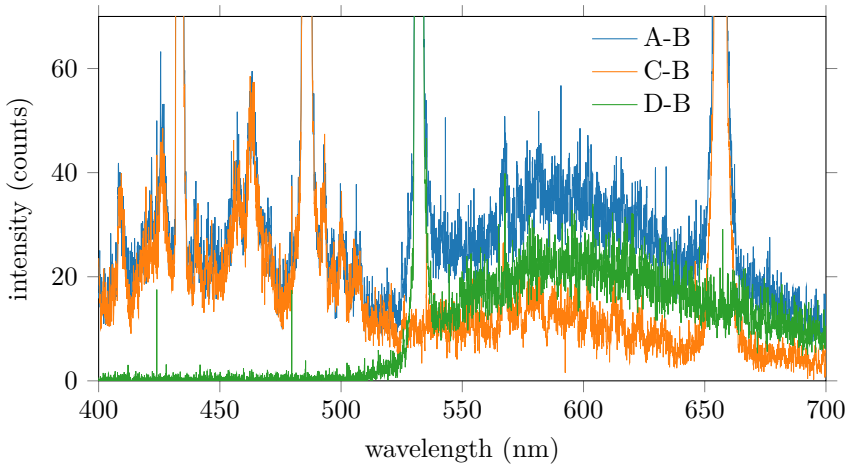

Figure 5.6: Illustration of the various sources of stray-light obtained from the subtraction of the electronic background (record—B) from the records acquired with: both the laser and plasma turned on (blue line), only the laser (orange line) and only the plasma (green line).

strong enough Thomson scattering signal at the observation position.

Despite the proximity between the observation and resonance positions, the observation of a Thomson scattering signal remained complicated. First, discharge conditions with low and steady reflected power were sought. This criterion proved to be insufficient to find plasma conditions with high density. instead, a method based on the search for discharge conditions with strong emission lines was used to identify conditions associated with the highest plasma density. When H_2 was used, the signal from the Balmer lines was observed. When other gases were used, the signal from emission lines of ionized species was observed.

For experimental conditions with high emission line intensities, we observed a slow decay of plasma emission when the power supply was turned off. This phenomenon was particularly pronounced for conditions with lower pressure inside the plasma chamber. The long-lived afterglow can be explained by the presence of highly energetic electrons (in the keV range) whose lifetime is much higher due to their low collision frequency [176]. This observation is another indication of the efficient energy transfer from the RF wave to the plasma.

The low signal from Thomson scattering obtained with this plasma source can be attributed to the low frequency of the RF wave used to heat the plasma. The resonance position being in the middle of the plasma chamber, the plasma wave has to propagate through the part of the plasma upstream of the resonance position. To do so the plasma density has to remain low enough for the plasma frequency (ω_p) to remain below the frequency of the RF wave(ω_{RF}). If this ordering is not respected, the RF wave is reflected before it reaches the resonance position. From this criterion, the critical electron density can be defined with the following formula

$$n_e = \frac{m_e \varepsilon_0 \omega_{RF}^2}{e^2} \tag{5.3}$$

This equation shows that the critical electron density rises with the square of the frequency of the wave used. At 2.45 GHz it gives a critical density of approximately $7.4 \times 10^{16}\,\mathrm{m}^{-3}$.

5.3 Results

As mentioned previously, the Thomson signals analyzed were obtained after the subtraction of the various sources of stray-light. This subtraction procedure is illustrated in Figure 5.6. In spite of the large stray-light contributions, the spectral distribution from Thomson scattering can be isolated. For the example shown, the Gaussian fit applied to the spectral range analyzed gives n_e=$(3.2 \pm 0.3) \times 10^{16}\,\mathrm{m}^{-3}$ and T_e=(5.3 ± 0.9) eV. For all the investigations of this chapter, no significant spectral shift of the spectra was observed. For this reason, the electron drift velocity estimated will not be presented.

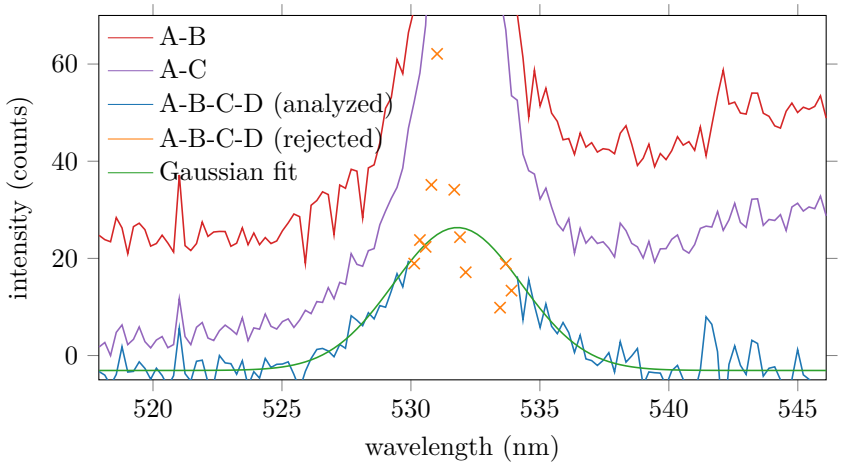

Figure 5.7: Illustration of the progressive subtraction procedure, from the raw spectrum with only the electronic noise subtracted ("A-B") to the spectrum obtained from the full noise subtraction "A-B-C-D". The Gaussian fit applied for electron properties estimation is shown with a green line.

5.3.1 With H_2 gas

5.3.1.1 Temporal exploration

As mentioned previously, before Thomson scattering investigations, we looked for discharge conditions with strong emission lines. The spectrograms shown in this section were obtained for discharge conditions giving emission lines with the maximum intensity. To record these spectrograms, different parameters of the detection branch from those used for Thomson investigations were used. A spectrometer slit width of 50 µm, a gating time of 1 µs, and the 600 lines mm^{-1} grating were used. With these experimental conditions, the signal from plasma emission was strong enough that neither pixel binning along the spectral direction nor long accumulation (only 60 exposures $frame^{-1}$) were required. For H_2, we examined the spectral range from 407 nm to 435 nm.

Low pressure

Figure 5.8 shows the spectrogram of the plasma emission spectrum obtained with 470 W of RF power and for the lowest operable pressure of dihydrogen (estimated to 8.3×10^{-3} Pa). Two groups of emission lines are visible inside the spectral range examined, each exhibiting different temporal behavior:

- The intensity of the two lines at 410 nm and 434 nm increases slowly during the first 1 ms of the RF pulse. The intensity of these lines reaches a plateau during the rest of the pulse and then decreases quickly at the end of the pulse. The wavelengths of these lines correspond to the H-γ and H-δ transition of the Balmer series of the hydrogen atom [177].

- The intensity of the lines from 414 nm to 428 nm reaches its maximum value 0.14 ms after plasma ignition. The intensity decreases progressively from 0.14 ms to 1 ms before reaching a stable value for the remaining time of the pulse. Similar to the Balmer lines, the intensity of these lines decreases steeply in the afterglow. The shape and spectral position of these lines indicate that they belong to the (6-0) vibrational band of the dihydrogen molecule [178, 179].

The temporal variations of these emission lines intensities can be explained by the progressive dissociation of H_2 molecules. At ignition of the plasma, the H_2 dissociation degree is low, such that the probability for electron collisional excitation is high. This leads to numerous rovibrational emission lines. Once the plasma ignited, the H_2 dissociation degree is expected to be higher due to processes such as electron impact dissociation. As a result, the density of hydrogen atoms is expected to be higher, along with the intensity of atomic hydrogen lines.

The temporal profile of the electron density, temperature, and reflected RF power is shown in Figure 5.9. Both electron density and temperature reach a steady value once the reflected power becomes

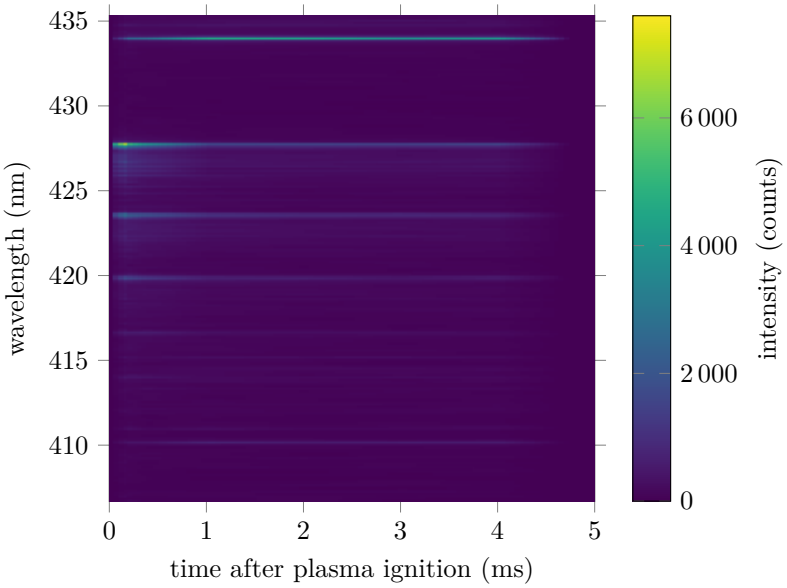

Figure 5.8: Spectrogram obtained during the 5 ms of the RF pulse. The instantaneous RF power and the dihydrogen pressure were respectively 470 W and 8.3×10^{-3} Pa.

negligible. At ignition and extinction of the plasma, electron properties vary rapidly. The temporal resolution required to probe these dynamics was usually too high to be accessible. This relatively low temporal resolution comes from the timing jitter at plasma ignition and extinction, which prevented temporal resolution below 30 µs. As shown in Chapter 4 temporal resolution down to 1 µs was achieved with sufficiently stable planar magnetron discharges.

The values of plasma density estimated remain below the critical electron intensity required for RF wave propagation (7.4×10^{16} m^{-3}). The relatively high electron temperatures estimated can be explained by both the large electron energy required for electron impact ionization of hydrogen atoms (13.6 eV) and the low operating pressure. As suggested by the presence of a long-lived afterglow (persisting for tens of seconds), a population of electrons with energies in the keV range (with much lower collision frequency than the bulk electrons) may be present for this low operating pressure. The associated spectral range and intensity level of the corresponding Thomson signal cannot be detected with the current configuration of the THETIS diagnostic.

The order of magnitude of both electron parameters and operating pressure allow the estimation of the ionization degree. For the experimental conditions presented in this section, we estimated an ionization degree on the order of 2.5 %. A higher ionization degree may have been obtained by reducing the operating pressure. Lower pressures were not investigated due to the limitation of the pumping speed as well as the impossibility for the mass flow controller to deliver a steady flow of H_2 below 1.78 µg s^{-1} (the flow rate for which the pressure inside the plasma chamber was estimated at 8.3×10^{-3} Pa).

High pressure

The operation of the discharge at higher pressure was usually more challenging in pulsed mode with H_2. Stable operating conditions with a plasma chamber pressure of 3.3 Pa were obtained at 470 W of incident RF power. The spectrogram of the plasma emission for these discharge conditions is shown in Figure 5.10 and Figure 5.11. As shown in Figure 5.10, the Balmer lines intensities are more than twice higher than at 8.3×10^{-3} Pa, which can be explained by the higher density of neutrals leading to a higher density of hydrogen atoms. In contrast, the intensity of the vibrational bands is one order of magnitude lower than at low pressure. The adapted intensity range of Figure 5.11 eases the observation of these lines. One possible explanation of this decreased intensity could be the lower density of energetic electrons which have a higher cross-section for excitation of the vibrational levels [180, 181]. The THETIS diagnostic is insensitive to the corresponding energy range, however, the absence of the long-lived afterglow for this higher pressure is an indication of the lower density of energetic electrons.

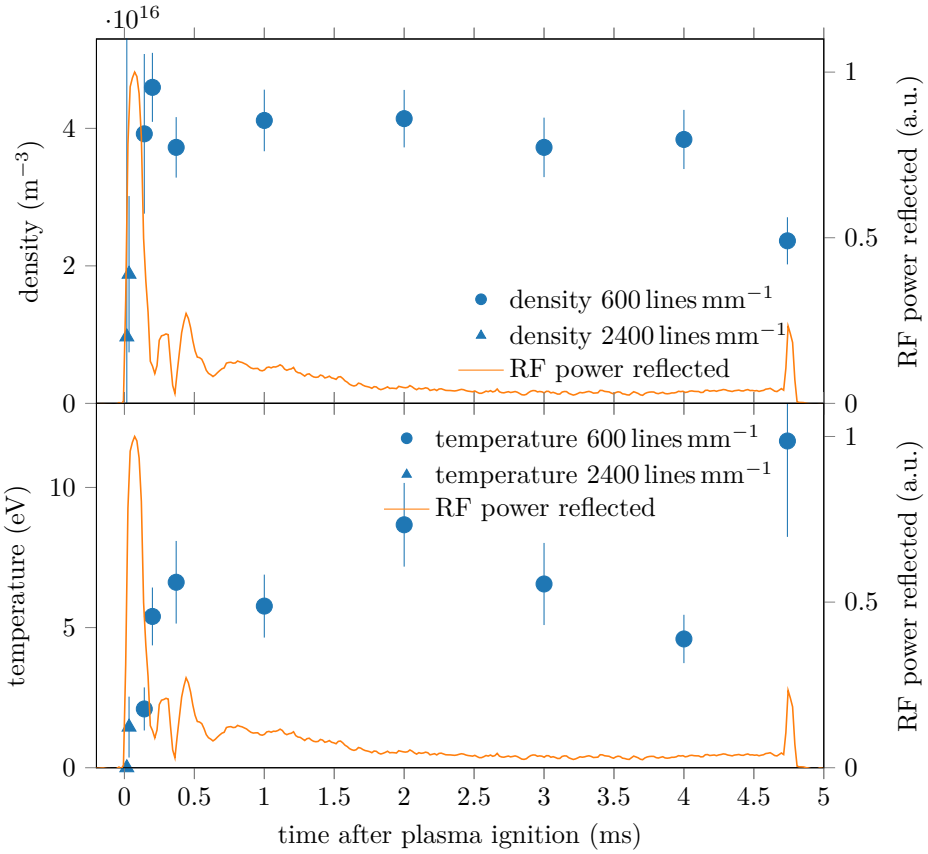

Figure 5.9: Temporal profile of electron density and temperature during the RF pulse. An indication of the reflected RF power is shown with an orange line. The dihydrogen pressure inside the plasma chamber was estimated at 8.3×10^{-3} Pa.

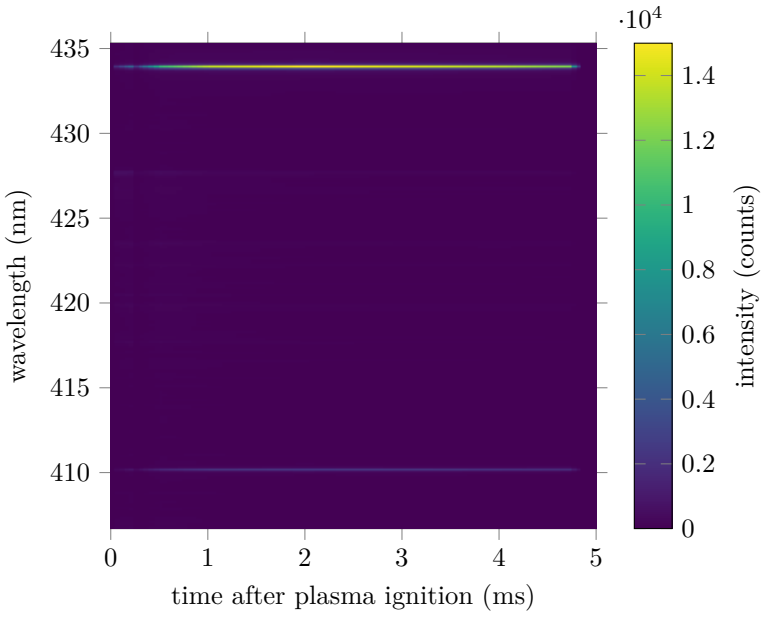

Figure 5.10: Spectrogram obtained during the 5 ms duration of the RF pulse. The instantaneous RF power and the dihydrogen pressure were, respectively, 470 W and 3.3×10^{-2} Pa.

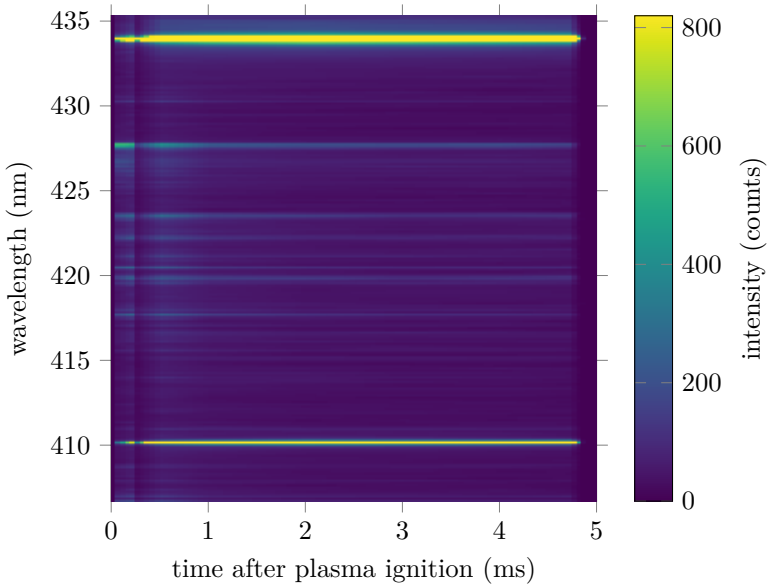

Figure 5.11: Spectrogram obtained during the 5 ms duration of the RF pulse. The instantaneous RF power and the dihydrogen pressure were, respectively, 470 W and 3.3×10^{-2} Pa. The intensity range was adapted to the intensity of the vibrational lines.

The temporal profile of the electron density, temperature and RF reflected power are shown in Figure 5.12. The trend of these temporal profiles is almost identical to the case at low pressure. However, the absolute value of electron density is slightly lower than in the low-pressure case while the temperature of the electron population probed is almost unchanged. This observation suggests a more efficient transmission of the RF power to the plasma or a more efficient diffusion of the plasma to the observation volume when the density of neutrals is lower.

5.3.1.2 Parametric exploration in DC mode

For parametric explorations, the plasma discharge was operated in DC mode. This operation mode, while not typical for the plasma source, simplified the exploration by removing the temporal parameter. It also allowed a broader range of discharge conditions to be investigated due to the increased efficiency of the automatic stub-tuner for impedance matching.

Pressure exploration

Pressure explorations were performed for a fixed RF power of 180 W. During this investigation, the plasma could be operated from 2.6×10^{-2} Pa to 0.12 Pa. In contrast to the pulsed mode, the discharge was not stable in the DC mode for pressures in the 10^{-3} Pa range. However, in the DC mode, the values of capacitance used for pressure estimation may no longer be not relevant due to the increased gas temperature that may be induced by the steady heating of neutrals by the plasma. As shown in Figure 5.14, the plasma expands through the orifice and may also contribute to the modification of its conductance.

The electron property dependence with the H_2 power is summarized in Figure 5.13.
The electron density firstly increases with the pressure, however, it rapidly stabilizes at a plateau around 3×10^{16} m^{-3} despite the higher density of neutrals available. The electron temperature peaks at low pressure (4×10^{-2} Pa) and stabilizes at a plateau around 4 eV for higher pressures.
Similar behavior of electron properties was reported in a previous study [182]. In this study, the authors describe an electron density increasing at low pressure but reaching a plateau at higher pressure, and also report a peaked electron temperature at low pressure followed by stabilization around lower values. However, the absolute values estimated are quantitatively different. From their investigation, they reported a density one order of magnitude higher and temperature twice lower. The difference in the

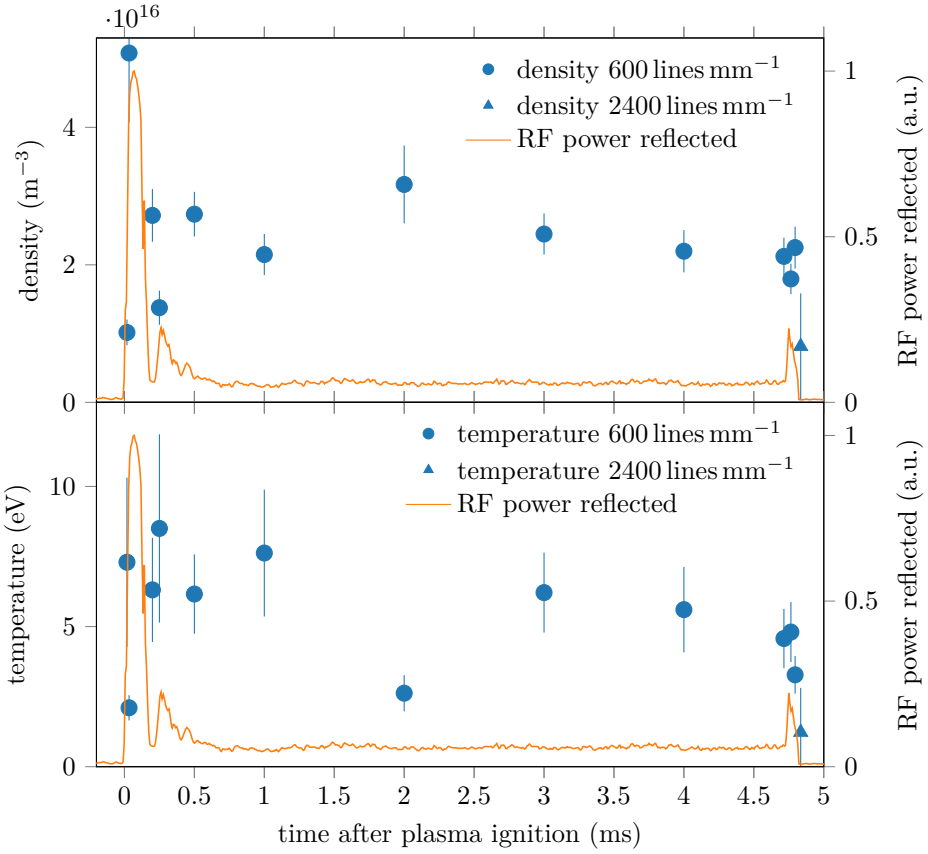

Figure 5.12: Temporal profile of electron density and temperature during the RF pulse. An indication of the reflected RF power is shown with an orange line. The dihydrogen pressure inside the plasma chamber was estimated at 3.3×10^{-2} Pa.

estimated density may arise from the different methods used for calibration of the transmission factor of the detection branch of the diagnostic. While Rayleigh scattering was used for the previous study, Raman scattering was used for the calibration of our THETIS diagnostic.

RF power exploration

RF power explorations were performed at a fixed pressure of 5.2×10^{-2} Pa. The power delivered by the RF source was varied from 100 W to 600 W. Inside this range, the plasma discharge was stable enough for accumulation over 6000 laser pulses. At lower pressures, the discharge was stable over a smaller range of powers.

The electron property dependence with the RF power is summarized in Figure 5.15. The electron density increases with power, except at the lowest power used, where a peak is observed. The electron temperature also increases with power; the apparent presence of the peak at 340 W has to be considered in the context of the larger uncertainty estimated at this point. This increased uncertainty arises mainly from the poorer quality of the fit convergence, due to noisier data. This was sometimes observed due to the high temperatures in the experiment room that sometimes led to fluctuations of the CCD camera temperature. The qualitative trend in the electron properties is again consistent with results from a previous study [182], however, the measurements diverge quantitatively.

5.3.2 Temporal explorations with monatomic gases

From investigations with dihydrogen, we observed, by monitoring the emission spectrum, that excitation of the vibrational level of the molecule plays a significant role in the ignition of the discharge. With

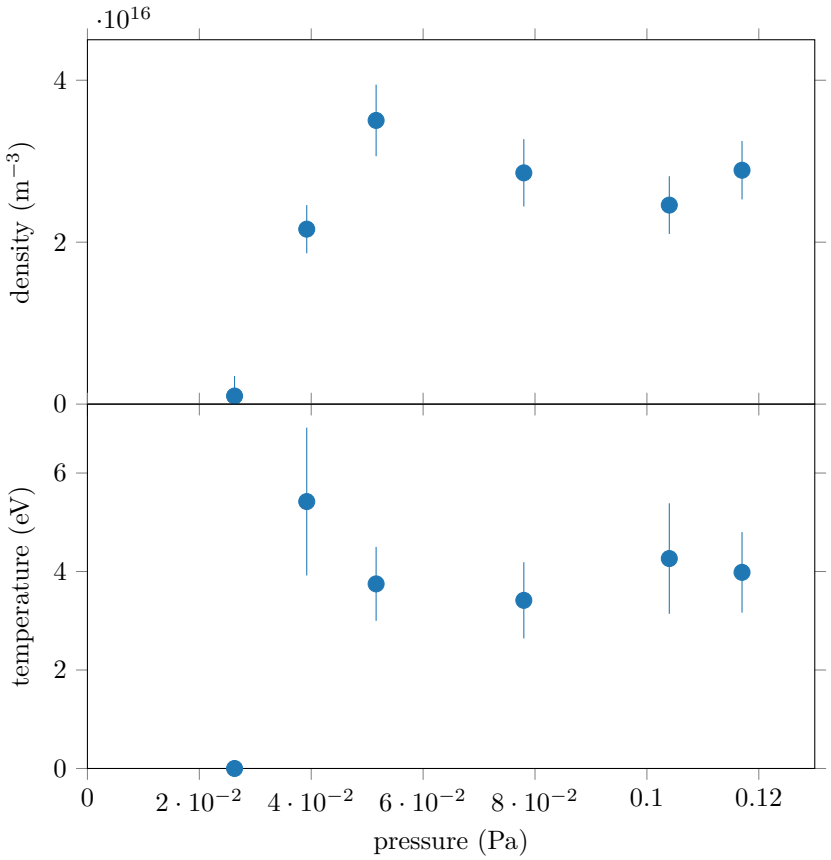

Figure 5.13: Variation of electron density and temperature for varying pressure and fixed RF power of 180 W.

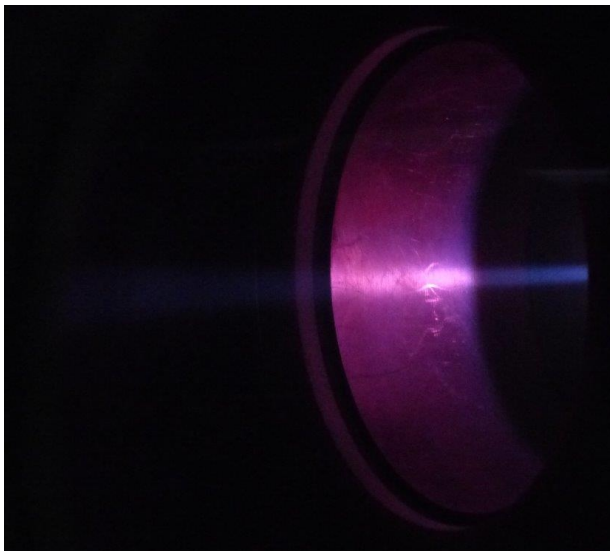

Figure 5.14: Plume of the ECR plasma generated by its expansion through the orifice of the plasma chamber. This plume is observed through a viewport located on the pumping column.

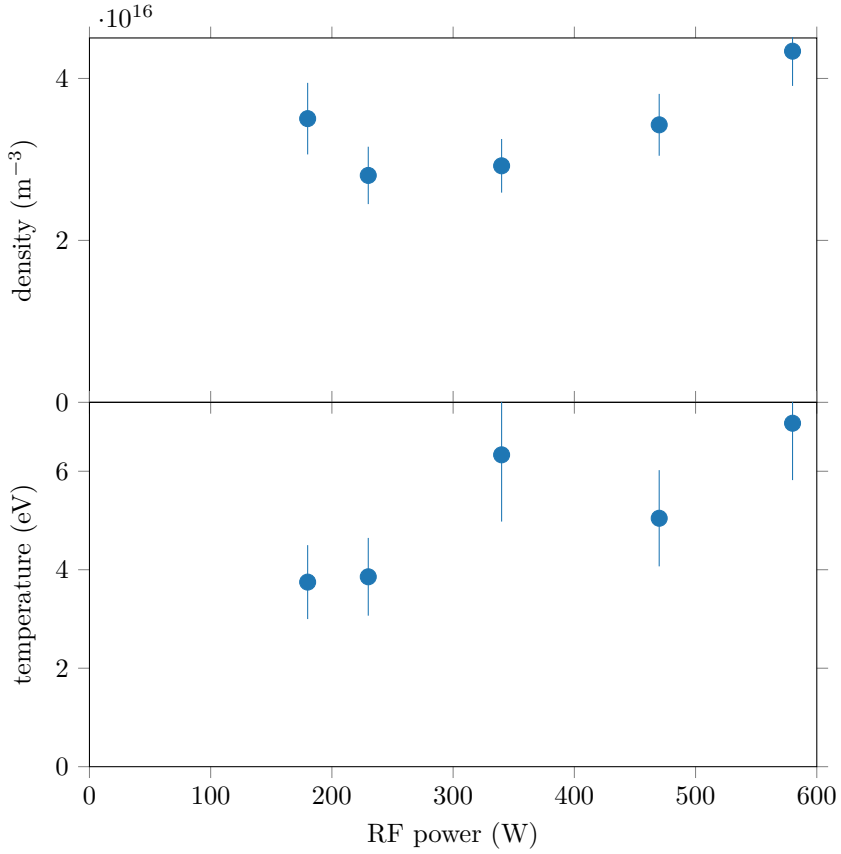

Figure 5.15: Variation of electron density and temperature for varying RF power and a fixed pressure of 5.2×10^{-2} Pa.

monatomic gases, the ignition process is expected to be simpler as no energy is lost in vibrational excitation. For comparison with the temporal explorations performed with H_2, we investigated the plasma discharge with He and Ar gases under the same RF power and with similar pressure levels.

5.3.2.1 With He gas

Figure 5.16 shows the spectrogram of the ECR plasma operated with helium, with incident power of 470 W and a pressure of 4.0×10^{-2} Pa. The spectrogram is centered around a strong line of helium atoms at approximately 588 nm. The faster increase of the atomic emission line compared to the dihydrogen study shows that vibrational excitations act as a buffer to the ignition of the discharge.

The steeper ignition is also visible on the temporal profile of electron properties estimated from Thomson scattering and shown in Figure 5.17. Both the electron temperature and density seem to reach their steady value faster than with H_2. Still, the time resolution is not high enough allow comparison of the characteristic times for ignition. The instability at ignition is expected to arise from the RF power supply. More stable discharges are expected using solid-state RF generators.

The steady values of electron density are on the same order of magnitude as for H_2. However, the electron temperature reaches a value around 10 eV, almost twice the value obtained with H_2. This higher value can be explained by the higher ionization energy of helium (first ionization at 24.6 eV) and the absence of vibrational modes to excite.

5.3.2.2 With Ar gas

The plasma discharge was operated with argon at 4.6×10^{-2} Pa and under the same RF power of 470 W. One surprising feature observed with these discharge conditions was the fast ignition of the plasma followed by weak plasma emission for the rest of the pulse.

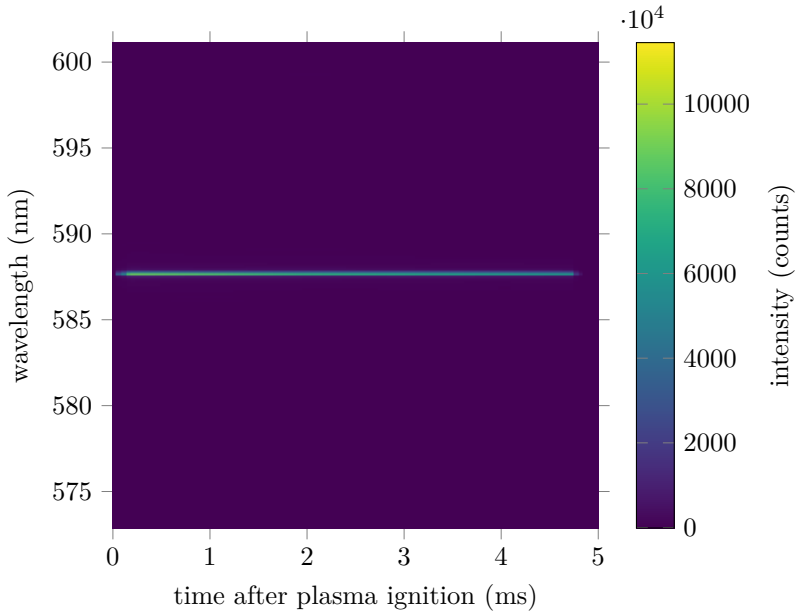

Figure 5.16: Spectrogram obtained during the 5 ms duration of the RF pulse. The instantaneous RF power and the helium pressure were, respectively, 470 W and 4.0×10^{-2} Pa.

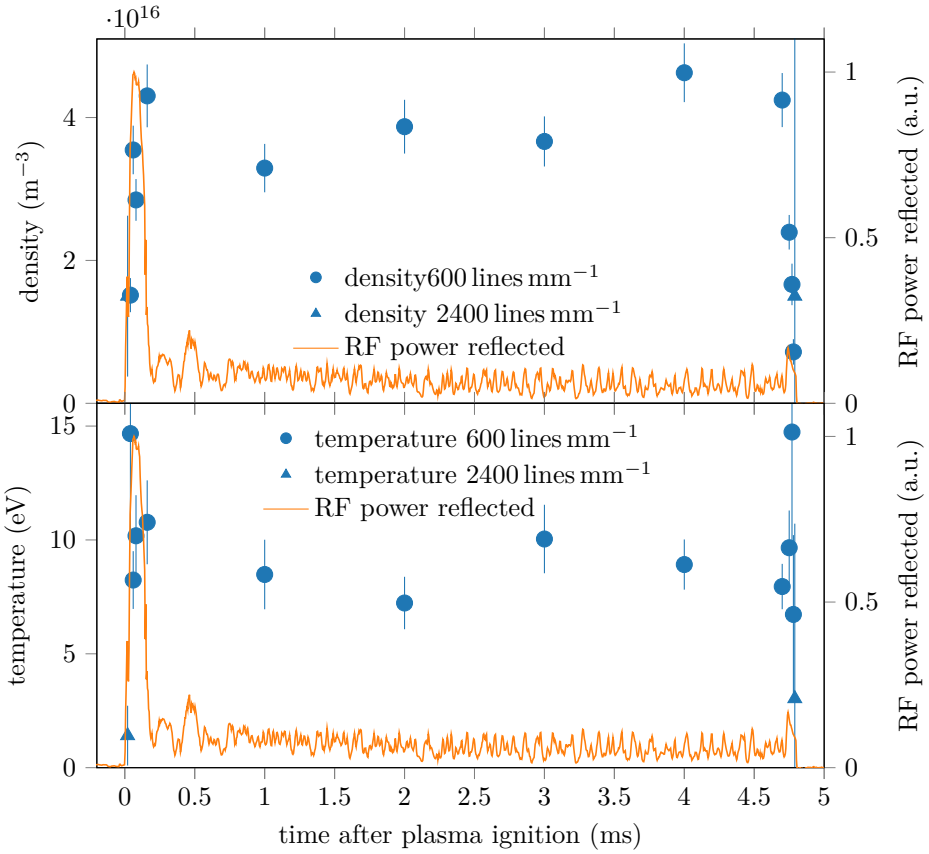

Figure 5.17: Temporal profile of electron density and temperature during the RF pulse. An indication of the reflected RF power is shown with an orange line. The helium pressure inside the plasma chamber was estimated at 4.0×10^{-2} Pa.

The electron properties estimated are shown in Figure 5.18. The presented profile focuses on the first 150 µs of the 5 ms-long RF pulse. At longer times inside the pulse, the signal from Thomson scattering was too low to be detected. As shown in Figure 5.18, both the electron density and temperature peak at their maximum value approximately 40 µs after the rising front of the RF power. The instant of these peak values correlates with a dip in the temporal profile of the reflected RF power. This might indicate that for this short duration, the coupling between the RF and the electrons of the plasma was optimal. This optimal coupling happens while the RF power is still on its rising edge (the RF generator has a typical rise time of 50 µs). However, later in the pulse, the estimated density and temperature decrease exponentially below the detection threshold of our diagnostic, despite the higher steady power available. Surprisingly, 1 ms after ignition the reflected RF power drops progressively to an unstable plateau. This indicates that some of the power is still absorbed by an electron population that may have a characteristic temperature or density outside the sensitivity of our diagnostic.

The absolute value of electron densities reached with these experimental conditions is the highest ever measured on the ECRIN source, nearly reaching the critical electron density value and more than twice that for H_2 at similar pressure (see Figure 5.12). The estimated value is an average value over 6000 pulses; the density may overshoot the critical density for a short duration that cannot be resolved given the actual jitter at ignition. The overshoot of the critical density may play a role in the temporal trend that follows. In contrast to the density, the temperature remains low with Ar, reaching 2.5 eV at maximum and decreasing sharply after this maximum. The use of the more dispersive 2400 lines mm^{-1} grating was required for accurate estimation of the temperature.

The higher density achievable for Ar than for He may be attributable to its lower ionization energy. Though the first ionization energy of H_2 is close to Ar, the covalent bond of H_2 may absorb energy in its vibrational modes without ionization, resulting in a lower density. The low electron temperatures seen with Ar (lower than both He and H_2) may be due to a combination of electron cooling from inelastic electron-argon atom collisions and ionization events.

5.4 Conclusion

In this chapter, we present the successful application of the THETIS diagnostic for studies of a type of ECR ion source used for the production of light ions for particle accelerators. It proves the feasibility of investigations of such a plasma source with Thomson scattering diagnostics. Measurement of electron density and temperature have been performed at a given position for different gases, pressures, RF powers. In pulsed mode, temporal profiles of electron properties were measured with temporal resolution on the order of 30 µs. For the experimental conditions used, the electron density estimated remained near the detection limit, in the range of $10^{16}\,\mathrm{m}^{-3}$. Electron temperatures were found to range from a few eV to nearly 15 eV.

To our knowledge, this implementation is only the second implementation of incoherent Thomson scattering on an ECR source. A previous study, performed on an ECR ion source used for plasma processing applications, reported a similar trend of electron properties as the ones we observed. However, the absolute values of the electron densities estimated in that study were significantly higher than those we estimated. The different methods used for calibration of the diagnostics might explain these discrepancies.

Plasma emission spectroscopy studies were also performed in order to better identify high-density regimes and obtain deeper insight into the ignition phase of the plasma. This study has shown interesting features with H_2 at ignition: a peak signal from vibrational emission was observed at ignition, followed by an emission spectrum dominated by Balmer lines during the rest of the pulse. More precise information on the dynamics of electron properties at ignition may be obtained with more stable RF power stable (using solid-state sources, for example). RF sources operating at higher frequency would increase the plasma density and ease the investigation of the ignition process.

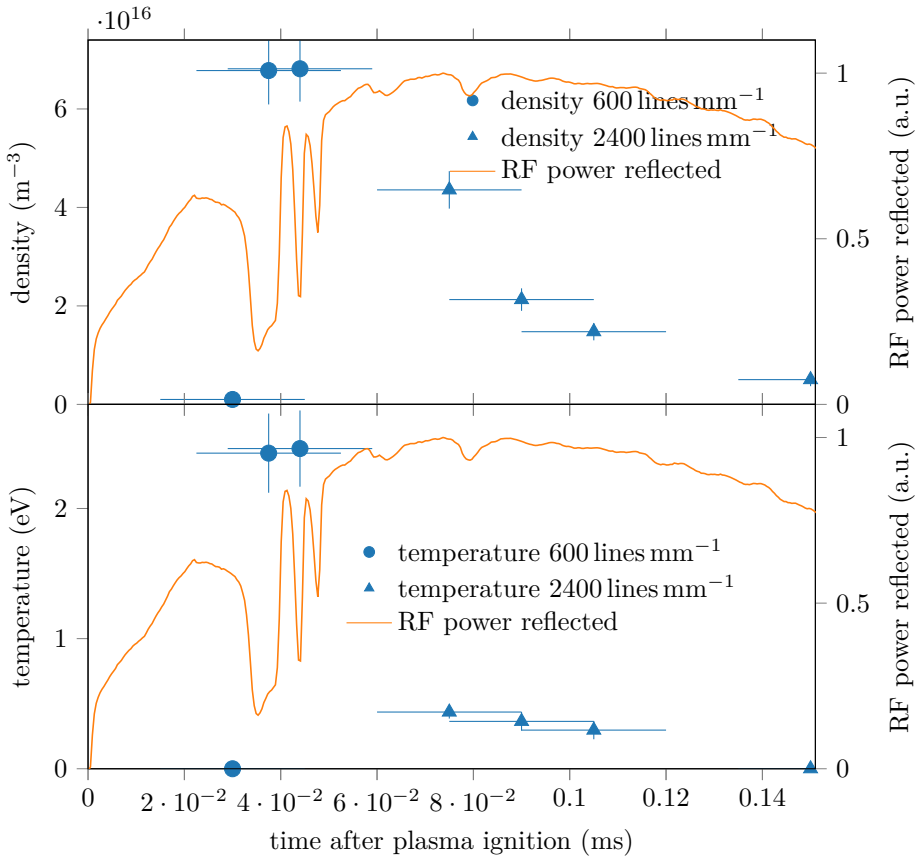

Figure 5.18: Temporal profile of electron density and temperature during the RF pulse. An indication of the reflected RF power is shown with an orange line. The argon pressure inside the plasma chamber was estimated at 4.6×10^{-2} Pa.

Chapter 6

Incoherent Thomson scattering investigations in the Hall thruster discharge

> The blue distance, the mysterious Heavens, the example of birds and insects flying everywhere –are always beckoning Humanity to rise into the air.
>
> — *Konstantin Tsiolkovsky, The Successes of Air Balloons in the XIX Century*

In this chapter, we present the results of the study of Hall thruster discharges with Thomson scattering. Results from this investigation gave information on electron properties along both the "azimuthal direction" and "radial direction", without perturbation of the plasma discharge. In particular, we investigated the influence of the magnetic field intensity, topology and direction. We observed anisotropic behavior of electron and clear deviations from thermal equilibrium in some operating regimes. Finally, we performed a study on the influence of the gas species used to sustain the discharge.

Contents

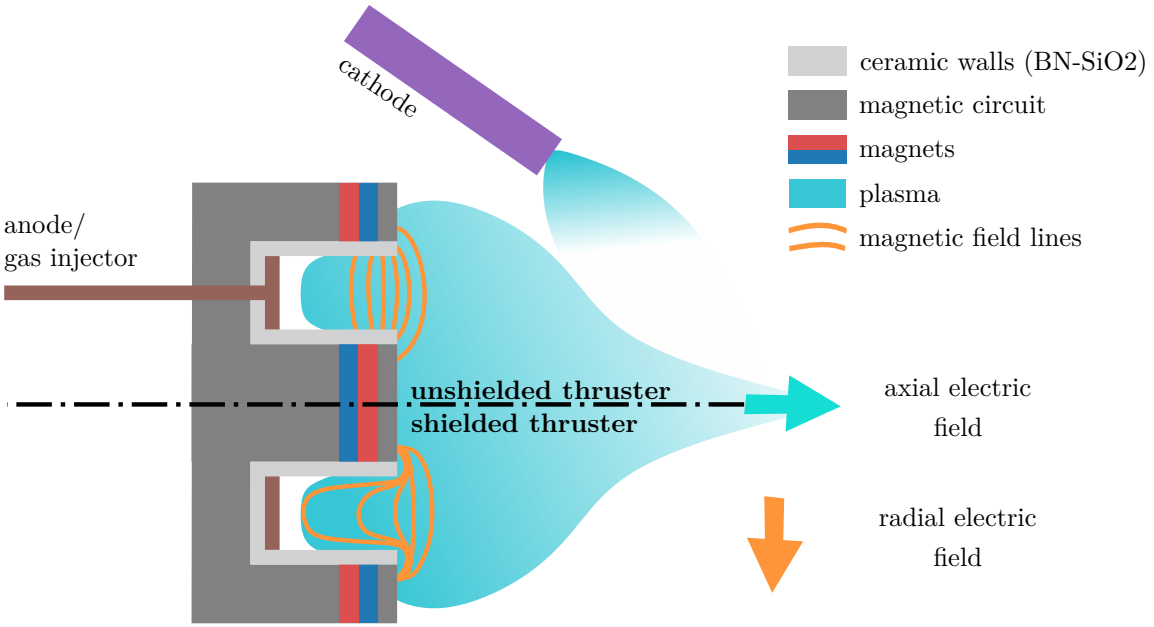

Figure 6.1: Hall thruster geometry and typical magnetic field line shapes for unshielded (top half) and shielded (bottom half) configurations.

6.1 Introduction

6.1.1 Motivation for Hall thruster technology

A Hall thruster is an electric propulsion device conceived and developed in the mid-1960s in the Soviet Union. This thruster operated for the first time in space aboard the USSR Meteor satellite in 1972 [20, 183–185]. Because of their relatively high thrust-to-power ratio ($\approx$50 mN kW^{-1}) and thrust density (>30 N m^{-2}), Hall thrusters have been used over the last decades for missions forgiving of the relatively low I_{sp} levels (<2000 s) [20] such as geosynchronous satellite attitude correction and station-keeping on telecommunications satellites. Despite the long flight heritage of these devices, an understanding of their underlying physics remains poor. Aspects such as multi-scale instabilities [186], non-Maxwellian electron velocity distribution functions [187, 188] and plasma-wall interaction through secondary electron emission [189–191] contribute to the complexity of Hall thruster physics. To date, simulations that can capture all aspects of such physics are lacking, though development efforts are underway in several research teams. Validation of these codes requires comparison of simulated electron properties with experimental values from accurate measurements.

Figure 6.1 illustrates the typical architecture of a Hall thruster. A potential difference applied between an anode, positioned at the back of a cylindrical channel, and a cathode, positioned outside the thruster channel, sustains the discharge. Injection of gas near the anode supplies the discharge with neutrals. Inert gases such as xenon or krypton are the most commonly used, mostly because of their relatively low first ionization energy and large atomic mass. The cathode is the element used to supply electrons to the discharge. The electron current delivered is produced from a heated thermo-emissive pellet, with BaO or LaB_6 crystals being the most commonly used materials because of their low work functions and robustness.

Electrons delivered by the cathode and accelerated toward the anode ignite the discharge. Because such plasma sources operate from low earth orbit, where the pressure is around 10^{-8} Pa, and in the interplanetary environment, where the pressure is typically below 10^{-14} Pa, the mean free path of the electrons are several meters long, such that the probability to ionize the gas injected near the anode is extremely low. To increase the ionization probability, an axisymmetric magnetic barrier, positioned near the exit plane of the thruster, traps electrons. This magnetic field of a few tens of mT is sufficiently large to magnetize electrons but too weak to influence ion trajectories. Because of the low mobility of magnetized electrons perpendicular to the radial magnetic lines, most of the potential gradient takes place in a restricted region where the magnetic field is the strongest. The variations of the magnetic field intensity along the radial and azimuthal directions are weak, and as a result the electric field is mainly along the axial direction of the thruster. Trapping of electrons in the axial direction is efficient. However, in the azimuthal direction, the strong $\vec{E} \times \vec{B}$ drift leads to a Hall current of electrons along this direction. Despite this strong drift, electrons have a large residence time in the magnetized region. Heated by the locally large electric field, they drift towards the anode and can efficiently ionize most of the neutrals upstream of the high electric field region. The ionized atoms are accelerated to speeds up to $30\,\mathrm{km\,s^{-1}}$ by the strong axial electric field. To prevent charge accumulation on the thruster and end the interaction of the accelerated particles with the electric field, the accelerated beam has to be neutralized. Part of the electron current delivered by the cathode guarantees beam neutralization. Typically, around 80 % of the cathode current is used to neutralize the ion beam while around 20 % goes toward the anode to sustain the ionization region.

Coils or magnets are used to generate the magnetic field. A magnetic circuit made of pure iron confines and shapes the magnetic field lines inside the thruster channel. To minimize sputtering, heat load, and short circuits of the electron current on the magnetic circuit, ceramic channel walls protect and insulate the magnetic circuit from the plasma. $BNSiO_2$ and BN are the most broadly used ceramics as they enable high thrust efficiency and long operational life [192].

The inherent limitations of the acceleration of particles with electric thrusters are fundamentally different from the ones encountered with chemical thrusters. For chemical thrusters, the propellant holds the source of energy use for acceleration. This propulsion relies on the use of the standard enthalpy of a chemical reaction between the propellants; the energy dissipated heats the products of the reaction and accelerate these products with an expansion through a nozzle to generate thrust. For this reason, the intrinsic limitation on the exhaust speed arises from the maximum chemical energy stored per unit mass of propellant.
In contrast, electric thrusters have the advantage of separating the energy source (electric power) from the propellant (usually a heavy noble gas for Hall thrusters). As a result, the upper limit for the exhaust velocity of the accelerated particles is the speed of light, in theory. In practice, the limitations arise from the electric power available on the spacecraft and the time required to perform a maneuver. For a fixed available electric power and without consideration of the conversion efficiency, the product between the thrust and the I_{sp} (proportional to the exhaust velocity) is constant. For example, for an I_{sp} of 1500 s (typical for Hall thrusters) and with approximately 10 kW of electric power available onboard for propulsion, we can only reach a thrust of approximately 0.5 N at best. This thrust level is at least two orders of magnitude below what most chemical thruster technologies can achieve. Still, when operated over long times, electric thrusters become interesting for maneuvers accepting longer times to change the spacecraft velocity.

The equation that gives the change of velocity (Δv) (in case of no external forces) as a function of the exhaust velocity (v_e), allows a better understanding of the advantage of electric propulsion. This famous equation, named the Tsiolkovsky ideal rocket equation, is expressed as

$$\Delta v = v_e \ln\left(1 + \frac{m_p}{m_f}\right) \tag{6.1}$$

where m_p is the mass of propellant consumed for the velocity change and m_f the mass of the spacecraft after the velocity change. The inversion of this equation shows an exponential decrease of the propellant proportion of the initial spacecraft mass to achieve a given Δv. For commercial and scientific missions the mass savings can either be used to reduce mission costs or to increase the instrumentation mass on the spacecraft.

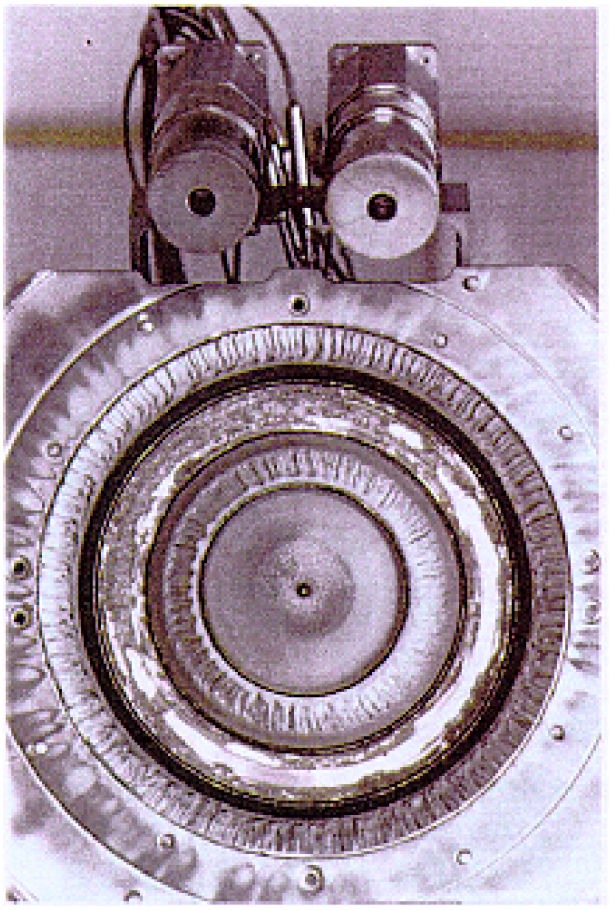

Figure 6.2: Erosion as seen on the PPS-1350 thruster after 3500 h of operation [1].

6.1.2 Magnetic configurations

In the last section, we have shown that Hall thrusters can compete with chemical thrusters for a broad range of contemporary missions that do not require fast maneuvers. The application of Hall thrusters to long duration missions makes their robustness an important issue. As shown in Figure 6.2, despite the use of resistant materials for channel wall protection, erosion from ion sputtering remains important and can constitute one of the main failure mechanisms of many Hall thrusters. More sputter-resistant materials may be used, however they result in lower performance [192]. Shaping the magnetic field lines is the most efficient way to mitigate erosion without signification degradation of performance.

Most Hall thrusters have been operated in the so-called standard configuration. The typical magnetic field lines of this configuration, shown in the top part of Figure 6.1, are associated with a relatively basic magnetic circuit design. With this configuration, the magnetic field lines are perpendicular to the channel walls near the exit plane and result in an electric field almost tangent to the walls. This configuration does not prevent the electrons from reaching the walls. Near the exit plane, in response to the high electron temperature, a strong sheath builds to compensate for the high flux of electrons. Near the walls, ions accelerated by the high electric field of this sheath impact the walls and contribute to the strong erosion rate for a standard configuration. Figure 6.1 illustrates significant erosion observed with these configurations after several thousands of hours of operation.

In 2010 researchers at NASA-JPL developed a new design for the Hall thruster magnetic configuration [26]. With this configuration, named “magnetic shielding”, the magnetic field lines adopt a shape similar to that shown in the bottom part of Figure 6.1. The main feature of this configuration relies on the shaping of the magnetic field direction near the wall. This requires specific methods not shared publicly. The so-called “grazing line” is characteristic of this configuration and is tangent to the channel wall in the regions of high electron temperature (as shown with the magnetic field line close to the anode in the bottom part of Figure 6.1). This configuration induces a radial electric field near the wall that increases

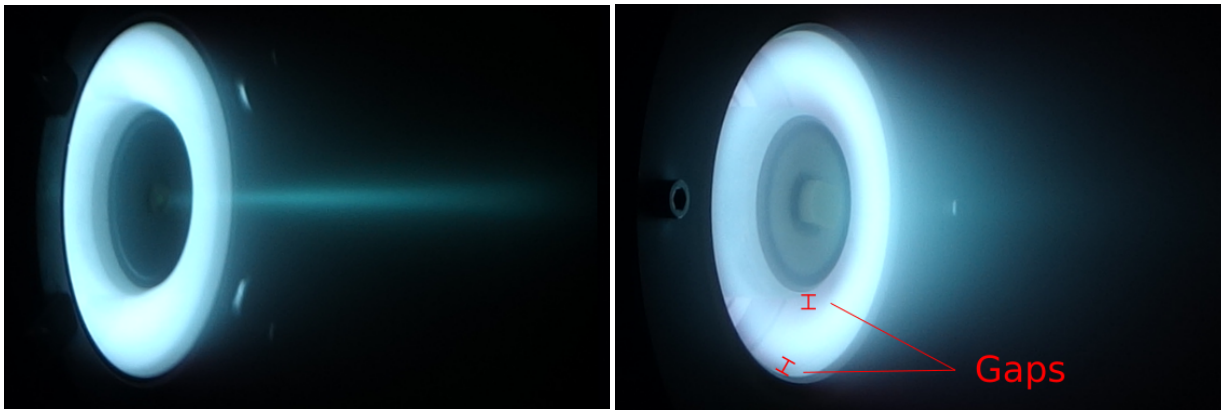

(a) (b)

Figure 6.3: Typical shape of the plasma for a Hall thruster in (a) standard configuration and in (b) "magnetic shielding" configuration.

the confinement of the plasma in the center of the channel. Moreover, the grazing line reaches the region near the anode, where it is believed that this cold region of the plasma can mitigate the temperature of electrons magnetized along this field line. This translates into a colder electron temperature along the magnetic field line near the walls of the channel and consequently a weaker sheath. Both of these phenomena lead to a significant decrease of channel erosion which may even disappear entirely once the steady-state erosion configuration is achieved [193]. With this configuration, the design of Hall thrusters with operation lifetimes exceeding 10 000 h is easier. For Hall thrusters in the kW range and above, studies report a negligible impact of the shielding configuration on performance.

The consequences of the magnetic field configuration can be observed from the shape of the plasma. As shown in Figure 6.3a, the discharge of a standard Hall thruster shows a plasma in contact with the channel wall. In contrast, as shown in Figure 6.3b, a gap is visible between the bulk plasma and the walls for the discharge of a Hall thruster in "magnetic shielding" configuration [193]. This observation suggests the absence of a dense plasma near the wall. The decreased ionization in these regions is considered to be one of the explanations for the poorer propellant utilization observed in small Hall thrusters with a "magnetic shielding" configuration [194].

6.1.3 Previous work on electron property investigations

Until now, most measurements of electron properties in Hall thrusters used Langmuir probes [29, 195–197] or optical emission spectroscopy [45, 46, 198, 199]. Such techniques are adequate for far plume measurements, however, their application in the acceleration region of the Hall thruster plasma has limitations [37]. The expected high electron densities and temperatures and the relatively strong magnetic fields in this region complicate signal measurement and interpretation.

As with the planar magnetron, it is worth highlighting recent efforts on implementing THz-TDS for the investigation of electron properties inside a Hall thruster [200]. This technique gives only line-integrated values of the electron density. The possibility of transmitting the probe beam across the ceramic channel walls compensates for the limitation of resolution. Such an implementation would allow the estimation of the electron density profile at positions upstream of the exit plane, without modification of thruster design.

Thomson scattering applied to Hall thrusters offers the possibility for unambiguous and perturbation-free measurement of electron properties. The challenge associated with this technique is the high diagnostic sensitivity required for the measurements of low densities encountered in Hall thruster plasmas. In the coherent regime, Thomson scattering has already proven to be an efficient technique to measure electron density fluctuations in such plasmas. The PRAXIS diagnostic [94] was the first CTS diagnostic ever implemented on a Hall thruster. In the incoherent regime, Thomson scattering allows the measurement of thermal properties of electrons. Recent studies by Washeleski [201, 202] have shown that the application of this technique is possible in Hall thrusters, but the low signal levels and large stray-light intensities

make its application challenging. An alternative Thomson scattering diagnostic, named CETS (Cavity Enhanced Thomson Scattering), aims at increasing the Thomson scattering signal with the buildup of the incident laser power inside an optical cavity [203]. A first implementation on a hollow cathode gave encouraging results [204], and optimizations for Hall thruster studies are in progress.
For all Thomson scattering diagnostics, investigations of electron properties inside the thruster channel would require significant modifications of the thruster design to transmit and collect light. These modifications might lead to even higher levels of stray-light from reflections.

6.2 Experimental setup

6.2.1 Test facility

Experiments were performed in the NExET (*New Experiments in Electric Thrusters*) vacuum chamber at ICARE. This chamber is a stainless steel cylinder 0.7 m in diameter and 1.7 m in length, equipped with a primary dry pump, turbomolecular pump, and cryogenic pump. The pumping assembly achieves a base pressure of 10^{-4} Pa and operating pressure below 2×10^{-2} Pa with a xenon mass flow rate up to $2.5\,\mathrm{mg\,s^{-1}}$. An SM1500 Delta Elektronika DC power supply sustains the discharges with a fixed voltage. A 0.5–1.0 W Stangenes current transformer probe is used to measure the discharge current. A LeCroy HDO6104 digital oscilloscope is used to monitor the discharge current fluctuations.

6.2.2 Plasma sources

Incoherent Thomson Scattering (ITS) measurements were performed on two 200 W Hall thrusters of the ISCT200 (*ICARE Small Customizable Thruster 200W*) type: the ISCT200-GEO and ISCT200-MS. Both thrusters, equipped with $BNSiO_2$ channels, have the same channel width and mean diameter characterized by the geometry referred to as "$2S_0$" in previous publications [205]. The so-called "$2S_0$" geometry corresponds to a configuration with a channel width to diameter ratio twice as large as the usual value. In this paper, the thrusters were operated with either a xenon or krypton flow injected upstream of the anode through a porous ceramic.

The ISCT200-GEO has been extensively studied at the ICARE laboratory [206]. It has a standard magnetic field topology, achieved using an assembly of permanent magnets, with the maximum field intensity at the center of the channel and inside the exit plane. Varying the number of magnets of the internal and external magnetic circuits allows modifications of the magnetic field intensity. We used three peak magnetic fields in this study: B_{low} (15 mT), B_{mid} (25 mT) and B_{high} (31.5 mT). Figure 6.4a shows a photo of the ISCT200-GEO. The upper half of Figure 6.1 illustrates the typical profile of the magnetic field lines for this thruster.

The ISCT200-MS has been studied in recent years [207, 208] and has a magnetic circuit designed for "magnetic shielding". The magnetic shielding concept has recently extended to miniature Hall thrusters (in the 300–500 W range) by Conversano and colleagues [209]. While this configuration is designed to reduce channel erosion [210], a side effect is the slight shift of the maximum magnetic field position downstream of the exit plane. In this work, we discuss measurements on such a thruster with a peak magnetic field of 15 mT (B_{low}). Figure 6.4b shows a photo of the ISCT200-MS and the lower half of Figure 6.1 illustrates the typical magnetic field line shape of this shielded thruster.

Both thrusters were operated with a 5 A MIREA-type hollow cathode equipped with a LaB_6 emissive element heated with 130 W of power. The cathode was operated with a gas flow rate of $0.2\,\mathrm{mg\,s^{-1}}$ of the same gas species injected near the thruster anode (xenon or krypton).

The laser beam position and the position of the thruster along the y-axis were kept fixed. Translation of the thruster along the x-axis (Figure 6.6) allowed axial exploration of electron properties. Displacements along the z-axis were used to switch between the azimuthal and radial scattering configurations.

6.2.3 The THETIS diagnostic

Chapter 3 gave a full description of the THETIS diagnostic design and the procedure for Thomson spectrum acquisition. This section focuses only on the specificities related to its implementation for Hall thruster investigations. A picture of the implementation of the THETIS diagnostic on the NExET vacuum chamber is shown in Figure 6.5.

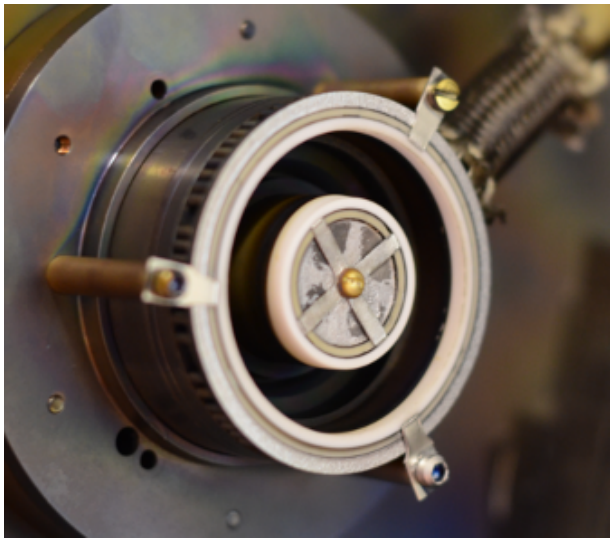

(a) The ISCT200-GEO Hall thruster (unshielded, standard)

(b) The ISCT200-MS Hall thruster (shielded)

Figure 6.4: Hall thruster models used for ITS investigations.

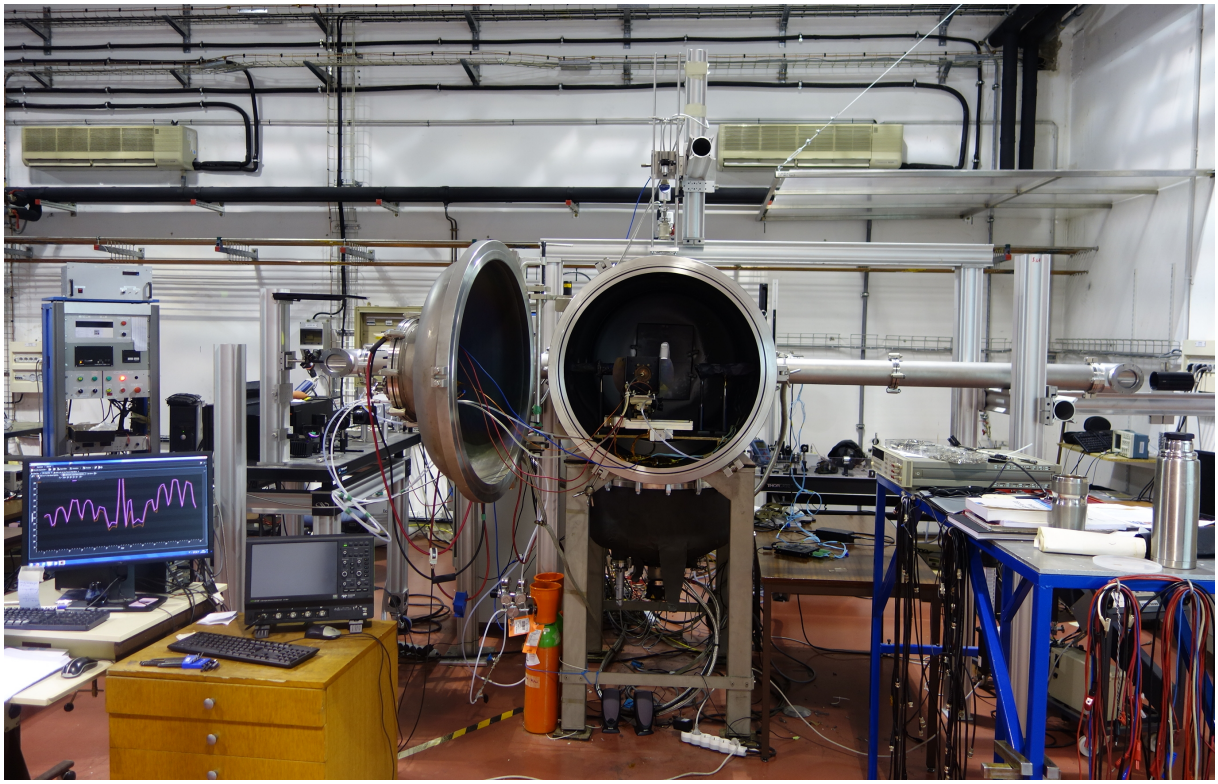

Figure 6.5: Picture of the THETIS diagnostic (left part) implemented on the NExET ion source (right part).

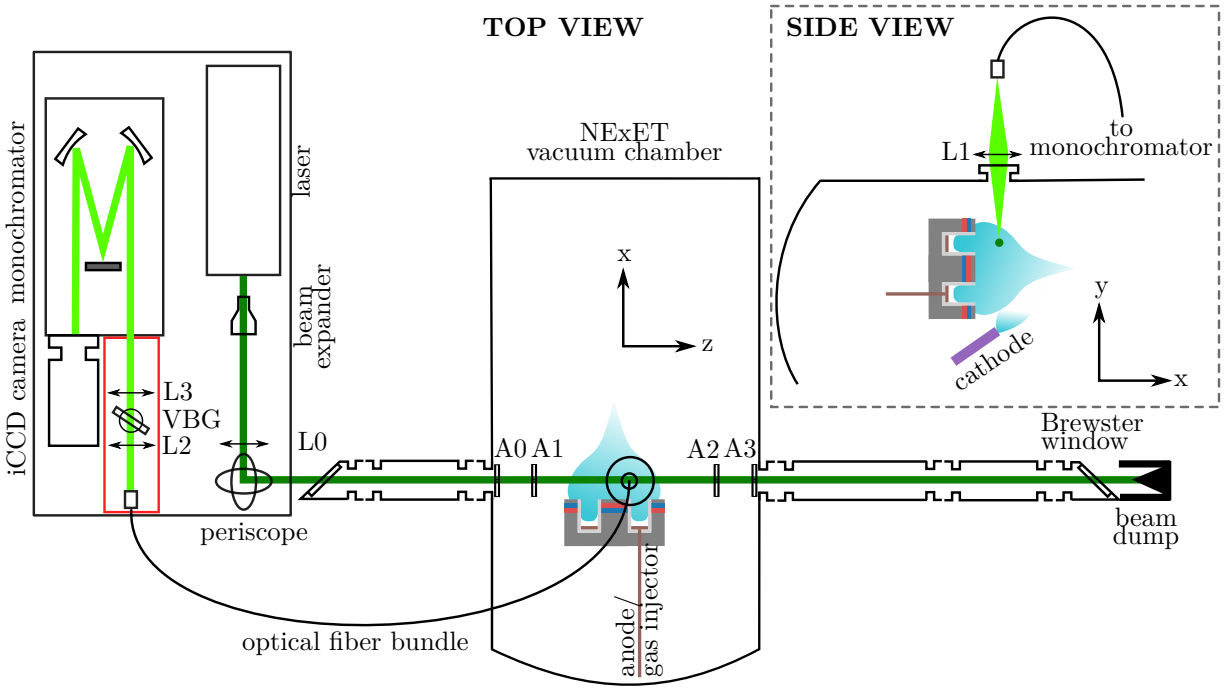

Figure 6.6: Schematic view of the THETIS diagnostic setup for Hall thruster investigations (not to scale). The transmission branch is indicated with a dark green line and the detection branch with a light green line. L0, L1, L2, and L3 indicate lenses; A0, A1, A2, and A3 indicate apertures; VBG indicates the notch filter. The blue area corresponds to the plasma volume.

6.2.3.1 Optical configuration

Figure 6.6 shows a schematic of the THETIS diagnostic transmission and detection branches. The characteristics of the transmission branch, used to produce the scattering signal, are identical to those used for the other investigations.

The detection branch, showed with a light green line in Figure 6.6, starts at the observation volume position, where the light from the transmission branch is focused. From this volume, the Thomson scattering radiation and other stray radiation is emitted. A collection lens images this light onto the entrance of an optical fiber bundle, composed of a 5×3 array of 300 µm-diameter fibers. In the configuration of these experiments, the collection lens, referred as L1, is a 100 mm-diameter plano-convex lens with a 200 mm focal length. Positioned at the top of the vacuum chamber, 0.564 m from the observation volume, the lens L1 images the observation volume with a magnification factor of 0.55. The fiber bundle transmits the collected light to the notch filter chamber on the optical table. At the entrance of this chamber, a 50 mm-diameter plano-convex lens of 125 mm focal length collimates the light emitted from the 1×15 array of this side of the fiber stack. Then, the 25 mm $\times$ 25 mm VBG-NF attenuates the stray-light from reflections and Rayleigh scattering. A 300 mm focal length lens focuses the remaining light onto the 1 mm-wide entrance slit of a spectrometer while respecting its f/9.7 numerical aperture acceptance. Afterwards, the spectrometer disperses the light with a 600 lines mm^{-1} grating suited for measurement of the high electron temperatures (tens of eV) expected at the Hall thruster exit plane. We sometimes used the 2400 lines mm^{-1} grating for dispersion of the Thomson scattering signal from lower-temperature electrons. Finally, the intensified CCD camera detects the dispersed light through a 10 ns gate, synchronized with the Q-switch signal from the laser.

6.2.3.2 Scattering configuration

With the detection branch configuration presented in last section, the observation volume is 0.3 mm in diameter and 2.7 mm in length. Plasma properties measured with the diagnostic correspond to an average over this volume.

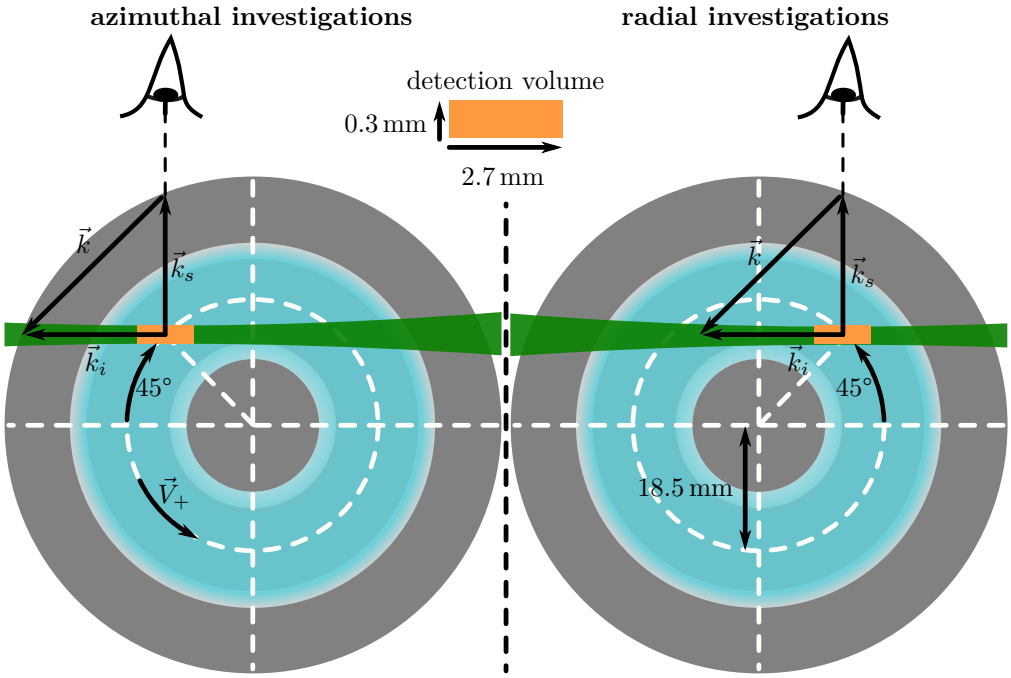

Figure 6.7: Scattering configurations (not to scale) used for investigation of electron properties along the azimuthal (left) and radial (right) directions. Both views are facing the thruster plume (in blue). The laser beam is in green and the detection volume in orange.

Electron properties along the observation wave vector $\vec{k}$ are probed with THETIS diagnostic. For the presented investigations, the thruster vertical position was chosen so that the laser beam passes at a height $r_{mean} \times \cos(\pi/4)$ above the midplane (where r_{mean} is the mean channel diameter), as shown in Figure 6.7. With this configuration, a lateral translation of the thruster allows the alignment of the observation wave vector along either the "radial direction" or "azimuthal direction", if the observation volume is in front of the channel mean diameter (as shown in Figure 6.7).

By convention, a positive spectral shift of the Thomson spectrum corresponds to a positive electron drift velocity. With the data analysis convention used, a positive drift velocity measured along the "azimuthal direction" corresponds to electrons drifting in the anti-clockwise direction (i.e. along $\vec{k}$). Along the "radial direction", a positive drift will correspond to an electron moving towards the internal pole of the thruster.

6.2.3.3 Diagnostic calibration

For calibration of the transmission factor of the detection branch, as discussed in Chapter 3, the same detection branch parameters as for Thomson scattering investigations were used. The vacuum chamber was filled with nitrogen up to a pressure of 1000 Pa and the signal from Raman scattering accumulated over 6000 laser pulses. Because of the high electron temperatures with the Hall thruster, we performed most Raman calibrations and Thomson spectrum acquisitions with the 600 lines mm^{-1} grating and a central wavelength of 532 nm. Because of the low electron density expected, the spectrometer slit width was set to 1 mm. This size allows the transmission of the entirety of the image of the fiber bundle through the notch chamber.

However, for a few cases, improved resolution of the Thomson spectrum was required for small wavelength shifts around the laser wavelength. For this reason, complementary measurements were performed at the same central wavelength but with the 2400 lines mm^{-1} grating. To analyze the two sets of Thomson signals measured with both gratings, the change of transmission efficiency and spectral width of each pixel were characterized. A correction on the signal from the 2400 lines mm^{-1} grating was made with the data from the 600 lines mm^{-1} grating considered as a reference. We estimated the adjustment coefficient to apply using the Raman scattering spectrum acquired for calibration. Figure 6.8 shows the Raman

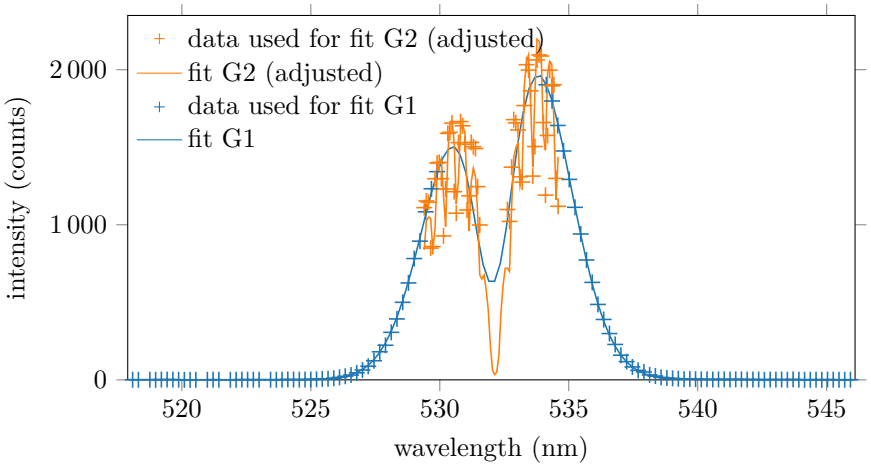

Figure 6.8: Raman spectra measured with the 600 lines mm^{-1} grating (referred to as G1) and 2400 lines mm^{-1} grating (referred to as G2). The intensity of the spectrum measured with the G2 grating was multiplied by an adjustment coefficient to maintain the same mean intensity as the fit of the spectrum obtained with the G1 grating.

signal and its fit measured with the 600 lines mm^{-1} grating (referred to as G1) and 2400 lines mm^{-1} grating (referred to as G2). The intensity of the signal measured with the 2400 lines mm^{-1} grating was multiplied by an adjustment coefficient. A least-squares method adjusted this coefficient to fit the shape of the Raman spectrum measured with the 2400 lines mm^{-1} grating to the shape of the Raman spectrum fit with the 600 lines mm^{-1} grating. The Thomson spectra obtained with the 2400 lines mm^{-1} grating were multiplied by this adjustment coefficient in order to merge them with the data obtained with the 600 lines mm^{-1} grating. The extended spectrum was analyzed in one step. All Thomson spectra (extended or not) followed the same pre-processing steps. This procedure is specific to investigations on Hall thrusters and is presented in the next section.

6.2.3.4 Data pre-processing

For previous investigations with the planar magnetron, the Thomson scattering signal analyzed from the plasma emission signal was isolated from the subtraction of two consecutive spectra types accumulated over 6000 laser pulses. The first record (referred to as record—A in Chapter 3), is obtained with the plasma and laser on. During this record, the signal detected by the camera is composed of signals from Thomson scattering, plasma emission, electronic noise and the remaining stray-light from Rayleigh and laser reflections. The second record, (referred to as record—C in Chapter 3), is obtained with the plasma on but the laser off. During this record, the signal detected by camera comes only from the plasma emission and electronic noise.

The analysis of the Thomson spectra presented in this chapter required a modification of data analysis procedure with respect to that described in Chapter 3. The necessity for an analysis method more robust to potential distortion from plasma emission lines justifies this modification. Because of the high electron temperatures, the spectral range covered by the Thomson scattering signal is large. Inside the 28.6 nm spectral range observed, there are several intense emission lines from the Hall thruster xenon plasma. Even during the 10 ns observation gate of the detector, some emission line intensities remain more than one order of magnitude above the maximum Thomson scattering signal. The subtraction of the plasma emission record can lead to some residual distortion of the Thomson spectrum at these spectral positions. Figure 6.9 and Figure 6.10 illustrate the typical distortions induced.

The presence of residual plasma emission disortions can be accounted for in two ways. A slow drift in the plasma conditions due to the thermalization of the thruster could lead to a drift of plasma emission intensity. This slight difference occurring between the A and C records would appear significant compared to the weak Thomson scattering signal. Another possible reason is that during “Thomson” records, the camera measured the intensity from plasma emission lines in the presence of the intense electric field of the laser. This electric field may induce significant Stark splitting and shifting [211, 212]. During

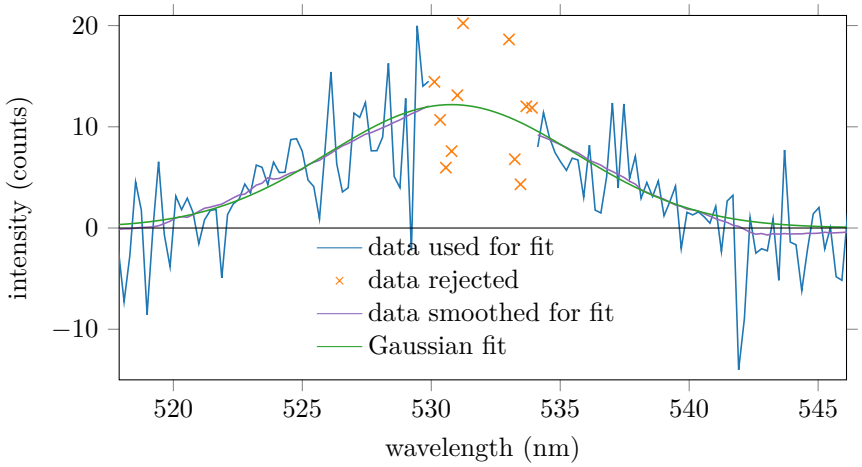

Figure 6.9: Thomson spectrum example obtained along the "azimuthal direction" with the ISCT200-GEO thruster. The corresponding electron density and temperature are $((2.6 \pm 0.2) \times 10^{16}\,\mathrm{m}^{-3}$ and $(20 \pm 2)\,\mathrm{eV}$, respectively. Discharge parameters are a xenon flow rate of $1.6\,\mathrm{mg\,s}^{-1}$, discharge voltage of 250 V and a discharge current of 1.13 A. This spectrum is obtained for an axial distance from the exit plane of 4 mm and peak magnetic field of 25 mT at the exit plane.

the acquisition of the record C, such a splitting is absent and the recorded emission lines would not be identical to those measured with the record A.

To limit distortion by the emission lines, a pre-processing method of Thomson spectra corrects the data before fitting. This pre-processing method aims to correct only distortions from poor plasma emission signal subtraction. Negative values of intensity (counts) below three times the standard deviation of the electronic noise level from the intensified CCD ($\sigma_{elec\ noise}$) have a high probability of coming from distortions induced by the subtraction of more intense plasma emission lines in the record C. The algorithm for pre-processing truncated intensities in the Thomson spectra below this critical threshold ($3 \times \sigma_{elec\ noise} \approx -2.5$ counts with the experimental parameters used during the campaign). Then, to mitigate the positive distortions of the Thomson spectrum (i.e., cases where the residual emission lines add up positively to the Thomson signal), the algorithm applied a SavitzkyGolay filter to the Thomson spectrum. This low-pass filter reduces the fast rises of intensity due to plasma emission lines distortions, while leaving unchanged the slowly varying Thomson spectral shape. This filter was applied independently on the left and right sides of the Thomson spectrum, separated by the rejected central spectral range around 532 nm. Figure 6.9 and Figure 6.10 illustrate this method with two examples; the blue line corresponds to the raw data analyzed and the purple line referred as "data smoothed for fit" shows the analytic function obtained by the pre-processing method.

The algorithm for Thomson spectral analysis presented in Chapter 3 uses the function obtained from this preliminary data processing as an input. A Gaussian function convoluted with the instrument function is used as a fitting function for the Thomson spectrum. The Gaussian standard deviation gives the electron temperature, while the shift of the Gaussian mean from the laser wavelength allows an estimation of the bulk electron drift velocity along the probed direction. Finally, the integrated intensity of the Thomson spectrum gives an estimation of the electron density averaged inside the observation volume.

The spectrum example provided in Figure 6.10 shows a case obtained for lower electron temperatures, for which both the $600\,\mathrm{lines\,mm}^{-1}$ grating and a less-dispersive $2400\,\mathrm{lines\,mm}^{-1}$ grating were used to complete the spectra. The end of this chapter will discuss on the origins of the weakly non-Gaussian spectrum shape and will introduce examples of Thomson spectra with even stronger deviations from the Gaussian profile.

6.2.4 Preliminary remarks

To determine whether the electron properties are isotropic, measurements along both the "radial direction" and "azimuthal direction" were performed by switching between the two scattering configurations

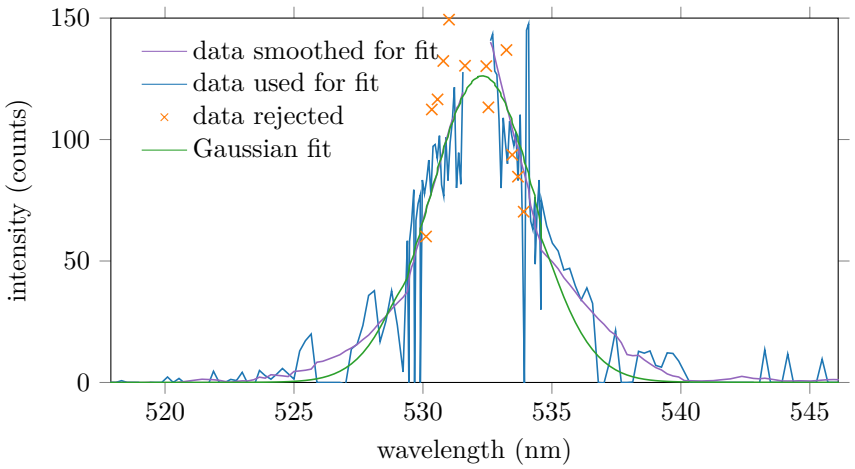

Figure 6.10: Thomson spectrum example measured along the "azimuthal direction" with the ISCT200-MS thruster. The corresponding electron density, temperature and drift velocity are $(1.3 \pm 0.1) \times 10^{17}\,\mathrm{m}^{-3}$, $(3.7 \pm 0.3)\,\mathrm{eV}$ and $(93 \pm 12)\,\mathrm{km\,s}^{-1}$, respectively. Discharge parameters are a xenon flow rate of $2.3\,\mathrm{mg\,s}^{-1}$, discharge voltage of 112 V and a discharge current of 2.67 A. This spectrum was obtained for an axial distance from the exit plane of 2 mm and a peak magnetic field of 15 mT at the exit plane.

presented in Section 6.2.3.2. In the subsequent plots, the electron properties estimated along the "azimuthal direction" are plotted with blue triangles and along the "radial direction" with orange circles. While the observation of non-isotropic electron temperature or drift velocity has a physical significance, this is not the case for electron density, which is expected to be the same for both scattering configurations. Differences in the electron density measured at the azimuthal and radial scattering positions may be due to (i) azimuthal plasma non-uniformity (possibly influenced by the cathode position or spatial inhomogeneities of the magnetic field or gas injection), or (ii) slight displacement (below 0.3 mm) of the measurement position as the thruster translates laterally to switch between the two scattering configurations.

Axial exploration of electron properties was performed for distances from the exit plane of the thruster ranging from typically 1–40 mm for the azimuthal scattering configuration and 2–40 mm for the radial scattering configuration. The closest approach to the exit plane for both directions is that for which stray-light from reflections is sufficiently attenuated to not obscure the Thomson signal. The difference in the closest approach for the two directions is due to the different levels of light reflected off the central pole and entering the detection branch. While with the radial scattering configuration the inner pole behind the observation volume is directly illuminated, this is not the case with the azimuthal scattering configuration. The furthest axial distance is that for which the plasma density remains sufficient for a signal to be detected. As shown with the Thomson spectrum example in Figure 6.9, a Gaussian curve can be fitted to the data with confidence despite the low electron density and large noise signal.

6.3 Magnetic field exploration

6.3.1 Magnetic field intensity (ISCT200-GEO)

Axial profiles of electron properties with the ISCT200-GEO for various magnetic field intensities were determined. For each magnetic field, the discharge power was 285 W, the corresponding discharge voltage and current were respectively 250 V and 1.14 A. The discharge current was kept at the desired value by adjusting the xenon mass flow rate to $1.18\,\mathrm{mg\,s}^{-1}$, $1.60\,\mathrm{mg\,s}^{-1}$ and $1.38\,\mathrm{mg\,s}^{-1}$ for respectively, the B_{low}, B_{mid} and B_{high} magnetic field intensities. Figure 6.11 shows the results from these explorations.

As shown in the first row of Figure 6.11, the electron density has only a weak dependence on the magnetic field intensity. The different values of electron density remain between $4.5 \times 10^{16}\,\mathrm{m}^{-3}$ and $0.8 \times 10^{16}\,\mathrm{m}^{-3}$ from 2 mm to 40 mm from the exit plane. The electron density is lowest with the B_{low} configuration (possibly attributable to less efficient confinement) and the highest electron density is

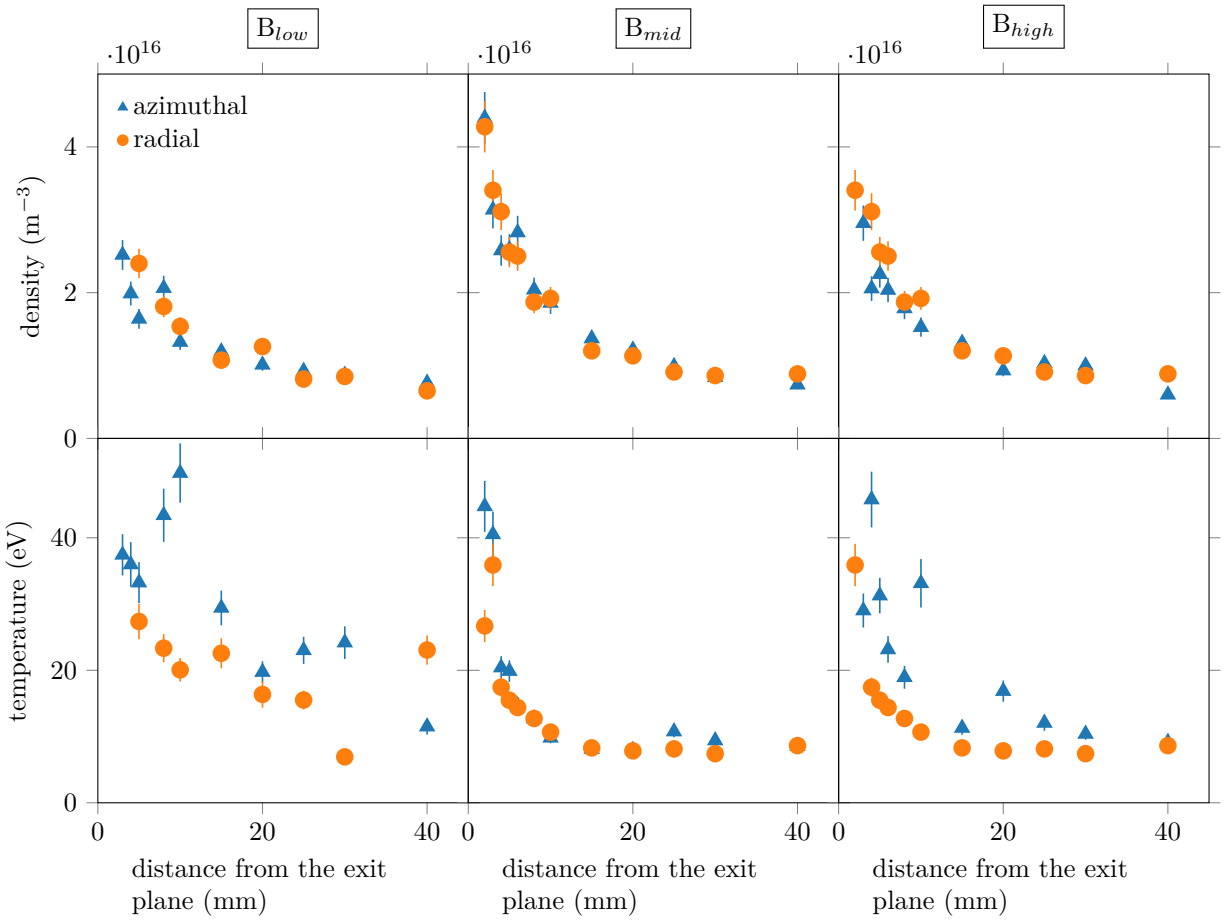

Figure 6.11: Comparison of electron density (first row) and electron temperature (second row) obtained with the ISCT200-GEO thruster at 250 V and 1.14 A for different magnetic field intensities. From left to right, the columns correspond to the B$_{low}$, B$_{mid}$ and B$_{high}$ configurations.

observed with the nominal B$_{mid}$ magnetic field.

In Figure 6.11, the electron temperatures of the B$_{mid}$ configuration decrease monotonically from approximately 40 eV near the exit plane to 10 eV at 40 mm downstream, for both "azimuthal direction" and "radial direction". These values are on the same order of magnitude as recent PIC simulations predictions [213].

In the B$_{low}$ configuration, the electron temperatures are higher than for the B$_{mid}$ case, and azimuthal temperatures exceed the radial temperatures. This latter observation might be due to a weaker magnetic trap leading to higher $\vec{E} \times \vec{B}$ drift and energization of electrons. For the B$_{high}$ configuration, the electron temperature profile is also anisotropic. To fully understand these tendencies, it will be necessary to determine the corresponding electric field profiles.

Figure 6.12 and Figure 6.13 show, respectively, the time-varying discharge current and the associated power spectrum density for the different magnetic fields. The integral of the power spectrum density over frequency between 10^3 Hz and 2×10^7 Hz gives 9.8×10^{-3} A^2, 3.6×10^{-3} A^2 and 81×10^{-3} A^2 for, respectively, the B$_{low}$, B$_{mid}$ and B$_{high}$ configurations. For these configurations, the electron density decreases as the power contained in discharge current oscillations increases. The larger discharge current oscillations observed in the B$_{low}$ and B$_{high}$ configurations may result from axial plasma oscillations (such as transit time oscillations [213]) which may contribute to a larger anisotropy in the electron temperatures and may lead to a poorer electron confinement.

We can estimate an order of magnitude of the expected electron density using the expression for the

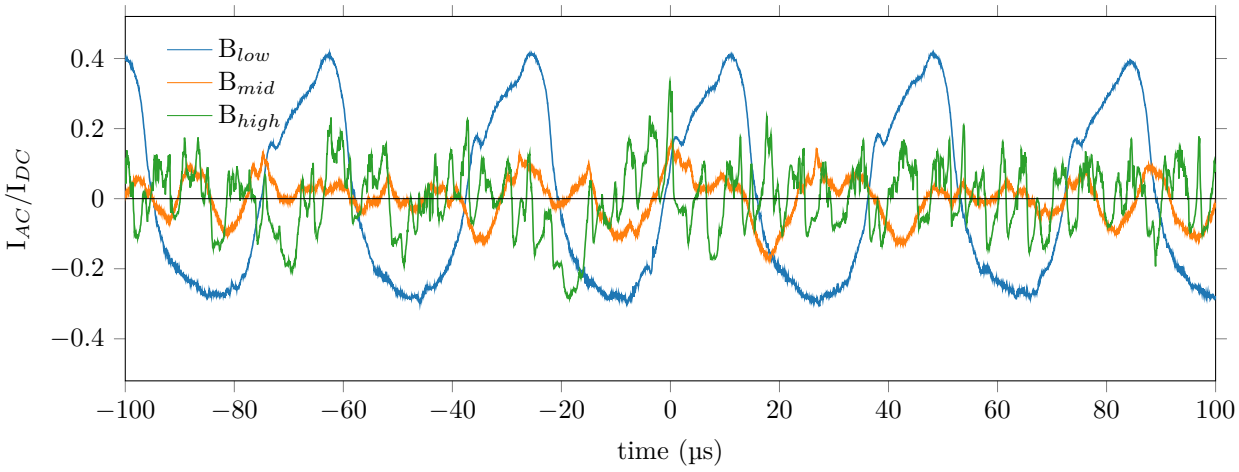

Figure 6.12: AC component of the discharge current for B$_{low}$, B$_{mid}$ and B$_{high}$ magnetic field intensities. The DC component of the current is 1.14 A and the discharge voltage 250 V.

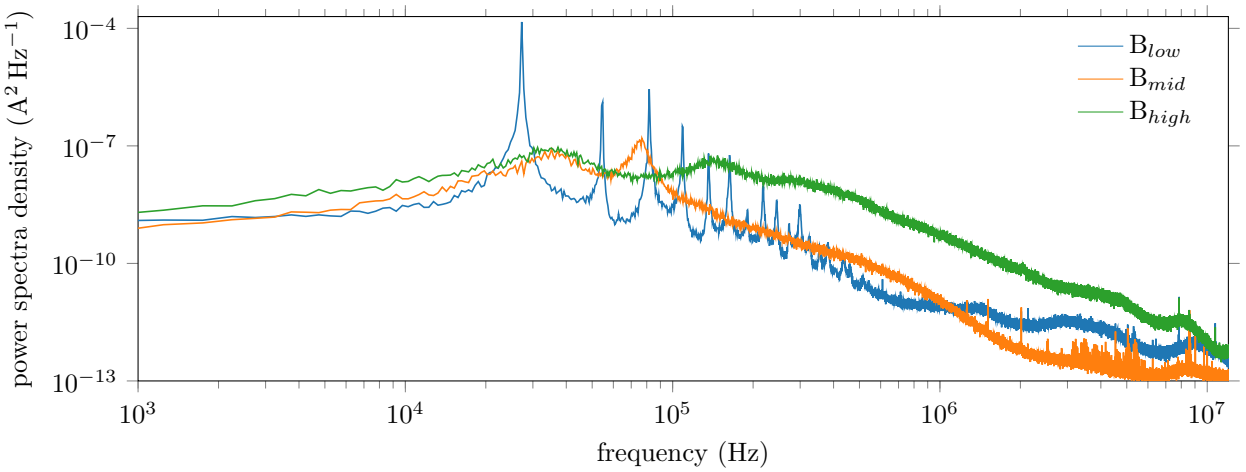

Figure 6.13: Power density spectra of the discharge current for the B$_{low}$, B$_{mid}$ and B$_{high}$ magnetic field intensities, for the conditions of Figure 6.12.

xenon mass flow rate injected through the anode

$$\dot{m_n} = \frac{1}{\eta_{prop}}\dot{m_i} = \frac{1}{\eta_{prop}} n_i m_i A v_i \tag{6.2}$$

where $\dot{m_n}$ and $\dot{m_i}$ are the mass flow rate of xenon atoms and ions, respectively, through a section A. η_{prop} is the propellant utilization efficiency. m_i and v_i correspond to, respectively, the mass and velocity of xenon ions while n_i is the density. Under the hypothesis of quasi-neutrality, this equation offers a way to estimate n_e through the following equation

$$n_e = \frac{\eta_{prop}\dot{m_n}}{m_i A v_i} \tag{6.3}$$

At the position 10 mm downstream of the exit plane, we may assume that most of the ions have been accelerated. Using previously-estimated values of the parameters of Equation 6.3.1 with the same thruster at similar discharge conditions (η_{prop} ≈80 % [194], v_i≈16 km s^{-1} [214] and the thruster channel surface A expanded by a 45° plume divergence angle) we obtain an estimated electron density of 10^{17} m^{-3} at 10 mm from the exit plane. We attribute the slightly lower values measured at this position (a few 10^{16} m^{-3} in Figure 6.11) to a lower ionization efficiency or higher thruster divergence than that used to estimate the density.

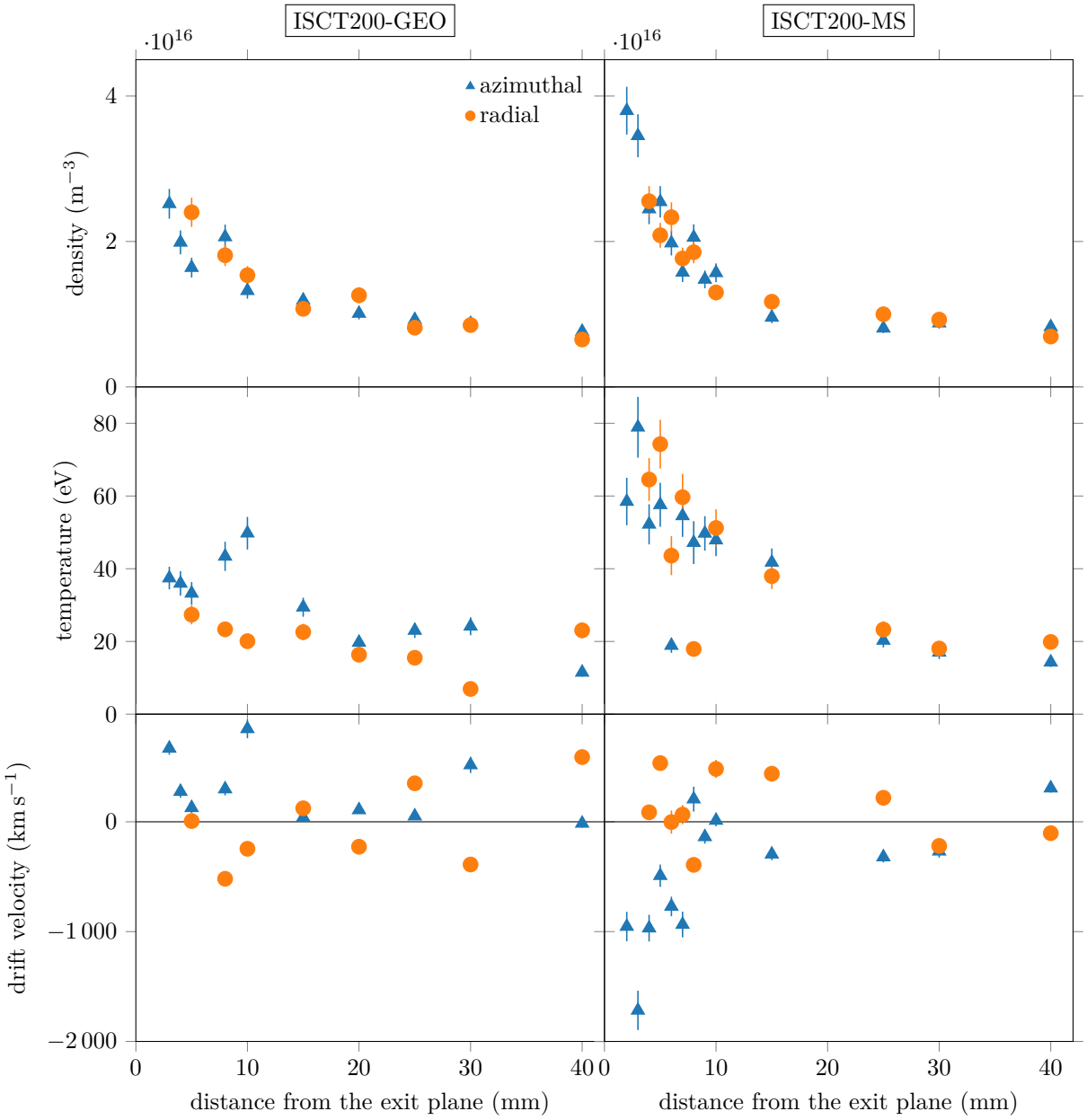

Figure 6.14: Comparison of electron density, temperature and drift velocity along both "azimuthal direction" and "radial direction". The discharge conditions are fixed at 250 V and 1.14 A for both magnetic field configurations: the standard ISCT200-GEO (left column) and unshielded ISCT200-MS (right column) configurations.

6.3.2 Magnetic field configuration (ISCT200-GEO & ISCT200-MS)

We investigated the difference in electron properties between the standard and magnetically-shielded configurations. For the ISCT200-GEO, discharge conditions identical to those of Section 6.3.1 in the B_{low} configuration (with the magnetic field directed towards the outer pole) were used. The shielded ISCT200-MS was operated at the same discharge conditions and magnetic field intensity (directed towards the inner pole). Reaching the same discharge conditions (250 V and 1.14 A) required a xenon flow rate of 1.05 mg s^{-1}).

Figure 6.14 shows a comparison between the two magnetic field configurations.

As seen in the first row of Figure 6.14, at similar positions, we reach a higher electron density with the

ISCT200-MS, where density goes up to $4 \times 10^{16}\,\mathrm{m}^{-3}$ near the exit plane. We explain this difference with the ISCT200-GEO, operated at the same discharge conditions, by the downstream shift of the ionization and acceleration region for the shielded configuration ISCT200-MS [207].

As shown in the second row of Figure 6.14, we found much higher electron temperatures with the ISCT200-MS Hall thruster. Again, electron temperature is highest near the exit plane, where it reaches 80 eV at maximum. Recent simulations also report much higher electron temperatures with a magnetically-shielded thruster than with a standard magnetic configuration, a feature associated with a downstream shift of the axial profile [215]. Nevertheless, absolute values of electron temperature from some simulations 215 remain lower than what we observe: these simulations predicted only 30 eV with the standard configuration and 53 eV with the MS configuration. The difference between the electron temperatures from simulations and experiments under similar conditions is yet to be understood, but it is possible that the contribution of plasma instabilities - not captured in the simulations - may contribute to electron heating to some degree.

The third row of Figure 6.14 shows the drift velocities for the two Hall thruster architectures. In the magnetic shielding configuration, the spectral shift of the Thomson spectra at positions near the exit plane is much more significant than for the standard architecture and as such the estimated drift velocity can be interpreted.
For previous measurements on a planar magnetron [133] discussed in Chapter 4, we reported sensitivity for electron drift velocity estimation which was equivalent to the Doppler shift velocity associated with a spectral width of one pixel (at the corresponding wavelength). This sensitivity would correspond to approximately $100\,\mathrm{km\,s}^{-1}$ with the $600\,\mathrm{lines\,mm}^{-1}$ grating and the 8-pixel wavelength binning used for this investigation. Nevertheless, the Thomson scattering signal obtained from the Hall thruster plasma is more challenging to analyze because of the lower signal-to-noise ratio and distortion of the Thomson spectrum by plasma emission lines. For this reason, electron drift velocities below $500\,\mathrm{km\,s}^{-1}$ obtained in this campaign were not considered for discussions on the estimated values. This lower limit corresponds to the drift velocity associated with the Doppler broadening of the FWHM of the instrument profile.
We expected the electron drift velocity direction and magnitude along the "azimuthal direction" to be easier to determine because the $\vec{E} \times \vec{B}$ should be one of the dominant contributions, especially in the acceleration region. For the investigations presented in this section, the magnetic field was directed toward the outer pole for the ISCT200-GEO and toward the inner pole for the ISCT200-MS. Given the electric field direction in the acceleration region, we expected the azimuthal drift velocity of electrons to be anti-clockwise with the ISCT200-GEO and clockwise for the ISCT200-MS (considering a view facing the ion beam). Along the "radial direction", it is more difficult to determine the drift velocity trend as other contributions, such as curvature and gradient drifts, may be on a similar order.

With the ISCT200-GEO the electron drift velocity along the azimuthal direction is systematically positive with only a few values above the threshold of $500\,\mathrm{km\,s}^{-1}$. As expected, these positive values correspond to electrons drifting in the clockwise direction. Along the "radial direction", the drift velocity is weaker and oscillates around zero.
With the ISCT200-MS the azimuthal drift velocity is significantly negative close to the thruster exit plane. These values are negative because of the reversed magnetic field direction and are consistent with a clockwise $\vec{E} \times \vec{B}$ drift. Such significant values of electron drift velocity are observable only with the ISCT200-MS because the acceleration region, where the electric field is strong, is shifted downstream, rendering it accessible to the ITS probing beam. As with the standard configuration, electron drift velocities in the "radial direction" are comparatively low.

6.3.3 Magnetic field direction (ISCT200-MS)

To gain further insight into the electron drift velocity values, we performed investigations on the same ISCT200-MS thruster with the magnetic field directed towards the outer, and then inner, poles. The same discharge conditions were used for comparison between the two magnetic field configurations presented in Section 6.3.2. With the magnetic field directed towards the outer pole, for a discharge voltage of 250 V, 1.14 A of discharge current required a xenon flow rate of $1.2\,\mathrm{mg\,s}^{-1}$. A $1.05\,\mathrm{mg\,s}^{-1}$ xenon flow rate was required for 1.14 A of discharge current at 250 V for the magnetic field directed towards the inner pole.

As shown in the two first rows of Figure 6.15 the magnetic field direction weakly affects the electron temperature and density profiles. In contrast, it significantly affects the electron drift velocity. Along both the "azimuthal direction" and "radial direction", the electron drift velocity switches in sign when the

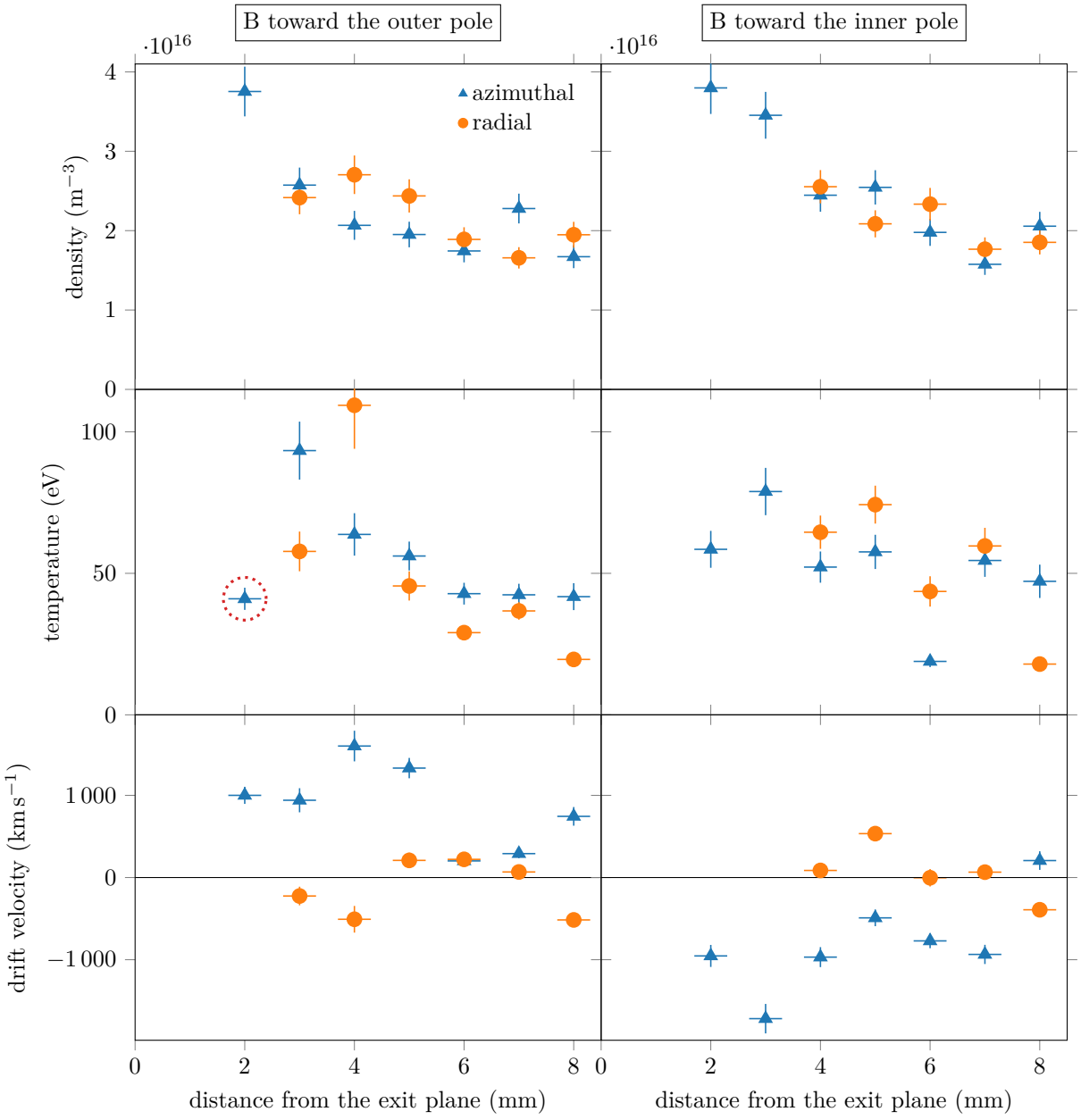

Figure 6.15: Comparison of electron density, temperature and drift velocity along both azimuthal (points in blue) and radial (points in orange) directions for the shielded ISCT200-MS thruster but with reversed magnetic field directions. The discharge conditions are fixed to 250 V and 1.14 A for both magnetic field directions: towards the outer pole (left column) and towards the inner pole (right column).

direction of the magnetic field direction is reversed. We expect the magnetic field gradient and curvature to remain the same with both directions, while the $\vec{E} \times \vec{B}$ contribution to the electron drift velocity should reverse and maintain the same magnitude if the electric field profile does not change.

The fact that the measured drift velocity along the "azimuthal direction" is of nearly the same magnitude, regardless of the magnetic field direction, suggests that the $\vec{E} \times \vec{B}$ drift dominates the diamagnetic and curvature drifts near the exit plane. This observation might differ at distances further downstream [144]. We can use the maximum electron drift velocity measured to estimate the maximum electric field in the part of acceleration region of the thruster probed. For a magnetic field of approximately 15 mT, where electron drift velocity reaches its maximum value of 1800 km s^{-1}, we estimated the electric field at 27 kV m^{-1}. LIF measurements performed on the same thruster at lower discharge voltage

(200 V and 1 mg s^{-1} of xenon flow) estimated a slightly higher maximum value (38 kV m^{-1}) [216]. The discrepancy between these two estimated values may come from limits on the hypothesis of a pure $\vec{E} \times \vec{B}$ drift velocity used for estimation of the electric field from the electron drift velocity. Also, we did not observe a decrease of the electric field further upstream; the highest electron drift velocity value may be even further upstream and would lead to a higher value on the estimated electric field.

6.3.4 Discussion on the high electron temperatures observed

The results from this first set of experiments show electron temperatures easily reaching 60 eV for certain conditions, a result that does not match any typical probe measurements on large and small thrusters. Previous investigations with Langmuir probes reported temperatures in the range of few tens of eV in the near-field region [29, 197, 217]. Even at a similar discharge voltage and for various sizes of thrusters, the electron temperature did not exceed 30 eV in the acceleration region.

For a discussion on these values, we first consider examples of temperatures in the 60 eV range, using spectra obtained on the ISCT200-MS 2 mm from the exit plane with the same discharge condition as Section 6.3.3. Figure 6.16 shows these spectra measured with the scattering configuration used for investigation of azimuthal electron properties and concern magnetic fields directed towards and away from the inner pole. The corresponding electron properties, estimated from parameters of Gaussian fits applied these spectra, are shown in the figure legend.

We may make the following observations for the presented spectra:

(i) As discussed in Section 6.3.3, the presence of strong drifts shift the center of the spectrum away from the laser frequency, and a switch in the magnetic field direction (from directed outwards to inwards) also switches the direction of this shift. This is visible in Figure 6.16. The large shift of the Thomson spectra required a supplementary acquisition with the 600 lines mm^{-1} grating centered on 522 nm or 542 nm depending on the direction of the drift. The data from these second records were directly merged with the data obtained with a 532 nm central wavelength.

(ii) In addition to the spectral shift, the spectra are asymmetric. A long tail is visible along the spectral direction associated with the electron drift velocity, while the opposite side of the spectrum shows a fast decrease of signal intensity. This suggests that the electrons are not in thermal equilibrium. While a Gaussian fit may not be strictly relevant, it can still reasonably fit one side of the spectrum, and the electron temperature is estimated from such a fit. The spectra shown, though much noisier than the example provided in Figure 6.12 and Figure 6.13, are still sufficiently well-resolved to show their wide spectral range.

(iii) Lastly, we consider challenges associated with the analysis of these spectra. The high-electron temperature, low-electron density regime of the cases shown results in low-amplitude, broad Thomson spectra. These spectral features, combined with the presence of several residual emission lines, contribute to the noisiness of the data. In spite of this, the large spectral width of the cases shown is unambiguous.

What contributes to this relatively large width? We may speculate that this observation is due to oscillatory discharge behavior, averaged out during the 10-minute acquisition time for each spectrum. Although we have sought to limit these investigations to regimes in which the discharge current standard deviation is low, this does not rule out the possible influence of high-frequency plasma instabilities [32] which may generate electric field fluctuations. The accelerating potential is not truly stationary. This may create oscillations in the bulk distribution which, when averaged, would appear as unusually broad spectra, leading to apparently higher electron temperatures than would be expected from the average applied potential. To avoid this, it would be necessary to obtain a highly time-resolved measurement (ideally, a single shot measurement with shorter laser pulse duration), at present beyond reach for these low plasma densities. In addition to this effect, high-frequency instabilities have been demonstrated to contribute to true electron heating in thrusters. This dynamic heating is discussed in a number of works [218], where electron temperatures reaching the 100 eV range have been mentioned. It is worth noting that these simulations do not fully account for the energy dissipation mechanisms for electrons. Nevertheless, a full understanding of the contribution of plasma oscillations to the experimentally-measured spectral widths may be achievable through numerical modeling, to be examined in future work.

We may obtain further insights into electron behavior from the calculation of the EEDF associated to the Thomson spectrum profile [95]. However, as shown in Section 6.5.1, a true discussion on the distri-

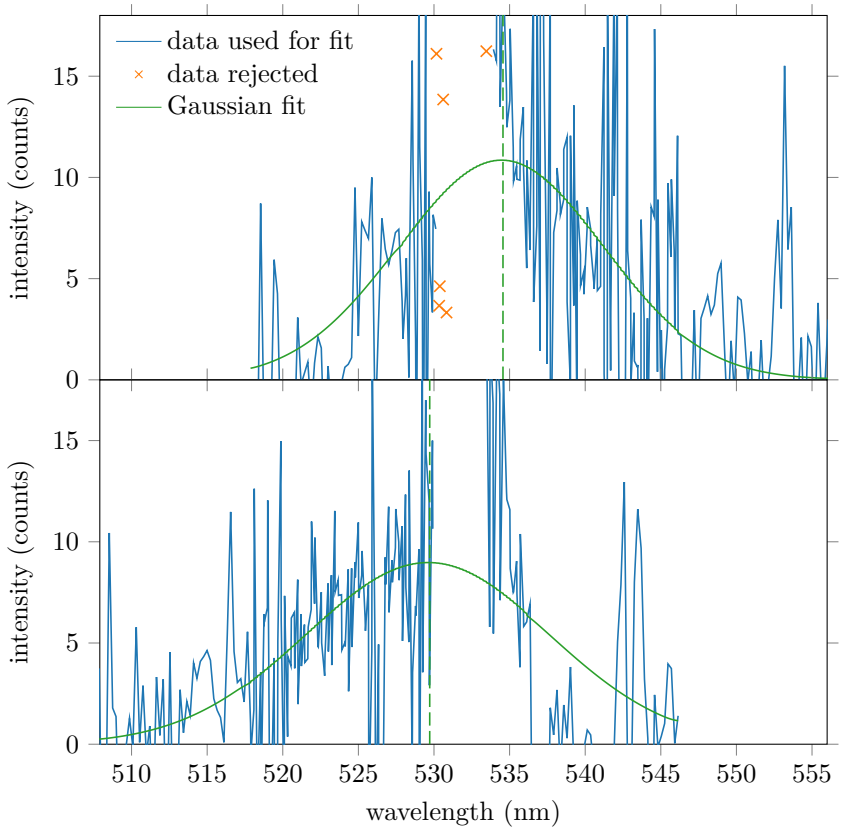

Figure 6.16: Thomson spectra obtained along the "azimuthal direction" 2 mm from the exit plane of the ISCT200-MS thruster, for 250 V discharge voltage and 1.14 A discharge current (same conditions as Section 6.3.3). The Gaussian fit and the position of its center are shown with respectively a solid and dashed (vertical) green line. Top: magnetic field directed towards the outer magnetic pole; n_e=$(3.8 \pm 0.3) \times 10^{16}\,\mathrm{m}^{-3}$, T_e=$(41 \pm 4)\,\mathrm{eV}$ and $v_{e,drift}$=$(1000 \pm 100)\,\mathrm{km\,s}^{-1}$. Bottom: magnetic field directed towards the inner magnetic pole; n_e=$(3.5 \pm 0.2) \times 10^{16}\,\mathrm{m}^{-3}$, T_e=$(58 \pm 7)\,\mathrm{eV}$ and $v_{e,drift}$=$(-950 \pm 130)\,\mathrm{km\,s}^{-1}$.

bution function derived requires a higher signal-to-noise ratio 96, obtained for example under discharge conditions that lead to higher electron densities.

6.4 Discharge conditions exploration

6.4.1 Influence of the discharge power (ISCT200-GEO)

We investigated the influence of the discharge power with the ISCT200-GEO thruster, at a fixed distance of 3 mm from the exit plane, with the scattering configuration for investigation of azimuthal electron properties. The thruster was operated in the B_{mid} magnetic configuration, with the magnetic field directed towards the outer pole of the thruster. With the convention used, the azimuthal electron drift velocity was expected to be positive in the acceleration region. The discharge power was varied between 140 W and 345 W by varying the discharge voltage between 126 V and 300 V and keeping a fixed xenon flow of $1.6\,\mathrm{mg\,s}^{-1}$. While the power exploration led to small variations of the discharge current, it remained between 1.11 A and 1.29 A and most of the power increase was due to the increase in discharge voltage.

Figure 6.17 shows the results from this exploration. The electron density does not vary significantly with the discharge power. It remains around $3 \times 10^{16}\,\mathrm{m}^{-3}$ for most of the discharge powers and suddenly increases to $6 \times 10^{16}\,\mathrm{m}^{-3}$ for the lowest discharge power investigated. This observation may arise from a mode change of the discharge at lower voltages. The electron temperature has larger variations: for low

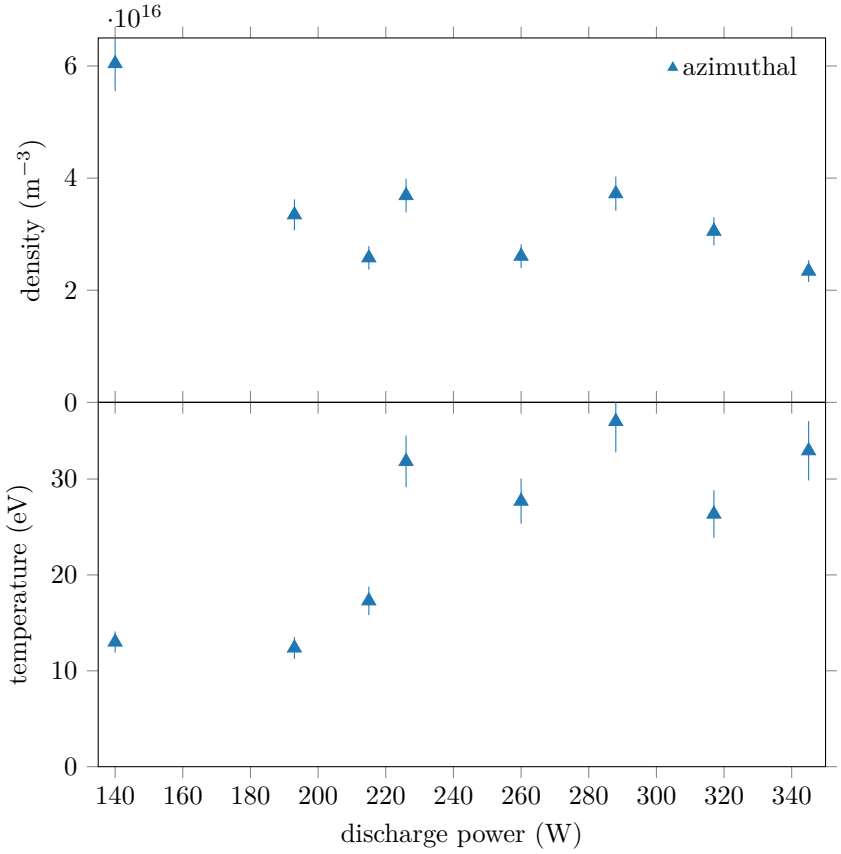

Figure 6.17: Electron density, temperature and drift velocity along the "azimuthal direction" 3 mm from the exit plane for the ISCT200-GEO thruster. Various discharge powers were investigated at a fixed xenon flow of 1.6 mg s^{-1}.

power it remains low, around 10 eV, and suddenly reaches a plateau around 30 eV for discharge powers above 220 W. We do not show the absolute values of the electron drift velocity because they remained below the sensitivity limit discussed in Section 6.3.2. A discussion on the physical meaning of drift velocity outside the acceleration region would require a higher spectral resolution.

Because the thruster is in the standard configuration, we can assume that at the probed position, most of the ions have already been accelerated. The absence of a large drift velocity along the "azimuthal direction" suggests the absence of a large electric field for the entire range of discharge powers investigated at this position. We can consider that we always probed the region of the plasma downstream of the acceleration region. In this region, we observe that a higher discharge power does not translate into a higher plasma density. Instead, the added power seems to contribute to electron heating to higher temperatures. Without magnetic shielding, this increased electron temperature leads to a more energetic sheath that increases the thermal load on the thruster wall and fixes a lower limit on the highest operable power [194].

6.4.2 Influence of the discharge voltage

6.4.2.1 In shielding configuration (ISCT200-MS)

A study of the influence of the discharge voltage on the electron properties at a fixed position 2 mm from the exit plane was performed, with the scattering configuration for investigation of azimuthal properties used. We scanned the discharge voltage from 112 V to 300 V at constant discharge power of 300 W, with a change of the xenon mass flow rate from 2.3 mg s^{-1} to 0.9 mg s^{-1}. The ISCT200-MS was operated with the magnetic field directed toward the external pole. At the axial position probed, because of axial shift of the discharge associated with the shielded configuration, it was possible to probe a region

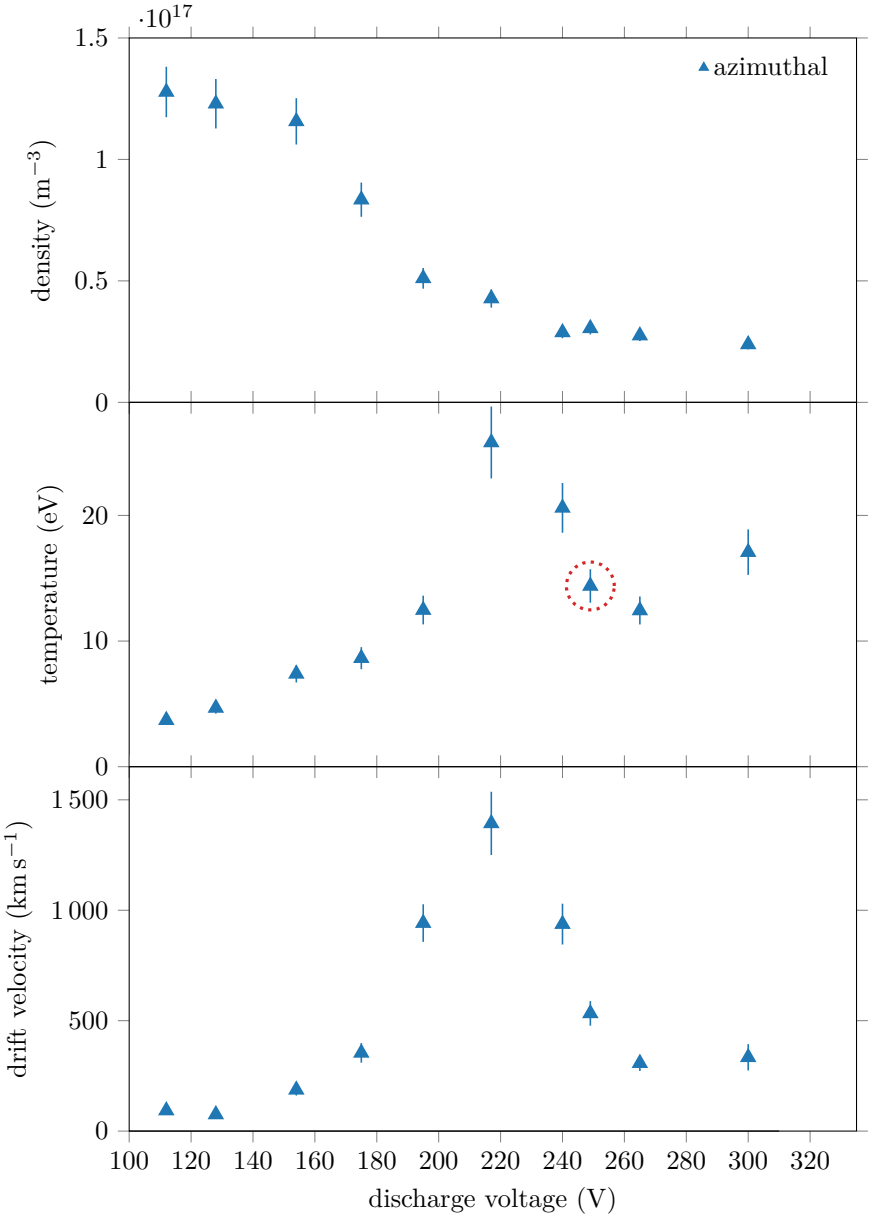

Figure 6.18: Electron density, temperature and drift velocity along the "azimuthal direction" 2 mm from the exit plane for the ISCT200-MS thruster. Various discharge voltages were investigated at a fixed power of 300 W.

with a relatively high electric field. The $\vec{E} \times \vec{B}$ drift may be the main contribution to the electron drift velocity measured, giving an anti-clockwise rotation of electrons. Figure 6.18 shows the results from this investigation.

As seen in Figure 6.18, the electron density is significantly lower at higher discharge voltages. This trend might derive from the decreased xenon mass flow rate supplied in order to maintain the discharge power at 300 W when the voltage is increased.

Making the rough assumption that most of the voltage drop has occurred at the position probed, we can approximate the ion velocity v_i to $\sqrt{qU_d/m_i}$, where U_d is the discharge voltage and q is the charge state of the ion (we will consider only singly-charged ions with $q = e$). Substituting this velocity into Equation 6.3.1, under the hypothesis of a constant ionization efficiency and divergence angle, the coefficient $n_e\sqrt{U_d}$ is expected to be proportional to the xenon mass flow rate $\dot{m}_n$. For constant discharge power (i.e., for a fixed value of the product $\dot{m}_n U_d$ as $I_d \propto \dot{m}_n$), $n_e U_d^{3/2}$ should be a constant (c). The

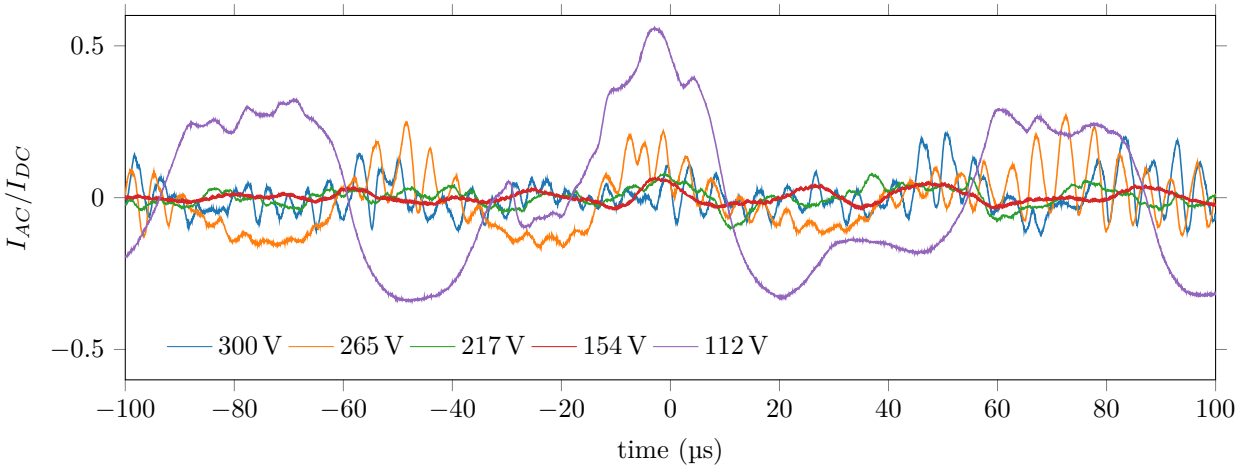

Figure 6.19: AC component of the discharge current for different discharge voltages for the ISCT200-MS thruster. The DC component of the current is 1.14 A.

value of c is slightly lower at300 V than at 112 V: this is likely due to a slight downstream axial shift in the accelerating electric field profile, which would translate into an ion beam less accelerated at the probed position and consequently a higher plasma density.

The relatively large electron densities obtained with the ISCT200-MS at low discharge voltages facilitate the analysis of the Thomson signal. Near the exit plane and at low voltages, we observed quantitative deviations from the typical Gaussian Thomson spectra shape at low voltages which will be analyzed and discussed in the next sections.

The variation in electron temperature shown in Figure 6.18 is non-monotonic. At low discharge voltage, the electron temperature first rises linearly from 8 eV to 13 eV before a fast increase to 25 eV at 217 V is observed, followed by a slow decrease to around 15 eV at higher voltages (see Figure 6.18).

Previous studies [219] using probes investigated the influence of channel width and discharge voltage on the maximum electron temperature. A linear increase of the maximum electron temperature at low discharge voltages was reported, regardless of the channel width, with a saturation in temperature observed around 60 eV at large discharge voltages.

The trend of the electron temperature observed in our case can best be interpreted by considering the effect of the varying voltage on the position of the peak electric field. There appears to be a tendency for the electric field to get broader and shift further outwards as the discharge voltage decreases [220, 221]. If the electron temperature correlates (as is expected [215]) with drift velocity, then the peak in the temperature at 217 V may be apparent because for this voltage, the peak electric field position coincides with the observation volume position 2 mm. The subsequent decrease in the electron temperature at higher voltages would merely be due to the peak electric field moving upstream of the observation volume position. A more complete experiment would involve investigations of the electron properties at several axial positions for each voltage.

As shown in Section 6.3.3, for a position of 2 mm from the exit plane, the $\vec{E} \times \vec{B}$ drift is usually the main contribution to the azimuthal electron drift velocity, and thus it is proportional to the axial electric field. This accounts for why the trend in electron drift velocity shown in Figure 6.18 is similar to that of the electron temperature, which, as we have discussed, is correlated with the electric field. As with the electron temperature, the drift velocity profile is a reflection of the progressive axial shift of the peak electric field into, and then out of, the fixed observation volume.

Figure 6.19 and Figure 6.20 show, respectively, the temporal profiles and the power density spectra of the discharge current for several discharge voltages. The main discharge current oscillations are in the 2×10^5 Hz range at higher discharge voltage and may be consistent with transit time oscillations. At lower discharge voltages, oscillations in the discharge current are more concentrated in the 4×10^4 Hz (breathing mode) range. At the lowest discharge voltage of 112 V, current oscillations are significant with a peak-to-peak amplitude as large as the mean current, in a regime for which with rotating spokes expected to appear [222, 223]. With this discharge mode, the power spectra of the oscillations cover a broadband in the 10^4 Hz range, but with one well-defined oscillation frequency at 15 kHz, synchronization

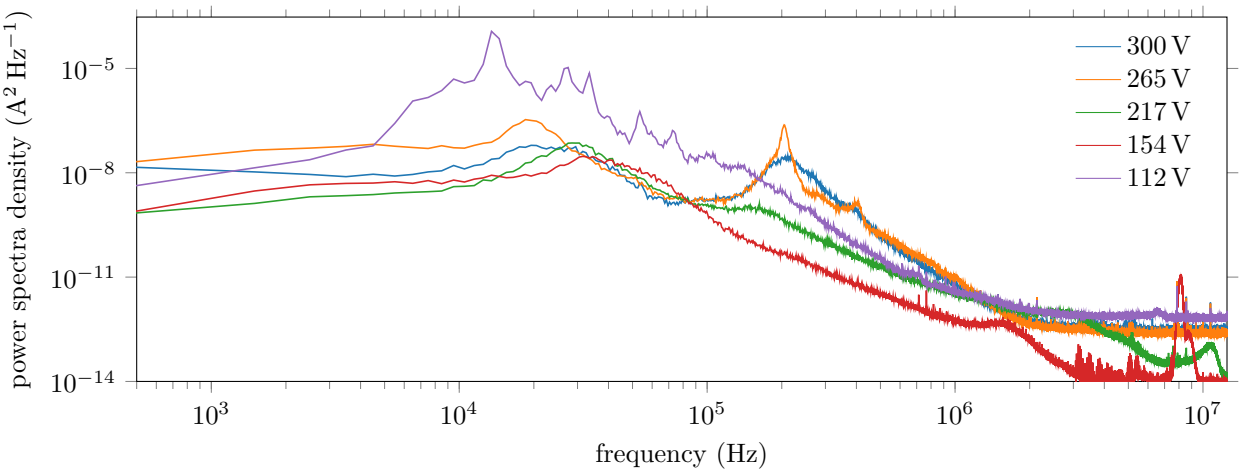

Figure 6.20: Power density spectra of the discharge current for different discharge voltages for the ISCT200-MS thruster, for the same conditions as Figure 6.19.

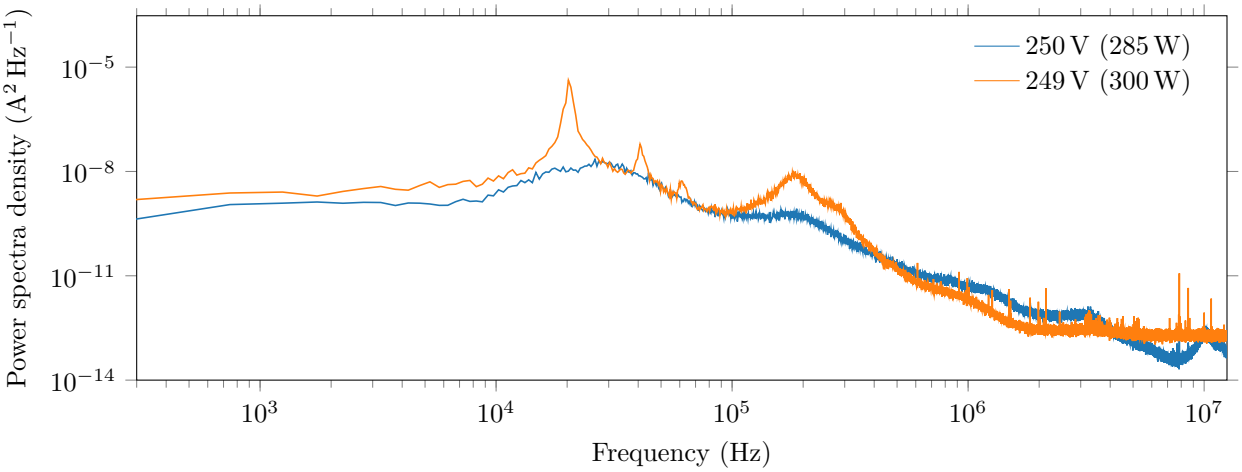

Figure 6.21: Power density spectra of the discharge current of the ISCT200-MS thruster associated with two similar discharge conditions. The 250 V (285 W) conditions were used for axial explorations in Section 6.3.2 and Section 6.3.3, while the 249 V (300 W) conditions were obtained during the discharge voltage exploration (at a fixed power) of this section.

of the Thomson signal acquisition with different points in the discharge current period appears achievable, giving access to time-resolved measurements of the electron properties.

The minimum in the power density integrated over the entire frequency range appears at intermediate voltages, near 217 V, yet the measured electron temperature is maximum for this voltage. As discussed previously, it is not yet possible to rule out the contributions of high-frequency instabilities (not visible in the discharge current measurement) to the observation of high electron temperatures in the acceleration region.

Overall, modifications of the discharge conditions when the discharge voltage is varied will change both electron properties and contribute to the electric field axial shift phenomenon discussed previously.

The discharge conditions at 249 V (300 W) investigated during the voltage variation are similar to those at 250 V (285 W) investigated during the axial exploration discussed in Section 6.3.2 and Section 6.3.3. However, at 249 V the azimuthal electron temperature at 2 mm (circled in Figure 6.18) is only about 14 eV, far below the 40 eV azimuthal temperature at the same position at 250 V (circled in Figure 6.15).

To explain this difference, we note first that the 249 V (300 W) discharge conditions correspond to a 5 % increase of the discharge power (from 285 W to 300 W). Given the 200 W nominal power of the thruster, it is not surprising that far from this power, small excursions in the discharge conditions induce

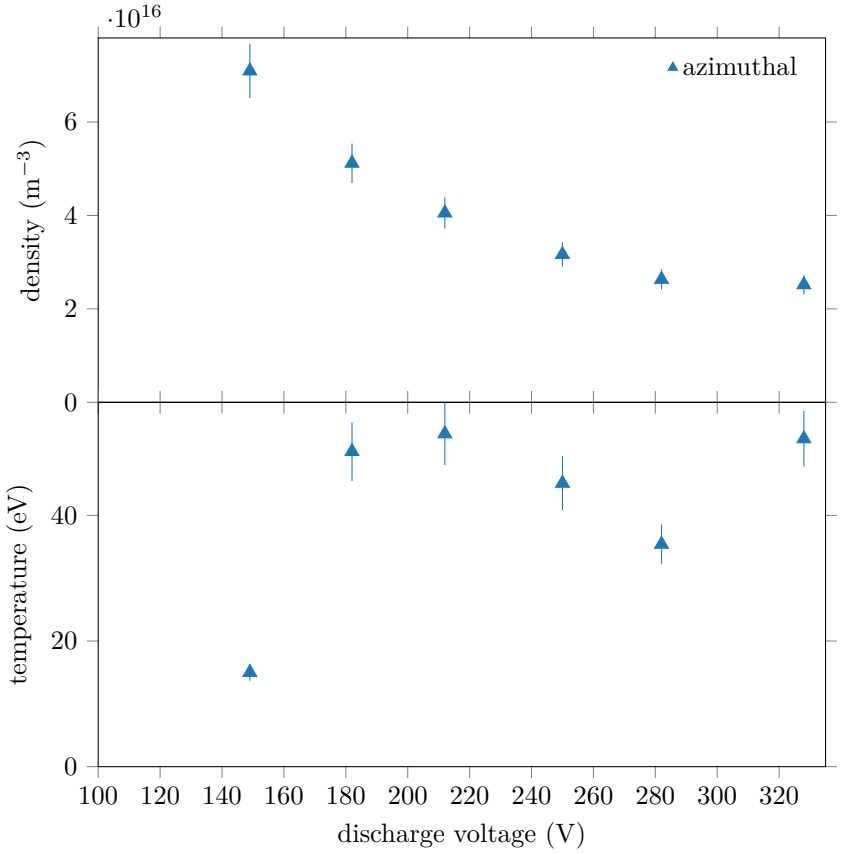

Figure 6.22: Electron density and temperature along the "azimuthal direction" 2.5 mm from the exit plane for the ISCT200-GEO thruster. Various discharge voltages were investigated at a fixed power of 240 W.

changes to the averaged plasma properties such as electron temperature. This point can most easily be illustrated by considering the discharge current oscillations for the 249 V (300 W) and 250 V (285 W) conditions.

Figure 6.21 shows the power density spectrum of the discharge current for the two discharge conditions. In the 10 kHz to 100 kHz frequency range, pronounced oscillations are present in the discharge current at 249 V (300 W) which are absent or attenuated at 250 V (285 W). The discharge conditions, though similar in voltage, show differing behavior which could partly account for the large difference in the measured electron temperatures for these conditions, due to modifications of the efficiency of energetic electron confinement.

6.4.2.2 In standard configuration (ISCT200-GEO)

As in Section 6.4.2.1, we performed a discharge voltage exploration with the ISCT200-GEO thruster. The exploration covered the voltage range from 149 V to 330 V, with the power fixed to 240 W by tuning the xenon flow rate from, respectively, 1.7 mg s^{-1} to 0.5 mg s^{-1}. Electron properties were determined at a distance of 2.5 mm from the thruster exit plane with the azimuthal scattering configuration. Figure 6.22 shows the axial profile of electron density and temperature measured with this configuration.

As shown in Figure 6.22, the electron density decreases monotonically from 7×10^{16} m^{-3} at 149 V to 2.5×10^{16} m^{-3} at 330 V. This trend is similar to what we observed with the shielded configuration in Section 6.4.2.1 and can also be explained by the reduced velocity of the ion beam at lower voltages. The profile of electron temperature is different; the profile rapidly reaches a plateau that appears to remain around 50 eV. The difference with the trend observed with the shielded configuration can be explained by the larger distance of the observation volume from the acceleration region. The electron properties in the observation volume may be less influenced by the displacement of the acceleration region when the

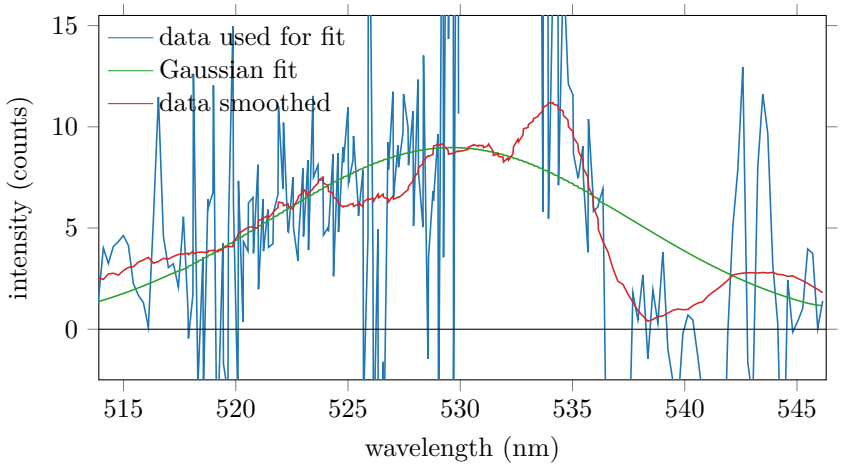

Figure 6.23: Thomson spectrum measured (blue line) at 2 mm from the exit plane with the same conditions as the bottom part of Figure 6.16. The Gaussian fit and smoothed function calculated for estimation of the derivative are shown with a green and red line, respectively.

discharge voltage is changed. As the results show, the temperature remains almost constant, behavior we may have observed with the shielded configuration at distances sufficiently far from the acceleration region. Again, we do not show the estimated drift velocity with this magnetic configuration because it remained below the diagnostic sensitivity. The absence of a large drift velocity is consistent with the hypothesis of a relatively large separation between the observation volume and the acceleration region.

6.5 Characterization of deviations from thermal equilibrium (ISCT200-MS)

6.5.1 Discussion on the limitations

One of the main advantages of Thomson scattering diagnostic lies in the sensitivity of the detected signal to the distribution function of the scattering particles (i.e., the electrons). As shown in Chapter 3, the Thomson spectrum is directly proportional to the one-dimensional electron velocity distribution function along the probed wave vector. However, the extraction of the more commonly used EEDF or EVDF involves some hypotheses as well as the smoothing and derivation of the acquired spectrum. This more complicated procedure requires a relatively high signal-to-noise ratio. From Section 6.3 we have shown that by moving the acceleration region, the shielded configuration makes regions with relatively large density accessible to the Thomson scattering diagnostic. As shown with the example of Figure 6.23, we obtained a Thomson signal with a relatively high signal at 2 mm from the exit plane for a discharge voltage of 250 V, a discharge current of 1.14 A and a xenon flow of 1.05 mg s^{-1}. The method presented in Chapter 3 to obtain a smoothed function of the experimental Thomson spectrum was used, with an interpolation by the Gaussian fit values inside the rejected range around 532 nm. The smoothed function roughly reproduces the shape of the spectrum, however, the relatively large peaks and dips generated by the weak reproducibility of plasma emission lines affected the smoothed function at some spectral positions.

Figure 6.24 shows the EEDF obtained from the derivative of both the Gaussian fit and smoothed function. The EEDF derived from the Gaussian spectrum corresponds to the theoretical shape expected for electrons at thermal equilibrium. The comparison of the EEDF obtained from the smoothed spectrum with the theoretical shape shows that the derivation exacerbates the distortions induced by plasma emission lines. For the case in Figure 6.24, we can only use the experimental EEDF to highlight deviations from thermal equilibrium. A real discussion on the shape of the EEDF requires spectra with fewer distortions.

As a reminder, the procedure used for the estimation of the EEDF assumes electrons with isotropic behavior. The large drift velocity observed and the absence of symmetry in the EEDF derived shows that

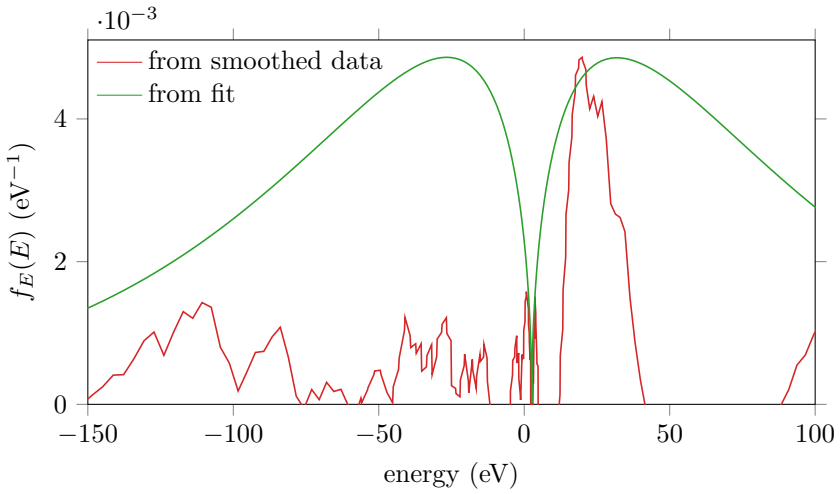

Figure 6.24: EEDF extracted from the Thomson spectrum shown in Figure 6.23.The green line shows the shape of the Gaussian fit and the red line the shape of the smoothed function shown in Figure 6.23.

the electron behavior may no longer respect this hypothesis. Still, we do present the distribution function associated with opposite electron displacements: in the "negative direction" (i.e., negative spectral shift) and "positive direction" (i.e., positive spectral shift). Indeed, this method and representation remains an efficient way to detect and quantify the anisotropic behavior of electrons. It is a unique feature of ITS diagnostic, not possible with other diagnostics such as Langmuir probes, for example. Contrary to the method used for the determination of the EVDF, the estimation of the one-dimensional electron velocity distribution function (1D-EVDF) requires a less restrictive hypothesis based on the independence of the electron behavior along the probed direction from the other orthogonal directions. Under this hypothesis, the 1D-EVDF is directly proportional to the Thomson spectrum distribution. However, such a distribution is less general and is not commonly used by the plasma simulation community.

6.5.2 Investigation at low discharge voltage with xenon

We have shown in Section 6.5.1 that the derivation of the EEDF is not reliable in the case of large distortions from plasma emission. A first path to consider in order to ease the derivation of the EEDF would be an increase of the plasma density. The takeaway information obtained from Section 6.4 suggested that operating at the lowest discharge voltage and highest discharge current gave access to the maximum plasma density inside the operable power range of the given thruster.

For this reason the investigations presented in this section focus on the operation of the ISCT200-MS at 150 V and 2.18 A (a discharge power of 327 W). These discharge conditions do not correspond to nominal values for which the performance of the thruster is optimal. Still, these lower-voltage conditions give access to EEDF investigations of the acceleration region and potentially, the chance to observe deviations from thermal equilibrium for electrons.

Figure 6.25 and Figure 6.26 show, respectively, the temporal profile and the corresponding power spectrum density of the discharge current for the chosen discharge conditions on the ISCT200-MS thruster with the magnetic field lines directed towards the inner pole. The discharge mode obtained is similar to what we obtained at 157 V during the discharge voltage exploration presented in Section 6.4.2.1 (see Figure 6.19 and Figure 6.20). Despite a 14 % increase in discharge power in the present case, we observe the same broad peak around 5×10^4 Hz and a sharp peak at frequencies just below 10^7 Hz with both discharge conditions.

6.5.2.1 Axial profile of electron properties

To verify the downstream shift of the acceleration region expected at a lower voltage, the axial profiles of electron properties were measured near the exit plane with the discharge conditions previously mentioned. The results from the axial exploration in the middle of the ISCT200-MS channel are presented

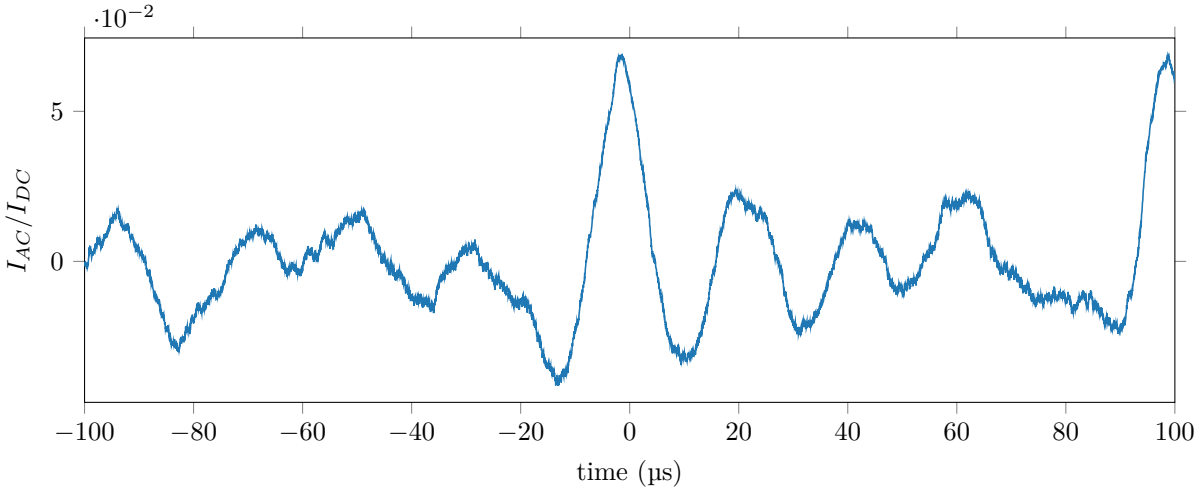

Figure 6.25: AC component of the discharge current for the ISCT200-MS operating under a voltage of 150 V and a xenon flow rate of 2.1 mg s^{-1}. The DC component of the current is 2.18 A and the magnetic field is directed toward the inner pole.

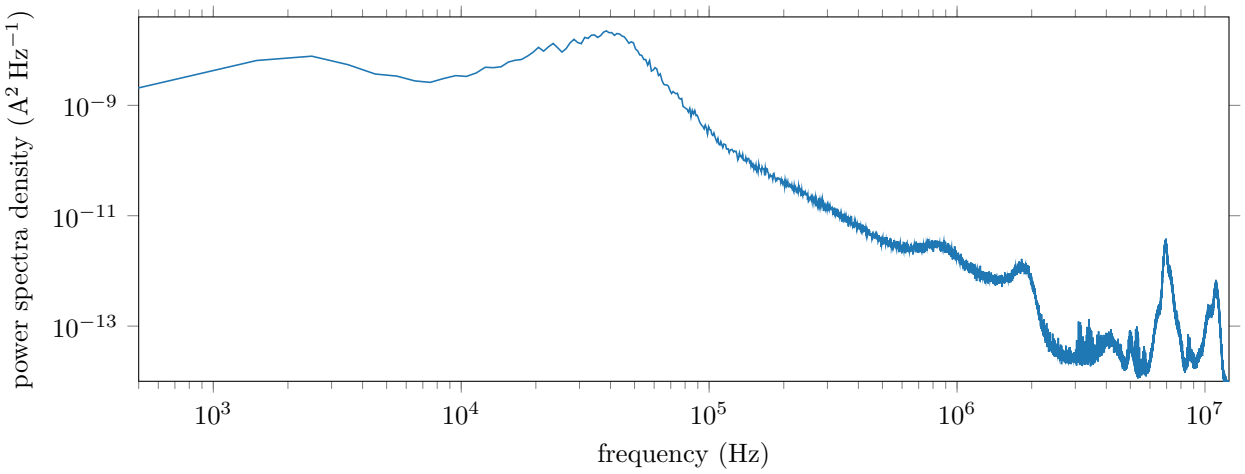

Figure 6.26: Power density spectra of the discharge current calculated from the temporal profile shown in Figure 6.25.

in Figure 6.27. Similar to Section 6.3.3, both directions of the magnetic field with the same discharge conditions were investigated. The thruster was operated with a xenon flow of 2.15 mg s^{-1} to reach a discharge current of 2.18 A at 150 V with the magnetic field directed toward the outer pole, while 2.1 mg s^{-1} was used for the magnetic field directed toward the inner pole to obtain the same discharge current.

With these discharge conditions, Thomson spectra with strongly non-Gaussian shapes near the exit plane were observed along the "azimuthal direction". For these spectra, with examples shown in Figure 6.28 for two opposite directions of the magnetic field and 2 mm from the exit plane, the reliability of a Gaussian fit is clearly questionable. For this reason, an alternative method, based on the analysis of the Thomson spectrum distribution for the estimation of the electron temperature and drift velocity, was used. A Savitzky-Golay filter was applied to the data to smooth the Thomson distribution and obtain an analytic distribution function of the spectrum, following interpolation by the Gaussian fit values inside the rejection interval around 532 nm. The integral, mean ($\lambda_{0,d}$) and standard deviation ($\Delta\lambda_{g,d}$) of the distribution were then estimated. From these parameters, equivalent to what is obtained from the Gaussian fit, alternative values of the electron density, temperature and drift velocity were calculated using similar equations. The blue squares shown in Figure 6.27 indicate the electron properties obtained from

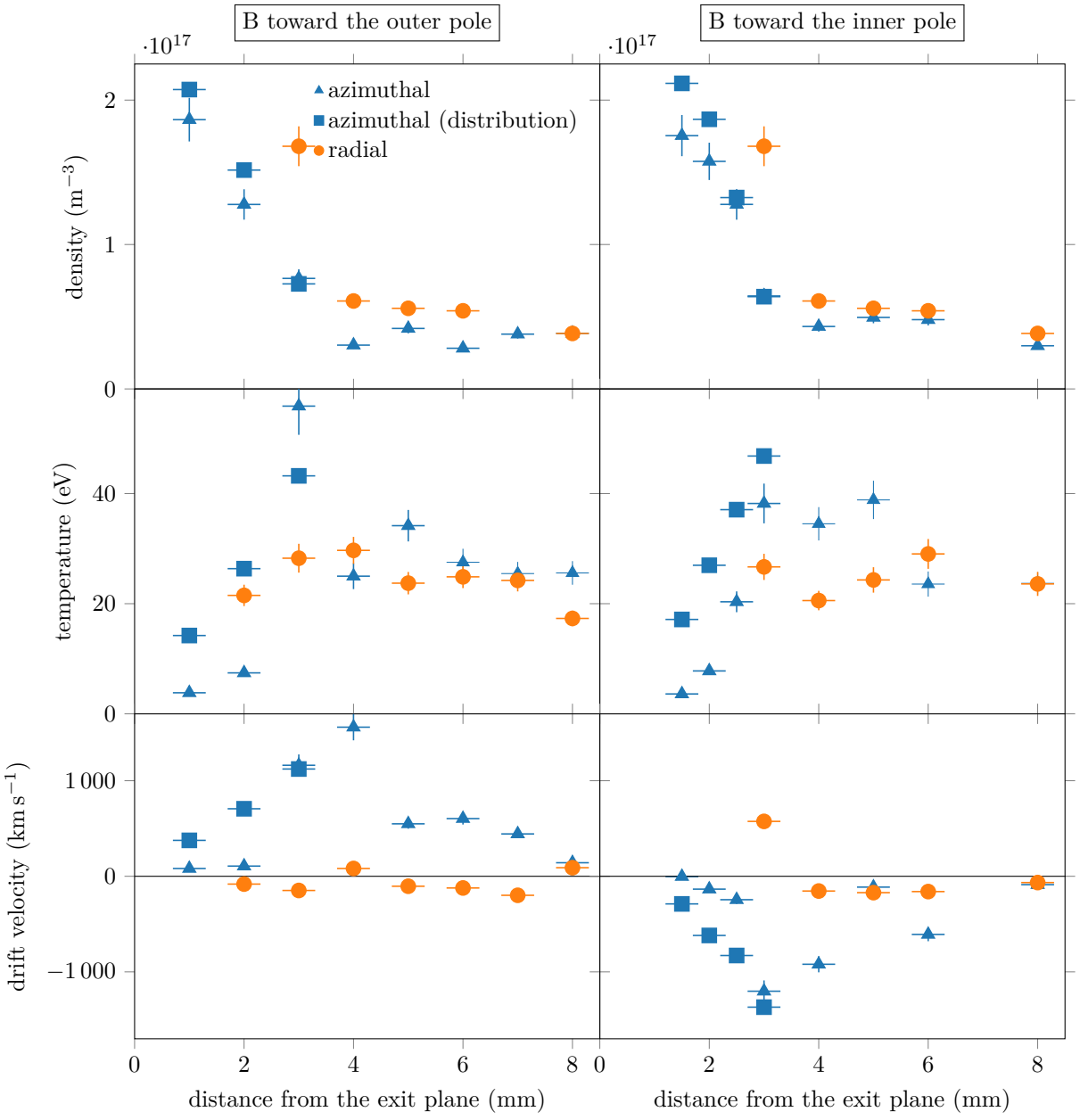

Figure 6.27: Axial profile of electron temperature, density and drift velocity measured for two opposite directions of the magnetic field with the ISCT200-MS thruster operating at 150 V and 2.18 A. The "azimuthal" and "radial" values were determined from the Gaussian fits applied to the spectra acquired in, respectively, the azimuthal and radial scattering configurations. The "azimuthal (distribution)" values correspond to values estimated from an analysis of moments of the smoothed Thomson spectrum distribution.

this method.

Similar to what was observed at 250 V in Section 6.3.3, the axial profile of electron density seems to be almost insensitive to the direction of the magnetic field. However, a slightly steeper increase near the exit plane for magnetic field lines directed toward the inner pole is apparent. A comparison with the profile measured at 250 V (see the first row in Figure 6.27) on the same thruster confirms the increase of electron density at lower voltages (with a constant power) deduced from the voltage investigations of Section 6.4.2. The steep increase of density close to the exit plane suggests that we may be probing the beginning of the acceleration region. In this region of strong deviation from Gaussian spectrum shape, the method used for estimation of the density has a negligible effect on the value obtained.

For the electron temperature, for the first time, a clear increase in the temperature with increasing distances from the exit plane is observed. The temperature increases almost linearly from approximately 1 mm to 3 mm where it reaches a plateau above 20 eV. This increase of electron temperature suggests that electrons subjected to the increasingly high electric field of the acceleration region were probed. The absolute value is again similar for both magnetic field directions, but the variations are again steeper with the case where the magnetic field is directed toward the inner pole.
The electron temperature obtained from the analysis of the Thomson spectrum distribution is usually much higher. For example, 2 mm from the exit plane, the Gaussian fit method gives 7.8 eV while the distribution method gives 27 eV. This large difference comes from the wings at large wavelength shifts that are not taken into consideration with the shape of the Gaussian fit. This Thomson spectrum distribution does not correspond to any canonical shapes and highlights the fact that electrons are out of thermal equilibrium at these axial locations.

The electron drift velocities estimated at a discharge voltage of 150 V are lower than those at 250 V. Still, if we consider that the drift arises mainly from the $\vec{E} \times \vec{B}$ contribution, the decrease is less significant than expected with a simple cross multiplication. We can explain this relatively large value by the fact that while it is possible to probe the electric field maximum at lower voltages, the maximum may have remained inaccessible at 250 V. Near the exit plane, we can explain the linear increase of the absolute of the drift velocity at 150 V by the broader acceleration region in low voltage operation, such that the electric field may increase progressively up to a maximum at approximately 3 mm from the exit plane. The downstream shift and broader profile of the electric field at lower voltages has already observed in LIF measurements in Hall thruster discharges operated at various voltages [220, 221].
Similar to the temperature, the electron drift velocity estimated from the mean of the spectrum distribution is much higher than the value estimated from the Gaussian fit. The tails on the spectrum, associated with highly energetic electrons, are again at the origin of this disparity. For both magnetic field directions, the drift velocities estimated have similar absolute values but opposite directions along the "azimuthal direction". This arises from the reversal of the $\vec{E} \times \vec{B}$ direction. Again, the variations are steeper with the magnetic field directed toward the inner pole, possibly consistent with the presence of a sharper electric field profile with this magnetic field direction.

Because we systematically investigated electron properties along "azimuthal direction" and "radial direction", it is possible to discuss the anisotropy of electron behavior quantitatively for this exploration. The weak anisotropy on electron density observed has no physical meaning; it may arise from either an inhomogeneity of the plasma between the two scattering configuration positions or a small axial displacement when the thruster is moved between the two scattering configurations. The anisotropy in electron temperature is relatively small, but on average, it seems that the temperature is higher along the "azimuthal direction". In contrast, for the electron drift velocity, the anisotropy is large and systematic. While almost no drift is observed along the "radial direction", electron drift velocities of up to 1200 $\mathrm{km\,s^{-1}}$ are observed in the "azimuthal direction". This phenomenon can easily be explained by the large $\vec{E} \times \vec{B}$ drift. This anisotropy of the drift velocity may contribute to the weak anisotropy observed for the temperature.

6.5.2.2 Derivation of the EEDF

As previously mentioned, the use of a magnetically shielded thruster at low discharge voltage allows a downstream shift of the acceleration region and an increase of the electron density (i.e., an increased signal from Thomson scattering and the ability to probe the acceleration region). These non-standard experimental conditions favor the observation of a clear deviation of the Thomson spectrum from a Gaussian distribution. Such distortions do not arise from an imperfect subtraction of the plasma emission

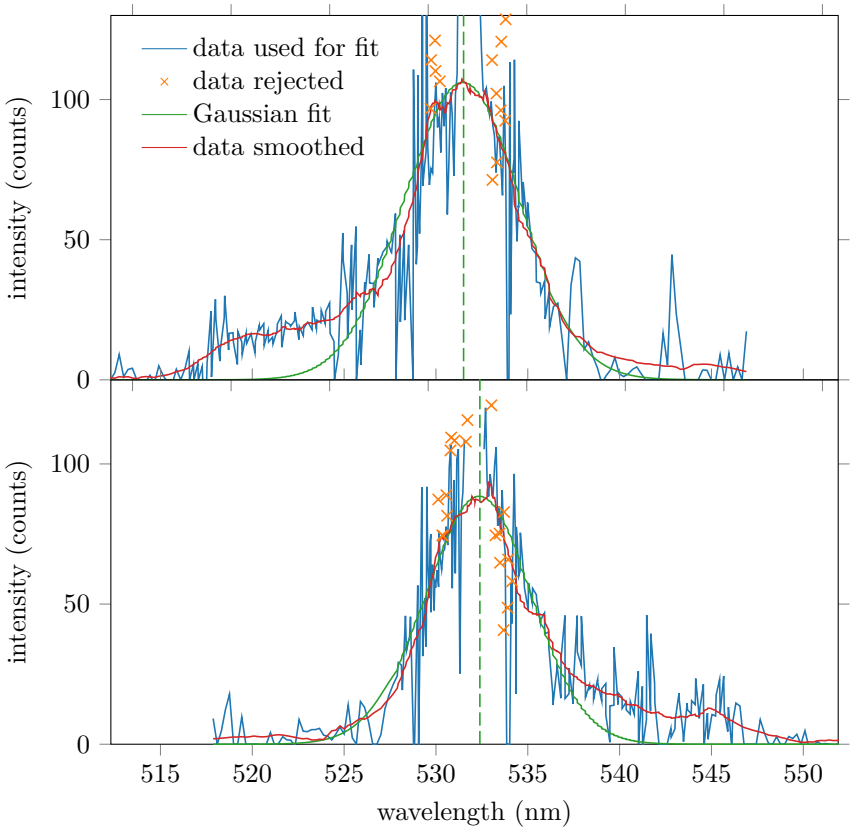

Figure 6.28: Thomson spectra obtained along the "azimuthal direction" 2 mm from the exit plane of the ISCT200-MS, for a discharge voltage of 150 V and a discharge current of 2.17 A. The Gaussian fit and the position of its center are shown with respectively a solid and dashed (vertical) green line. Top: magnetic field lines directed towards the inner pole and injection of a xenon flow of $2.1\,\mathrm{mg\,s^{-1}}$ near the anode; the Gaussian fit gives n_e=$(1.6 \pm 0.1) \times 10^{17}\,\mathrm{m^{-3}}$, T_e =$(7.9 \pm 0.7)\,\mathrm{eV}$ and $v_{e,drift}$ =$(130 \pm 20)\,\mathrm{km\,s^{-1}}$. Bottom: magnetic field directed towards the outer magnetic pole (xenon mass flow rate was adjusted to $2.15\,\mathrm{mg\,s^{-1}}$ to keep the discharge current at the nominal value); the Gaussian fit gives n_e=$(1.3 \pm 0.1)\,\mathrm{m^{-3}}$, T_e =$(7.4 \pm 0.7)\,\mathrm{eV}$ and $v_{e,drift}$ =$(110 \pm 20)\,\mathrm{km\,s^{-1}}$.

records. As shown in Figure 6.28, at similar discharge conditions, but with a reversed magnetic field, the spectral side associated with the non-Gaussian tail reverses. This observation shows that this distortion has a physical meaning and is related to the direction of the $\vec{E} \times \vec{B}$ drift.

Because the shape of the Thomson spectrum does not follow any canonical distribution (fully defined with the temperature and drift velocity), it becomes less relevant to try to fit it with a given function. Instead, it is more relevant to estimate the EEDF associated with this spectrum shape. From the method presented in Chapter 3 we calculated the EEDF associated with the spectra of Figure 6.28. Figure 6.29 shows the distributions calculated from these spectra. The green line corresponds to the EEDF calculated from the Gaussian function used for the fitting (i.e., under the hypothesis of thermal equilibrium). We normed this analytic function such that its integral is 1. The red line represents the experimental EEDF calculated from the derivative of the smoothed Thomson spectrum shape. To ease the comparison, this function was multiplied by a coefficient so that both the red and green lines have the same maximum value.

For both directions of the magnetic field, the experimental EEDFs obtained exhibit an asymmetric shape relative to the vertical line at 0 eV.
Along the direction associated with the $\vec{E} \times \vec{B}$ drift, systematic dips in the low energy side make the density for this energy range lower than in the case of thermal equilibrium. In contrast, for the high energy side, a hump around 40 eV, present for both magnetic field directions, makes the density higher than the case at thermal equilibrium. The other broad humps visible around 80 eV may have a physical

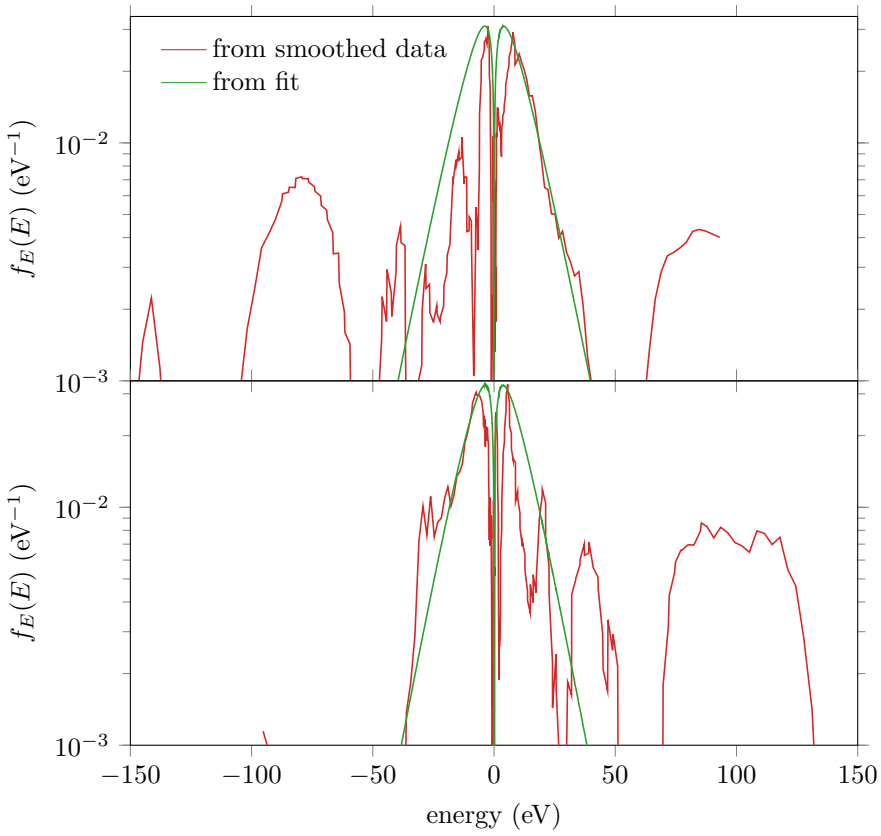

Figure 6.29: Estimated EEDF derived from the Thomson spectra presented in Figure 6.28. The green lines correspond to the spectrum calculated from the theoretical Gaussian fit. The red lines are the EEDF obtained from the derivative of the smoothed shape of the Thomson spectra. Top: magnetic field lines directed towards the inner pole. Bottom: magnetic field directed towards the outer pole.

meaning, however, the decreased signal-to-noise ratio associated with these spectral shifts (at the end of the tail, 13 nm from the laser wavelength) would make its interpretation less reliable.
Along the opposite direction of the drift velocity, for both magnetic field directions, the distributions follow a shape relatively close to what we expect for electrons at thermal equilibrium. This observation suggests that, in addition to not being isotropic, electron behavior is not symmetric along a given direction. This absence of symmetry has a deeper significance than only a macroscopic drift of electrons that would be at thermal equilibrium.

In our team, investigations on the ISCT200-GEO operated at 200 V and with 1 mg s^{-1} of xenon, with Langmuir probes installed on a fast-moving translation stage, were performed to measure the electron energy probability function from the acceleration region to the plume [197]. Despite the difference in the discharge conditions and thruster magnetic configuration, multiple humps in the distribution, including one at 40 eV, were also observed. This hump at 40 eV was observed in the acceleration region (positioned inside the channel for the ISCT200-GEO), 0.9 mm upstream of the exit plane. This hump was explained by electrons produced inside the thruster channel and subsequently accelerated by the electric field of the acceleration region. With our ITS diagnostic, it was necessary to operate the ISCT200-MS at low discharge voltage, to be able to probe the acceleration region and observe similar shapes in the EEDF. As with the Langmuir probe measurement, we observed multiple humps in the distribution, also with one hump at approximately 40 eV for both magnetic field directions. These multiple humps in the energy distribution of electrons may be characteristic of the acceleration region, independent of the thruster design and discharge voltage. However, the number and exact position of the humps seems difficult to predict. As shown in Figure 6.29, with the discharge conditions unchanged, even a simple reversal of the magnetic field direction can affect the exact position of some humps.

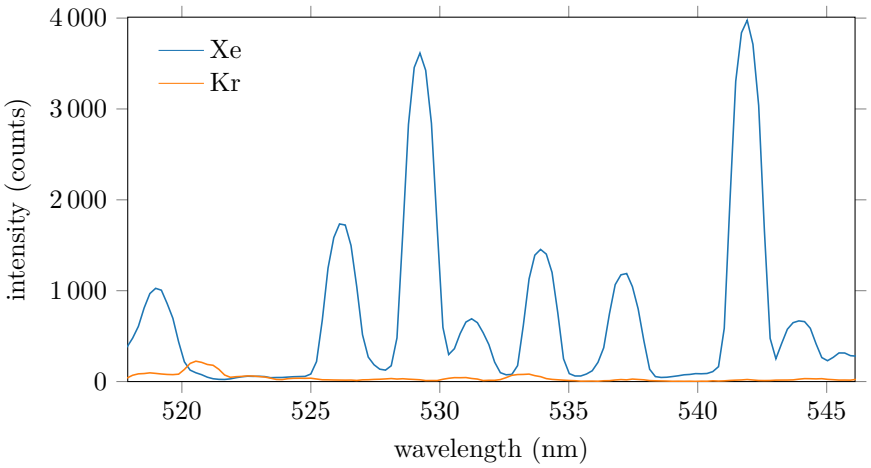

Figure 6.30: Comparison of the plasma emission spectrum measured from the discharge of an ISCT200-MS thruster operating under xenon and krypton flow. Both spectra were acquired at 1.5 mm from the exit plane with the thruster operating at 150 V and 2.18 A.

6.5.3 Investigation at low discharge voltage with krypton

We have shown in Section 6.5.2 that the investigation of discharge conditions at low voltages reduced the relative contribution from plasma emission, by increasing the Thomson signal intensity from an increased plasma density. Small distortions of the Thomson spectrum from plasma emission remained, however, the increased signal allowed a more reliable estimation of the EEDF.

In this section, minimization of the absolute intensity of plasma emission is attempted. To do so, the thruster was operated with krypton, a heavy noble gas with a relatively low first ionization energy and one of the main alternatives to xenon. For some types of missions, the significantly lower price of this propellant can balance the reduced efficiency reported for Hall thrusters operated with krypton [224].

For comparison, the ISCT200-MS was operated with the same discharge conditions as Section 6.5.2, instead using krypton and with the magnetic field directed toward the outer pole. Operation at 150 V and 2.18 A required the injection of a krypton mass flow rate of 1.49 mg s^{-1}. The cathode element was operated with krypton at a mass flow rate of 0.2 mg s^{-1} and heating power of 130 W.

The intensity of plasma emission lines was characterized with record C using the same detection branch parameters as for the Thomson scattering acquisition (record A). The signal from plasma emission was isolated by a subtraction of the electronic noise acquisition (record B). Figure 6.30 shows a comparison of the emission spectra measured with xenon and krypton with the same discharge conditions. These spectra were measured for the discharge conditions previously presented, at 1.5 mm from the exit plane and with the scattering configuration used for the investigation of azimuthal properties of electrons. The spectrum with xenon shows that even during the camera gating window of few nanoseconds, the intensity of some plasma emission lines can be two orders of magnitude higher than the order of magnitude of the Thomson scattering intensity detected at the same position (typically 40 mm at 1.5 mm from the exit plane). This observation explains the sensitivity of the Thomson spectra to the weak fluctuations in the level of plasma emission. In contrast, inside the spectral range scanned for Thomson spectrum detection, the signal from plasma emission lines with krypton remains relatively low. The most intense emission line with krypton reaches only 200 counts and is spectrally far from the bulk of the Thomson spectrum (around 521 nm). These observations suggest that if the plasma reaches similar electron density levels with krypton, the Thomson spectrum will be much less affected by plasma emission lines fluctuations.

6.5.3.1 Axial profile of electron properties

As in Section 6.5.2, the axial profile of electron properties at a low discharge voltage was investigated, now using krypton. The investigation was performed with the typical low discharge voltage conditions mentioned previously. Figure 6.31 shows the corresponding axial profile. Despite the change of gas, deviations of the spectrum from the Gaussian shape remain strong for a short distance from the exit

distance from the	Gaussian fit			Distribution analysis		
exit plane (mm)	$n_e(\mathrm{m}^{-3})$	$T_e(\mathrm{eV})$	$v_{e,drift}(\mathrm{km\,s}^{-1})$	$n_e(\mathrm{m}^{-3})$	$T_e(\mathrm{eV})$	$v_{e,drift}(\mathrm{km\,s}^{-1})$
1	8.9×10^{16}	7.8	190	1.0×10^{17}	23	490
1.5	6.8×10^{16}	17	340	7.3×10^{16}	33	640
2	5.4×10^{16}	19	460	5.7×10^{16}	32	630
2.5	5.0×10^{16}	29	640	5.2×10^{16}	40	860

Table 6.1: Comparison of the electron properties estimated from the Gaussian fit and from the analysis of the moments of the smoothed Thomson spectra. These values were determined with Thomson spectra corresponding to the "azimuthal direction" of observation, at distances ranging from 1 mm to 2.5 mm from the exit plane (see Figure 6.32).

plane and when the probing wave vector is along the "azimuthal direction". Figure 6.32 shows examples of the Thomson spectra obtained with krypton for distances from the exit plane from 1 mm to 2.5 mm, for observation along the "azimuthal direction". These similar deviations, observed even with krypton, are additional proof that the non-thermal electron behavior measured does not merely arise from a poor subtraction of plasma emission lines. For these cases with large distortions, in addition to the values estimated from the Gaussian fit method, the electron properties estimated from the analysis of the Thomson spectrum moments are also shown with blue squares in Figure 6.31. Table 6.1 details the large differences in the estimated electron parameters depending on the method used for the analysis of the Thomson spectra. Once more, it illustrates the weakness of the Maxwell-Boltzmann EVDF for electrons in the acceleration region of a Hall thruster. For this reason, we will present the true EEDF in the next section.

In comparison to identical discharge conditions with xenon, the plasma density obtained with the krypton is almost twice lower. We can explain this reduced density by the increased proportion of the discharge power used for ionization of krypton; its first ionization needs electrons with 14.0 eV of energy, while xenon needs only 12.1 eV. Surprisingly, despite the higher first ionization energy, the electron temperature with krypton is slightly lower than with xenon. The drift velocity is also lower with krypton. These observations suggest that the electric field is less intense with krypton. A broader electric field profile because of a weaker electron confinement could explain this behavior.

6.5.3.2 Derivation of the EEDF

As shown previously, the Thomson spectra measured with krypton are weakly affected by plasma emission lines while remaining relatively intense at low discharge voltages, near the exit plane of the thruster. These conditions are favorable for a more robust and cleaner estimation of the EEDF. Figure 6.33 shows examples of the EEDF estimated from the spectra shown in Figure 6.32.

Similar to what was observed in Section 6.5.2.2 with xenon, the EEDF obtained with krypton is also systematically more distorted along the direction associated with the $\vec{E} \times \vec{B}$ drift. A distribution with multiple humps is again visible along the drift direction. The energy of the first hump is a few electronvolts below the hump observed with xenon but is systematically observed. Under the hypothesis that this population comes from electrons generated inside the acceleration region and subsequently accelerated [197], the lower energy of this low energy hump obtained with krypton is consistent with the lower drift velocity measured, suggesting a lower electric field. A broadband electron population is again observed around 100 eV, which may suggest that this population, already observed with xenon, is not an artifact. The density of electrons corresponding to this population around 100 eV seems to increase at closer distances to the exit plane. Investigations further upstream, in the ionization region, could likely strengthen this observation. Even in the shielded configuration at low voltage, this region was not accessible. The study of a Hall thruster discharge in wall-less configuration [225, 226] at low voltage may give access to the complete axial profile of electron properties inside the ionization, acceleration and plume region.

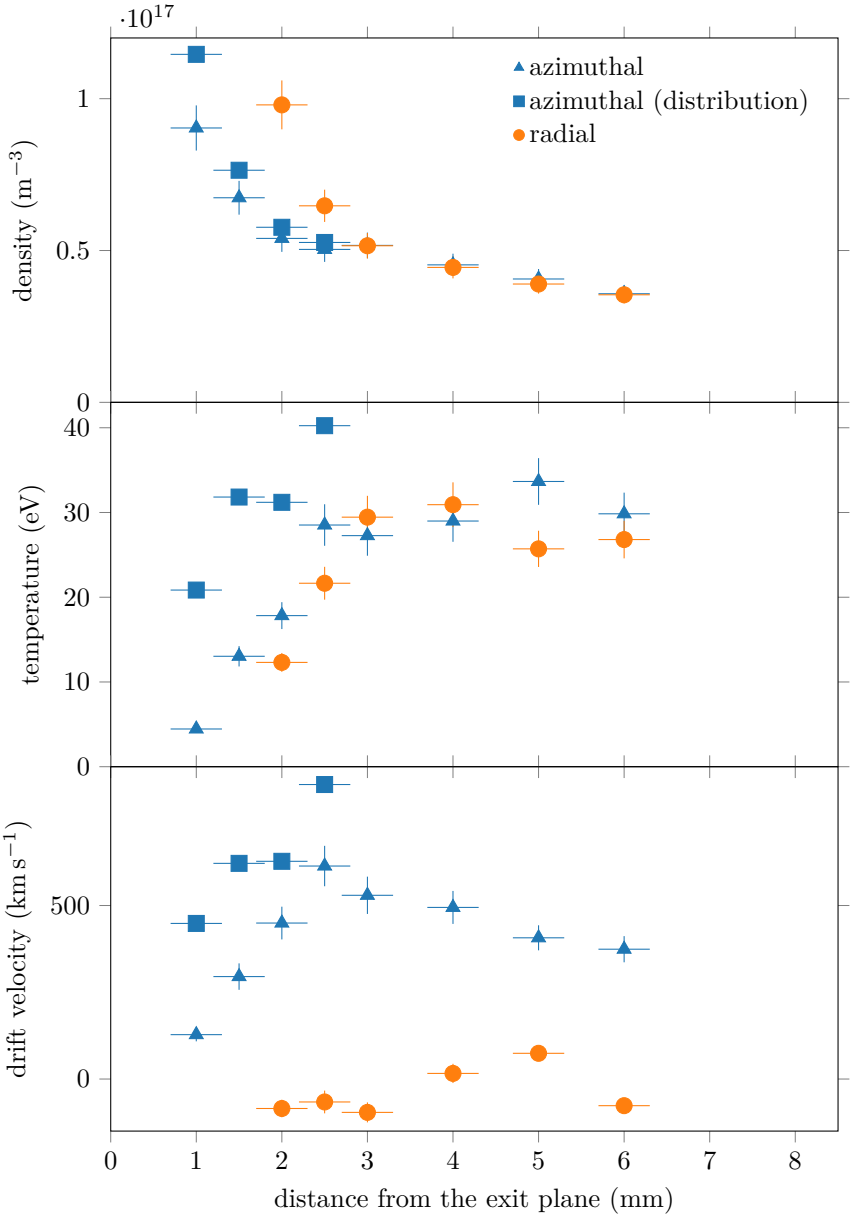

Figure 6.31: Axial profile of electron temperature, density and drift velocity measured with the ISCT200-MS thruster operating at 150 V and 2.18 A with krypton. The "azimuthal" and "radial" values are obtained from the parameters of the Gaussian fit applied to the spectrum acquired with respectively the azimuthal and radial scattering configurations. The "azimuthal (distribution)" values are obtained from an analysis of moments of the Thomson spectrum distribution.

6.6 Conclusion

In this chapter, we presented the results from the first in-depth study of Hall thruster electron properties with an ITS diagnostic. The main difficulties encountered during these investigations arose from both the low density of the plasma and the intense light emission from the xenon plasma, which may vary during acquisition and distort the estimated Thomson spectra. We introduced methods to mitigate these effects.

A study with various magnetic field intensities showed that, for identical discharge conditions, low frequency current oscillations correlate with higher electron densities and fewer fluctuations in the electron temperature downstream in the plume. A comparison of the axial profile of electron properties obtained

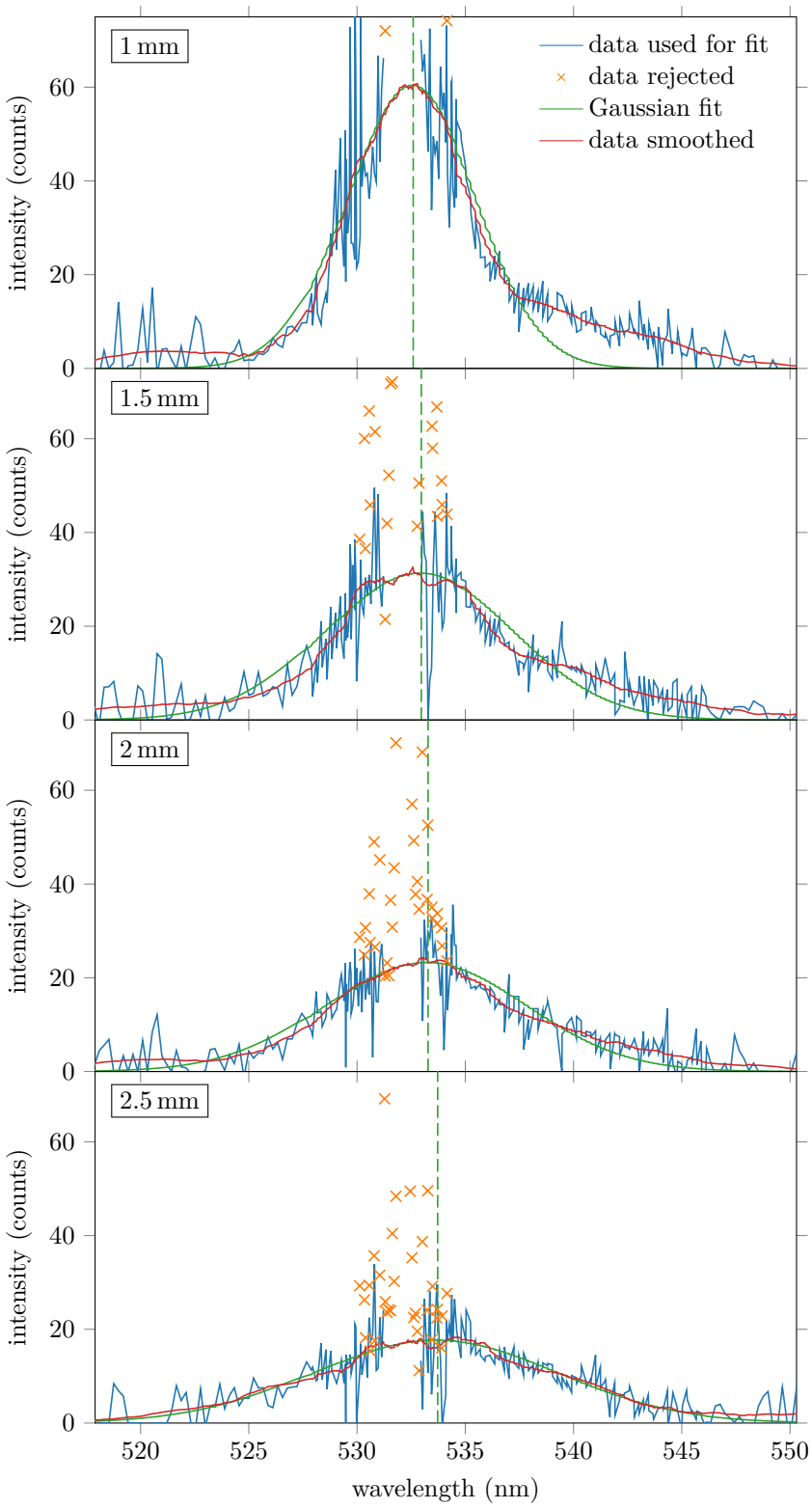

Figure 6.32: Thomson spectra measured at the scattering configuration for estimation of electron properties along the "azimuthal direction" with the ISCT200-MS thruster operating at 150 V and 2.18 A under a krypton flow. The Gaussian fit and the position of its center are shown with respectively a solid and dashed (vertical) green line. Measured spectra as well as the Gaussian fit and function obtained from the smoothing procedure are shown for distances from 1 mm to 2.5 mm from the exit plane.

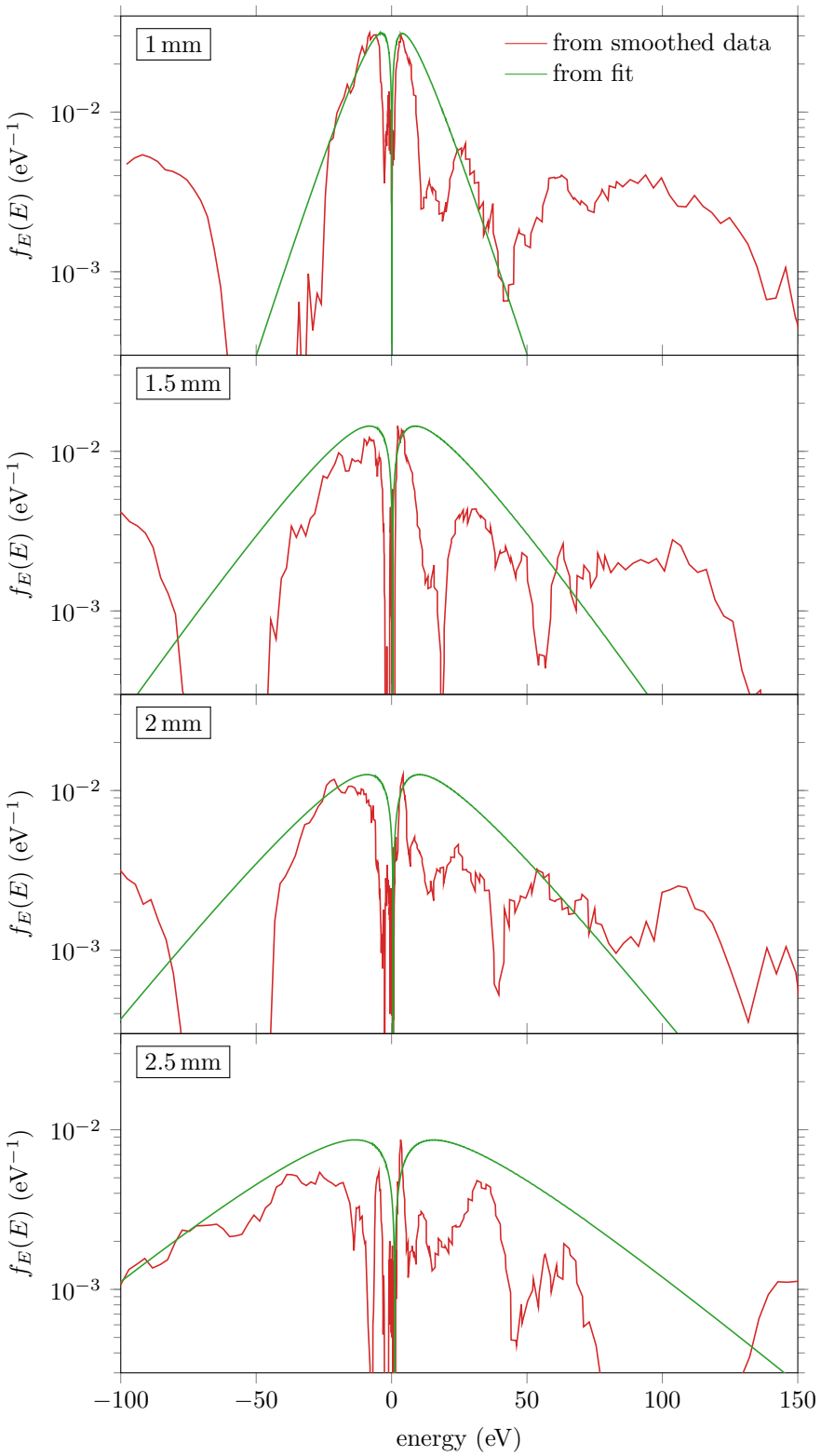

Figure 6.33: EEDF calculated for the spectra shown in Figure 6.32. The EEDF from the Gaussian fit and that derived from the smoothed shape of the spectrum are shown with a green and red line, respectively.

with standard and shielded magnetic configuration proved the downstream shift of the discharge with shielded configuration. This downstream shift gave access to part of the acceleration region. In this region, the $\vec{E} \times \vec{B}$ was strong enough to induce an overall Doppler shift of the Thomson spectrum that could be detected with our diagnostic. Studies with a reversed magnetic field direction demonstrated that the $\vec{E} \times \vec{B}$ drift was the main contribution to the Doppler shift observed.

An investigation, at a fixed axial position, of the influence of the discharge conditions on the electron properties was performed. The increase of the discharge power at a fixed mass flow rate of gas seems to mainly increase the electron temperature. With an increase of the discharge voltage at a fixed power, we observed a decrease in the electron density, an increase in the electron temperature, and a displacement of the discharge in the upstream direction.

At low voltages, strong deviations of Thomson spectra from the typical Gaussian shape were observed in the acceleration region in the "azimuthal direction". These observations indicate the presence of electrons out of thermal equilibrium. Various methods to quantify this phenomenon were used. The derivation of the EEDF was used, however, distortions from poor subtraction of plasma emission lines, more significant with xenon, can be amplified and lead to artifacts in the estimated EEDF. The use of krypton instead of xenon to sustain the discharge was proposed as an efficient method to mitigate the contribution from this source of stray-light and obtain more reliable EEDFs.

Conclusion

I have offended God and mankind because my work did not reach the quality it should have.

— *Leonardo da Vinci, Italian artist and scientist*

Contents

Summary

This dissertation has shown the possibility of developing a compact ITS diagnostic with a sufficiently large sensitivity for the study of various low-pressure plasma sources. The multiple implementations discussed in this work have proven the sensitivity of the diagnostic down to the $10^{15}\,\mathrm{m}^{-3}$ range. The flexibility of the setup allowed investigation of electron temperatures from below 1 eV to approximately 100 eV.

In the plasma sources on which this diagnostic was implemented, the electron dynamics are the key parameters to explain and understand most of the physics and behavior of the discharge. For this reason, knowledge of their properties, such density, temperature and drift velocity, are critical. An experimental investigation of these parameters, followed by a comparison with the values extracted from simulations, will be key for the validation of predictive simulations to be applied to source development and design. To measured electron properties, several diagnostics already exist. Incoherent Thomson scattering is the only diagnostic technique which provides access to thermal properties of electrons or even their EEDFs with negligible perturbation and with a high spatiotemporal resolution. The directional sensitivity of this diagnostic is another key feature for investigations of magnetized plasma sources where expected anisotropic behavior of electrons is expected.

The theory behind an ITS diagnostic is relatively simple. It involves the elastic scattering of photons by free electrons in the incoherent regime. The scattering configuration, defined by the relative direction between the incident and scattering wave vector, sets the characteristics of the probed wave vector. The norm and direction of this vector give information on both the spatial scale and direction of the electron fluctuations probed. For all the investigations of this thesis, the Debye screening length was much larger than the probed wave vector length scale, providing access to the incoherent regime, where, under the hypothesis of a Maxwell-Boltzmann distribution, Gaussian fits give access to the thermal properties of electrons. Under the hypothesis of isotropic electron behavior, the derivative of the Thomson spectrum is directly related to the EEDF.

As with most ITS diagnostics, the transmission branch of the diagnostic developed in this thesis, named THETIS, uses light from a pulsed Q-switch laser to generate the Thomson scattering signal. The choice of the laser wavelength (532 nm) was motivated by the necessity to be in the incoherent regime and the availability of detectors with high quantum efficiency. A key element of the detection branch of this diagnostic uses a recently-commercialized type of notch filter to attenuate stray-light from reflection and Rayleigh scattering at the laser wavelength. Coupled to a single grating spectrometer

for dispersion and an intensified camera for detection, this disruptive technology allows for a much more compact ITS diagnostic than any diagnostic based on triple grating spectrometers. The use of a gated intensified camera is another key feature necessary for the mitigation of stray-light from plasma emission. For calibration of the transmission efficiency of the detection branch, Raman scattering was used, with an identical acquisition configuration to Thomson scattering measurements. Thomson spectra were systematically analyzed by the optimization of a Gaussian fit for estimation of electron density, temperature, and drift velocity. For the cases with a strong enough signal-to-noise ratio, we presented a method using a smoothing and derivative procedure of the Thomson spectra, based on a Savitzky-Golay filter, to compute the electron velocity or energy distribution functions. The importance of limitations related to laser induced plasma perturbation and spectrum distortion in the presence of magnetized electrons relevant to our setup was discussed.

The first implementation of the THETIS diagnostic on a magnetized low-temperature plasma source was performed on a planar magnetron. Both the DCMS and HiPIMS discharge regimes were investigated. While the presence of parasitic lines inhibited early investigations in the DCMS regime with argon, studies in the DCMS regime with helium gas illustrated the high sensitivity of the diagnostic in low density plasmas, down to the $10^{16}\,\mathrm{m}^{-3}$ range.
Investigations with the HiPIMS regime were performed with both argon and helium. We efficiently resolved the entire spatiotemporal variations of electron properties in some HiPIMS pulses, illustrating the diagnostic resolution down to the millimeter spatial scale and microsecond temporal scale for repeatable plasma pulses. Observation of strong shifts of the entire Thomson spectra allowed the estimation of the electron drift velocity as well as weak distortions of the estimated EVDF from the Maxwell-Boltzmann case. Under some assumptions, it was possible to estimate values of drift velocities to estimate the axial profile of the electric field along the axial direction. In HiPIMS regimes, a study with increasing intensity of the magnetic field showed decreasing electron density for larger magnetic field intensities.

From the implementation of the THETIS diagnostic on an ECR ion source, we investigated aspects such as the influence of the H_2 pressure on electron properties. In pulsed mode, a weak increase of plasma density at a lower pressure was observed. While the influence of pressure on the ignition phase was not resolved because of the jitter of the microwave generator, analyses of the plasma emission spectra showed an influence of the pressure on the relative intensity between lines from the vibrational bands and lines from the Balmer series at the ignition phase. This suggests an interesting transition that requires further investigation. In DC operation, within the stability range of the discharge, weak dependencies of the electron properties on the gas pressure and RF power were identified.
Studies with other gases such as He and Ar performed in this work suggested that the ignition is faster for monoatomic gases, which we explained as a product of the fewer processes available for electron energy dissipation in such species.

For Hall thruster studies, the THETIS diagnostic was used to investigate aspects such as the influence of the magnetic field intensity, configuration, and direction. The axial profiles of electron properties estimated showed that the optimal discharge condition, with low oscillations of the discharge current, is associated with a larger plasma density profile and weaker fluctuations in the electron temperature. For a Hall thruster operated with a magnetic shielding configuration, a downstream shift of the axial profiles was observed. This shift gave access to part of the acceleration region where strong drift velocities were observed along the "azimuthal direction". Investigation with a reversed magnetic field direction proved that the $\vec{E} \times \vec{B}$ drift is the main contribution to this drift velocity.
A study on the influence of discharge power at a fixed mass flow rate was also performed. The estimated electron density did not significantly increase at higher power, with most of the power increase contributing to electron heating. Investigations at a fixed power, with a varying mass flow rate, showed a clear increase in the electron density and velocity and a decrease in the temperature when the mass flow rate increases. Some of the observations made suggested a displacement of the whole discharge. The downstream displacement observed with low voltage discharge conditions allowed the investigation of electron properties further upstream in the acceleration region. In this region, with a large electric field, we observed strong deviations of the Thomson spectrum from the Gaussian shape. The robustness of these observations was reinforced by similar observations made with a reversed magnetic field direction and a different discharge gas.

Perspectives

This work focused on the design of a VBG-NF-based ITS diagnostic and illustrated its performance, which is equivalent to the best ITS diagnostics ever built. However, it remains a first version of the diagnostic, and room for improvement remains.
For the transmission branch, a further increase of the laser pulse energy may lead to perturbation for the plasma sources investigated in this thesis. Nonetheless, more compact Q-switch lasers with higher repetition rate but similar pulse energy would respectively ease the alignment procedure and reduce the duration of accumulations.
For the detection branch, the use of an intensified CCD camera with higher quantum efficiency would allow a four-fold increase in the diagnostic sensitivity. Other paths such as the increase of the size of the notch filter as well as the direct imaging of the observation volume on the spectrometer entrance slit would lead to fewer photon losses and contribute to an increased sensitivity.
The application of several of these solutions for improvement could lead to sensitivity down to the $10^{14}\,\mathrm{m}^{-3}$ range.

Due to limitations on the durations of the experimental campaigns and configurations of the plasma sources studied, some interesting investigations were not performed and would require further study.

For planar magnetron discharges, from a plasma source point of view, key pieces of information could be obtained on pre-sheath behavior with a guard ring positioned at the same axial position as the target anode disc. However, the changes induced in the plasma discharge behavior should be first investigated. Also, adding two translation degrees to the plasma source, similar to what was available with Hall thruster investigations, would ease the positioning at two different scattering configurations dedicated to investigations of purely azimuthal and radial electron properties. From these added degrees of translation, probing electron behavior over the revolution axis of the magnetron, up to the null magnetic field position, would give information on the impact of demagnetization on electron properties. As discussed in Section 3.6.2.2, measurements near the target (on the axis of the magnetron) may allow observation of modulations inside the Thomson spectrum due to the magnetic field, and could possibly be applicable to obtaining information on the magnetic field.
The explorations presented in this thesis focused on the impact of the discharge regime and magnetic field intensity on electron properties. However, further investigations in DCMS should be performed. As an example, the lines observed in the Thomson spectra obtained with argon are not yet fully explained. The presented explanation based on the formation of molecules such as Ti_{02} needs verification with investigations on a magnetron equipped with other targets materials, for example. In the HiPIMS regime, a broader range of magnetic field intensities could complete the investigations performed in this thesis. Finally, more parametric studies on the influence of the background pressure, repetition rate and pulse duration may help to understand their influence on ignition and afterglow dynamics.

For the ECR ion source investigation, the next campaign will aim to study the same plasma source, but in extraction mode. With the differential pumping induced by the extraction, we may obtain lower pressures inside the plasma chamber. According to the trend observed, it may lead to a higher plasma density. More importantly, operation in extraction mode is more relevant to accelerator applications and would be the source of new insights into electron behavior.
Using a solid-state based microwave generator may lead to a more stable discharge and allow for a more precise resolution of the temporal profile of electron properties during the ignition and extinction phases. The use of a higher frequency of the microwave generator would give access to higher plasma density and ease investigations on such plasma sources. Finally, the deposition of copper over the window used for transmission of the scattered light needs to be mitigated in order to reduce progressive degradation of the detection branch transmission coefficient; this might be achieved with the use of a shutter or by positioning the window further away from the plasma volume.

Studies on the Hall thruster focused on the two main magnetic configurations of Hall thrusters. Investigations on thrusters in the so-called "wall-less" configuration should give access to a broader axial profile of electron properties, including part of the ionization region and the whole acceleration region. During this thesis, electron properties were estimated only above the mean diameter of the channel of the discharge; the high erosion observed over the central pole of the thruster (particularly in magnetic shielding configuration) would motivate a study of electron properties in the pole regions. Observations further downstream of the thruster axis could give interesting information on the region where the diametrally opposite plasma beams merge and generate the luminous elongated plume inside a region with a weak

magnetic field intensity. Finally, using a similar setup to that used for time-resolved LIF measurements, the plasma discharge could be stabilized in order to perform time-resolved measurements of electron properties by Thomson scattering. Such an implementation, already under study, could provide insights into the impact of rotating spokes on electron properties. Similar investigations on planar magnetron discharges are possible.

Appendix A

List of publications

> I have no trouble publishing in Soviet astrophysical journals, but my work is unacceptable to the American astrophysical journals.
>
> —*Hannes Alfvén, Dean of the Plasma Dissidents*

Journal articles (published)

- B. Vincent, S. Tsikata, S. Mazouffre, S. Mazouffre, T. Minea, and J. Fils, *"A compact new incoherent Thomson scattering diagnostic for low-temperature plasma studies," Plasma Sources Science and Technology,* vol. 27, no. 5, p. 0055002, may. 2018.

- S. Tsikata, B. Vincent, T. Minea, A. Revel, and C. Ballage, *"Time-resolved electron properties of a HiPIMS argon discharge via incoherent Thomson scattering," Plasma Sources Science and Technology,* vol. 28, no. 3, p. 03LT02, mar. 2019.

Journal articles (submitted)

- B. Vincent, S. Tsikata, and S. Mazouffre, *"Incoherent Thomson scattering measurements of electron properties in a conventional and magnetically-shielded Hall thruster," Plasma Sources Science and Technology*, 2019.

Conference proceedings

- B. Vincent, S. Tsikata, G. C. Potrivitu, and S. Mazouffre, *"Incoherent Thomson scattering diagnostic development for plasma propulsion investigations,"* in 35th International Electric Propulsion Conference, 2017, p. IEPC-2017-442.

- B. Vincent, S. Tsikata, S. Mazouffre, and C. Boniface, *"Thomson scattering investigations of a low-power Hall thruster in standard and magnetically-shielded configurations,"* in 36th International Electric Propulsion Conference, 2019, p. IEPC-2019-384.

- L. Garrigues, G. Sary, B. Vincent, S. Tsikata, and S. Mazouffre, *"Numerical modeling and incoherent Thomson scattering measurements of a 5A cathode with LaB6 emitter,"* in 36th International Electric Propulsion Conference, 2019, p. IEPC-2019-783.

- S. Mazouffre, R. Joussot, B. Vincent, S. Tsikata, S. Oriol, and F. Masson, *"Characterization of a 100A-class LaB6 hollow cathode for high-power Hall thrusters,"* in 36th International Electric Propulsion Conference, 2019, p. IEPC-2019-776.

- K. Hara, Y. Yamashita, S. Tsikata, B. Vincent, S. Mazouffre, and S. Cho, *"New insights into electron transport due to azimuthal drift in a Hall effect thruster,"* in 36th International Electric Propulsion Conference, 2019, p. IEPC-2019-691.

Appendix B

Version française

Le silence éternel de ces espaces infinis m'effraie.

—*Blaise Pascal, Pensées*

B.1 Introduction

Test Le plasma est un état de la matière dont les manifestations naturelles telles que les constellations d'étoiles, les aurores boréales et la foudre ont toujours fasciné l'homme. On estime que 30 000 avant notre ère, l'homme analysait déjà le mouvement relatif des étoiles pour prédire l'alternance des saisons. Cependant, c'est uniquement à partir de l'invention de l'écriture que des preuves irréfutables de ces observations ce sont accumulées. Ces preuves montrent qu'en absence de connaissances scientifiques pour expliquer ces événements, l'homme à souvent invoqué des explications théologiques. Par exemple, les constellations d'étoiles étaient souvent vues comme la représentation de personnages et créatures mythiques tandis que les aurores boréales étaient considérées comme la manifestation des esprits. La foudre est certainement la manifestation de l'état plasma qui a le plus impacté et impressionné l'homme, la récurrence de divinités associées à la foudre dans toutes les cultures en est une preuve. De fait de son implication dans les départs des feux de forêts, la foudre a longtemps été associée à tort au concept de feu.

Malgré de nombreux biais d'interprétation, Benjamin Franklin fut le premier physicien à tenter de décrire de manière scientifique de cet état de la matière et à la maitriser via l'utilisation de paratonnerre. La découverte des particules fondamentales et le développement de l'électromagnétisme donnèrent des bases théoriques plus adaptées à la description de cet état aux successeurs de Benjamin Franklin. Le développement de sources reproduisant ces plasmas en laboratoire ainsi l'invention de diagnostiques pour les sonder permirent la caractérisation et la compréhension de phénomènes physique en jeu dans cet état de la matière. Ces avancées en physique théorique et expérimental permirent à Irving Langmuir d'enfin attribuer le nom plasma a cet état de la matière auquel il donna une définition claire et précise. Il définit cet état de la matière comme un milieu composé de particules neutres (atomes et/ou molécules) ainsi que de particules chargées (électrons et ions) dont les proportions garantissent une neutralité globale (à l'exception de la gaine qui se forme à la périphérie du plasma).

La compréhension accrue cet état de la matière donna lieu à de nombreuses applications. Aujourd'hui, les plasmas sont régulièrement utilisés dans des applications allant de l'éclairage, au dépôt de couches mince en passant par la propulsion spatiale ainsi que la production de particules chargées pour les accélérateurs de particules. Des applications dans le domaine de la fusion nucléaire, de la conversion du CO_2 ainsi que le traitement de cellules cancéreuses font partie des applications envisagées dans un avenir plus ou moins lointain.

Le grand nombre d'applications auquel peut donner lieu cet état de la matière provient de la diversité de sources plasma ainsi que la sensibilité du comportement de la décharge aux conditions expérimentales. Cependant, la diversité et le nombre important de particules et instabilités à prendre en compte augmentent significativement le degré de complexité des simulations nécessaires pour prédire le comportement de ces décharges. Afin de vérifier que les simulations simulent de manière réaliste la physique de

la décharge, une comparaison avec des résultats expérimentaux est indispensable. Du fait de leur grande mobilité, de leur sensibilité aux paramètres externes et de leur efficacité à transmettre l'énergie, le comportement des électrons est un des paramètres clefs pour caractériser le comportement d'une décharge plasma. La capacité d'une simulation à prédire les valeurs de propriétés électroniques est une indication pertinente pour juger de sa validité.

Pour effectuer cette comparaison, plusieurs diagnostics capables d'estimer les propriétés électroniques sont disponibles. Parmi les différentes méthodes, la diffusion Thomson se distingue des autres puisqu'elle est la seule à donne accès de manière directe à l'intégralité des propriétés thermiques des électrons (température, densité et vitesse de dérive). En fonction du de laser utilisé pour induire la diffusion Thomson, cette méthode donne accès à de relativement bonnes résolutions spatiotemporelle tout en garantissant l'absence de perturbation de la décharge. Le seul inconvénient d'un tel diagnostic réside dans la grande sensibilité nécessaire pour détecter et analyser le faible nombre de photon émis par diffusion Thomson. Ce faible nombre de photon diffusé complexifie l'implémentation de tels diagnostics sur des sources plasma où la densité électronique est faible.

Les travaux de cette thèse se concentrent sur l'étude d'un nombre réduit de sources plasma: les magnétrons planaires, les sources d'ions ECR et les propulseurs de Hall. Le point commun de ces sources est de fonctionner à des niveaux de pressions au moins 1000 fois inférieur à la pression atmosphérique. Pour atteindre des densités électroniques relativement élevées malgré une faible densité de neutre, ces sources plasmas utilisent un champ magnétique pour augmenter le temps de résidence des électrons et maximiser la probabilité d'ionisation. Ce confinement des électrons optimise le transfert de puissance vers les électrons qui peuvent atteindre des températures extrêmement élevées dans les zones de fort champs magnétiques. Ces conditions sont inadaptées pour de nombreux diagnostiques intrusifs qui risquent de soit perturbé la décharge ou d'être détruit par cette dernière. Le manque de connaissances qui en résulte empêchent l'accès à une compréhension fine de la physique de ces décharges. Ces lacunes se traduisent par l'absence de modèles prédictifs pour assister le développement et l'optimisation de ces sources plasma. Encore aujourd'hui ces tâches se basent sur des méthodes purement empiriques. De telles méthodes impliquent des couts de développement élevés pour des configurations qui peuvent être sous optimales.

Dans cette thèse le développement d'un nouveau diagnostic de diffusion Thomson est proposé pour de combler le manque d'information sur les propriétés électroniques. Du fait du niveau de densité électronique attendu dans les sources plasmas étudiés, la sensibilité du diagnostic à développer doit atteindre des seuils de détection similaires aux meilleurs jamais atteints. En plus d'être sensible, le diagnostic développé doit être suffisamment compact pour être transporté et implémenté sur diverses sources plasma. Face au même besoin une collaboration est née entre trois laboratoires pour soutenir financièrement le développement de ce diagnostic et mettre à disposition les différentes sources plasmas à étudier. Le LPGP du CNRS d'Orsay a apporté son expertise relative au magnétrons planaire, l'ICARE du CNRS d'Orléans a permis l'implémentation du diagnostic sur des propulseurs de Hall, enfin, le LEDA du CEA de Saclay a permis l'étude d'une source d'ions ECR. À court terme, ces implémentations doivent illustrer la possibilité de caractériser des sources plasma basses pression avec un diagnostic de diffusion Thomson et aider à la compréhension de phénomènes physiques de base lié à la dynamique des électrons. À plus long terme, le but est de fournir des données fiables des propriétés électroniques afin de contribuer à la validation de simulations en cours de développement.

Cette thèse commence par rappeler dans le Chapitre 2 les aspects théoriques relatifs à l'utilisation de la diffusion Thomson incohérente dans les plasmas.
Le Chapitre 3 décrit le diagnostic développé au cours de cette thèse, les motivations qui justifient les choix technologiques effectués sont expliquées. Ce même chapitre décrit les méthodes expérimentales de calibration et d'acquisition des spectres Thomson.
Les chapitres 4, 5 et 6 présentent les résultats issus des investigations sur respectivement le magnétron planaire, la source d'ion ECR et les propulseurs de Hall. Systématiquement, les sources plasma y sont décrites avant de décrire certaines spécificités propres à chaque implémentation et enfin présenter les résultats expérimentaux obtenus.
Ce manuscrit se clôt par une brève conclusion et la proposition de futurs axes de recherche.

B.2 Principes de base de la diffusion de Thomson

Cette thèse se focalise sur l'analyse d'un processus de diffusion entre des particules pour remonter à des informations sur le milieu. La diffusion est un phénomène physique assez général, la force à l'origine qui l'induit dépend fortement du type de particules considéré. Dans le cas de la diffusion Thomson, c'est la force de Lorentz entre un photon incident et une particule chargé qui génère la diffusion. Dans notre cas, les propriétés du photon incident sont parfaitement connues, tandis que la particule chargée sera la particule diffusante que l'on cherche à caractériser. L'analyse de l'intensité diffusée en fonction de la direction et de l'énergie de la particule diffusante donne accès à de nombreuses informations. La distribution spatiale de l'intensité diffusée est reliée à la section efficace différentielle du type de diffusion considérée, elle donne des indications sur le type de diffusion ainsi que sur nombre de particules diffusantes. La distribution spectrale de la lumière diffusé selon une direction spécifique donne accès à des informations relatives à la dynamique des particules diffusantes selon le vecteur d'onde sondé ($\vec{k}$). Ce vecteur d'onde est définie par la relation $\vec{k} = \vec{k}_i - \vec{k}_s$, avec $\vec{k}_i$ le vecteur d'onde du photon incident et $\vec{k}_s$ le vecteur d'onde du photon diffusé.

Afin d'étudier les propriétés électroniques, le diagnostic développé a pour but de générer, détecter, et analyser le signal de diffusion Thomson issu des électrons libres du plasma. Ce type de diffusion étant la limite élastique de la diffusion entre un photon incident et un électron, l'énergie du photon incident ne devra pas modifier significativement l'énergie cinétique de l'électron. Ce critère est respecté pour des photons ayant une énergie inférieure à 5 keV (i.e., la longueur d'onde doit être supérieure à 240 pm). Cependant, l'énergie du photon incident doit être suffisante pour ne pas être réfléchie et se propager avec une faible atténuation au travers des plasmas sondés, pour cela l'énergie des photons doit être supérieure à 0.1 meV (i.e, la longueur d'onde doit être inférieure à 10 mm).

Si l'on considère la diffusion Thomson sur un seul électron, la lumière émise peut être vu comme la conséquence de l'accélération d'un électron sous l'influence du champ électrique oscillant d'un photon incident. Avec cette approche, la section efficace différentielle de diffusion Thomson est obtenue directement, elle dépend uniquement de la direction relative entre le vecteur d'onde d'observation et le vecteur de polarisation du photon incident.

Le processus de diffusion Thomson sur une multitude d'électrons implique la sommation du champ électrique émis par chaque particule diffusante. Expérimentalement, du fait de la cohérence des sources de lumière utilisés pour générer la diffusion Thomson, la présence de structure électroniques cohérentes dans le plasma peut donner lieu à une diffusion cohérente de la lumière. Dans ce régime les caractéristiques de la lumière diffusé est influencé par le comportement collectif et individuel des électrons. Le diagnostic développé dans cette thèse a pour but de se placer dans le régime incohérent pour se focaliser uniquement sur les propriétés thermiques des électrons. Le régime de diffusion incohérent est assuré en faisant en sorte que la distance caractéristique associé au vecteur d'onde sondé ($2\pi/||\vec{k}||$) soit inférieur à la distance d'écrantage des disparités de chargé, nommé longueur de Debye (λ_{De}).

Dans le régime incohérent, la distribution spectrale des photons diffusés reflète directement les propriétés thermiques des électrons. Plus précisément, la distribution spectrale est directement proportionnelle à la fonction de distribution de la vitesse des électrons projeté selon la direction du vecteur d'onde sondé. Sous l'hypothèse d'électrons l'équilibre thermique (fonction de distribution en vitesse de type Maxwell-Boltzmann) cette fonction est une Gaussienne. L'intensité totale contenu dans cette distribution ainsi que sa déviation standard et sa moyenne permettent l'estimation de respectivement la densité, température, et vitesse de dérive des électrons dont la lumière analysée est issue. De manière plus générale, sous l'hypothèse d'un comportement isotrope des électrons, la dérivée de la fonction de distribution spectrale de la lumière diffusé peut être utilisé pour extraire les fonctions de distribution en énergie et vitesse des électrons. Cette spécificité de la diffusion Thomson permet d'être sensible aux déviations de l'équilibre thermodynamique ainsi qu'à des comportements non isotropiques des électrons.

B.3 Le diagnostic THETIS

Le diagnostic de diffusion Thomson incohérente développé au cours de cette, baptisé THETIS (THomson scattering Experiment for low-Temperature Ion Sources), devait être à la fois compact et sensible pour être facilement implémenté sur différentes sources plasma basse pression. Tout diagnostic de diffusion Thomson peut être divisé en une branche de transmission et une branche de détection. La branche de

transmission est la partie du diagnostic qui est utilisé pour générer le signal de diffusion Thomson. La branche de détection est la partie du diagnostic utilisée pour collecter et analyser une partie de la lumière diffusée. L'optimisation de chacune de ces branches est déterminante pour respecter le cahier des charges fixé. Le diagnostic THETIS doit sont originalités principalement du design de sa branche de détection. La branche de détection utilise une nouvelle technologie de filtre notch qui permet une synergie entre l'augmentation de la compacité et de la sensibilité du diagnostic.

Le design de la branche de transmission standard est relativement standard. La source de lumière de cette branche est un laser Nd:YAG doublé en fréquence à 532 nm qui délivre des pulses laser à 10 Hz. Les pulses laser durent 5 ns et contiennent une énergie de 430 mJ. La taille du faisceau en sortie du laser est dans un premier temps augmentée pour être plus facilement transportée et augmenter la capacité à focaliser, avec une lentille de 2 m de focale, le faisceau au niveau du volume à sonder. Pour minimiser les sources de lumière parasite liées aux réfections, le faisceau traverse la chambre à vide au travers de fenêtres Brewsters et d'orifices adapté a la taille du faisceau, et finit son chemin dans un large "beam dump".

La source de lumière de la branche de détection est constituée de l'ensemble de la lumière émise par le volume d'observation au travers la lentille de collection qui image ce volume sur un ensemble de fibre optiques. Cette lumière peut provenir de plusieurs contributions. Pour des sources plasmas utilisant un gaz monoatomique, cette lumière peut provenir de la diffusion Thomson et Rayleigh ainsi l'émission propre du plasma et la lumière issue de la réflexion ou fluorescence induit par l'illumination de surfaces à proximité du volume d'observation par le faisceau laser. En plus danalyser la lumière émise par diffusion Thomson, la branche de détection a pour but de contribuer à minimiser certaines sources de lumière parasites.
Les fibres optiques transportent la lumière collectée vers la table optique où la lumière issue des fibres est collimatée pour être filtré par un filtre notch à réseau de Bragg. Ce filtre notch atténue fortement la lumière sur un intervalle très fin autour de la longueur d'onde du laser tout en garantissant un facteur de transmission important à l'extérieur de cet intervalle. Ce filtre optique est l'élément clé de diagnostic THETIS, il permet une atténuation efficace des sources de lumière parasite issues de la diffusion Rayleigh et des réflexions du laser tout en gardant un diagnostic compact.
Cette lumière filtrée est ensuite dispersée avec un spectromètre simple puis détecté avec une caméra intensifiée. L'utilisation d'une caméra intensifiée permet de minimiser la contribution de l'émission plasma en amplifiant ce signal uniquement lorsque le signal Thomson arrive sur la CCD et en atténuant toute source de lumière à l'extérieur de cet intervalle temporel.

Avant toute campagne expérimentale, la branche de détection est caractérisé avec les paramètres expérimentaux choisi. Cela implique une calibration spectrale ainsi que la mesure de la fonction d'instrument qui caractérise la redistribution de la lumière propre au diagnostic. Pour calibrer le coefficient de transmission du diagnostic, le signal issu de la diffusion Raman sur une pression connue de diazote est mesuré. Cette calibration est effectuée avec une configuration de la branche de détection identique à celle utilisé pour l'acquisition des spectres Thomson.

Une fois le diagnostic calibré, l'acquisition de spectres Thomson est effectué. Les acquisitions Thomson sont réalisées lorsque la source plasma et le laser sont allumés et sont le résultat d'un moyennage sur 6000 pulses laser. Malgré leur minimisation, certaines sources de signal parasite s'additionnent au signal de diffusion Thomson obtenu lors de chaque acquisition. Afin d'isoler le signal issu de la diffusion Thomson, la soustraction de signal obtenu lors d'acquisitions supplémentaires est parfois nécessaire (en l'absence de laser et plasma ou uniquement avec le laser ou le plasma allumé).

Le signal de diffusion Thomson isolé peut être analysé de deux manière différentes.
Une fonction Gaussienne peut être ajusté au spectre Thomson mesuré. La valeur des paramètres de cette Gaussienne permet d'estimer la densité, température et vitesse de dérive des électrons à l'intérieur du volume d'observation.
Dans les cas où le rapport signal sur bruit est suffisamment élevé, un filtre de Savitzky-Golay peut être utilisé pour estimer la dérivée de la distribution spectrale du signal de diffusion Thomson. De la valeur de cette dérivée, les fonctions de distribution en énergie et vitesse des électrons sont estimés.

Le signal Thomson mesuré avec le diagnostic THETIS reflète les propriétés électroniques à l'intérieur du volume sondé. Les fortes fluences utilisées pour induire le signal de diffusion Thomson peuvent donner lieu a des perturbations des propriétés électroniques à l'intérieur de ce volume. Par exemple, l'absorption de l'énergie des pulses laser par effet bremsstrahlung inverse peut donner lieu a un chauffage électronique tandis que la photo-absorption, le photo-détachement ou la force pondéromotrice peuvent entrainer une

modification de la densité électronique localement. L'estimation des différents seuils de perturbations pour les conditions plasma étudiées prédit l'absence de perturbation avec les fluences générées par le laser de la branche de transmission de THETIS dans le volume d'observation.

Même en l'absence de perturbation, la théorie de base présenté dans le chapitre précédent peut devenir invalide. Par exemple, le fait que tous les électrons ne restent pas à l'intérieur de volume d'observation pendant toute la durée d'observation mène à un élargissement supplémentaire du spectre des photons diffusés. La présence d'un champ magnétique peut modifier la polarisation du faisceau incident ou le spectre de diffusion Thomson du fait de l'impact qu'a ce champ magnétique sur la mobilité électronique. Finalement, l'utilisation d'intensités laser extrêmes pour générer le signal de diffusion peut donner lieu à des effets non linéaires et la génération d'harmoniques à l'intérieur du spectre de la lumière diffusée. La plupart de ces phénomènes est totalement négligeable pour la configuration du diagnostic THETIS et pour les caractéristiques des sources plasma étudiées. Cependant, pour le magnétron planaire, à des positions bien spécifiques et pour une configuration de diffusion bien précises, la modulation du spectre Thomson induite par la trajectoire hélicoïdale des électrons est susceptible d'être observable.

B.4 Études par diffusion Thomson incohérente d'un magnétron planaire

Les magnétrons planaire sont des sources plasma utilisées pour des applications tel que le dépôt de couches minces. Typiquement, la décharge est générée par une différence de potentiel appliqué entre un anneau de garde (anode) et une cible circulaire (cathode) composé du matériau que l'on souhaite déposer. La cible est généralement située en retrait et au centre de l'anneau de garde. Pour garantir un fonctionnement de la décharge plasma à basse pression, un champ magnétique radial est généré proche de la cible grâce à un assortiment d'aimants positionnés derrière. Cette configuration génère un plasma dense proche de la cible où le champ électrique de le pré-gaine accélère les ions vers la cible pour en ablater des atomes.

La différence de potentiel entre l'anode et la cathode peut être appliqué de manière continue ou pulsé. Pour le régime continu, nommé DCMS, la densité de puissance de la décharge est rapidement limité par le seuil d'endommagement de la cible. Ce régime est caractérisé par un fort taux de déposition mais un faible taux d'ionisation des particules ablatées de la cible, cela empêche une maitrise fine du processus de déposition des particules ablatées.
Pour le régime pulsé, nommé HiPIMS, la densité de puissance peut être relativement élevée du fait de la diminution de rapport cyclique de la puissance appliqué à la cible. Ce régime est caractérisé par de fortes densités électronique mais un faible taux de déposition. Le plasma dense en face de la cible ionise une fraction significative des atomes ablatés. L'énergie et la direction du flux d'ions peut être contrôlé si un champ électrique est appliqué à proximité du substrat. Ce contrôle sur les particules déposées permet d'obtenir des couches minces de meilleur qualité et moins sensible aux effets d'ombre.

Pour son implémentation sur le magnétron planaire, le diagnostic THETIS a été monté sur la chambre à vide DIVA du LPGP. La configuration de diffusion a donnée accès aux propriétés électroniques au-dessus du "racetrack" selon la direction de la bissectrice entre la direction radiale et azimuthale du magnétron. Le déplacement du magnétron planaire selon sa direction axiale a permis l'estimation des propriétés électroniques à différentes distances de la cible. L'anneau de garde, positionné à 8 mm de la cible, empêche l'étude des propriétés électroniques a des positions axiales inférieures à 9 mm de la cible.

Avec le régime DCMS, l'utilisation d'argon pour soutenir la décharge n'a pas permis l'obtention de spectres Thomson interprétables du fait de la présence de raies parasites. Ces raies ont été attribuées à de la diffusion Raman sur des molécules d'oxyde de titane en suspension dans la décharge. L'utilisation d'hélium pour soutenir la décharge a permis l'obtention de spectres Thomson dont l'analyse est possible, ces derniers illustrent la sensibilité du diagnostic THETIS jusqu'à des densités électroniques de l'ordre de $10^{16}\,\mathrm{m}^{-3}$. Cependant le faible niveau de signal détecté limite la diversité des explorations possibles.

Avec le régime HiPIMS, le générateur de pulses a été synchronisé avec le l'horloge à 10 Hz délivré par le laser du diagnostic THETIS. Dans ce régime, les fortes densités électroniques ont facilité l'étude approfondit de propriétés électroniques, à la fois de l'argon et de l'hélium ont pu être utilisé pour soutenir la décharge.
Des profils temporels des propriétés électroniques furent réalisés à différents au cours du pulse de courant. Avec un faible taux de répétition, la résolution temporelle était limitée au début du pulse du fait des

fluctuations de l'instant de démarrage de la décharge au cours des 6000 accumulations nécessaires pour l'acquisition de chaque spectre Thomson. Ces fluctuations furent amoindries en augmentant le taux de répétition de la décharge plasma. Avec des pulses suffisamment stables, une résolution temporelle de l'ordre de la microseconde a été atteinte. Tandis que la densité semble suivre systématiquement le profil temporel du courant de décharge, différents types de profils temporel de la température électronique ont été observés en fonction du gaz et du taux de répétition utilisé.
Les profils axiaux des propriétés électroniques, à la fin des pulses de courant, permirent l'observation d'une inversion du sens de la vitesse de dérive des électrons lorsque de l'hélium fut utilisé pour soutenir la décharge. Cette inversion est expliquée l'inversion du sens du champ électrique axiale. La valeur de la composante axiale du champ électrique fut estimée par l'intermédiaire de l'intensité du champ magnétique et des propriétés électroniques. Des profils axiaux effectués avec une décharge soutenue avec de l'argon et pour différentes intensités de champ magnétique suggèrent une décroissance de la densité plasma lorsque l'intensité du champ magnétique est augmentée.

B.5 Études par diffusion Thomson incohérente d'une source d'ions ECR

La source d'ion ECR étudié dans cette thèse a pour but de générer des particules chargées qui seront extraites et accéléré pour être injecté dans un accélérateur de particules et être utilisé pour diverses types d'applications. Ce type de source plasma utilise la résonance du mouvement cyclotronique des électrons autour des lignes de champ magnétique avec une onde électromagnétique pour les chauffer efficacement. Pour la source étudiée, l'onde utilisée appartient au domaine micro-onde, elle est délivre de manière continue ou pulsé avec un magnétron. La fréquence micro-onde utilisé de 2.45 GHz entre en résonance avec le mouvement cyclotronique lorsque l'intensité du champ magnétique est égale à 87.5 mT. Ce champ magnétique est généré à l'aide de deux bobines qui induisent un champ magnétique axial. Puisque la source d'ions ECR, nommé ECRIN, est censée fonctionner avec des gaz légers, la présence d'électrons extrêmement chaud doit être limité puisqu'ils ne participent plus efficacement à l'ionisation. Pour minimiser la température électronique, la configuration magnétique réfléchi les électrons énergétiques vers un matériau possédant un fort coefficient d'émission secondaire. Ce matériau, positionné à proximité l'injection de l'onde RF, est une source d'électrons secondaires relativement froids lorsque des ions ou électrons énergétiques l'impactent.
La chambre de plasma de la source ECRIN est pompé au travers d'un orifice. Les mesures effectuées dans le cadre de cette thèse ce sont fait sans extraction, cependant en mode extraction l'orifice serait polarisé relativement à une seconde électrode pour extraire des particules chargées de la source plasma.

Pour son implémentation sur la source d'ion ECRIN, la configuration de diffusion du diagnostic THETIS donne accès aux propriétés électroniques au centre de la chambre plasma selon la direction radiale de la source. L'architecture de la source ne permet pas l'étude des propriétés électroniques à différentes positions. Cependant la synchronisation de la source micro-onde et du laser avec une horloge maitresse permet la réalisation de profils temporel.

En régime pulsé, lorsque du dihydrogène est utilisé pour soutenir la décharge plasma, une légère augmentation de la densité électronique et de la température a été observé à basse pression. Du fait de l'instabilité de la source micro-onde, la dynamique des propriétés électronique n'a pas pu être résolue au démarrage et à l'extinction du plasma. Cependant, une étude complémentaire du spectre d'émission du plasma suggère que la dynamique de dissociation du dihydrogène et significativement plus lente. En régime continu, l'étude pour différentes pressions de dihydrogène et puissances RF rapporte des variations des propriétés électroniques relativement faibles.
De l'hélium et de l'argon ont été utilisé pour étudier de l'influence type de gaz sur le comportement de la décharge. Cette étude a montré que le gaz utilisé à une influence non seulement sur les valeurs mais aussi sur la dynamique des propriétés électroniques mesurées au cours du pulse de RF.

B.6 Études par diffusion Thomson incohérente d'un propulseur de Hall

Les propulseurs de Hall sont des sources plasma utilisées pour la propulsion spatiale. Ce type de décharge plasma est générée par une différence de potentiel entre une anode (positionné au fond d'un canal cylindrique du propulseur) et une cathode (positionné à l'extérieur du propulseur). La cathode utilise une pastille thermoémissive pour fournir des électrons à la décharge. Une partie de ces électrons se dirige vers l'anode, mais sont piégés au niveau du plan de sortie du propulseur par un champ magnétique radial. Les atomes de gaz (généralement du xénon), injectés au niveau de l'anode, sont ionisés par les électrons lorsqu'ils atteignent le plan de sortie du propulseur. Le fort champ électrique axial, concentré en aval de la zone d'ionisation, accélère les ions jusqu'à des vitesses de l'ordre de plusieurs dizaines de mètres par seconde. Afin d'empêcher le retour des ions vers le propulseur, une partie des électrons fournis pas la cathode est utilisé pour neutraliser le flux d'ions accéléré.

La puissance électrique utilisé par les propulseurs de Hall pour accélérer les ions est directement limité par la puissance électrique disponible à bords des satellites. Cette limitation en puissance couplée à la haute vitesse d'éjection des ions implique nécessairement une faible poussée pour ces types de propulseurs. Pour des missions tolérant des transferts d'orbites plus long, l'inconvénient lié à cette faible poussée est largement compensé par le gain en masse d'ergol obtenu. La robustesse de tels propulseurs est donc un des points clé pour sa compétitivité. La détérioration de la céramique isolant le circuit ferromagnétique du plasma est généralement le facteur limitant la durée de vie des propulseurs de Hall. Tandis que la configuration magnétique dite "standard" peut présenter une usure significative au bout de plusieurs milliers d'heures de fonctionnement, la configuration dite "magnetic shielding" a été récemment introduite et permet l'annulation presque totale de l'usure du canal propulseur.

Le diagnostic THETIS a été utilisé pour étudier les propriétés électroniques à l'intérieur d'un propulseur en configuration "standard" (avec l'ISCT200-GEO) et "magnetic shielding" (avec l'ISCT200-MS). Pour ces implémentations, le diagnostic a été monté sur la chambre à vide NExET de ICARE. L'utilisation de deux configurations de diffusion a permis l'étude des propriétés électroniques selon la direction radiale et azimuthale. L'utilisation d'un système de translation 3 axes a été utilisé pour le déplacement entre les deux configurations de diffusion ainsi que le positionnement du volume d'observation au centre du canal de décharge et sont déplacement axial pour la réaliser de profils des propriétés électroniques. Systématiquement, le plan de sortie du propulseur et l'obstacle limitant l'investigation des propriétés électroniques en amont de la zone d'accélération.

Pour commencer, l'influence du champ magnétique a été étudié. Une étude avec différentes intensités e champ magnétique a été effectué avec l'ISCT200-GEO, elle suggère la présence d'une intensité optimale pour le confinement électronique.
Un déplacement de l'ensemble de la décharge plasma vers l'aval a été observé avec la configuration "magnetic shielding". Ce déplacement a permis l'accès du diagnostic de diffusion Thomson à la zone d'accélération. Dans cette zone d'accélération, une vitesse de dérive significative a été observé selon la direction azimuthale. L'étude de l'influence de l'inversion du sens des lignes de champ magnétique a validé l'hypothèse selon laquelle la dérive $\vec{E} \times \vec{B}$ est la contribution majoritaire à la vitesse de dérive électronique selon la direction azimuthale.
L'étude de l'influence de la puissance et de la tension de décharge à également été réalisé. Un déplacement de la décharge en aval ainsi que l'augmentation de la densité électronique a été observé pour les cas à faible tension de décharge. Ces fortes densités électroniques dans la zone d'accélération ont permis l'observation de spectres Thomson associés à des populations électroniques déviant significativement de l'équilibre thermodynamique. Afin de réduire les distorsions engendrées par les raies d'émission dans le spectre Thomson, du krypton a été utilisé à la place du xénon. L'utilisation de krypton a permis une analyse plus fine et plus fiable des fonctions de distribution en énergie des électrons estimées après lissage et dérivation des spectres Thomson.

B.7 Conclusion

La disponibilité d'une nouvelle technologie de filtre notch à réseau de Bragg a été déterminante pour le design du banc de diffusion Thomson incohérente présenté dans cette thèse sous le nom de THETIS. Ce nouveau type de filtre notch offre un gain significatif en compacité du diagnostic tout en permettant une

sensibilité similaire aux meilleurs diagnostics de diffusion Thomson jamais conçu. Le diagnostic THETIS utilise ce type de filtre tout en s'attachant à minimiser autant que possible les pertes de photons au sein de la branche optique utilisé pour analyser et filtrer la lumière diffusée. Cette optimisation du facteur de transmission permet d'éviter l'augmentation de la puissance du laser utilisé pour générer le signal de diffusion, cette stratégie serait susceptible de générer une perturbation du plasma pour les sources étudiées.

Le diagnostic THETIS a été implémenté avec succès sur un magnétron planaire, une source d'ion ECR ainsi qu'un propulseur de Hall. Ces implémentations ont prouvé la sensibilité du diagnostic jusqu'à des densités électroniques de l'ordre de $10^{16}\,\mathrm{m}^{-3}$, des températures comprises entre 0.5 eV et 100 eV, et des vitesses de dérives au moins supérieures à $50\,\mathrm{km\,s}^{-1}$. En plus d'une résolution spatiale de l'ordre du millimètre, une résolution temporelle de l'ordre de la microseconde a été obtenu pour des sources plasma suffisamment stables. Enfin, en présence de fortes vitesses de dérive électroniques, les fonctions de distribution électroniques ont été estimés afin de mieux interpréter les spectres Thomson non symétriques et non Gaussien observés.

Le diagnostic présenté dans cette thèse est une première version, un certains nombre d'améliorations est envisageable. Une simplification de la branche de détection pourrait être réalisée pour encore augmenter sa compacité et son facteur de transmission. L'utilisation de laser avec un taux de répétition plus élevé et l'implémentation d'un détecteur avec une plus haute efficacité quantique pourraient réduire la durée des accumulations nécessaire. Ces améliorations pourraient assez facilement abaisser le seuil de détection du diagnostic en dessous de $10^{15}\,\mathrm{m}^{-3}$.

Les études des sources plasma présentées dans cette thèse nécessiteraient également un approfondissement grâce à des campagnes supplémentaires.
Pour le magnétron planaire, la possibilité de sonder des configurations de diffusion associés uniquement aux propriétés radiales et azimuthales des électrons simplifierait l'interprétation des résultats. De plus, la mesure des propriétés électroniques sur l'axe de symmétrie du magnétron pourrait permettre l'observation de modulations à l'intérieur du spectre Thomson du fait de la trajectoire cyclotroniques des électrons. Enfin, de nombreuses autres études paramétriques (intensité du champ magnétique, pression, taux de répétion, ...) restent à faire, aussi bien avec le régime DCMS qu'avec le régime HiPIMS.
Pour la source d'ion ECR, une source micro-onde utilisant des transistors pourraient augmenter la stabilité de la décharge et permettre l'étude de la dynamique électronique lors de l'allumage et de l'extinction de la décharge plasma. De plus, l'étude de la source plasma en mode extraction permettrait d'obtenir des conditions de fonctionnement de la source plus réalistes et la tension d'extraction offrirait un autre paramètre pour effectuer des études systématiques.
Pour le propulseur de Hall, l'étude d'un propulseur en configuration "wall-less" (avec l'anode au niveau du plan de sortie) pourrait permettre l'accès aux propriétés électroniques non seulement dans la zone d'accélération mais aussi dans la zone d'ionisation. Couplé à des données obtenues par LIF, une telle étude donnerait accès au profil complet d'ionisation et d'accélération d'un propulseur de Hall. Enfin l'implémentation du diagnostic THETIS sur le même type de propulseur mais à l'intérieur d'une chambre à vide de plus grande dimension permettrait de vérifier l'influence du niveau de vide et de la taille du caisson sur les propriétés électroniques .

Bibliography

[1] M. Lyszyk, E. Klinger, O. Sécheresse, J. P. Bugeat, D. Valentian, A. Cadiou, T. Beltan, and C. Gelas, "Qualification status of the pps 1350 plasma thruster," *35th Joint Propulsion Conference and Exhibit*, no. June, 1999. (Cited on pages xv and 110.)

[2] C. Ruggles and M. Cotte, *Heritage Sites of Astronomy and Archaeoastronomy in the context of the UNESCO World Heritage Convention*. ICOMOS, 2010, no. June. (Cited on page 2.)

[3] O. Spaeth, "Dating the Oldest Egyptian Star Map," *Centaurus*, vol. 42, no. 3, pp. 159–179, jul 2000. [Online]. Available: http://doi.wiley.com/10.1034/j.1600-0498.2000.420301.x (Cited on page 2.)

[4] J. P. Mallory and D. Q. Adams, *The Oxford Introduction to Proto-Indo-European and the Proto-Indo-European World*. Oxford University Press, 2006. [Online]. Available: http://global.oup.com/ukhe/product/the-oxford-introduction-to-proto-indo-european-and-the-proto-indo-european-world-9780199296682?cc=us{&}lang=en (Cited on page 2.)

[5] D. W. Anthony and D. Ringe, "The Indo-European Homeland from Linguistic and Archaeological Perspectives," *Annual Review of Linguistics*, vol. 1, no. 1, pp. 199–219, jan 2015. [Online]. Available: http://www.annualreviews.org/doi/10.1146/annurev-linguist-030514-124812 (Cited on page 2.)

[6] F. R. Stephenson, D. M. Willis, and T. J. Hallinan, "The earliest datable observation of the aurora borealis," *Astronomy and Geophysics*, vol. 45, no. 6, pp. 6.15–6.17, dec 2004. [Online]. Available: https://academic.oup.com/astrogeo/article-lookup/doi/10.1046/j.1468-4004.2003.45615.x (Cited on page 2.)

[7] E. P. Krider, "Benjamin Franklin and lightning rods," *Physics Today*, vol. 59, no. 1, pp. 42–48, jan 2006. [Online]. Available: http://physicstoday.scitation.org/doi/10.1063/1.2180176 (Cited on page 2.)

[8] B. Franklin and N. G. N. G. Goodman, *The ingenious Dr. Franklin selected scientific letters of Benjamin Franklin,*. University of Pennsylvania Press, 1931. (Cited on page 3.)

[9] W. Crookes, "On radiant matter; a lecture delivered to the British Association for the Advancement of Science, at Sheffield, Friday, August 22, 1879," *American Journal of Science*, vol. s3-18, no. 106, pp. 241–262, oct 1879. [Online]. Available: http://www.nature.com/articles/020436a0http://www.ajsonline.org/cgi/doi/10.2475/ajs.s3-18.106.241 (Cited on page 3.)

[10] J. J. Thomson, "XL. Cathode Rays," *The London, Edinburgh, and Dublin Philosophical Magazine and Journal of Science*, vol. 44, no. 269, pp. 293–316, oct 1897. [Online]. Available: https://www.tandfonline.com/doi/full/10.1080/14786449708621070 (Cited on page 3.)

[11] K. Birkeland, *The Norwegian aurora polaris expedition, 1902-1903*. Christiania: H. Aschelhoug, 1908. [Online]. Available: http://www.biodiversitylibrary.org/bibliography/17857 (Cited on page 3.)

[12] I. Langmuir and H. M. Mott-Smith, "Langmuir probe technique," *Gen. Elec. Rev*, vol. 27, p. 449, 1924. (Cited on pages 3 and 7.)

[13] H. M. Mott-Smith and I. Langmuir, "The Theory of Collectors in Gaseous Discharges," *Physical Review*, vol. 28, no. 4, pp. 727–763, oct 1926. [Online]. Available: https://link.aps.org/doi/10.1103/PhysRev.28.727 (Cited on pages 3 and 7.)

[14] I. Langmuir, "Oscillations in Ionized Gases," *Proceedings of the National Academy of Sciences*, vol. 14, no. 8, pp. 627–637, aug 1928. [Online]. Available: http://www.ncbi.nlm.nih.gov/pubmed/1085653http://www.pnas.org/cgi/doi/10.1073/pnas.14.8.627 (Cited on page 3.)

[15] ——, "Flames of Atomic Hydrogen 1,2," *Industrial & Engineering Chemistry*, vol. 19, no. 6, pp. 667–674, jun 1927. [Online]. Available: http://pubs.acs.org/doi/abs/10.1021/ie50210a009 (Cited on page 4.)

[16] I. Langmuir and P. P. Alexander, "Method and apparatus for electric arc welding," 1930. [Online]. Available: https://patents.google.com/patent/US1746196A/en (Cited on page 4.)

[17] J. Lancaster, "The physics of welding," *Physics in Technology*, vol. 15, no. 2, pp. 73–79, mar 1984. [Online]. Available: http://stacks.iop.org/0305-4624/15/i=2/a=I05?key=crossref.42af60eef627fe9af90f1f43d374337a (Cited on page 4.)

[18] J. Shohet, "Plasma-aided manufacturing," *IEEE Transactions on Plasma Science*, vol. 19, no. 5, pp. 725–733, 1991. [Online]. Available: http://ieeexplore.ieee.org/document/108405/ (Cited on page 4.)

[19] E. Heinicke, K. Bethge, and H. Baumann, "A universal ion source for tandem accelerators," *Nuclear Instruments and Methods*, vol. 58, no. 1, pp. 125–133, jan 1968. [Online]. Available: https://linkinghub.elsevier.com/retrieve/pii/0029554X68900384 (Cited on page 4.)

[20] S. Mazouffre, "Electric propulsion for satellites and spacecraft: established technologies and novel approaches," *Plasma Sources Science and Technology*, vol. 25, no. 3, p. 033002, jun 2016. [Online]. Available: http://stacks.iop.org/0963-0252/25/i=3/a=033002?key=crossref.9c6a720db6c50120415318928e7b3f98 (Cited on pages 4 and 108.)

[21] D. Estublier, G. Saccoccia, and J. Gonzales Del Amo, "Electric propulsion on SMART-1 - a technology milestone," *ESA Bulletin*, vol. 129, pp. 40–46, 2007. (Cited on page 4.)

[22] A. Bogaerts, T. Kozák, K. van Laer, and R. Snoeckx, "Plasma-based conversion of CO 2 : current status and future challenges," *Faraday Discussions*, vol. 183, pp. 217–232, 2015. [Online]. Available: http://xlink.rsc.org/?DOI=C5FD00053J (Cited on page 4.)

[23] D. B. Graves, "Low temperature plasma biomedicine: A tutorial review," *Physics of Plasmas*, vol. 21, no. 8, p. 080901, aug 2014. [Online]. Available: http://aip.scitation.org/doi/10.1063/1.4892534 (Cited on page 4.)

[24] E. Doyle, W. Houlberg, Y. Kamada, V. Mukhovatov, T. Osborne, A. Polevoi, G. Bateman, J. Connor, J. Cordey, T. Fujita, X. Garbet, T. Hahm, L. Horton, A. Hubbard, F. Imbeaux, F. Jenko, J. Kinsey, Y. Kishimoto, J. Li, T. Luce, Y. Martin, M. Ossipenko, V. Parail, A. Peeters, T. Rhodes, J. Rice, C. Roach, V. Rozhansky, F. Ryter, G. Saibene, R. Sartori, A. Sips, J. Snipes, M. Sugihara, E. Synakowski, H. Takenaga, T. Takizuka, K. Thomsen, M. Wade, H. Wilson, I. T. P. T. Group, I. C. D. Group, Model, I. P. Group, and E. Topical, "Chapter 2: Plasma confinement and transport," *Nuclear Fusion*, vol. 47, no. 6, pp. S18–S127, jun 2007. [Online]. Available: http://stacks.iop.org/0029-5515/47/i=6/a=S02?key=crossref.36e162162f67e92c3a62080002fc7583http://stacks.iop.org/0029-5515/39/i=12/a=302?key=crossref.c457c1e0ef9f22c2316445d85184a82d (Cited on page 4.)

[25] A. Fridman and L. A. Kennedy, *Plasma Physics and Engineering*. Abingdon, UK: Taylor & Francis, 2004, vol. 91. [Online]. Available: https://www.taylorfrancis.com/books/9780203334874 (Cited on page 5.)

[26] I. Mikellides, I. Katz, R. Hofer, D. Goebel, K. de Grys, and A. Mathers, "Magnetic Shielding of the Acceleration Channel Walls in a Long-Life Hall Thruster," in *46th AIAA/ASME/SAE/ASEE Joint Propulsion Conference & Exhibit*. Reston, Virginia: American

Institute of Aeronautics and Astronautics, jul 2010, pp. 1–25. [Online]. Available: http://arc.aiaa.org/doi/abs/10.2514/6.2010-6942 (Cited on pages 5 and 110.)

[27] V. V. Zhurin, H. R. Kaufman, and R. S. Robinson, "Physics of closed drift thrusters," *Plasma Sources Science and Technology*, vol. 8, no. 1, pp. R1–R20, feb 1999. [Online]. Available: http://stacks.iop.org/0963-0252/8/i=1/a=021?key=crossref.a11467fcb41bf525f255b07e8eab3010 (Cited on page 5.)

[28] D. G. Swanson, "Plasma Waves (2nd edition)," *Plasma Physics and Controlled Fusion*, vol. 45, no. 6, pp. 1069–1069, jun 2003. [Online]. Available: http://stacks.iop.org/0741-3335/45/i=6/a=701?key=crossref.57cbf0c44f6f24aa9d707c91600ba6b8 (Cited on page 6.)

[29] Y. Raitses, D. Staack, M. Keidar, and N. J. Fisch, "Electron-wall interaction in Hall thrusters," *Physics of Plasmas*, vol. 12, no. 5, p. 057104, may 2005. [Online]. Available: http://aip.scitation.org/doi/10.1063/1.1891747 (Cited on pages 6, 111, and 124.)

[30] M. I. Patino, R. E. Wirz, Y. Raitses, and B. E. Koel, "Angular, temperature, and impurity effects on secondary electron emission from Ni(110)," *Journal of Applied Physics*, vol. 124, no. 9, p. 093301, sep 2018. [Online]. Available: http://aip.scitation.org/doi/10.1063/1.5025344 (Cited on page 6.)

[31] A. Revel, T. Minea, and S. Tsikata, "Pseudo -3D PIC modeling of drift-induced spatial inhomogeneities in planar magnetron plasmas," *Physics of Plasmas*, vol. 23, no. 10, p. 100701, oct 2016. [Online]. Available: http://dx.doi.org/10.1063/1.4964480http://aip.scitation.org/doi/10.1063/1.4964480 (Cited on pages 6 and 10.)

[32] J. C. Adam, A. Héron, and G. Laval, "Study of stationary plasma thrusters using two-dimensional fully kinetic simulations," *Physics of Plasmas*, vol. 11, no. 1, pp. 295–305, 2004. (Cited on pages 6 and 124.)

[33] Y. M. Kagan and V. I. Perel', "Probe methods in plasma research," *Soviet Physics Uspekhi*, vol. 6, no. 6, pp. 767–793, jun 1964. [Online]. Available: http://iopscience.iop.org/article/10.1070/PU1964v006n06ABEH003611/metahttp://stacks.iop.org/0038-5670/6/i=6/a=R01?key=crossref.7e9a8f23bfc6ff2d6ace210cfa64d55f (Cited on page 7.)

[34] B. Reid and A. Gallimore, "Langmuir Probe Measurements in the Discharge Channel of a 6-kW Hall Thruster," in *44th AIAA/ASME/SAE/ASEE Joint Propulsion Conference & Exhibit*, no. July. Reston, Viriginia: American Institute of Aeronautics and Astronautics, jul 2008, pp. 1–14. [Online]. Available: http://www.pepl.engin.umich.edu/pdf/AIAA-2008-4920.pdfhttp://arc.aiaa.org/doi/abs/10.2514/6.2008-4920 (Cited on page 7.)

[35] F. Magnus and J. T. Gudmundsson, "Digital smoothing of the Langmuir probe I-V characteristic," *Review of Scientific Instruments*, vol. 79, no. 7, 2008. (Cited on page 7.)

[36] M. J. Druyvesteyn, "Der Niedervoltbogen," *Zeitschrift für Physik*, vol. 64, no. 11-12, pp. 781–798, sep 1930. [Online]. Available: http://informahealthcare.com/doi/abs/10.3109/00016483009127578http://link.springer.com/10.1007/BF01773007 (Cited on page 7.)

[37] L. Grimaud, A. Pétin, J. Vaudolon, and S. Mazouffre, "Perturbations induced by electrostatic probe in the discharge of Hall thrusters," *Review of Scientific Instruments*, vol. 87, no. 4, p. 043506, apr 2016. [Online]. Available: http://dx.doi.org/10.1063/1.4945563 (Cited on pages 7 and 111.)

[38] K. Dannenmayer and S. Mazouffre, "Compact high-speed reciprocating probe system for measurements in a Hall thruster discharge and plume," *Review of Scientific Instruments*, vol. 83, no. 12, 2012. (Cited on page 7.)

[39] R. R. Arslanbekov, N. A. Khromov, and A. A. Kudryavtsev, "Probe measurements of electron energy distribution function at intermediate and high pressures and in a magnetic field," *Plasma Sources Science and Technology*, vol. 3, no. 4, pp. 528–538, nov 1994. [Online]. Available: http://stacks.iop.org/0963-0252/3/i=4/a=010?key=crossref.96e62827b907a4a116e395a9fe1c0ad1 (Cited on page 7.)

[40] E. Passoth, P. Kudrna, C. Csambal, J. F. Behnke, M. Tichý, and V. Helbig, "An experimental study of plasma density determination by a cylindrical Langmuir probe at different pressures and magnetic fields in a cylindrical magnetron discharge in heavy rare gases," *Journal of Physics D: Applied Physics*, vol. 30, no. 12, pp. 1763–1777, jun 1997. [Online]. Available: http://stacks.iop.org/0022-3727/30/i=12/a=013?key=crossref.e8dcfe9379d18ca5c236ca98fd999a31 (Cited on page 7.)

[41] M. J. Seaton and D. E. Osterbrock, "Relative [o II] Intensities in Gaseous Nebulae." *The Astrophysical Journal*, vol. 125, no. 6, p. 66, jan 1957. [Online]. Available: http://adsabs.harvard.edu/doi/10.1086/146282 (Cited on page 7.)

[42] A. K. Pradhan and S. N. Nahar, *Atomic Astrophysics and Spectroscopy*. Cambridge: Cambridge University Press, 2011. [Online]. Available: http://ebooks.cambridge.org/ref/id/CBO9780511975349 (Cited on page 7.)

[43] R. Wilson, "The spectroscopy on non-thermal plasmas," *Journal of Quantitative Spectroscopy and Radiative Transfer*, vol. 2, no. 4, pp. 477–490, oct 1962. [Online]. Available: https://linkinghub.elsevier.com/retrieve/pii/002240736290033X (Cited on page 7.)

[44] U. Fantz, "Basics of plasma spectroscopy," *Plasma Sources Science and Technology*, vol. 15, no. 4, pp. S137–S147, nov 2006. [Online]. Available: http://stacks.iop.org/0963-0252/15/i=4/a=S01?key=crossref.55c2687ff5694740c0db81c4b07cacd0 (Cited on pages 7 and 8.)

[45] Y. H. Chiu, B. L. Austin, S. Williams, R. A. Dressler, and G. F. Karabadzhak, "Passive optical diagnostic of Xe-propelled Hall thrusters. I. Emission cross sections," *Journal of Applied Physics*, vol. 99, no. 11, p. 113304, jun 2006. [Online]. Available: http://aip.scitation.org/doi/10.1063/1.2195018 (Cited on pages 8 and 111.)

[46] G. F. Karabadzhak, Y. H. Chiu, and R. A. Dressler, "Passive optical diagnostic of Xe propelled Hall thrusters. II. Collisional-radiative model," *Journal of Applied Physics*, vol. 99, no. 11, 2006. (Cited on pages 8 and 111.)

[47] V. M. Donnelly, "Plasma electron temperatures and electron energy distributions measured by trace rare gases optical emission spectroscopy," *Journal of Physics D: Applied Physics*, vol. 37, no. 19, pp. R217–R236, oct 2004. [Online]. Available: http://stacks.iop.org/0022-3727/37/i=19/a=R01?key=crossref.1829a23b040f928ac99620316e19d443 (Cited on page 8.)

[48] R. Mills and P. Ray, "Extreme ultraviolet spectroscopy of heliumhydrogen plasma," *Journal of Physics D: Applied Physics*, vol. 36, no. 13, pp. 1535–1542, jul 2003. [Online]. Available: http://stacks.iop.org/0022-3727/36/i=13/a=316?key=crossref.e576f5a0992daff9b42353b32501e8f4 (Cited on page 8.)

[49] M. A. Biondi and S. C. Brown, "Measurements of Ambipolar Diffusion in Helium," *Physical Review*, vol. 75, no. 11, pp. 1700–1705, jun 1949. [Online]. Available: https://link.aps.org/doi/10.1103/PhysRev.75.1700 (Cited on page 8.)

[50] M. A. Biondi, "Measurement of the electron density in ionized gases by microwave techniques," *Review of Scientific Instruments*, vol. 22, no. 7, pp. 500–502, 1951. (Cited on page 8.)

[51] J. P. Gordon, H. J. Zeiger, and C. H. Townes, "Molecular microwave oscillator and new hyperfine structure in the microwave spectrum of NH3 [7]," pp. 282–284, jul 1954. [Online]. Available: https://link.aps.org/doi/10.1103/PhysRev.95.282 (Cited on page 8.)

[52] ——, "The MaserNew Type of Microwave Amplifier, Frequency Standard, and Spectrometer," *Physical Review*, vol. 99, no. 4, pp. 1264–1274, aug 1955. [Online]. Available: https://link.aps.org/doi/10.1103/PhysRev.99.1264 (Cited on page 8.)

[53] D. E. Ashby and D. F. Jephcott, "Measurement of plasma density using a gas laser as an infrared interferometer," *Applied Physics Letters*, vol. 3, no. 1, pp. 13–16, 1963. (Cited on page 8.)

[54] R. Turner and T. O. Poehler, "FarInfrared Laser Interferometry for Electron Density Measurements," *Journal of Applied Physics*, vol. 39, no. 12, pp. 5726–5731, nov 1968. [Online]. Available: http://aip.scitation.org/doi/10.1063/1.1656040 (Cited on page 8.)

[55] G. Neumann, U. Bänziger, M. Kammeyer, and M. Lange, "Plasmadensity measurements by microwave interferometry and Langmuir probes in an rf discharge," *Review of Scientific Instruments*, vol. 64, no. 1, pp. 19–25, jan 1993. [Online]. Available: http://aip.scitation.org/doi/10.1063/1.1144432 (Cited on page 8.)

[56] M. van Exter and D. Grischkowsky, "Carrier dynamics of electrons and holes in moderately doped silicon," *Physical Review B*, vol. 41, no. 17, pp. 12 140–12 149, jun 1990. [Online]. Available: https://link.aps.org/doi/10.1103/PhysRevB.41.12140 (Cited on page 8.)

[57] R. Huber, F. Tauser, A. Brodschelm, M. Bichler, G. Abstreiter, and A. Leitenstorfer, "How many-particle interactions develop after ultrafast excitation of an electronhole plasma," *Nature*, vol. 414, no. 6861, pp. 286–289, nov 2001. [Online]. Available: http://www.nature.com/articles/35104522 (Cited on page 9.)

[58] S. P. Jamison, J. Shen, D. R. Jones, R. C. Issac, B. Ersfeld, D. Clark, and D. A. Jaroszynski, "Plasma characterization with terahertz timedomain measurements," *Journal of Applied Physics*, vol. 93, no. 7, pp. 4334–4336, apr 2003. [Online]. Available: http://aip.scitation.org/doi/10.1063/1.1560564 (Cited on page 9.)

[59] A. Ando, T. Kurose, V. Reymond, K. Kitano, H. Kitahara, K. Takano, M. Tani, M. Hangyo, and S. Hamaguchi, "Electron density measurement of inductively coupled plasmas by terahertz time-domain spectroscopy (THz-TDS)," *Journal of Applied Physics*, vol. 110, no. 7, p. 073303, oct 2011. [Online]. Available: http://aip.scitation.org/doi/10.1063/1.3633488 (Cited on page 9.)

[60] S. M. Meier, A. Hecimovic, T. V. Tsankov, D. Luggenhölscher, and U. Czarnetzki, "First measurements of the temporal evolution of the plasma density in HiPIMS discharges using THz time domain spectroscopy," *Plasma Sources Science and Technology*, vol. 27, no. 3, pp. 348–360, aug 2018. (Cited on pages 9 and 66.)

[61] S. M. Meier, T. V. Tsankov, D. Luggenhölscher, and U. Czarnetzki, "Measurement of plasma densities by dual frequency multichannel boxcar THz time domain spectroscopy," *Journal of Physics D: Applied Physics*, vol. 50, no. 24, p. 245202, jun 2017. [Online]. Available: http://stacks.iop.org/0022-3727/50/i=24/a=245202?key=crossref.f8a455d7d17403e2d326e6b98057443d (Cited on page 9.)

[62] J. J. Thomson, *The corpuscular theory of matter*. New York, Scribner's Sons, 1907. [Online]. Available: https://archive.org/details/corpusculartheory00thomrich/page/n6 (Cited on page 9.)

[63] A. DeSilva, "The Evolution of Light Scattering as a Plasma Diagnostic," *Contributions to Plasma Physics*, vol. 40, no. 1-2, pp. 23–35, apr 2000. [Online]. Available: http://doi.wiley.com/10.1002/{%}28SICI{%}291521-3986{%}28200004{%}2940{%}3A1/2{%}3C23{%}3A{%}3AAID-CTPP23{%}3E3.0.CO{%}3B2-7 (Cited on pages 9 and 59.)

[64] M. van de Sande, "Laser scattering on low temperature plasmas High resolution and stray light rejection Laser scattering on low temperature plasmas High resolution and stray light rejection," Ph.D. dissertation, Technische Universiteit Eindhoven, 2002. (Cited on pages 9, 10, 29, and 41.)

[65] S. H. Glenzer, D. H. Froula, N. C. Luhmann, and J. Sheffield, *Plasma Scattering of Electromagnetic Radiation*. Elsevier, 2011. [Online]. Available: https://linkinghub.elsevier.com/retrieve/pii/C20090200481 (Cited on pages 9, 29, 57, 59, 60, and 61.)

[66] K. L. Bowles, "Observation of Vertical-Incidence Scatter from the Ionosphere at 41 Mc/sec," *Physical Review Letters*, vol. 1, no. 12, pp. 454–455, dec 1958. [Online]. Available: https://link.aps.org/doi/10.1103/PhysRevLett.1.454 (Cited on page 9.)

[67] V. C. Pineo, L. G. Kraft, and H. W. Briscoe, "Some characteristics of ionospheric backscatter observed at 440 Mc/s," *Journal of Geophysical Research*, vol. 65, no. 9, pp. 2629–2634, 1960. (Cited on page 9.)

[68] K. L. Bowles, "Incoherent scattering by free electrons as a technique for studying the ionosphere and exosphere: some observations and theoretical considerations," *Journal of Research of the National Bureau of Standards, Section D: Radio Propagation*, vol. 65D, no. 1, p. 1, jan 1961. [Online]. Available: https://nvlpubs.nist.gov/nistpubs/jres/65D/jresv65Dn1p1_A1b.pdf (Cited on page 9.)

[69] E. E. Salpeter, "Electron density fluctuations in a plasma," *Physical Review*, vol. 120, no. 5, pp. 1528–1535, 1960. (Cited on page 9.)

[70] F. J. McClung and R. W. Hellwarth, "Giant Optical Pulsations from Ruby," *Journal of Applied Physics*, vol. 33, no. 3, pp. 828–829, mar 1962. [Online]. Available: http://aip.scitation.org/doi/10.1063/1.1777174 (Cited on page 9.)

[71] H. Iams and B. Salzberg, "The Secondary Emission Phototube," *Proceedings of the IRE*, vol. 23, no. 1, pp. 55–64, jan 1935. [Online]. Available: http://ieeexplore.ieee.org/document/1685754/ (Cited on page 9.)

[72] G. Fiocco and E. Thompson, "Thomson Scattering of Optical Radiation from an Electron Beam," *Physical Review Letters*, vol. 10, no. 3, pp. 89–91, feb 1963. [Online]. Available: https://link.aps.org/doi/10.1103/PhysRevLett.10.89 (Cited on page 9.)

[73] H. Kunze, E. Fünfer, B. Kronast, and W. Kegel, "Measurement of the spectral distribution of light scattered by a Θ-pinch plasma," *Physics Letters*, vol. 11, no. 1, pp. 42–43, jul 1964. [Online]. Available: https://linkinghub.elsevier.com/retrieve/pii/0031916364902501 (Cited on page 9.)

[74] A. W. DeSilva, D. E. Evans, and M. J. Forrest, "Observation of thomson and co-operative scattering of ruby laser light by a plasma," *Nature*, vol. 203, no. 4952, pp. 1321–1322, 1964. (Cited on page 9.)

[75] T. S. Brown and D. J. Rose, "Plasma diagnostics using lasers: Relations between scattered spectrum and electron-velocity distribution," *Journal of Applied Physics*, vol. 37, no. 7, pp. 2709–2714, 1966. (Cited on pages 9 and 31.)

[76] N. J. Peacock, D. C. Robinson, M. J. Forrest, P. D. Wilcock, and V. V. Sannikov, "Measurement of the Electron Temperature by Thomson Scattering in Tokamak T3," *Nature*, vol. 224, no. 5218, pp. 488–490, nov 1969. [Online]. Available: http://adsabs.harvard.edu/abs/1969Natur.224..177Khttp://www.nature.com/doifinder/10.1038/224488a0http://www.nature.com/articles/224488a0 (Cited on page 9.)

[77] D. E. Evans, M. J. Forrest, and J. Katzenstein, "Asymmetric Co-operative Scattered Light Spectrum in a Thetatron Plasma," *Nature*, vol. 212, no. 5057, pp. 21–23, oct 1966. [Online]. Available: http://www.nature.com/articles/212021a0 (Cited on page 9.)

[78] M. C. M. van de Sanden, G. M. Janssen, J. M. de Regt, D. C. Schram, J. A. M. van der Mullen, and B. van der Sijde, "A combined ThomsonRayleigh scattering diagnostic using an intensified photodiode array," *Review of Scientific Instruments*, vol. 63, no. 6, pp. 3369–3377, jun 1992. [Online]. Available: http://aip.scitation.org/doi/10.1063/1.1142554 (Cited on page 10.)

[79] J. M. de Regt, R. A. H. Engeln, F. P. J. de Groote, J. A. M. van der Mullen, and D. C. Schram, "Thomson scattering experiments on a 100 MHz inductively coupled plasma calibrated by Raman scattering," *Review of Scientific Instruments*, vol. 66, no. 5, pp. 3228–3233, may 1995. [Online]. Available: http://aip.scitation.org/doi/10.1063/1.1146444 (Cited on pages 10 and 47.)

[80] M. D. Bowden, M. Kogano, Y. Suetome, T. Hori, K. Uchino, and K. Muraoka, "Comparison of electron property measurements in an inductively coupled plasma made by Langmuir probe and laser Thomson scattering techniques," *Journal of Vacuum Science & Technology A: Vacuum, Surfaces, and Films*, vol. 17, no. 2, pp. 493–499, mar 1999. [Online]. Available: http://avs.scitation.org/doi/10.1116/1.581610http://link.aip.org/link/JVTAD6/v17/i2/p493/s1{&}Agg=doi (Cited on page 10.)

[81] D. L. Crintea, U. Czarnetzki, S. Iordanova, I. Koleva, and D. Luggenhölscher, "Plasma diagnostics by optical emission spectroscopy on argon and comparison with Thomson scattering," *Journal of Physics D: Applied Physics*, vol. 42, no. 4, p. 045208, feb 2009. [Online]. Available: http://stacks.iop.org/0022-3727/42/i=4/a=045208?key=crossref.53cd830561e15910a00bceb418e7b0c9 (Cited on page 10.)

[82] E. A. D. Carbone, S. Hübner, J. M. Palomares, and J. J. A. M. van der Mullen, "The radial contraction of argon microwave plasmas studied by Thomson scattering," *Journal of Physics D: Applied Physics*, vol. 45, no. 34, p. 345203, aug 2012. [Online]. Available: http://stacks.iop.org/0022-3727/45/i=34/a=345203?key=crossref.27f26d940dca8fbdc7484f9103113f8e (Cited on page 10.)

[83] B. H. Seo, S. J. You, and J. H. Kim, "Analysis of uncertainty of electron density and temperature using laser Thomson scattering in helicon plasmas," *Japanese Journal of Applied Physics*, vol. 54, no. 8, p. 086102, aug 2015. [Online]. Available: http://stacks.iop.org/1347-4065/54/i=8/a=086102?key=crossref.0ac50d0a2680e611974ab9b95ef4146c (Cited on page 10.)

[84] E. A. D. Carbone, J. M. Palomares, S. Hübner, E. Iordanova, and J. J. A. M. van der Mullen, "Revision of the criterion to avoid electron heating during laser aided plasma diagnostics (LAPD)," *Journal of Instrumentation*, vol. 7, no. 01, pp. C01 016–C01 016, jan 2012. [Online]. Available: http://stacks.iop.org/1748-0221/7/i=01/a=C01016?key=crossref.de078466027c4248db626fed535a0e86 (Cited on pages 10 and 56.)

[85] M. N. Shneider, "Ponderomotive perturbations of low density low-temperature plasma under laser Thomson scattering diagnostics," *Physics of Plasmas*, vol. 24, no. 10, p. 100701, oct 2017. [Online]. Available: http://aip.scitation.org/doi/10.1063/1.4998137 (Cited on pages 10 and 57.)

[86] I. Adamovich, S. D. Baalrud, A. Bogaerts, P. J. Bruggeman, M. Cappelli, V. Colombo, U. Czarnetzki, U. Ebert, J. G. Eden, P. Favia, D. B. Graves, S. Hamaguchi, G. Hieftje, M. Hori, I. D. Kaganovich, U. Kortshagen, M. J. Kushner, N. J. Mason, S. Mazouffre, S. M. Thagard, H.-R. Metelmann, A. Mizuno, E. Moreau, A. B. Murphy, B. A. Niemira, G. S. Oehrlein, Z. L. Petrovic, L. C. Pitchford, Y.-K. Pu, S. Rauf, O. Sakai, S. Samukawa, S. Starikovskaia, J. Tennyson, K. Terashima, M. M. Turner, M. C. M. van de Sanden, and A. Vardelle, "The 2017 Plasma Roadmap: Low temperature plasma science and technology," *Journal of Physics D: Applied Physics*, vol. 50, no. 32, p. 323001, aug 2017. [Online]. Available: http://stacks.iop.org/0022-3727/50/i=32/a=323001?key=crossref.b7a12065bd1a5b12c19adaeda2ac4056 (Cited on page 10.)

[87] N. Brenning, J. T. Gudmundsson, M. A. Raadu, T. J. Petty, T. Minea, and D. Lundin, "A unified treatment of self-sputtering, process gas recycling, and runaway for high power impulse sputtering magnetrons," *Plasma Sources Science and Technology*, vol. 26, no. 12, p. 125003, nov 2017. [Online]. Available: http://stacks.iop.org/0963-0252/26/i=12/a=125003?key=crossref.2870e4d2659ea237610377f93850fcca (Cited on pages 10 and 80.)

[88] S. Janhunen, A. Smolyakov, O. Chapurin, D. Sydorenko, I. Kaganovich, and Y. Raitses, "Nonlinear structures and anomalous transport in partially magnetized E×B plasmas," *Physics of Plasmas*, vol. 25, no. 1, p. 011608, jan 2018. [Online]. Available: http://aip.scitation.org/doi/10.1063/1.5001206 (Cited on page 10.)

[89] S. Tsikata and T. Minea, "Modulated Electron Cyclotron Drift Instability in a High-Power Pulsed Magnetron Discharge," *Physical Review Letters*, vol. 114, no. 18, p. 185001, may 2015. [Online]. Available: https://link.aps.org/doi/10.1103/PhysRevLett.114.185001 (Cited on page 10.)

[90] A. Revel, T. Minea, and C. Costin, "2D PIC-MCC simulations of magnetron plasma in HiPIMS regime with external circuit," *Plasma Sources Science and Technology*, vol. 27, no. 10, p. 105009, oct 2018. [Online]. Available: http://stacks.iop.org/0963-0252/27/i=10/a=105009?key=crossref.bb7e284e92a5a74343a999ed645ee000 (Cited on pages 11 and 87.)

[91] O. Tuske, G. Adroit, O. Delferriere, D. De Menezes, Y. Gauthier, R. Gobin, and F. Harrault, "BETSI, a new test bench for ion sources optimization at CEA SACLAY," *Review of Scientific Instruments*, vol. 79, no. 2, p. 02B710, 2008. [Online]. Available: http://scitation.aip.org/content/aip/journal/rsi/79/2/10.1063/1.2805625 (Cited on page 11.)

[92] O. Delferrière, O. Tuske, G. Adroit, F. Harrault, D. De Menezes, R. Gobin, Y. Gauthier, and P.-Y. Beauvais, "A 140 mA cw deuteron electron cyclotron resonance source for the IFMIF-EVEDA project," *Review of Scientific Instruments*, vol. 79, no. 2, p. 02B303, 2008. (Cited on page 11.)

[93] John David Jackson, *Classical Electrodynamics, 3rd Edition.* John Wiley & Sons, Inc., 1998. (Cited on page 17.)

[94] S. Tsikata, "Small-scale electron density fluctuations in the Hall thruster, investigated by collective light scattering," Ph.D. dissertation, Ecole Polytechnique, 2009. [Online]. Available: https://pastel.archives-ouvertes.fr/tel-00484027 (Cited on pages 26 and 111.)

[95] M. Huang, K. Warner, S. Lehn, and G. M. Hieftje, "A simple approach to deriving an electron energy distribution from an incoherent Thomson scattering spectrum," *Spectrochimica Acta Part B: Atomic Spectroscopy*, vol. 55, no. 9, pp. 1397–1410, sep 2000. [Online]. Available: http://linkinghub.elsevier.com/retrieve/pii/S0584854700002445 (Cited on pages 29, 53, 81, and 124.)

[96] B. Vincent, S. Tsikata, S. Mazouffre, T. Minea, and J. Fils, "A compact new incoherent Thomson scattering diagnostic for low-temperature plasma studies," *Plasma Sources Science and Technology*, vol. 27, no. 5, p. 055002, may 2018. [Online]. Available: http://stacks.iop.org/0963-0252/27/i=5/a=055002?key=crossref.024eb31b4d726409e335df21c76aec11 (Cited on pages 38 and 125.)

[97] H. J. van der Meiden, R. S. Al, C. J. Barth, A. J. H. Donné, R. Engeln, W. J. Goedheer, B. de Groot, A. W. Kleyn, W. R. Koppers, N. J. Lopes Cardozo, M. J. van de Pol, P. R. Prins, D. C. Schram, A. E. Shumack, P. H. M. Smeets, W. A. J. Vijvers, J. Westerhout, G. M. Wright, and G. J. van Rooij, "High sensitivity imaging Thomson scattering for low temperature plasma," *Review of Scientific Instruments*, vol. 79, no. 1, p. 013505, jan 2008. [Online]. Available: http://www.royalsocietypublishing.org/doi/10.1098/rspa.1962.0101http://aip.scitation.org/doi/10.1063/1.2832333 (Cited on page 41.)

[98] E. Carbone and S. Nijdam, "Thomson scattering on non-equilibrium low density plasmas: principles, practice and challenges," *Plasma Physics and Controlled Fusion*, vol. 57, no. 1, p. 014026, jan 2015. [Online]. Available: http://stacks.iop.org/0741-3335/57/i=1/a=014026?key=crossref.5c235d81ea761c45c634ce53d65ba1e7 (Cited on pages 41 and 56.)

[99] L. P. Bakker, J. M. Freriks, F. J. de Hoog, and G. M. W. Kroesen, "Thomson scattering using an atomic notch filter," *Review of Scientific Instruments*, vol. 71, no. 5, pp. 2007–2014, may 2000. [Online]. Available: http://link.aip.org/link/?RSI/71/2007/1http://aip.scitation.org/doi/10.1063/1.1150569 (Cited on pages 42 and 47.)

[100] W. Lee and W. Lempert, "Rubidium Vapor Filter Spectrally Filtered Thomson Scattering," in *22nd AIAA Aerodynamic Measurement Technology and Ground Testing Conference*, vol. 40, no. 12. Reston, Virigina: American Institute of Aeronautics and Astronautics, jun 2002. [Online]. Available: http://arc.aiaa.org/doi/10.2514/6.2002-3236 (Cited on page 42.)

[101] W. Lee, "Development of Ramand and Thomson scattering diagnostics for study of energy transfer in nonequilibrium, molecular plasma," Ph.D. dissertation, The ohio state university, 2003. (Cited on page 42.)

[102] M. Boguszko and G. Elliott, "Property measurement utilizing atomic/molecular filter-based diagnostics," *Progress in Aerospace Sciences*, vol. 41, no. 2, pp. 93–142, feb 2005. [Online]. Available: https://linkinghub.elsevier.com/retrieve/pii/S037604210500028X (Cited on page 42.)

[103] A. Pitzschke, "Pedestal Characteristics and MHD Stability of H-Mode Plasmas in TCV," Ph.D. dissertation, Ecole polytechnique fédérale de Lausanne, 2011. (Cited on page 42.)

[104] M. Paillet, F. Meunier, M. Verhaegen, S. Blais-Ouellette, and R. Martel, "High performance resonance Raman spectroscopy using volume Bragg gratings as tunable light filters," *Review of Scientific Instruments*, vol. 81, no. 5, p. 053111, may 2010. [Online]. Available: http://aip.scitation.org/doi/10.1063/1.3405839 (Cited on page 42.)

[105] B. L. M. Klarenaar, F. Brehmer, S. Welzel, H. J. van der Meiden, M. C. M. van de Sanden, and R. Engeln, "Note: Rotational Raman scattering on CO 2 plasma using a volume Bragg grating as a notch filter," *Review of Scientific Instruments*, vol. 86, no. 4, p. 046106, apr 2015. [Online]. Available: http://dx.doi.org/10.1063/1.4918730http://aip.scitation.org/doi/10.1063/1.4918730 (Cited on page 42.)

[106] B. L. M. Klarenaar, "Vibrational kinetics of CO 2 in non-thermal plasma," Ph.D. dissertation, Eindhoven university of technology, 2018. (Cited on page 42.)

[107] I. V. Ciapurin, "Errata: Modeling of phase volume diffractive gratings, part 2: reflecting sinusoidal uniform gratings, Bragg mirrors," *Optical Engineering*, vol. 51, no. 5, p. 059803, may 2012. [Online]. Available: http://opticalengineering.spiedigitallibrary.org/article.aspx?doi=10.1117/1.OE.51.5.059803 (Cited on page 42.)

[108] A. L. Glebov, O. Mokhun, A. Rapaport, S. Vergnole, V. Smirnov, and L. B. Glebov, "Volume Bragg gratings as ultra-narrow and multiband optical filters," in *Micro-Optics 2012*, H. Thienpont, J. Mohr, H. Zappe, and H. Nakajima, Eds., vol. 8428, jun 2012, p. 84280C. [Online]. Available: http://proceedings.spiedigitallibrary.org/proceeding.aspx?doi=10.1117/12.923575 (Cited on page 42.)

[109] R. Paschotta, "Volume Bragg Gratings," 2019. [Online]. Available: https://www.rp-photonics.com/volume_bragg_gratings.html (Cited on page 43.)

[110] J. M. Palomares, E. I. Iordanova, A. Gamero, A. Sola, and J. J. A. M. v. d. Mullen, "Atmospheric microwave-induced plasmas in Ar/H 2 mixtures studied with a combination of passive and active spectroscopic methods," *Journal of Physics D: Applied Physics*, vol. 43, no. 39, p. 395202, oct 2010. [Online]. Available: http://stacks.iop.org/0022-3727/43/i=39/a=395202?key=crossref.735572df35ea1fb80285b4319dae6f08 (Cited on page 47.)

[111] K. Muraoka and A. Kono, "Laser thomson scattering for low-temperature plasmas," p. 043001, feb 2011. [Online]. Available: http://stacks.iop.org/0022-3727/44/i=4/a=043001?key=crossref.e53f26e118fc8112b380aef29f954d16 (Cited on page 47.)

[112] M. J. van de Sande, R. H. M. Deckers, F. Lepkojus, W. Buscher, and J. J. A. M. van der Mullen, "Time resolved electron density and temperature measurements on a capacitively coupled helium RF discharge," *Plasma Sources Science and Technology*, vol. 11, no. 4, pp. 466–475, nov 2002. [Online]. Available: http://stacks.iop.org/0963-0252/11/i=4/a=313?key=crossref.16693b0af04293d267490c30d044af22 (Cited on page 47.)

[113] A. F. H. van Gessel, E. A. D. Carbone, P. J. Bruggeman, and J. J. A. M. van der Mullen, "Laser scattering on an atmospheric pressure plasma jet: disentangling Rayleigh, Raman and Thomson scattering," *Plasma Sources Science and Technology*, vol. 21, no. 1, p. 015003, feb 2012. [Online]. Available: http://stacks.iop.org/0963-0252/21/i=1/a=015003?key=crossref.e16a00ad074075da0945bb1f1b69bff7 (Cited on page 47.)

[114] C. M. Penney, R. L. St. Peters, and M. Lapp, "Absolute rotational Raman cross sections for N_2, O_2, and CO_2," *Journal of the Optical Society of America*, vol. 64, no. 5, p. 712, may 1974. [Online]. Available: http://www.opticsinfobase.org/abstract.cfm?URI=josa-64-5-712https://www.osapublishing.org/abstract.cfm?URI=josa-64-5-712 (Cited on pages 49, 50, and 53.)

[115] P. F. Bernath and A. Dalgarno, *Spectra of Atoms and Molecules*, 1996, vol. 49, no. 3. [Online]. Available: http://physicstoday.scitation.org/doi/10.1063/1.2807548 (Cited on page 49.)

[116] T. Hori, M. Kogano, M. D. Bowden, K. Uchino, and K. Muraoka, "A study of electron energy distributions in an inductively coupled plasma by laser Thomson scattering," *Journal of Applied Physics*, vol. 83, no. 4, pp. 1909–1916, feb 1998. [Online]. Available: http://aip.scitation.org/doi/10.1063/1.366915 (Cited on page 53.)

[117] A. Kono and H. Funahashi, "Thomson-scattering observation of non-Maxwellian electron energy distribution in inductively coupled C4F8/Ar and CF4/Ar plasmas and the effect of vibrational excitation and nonlocal electron kinetics," *Journal of Applied Physics*, vol. 92, no. 4, pp. 1757–1763, aug 2002. [Online]. Available: http://aip.scitation.org/doi/10.1063/1.1493659 (Cited on page 53.)

[118] A. Savitzky and M. J. E. Golay, "Smoothing and Differentiation of Data by Simplified Least Squares Procedures." *Analytical Chemistry*, vol. 36, no. 8, pp. 1627–1639, jul 1964. [Online]. Available: http://pubs.acs.org/doi/abs/10.1021/ac60214a047 (Cited on page 54.)

[119] A. T. Powis and M. N. Shneider, "Particle-in-cell modeling of laser Thomson scattering in low-density plasmas at elevated laser intensities," *Physics of Plasmas*, vol. 25, no. 5, p. 053513, may 2018. [Online]. Available: http://arxiv.org/abs/1803.06278http://aip.scitation.org/doi/10.1063/1.5029820 (Cited on page 57.)

[120] N. Yamamoto, K. Tomita, K. Sugita, T. Kurita, H. Nakashima, and K. Uchino, "Measurement of xenon plasma properties in an ion thruster using laser Thomson scattering technique," *Review of Scientific Instruments*, vol. 83, no. 7, p. 073106, jul 2012. [Online]. Available: http://aip.scitation.org/doi/10.1063/1.4737144 (Cited on page 58.)

[121] V. Canuto, J. Lodenquai, and M. Ruderman, "Thomson Scattering in a Strong Magnetic Field," *Physical Review D*, vol. 3, no. 10, pp. 2303–2308, may 1971. [Online]. Available: https://link.aps.org/doi/10.1103/PhysRevD.3.2303 (Cited on page 59.)

[122] H. Herold, "Compton and Thomson scattering in strong magnetic fields," *Physical Review D*, vol. 19, no. 10, pp. 2868–2875, may 1979. [Online]. Available: https://link.aps.org/doi/10.1103/PhysRevD.19.2868 (Cited on page 59.)

[123] S.-y. Chen, A. Maksimchuk, and D. Umstadter, "Experimental observation of relativistic nonlinear Thomson scattering," *Nature*, vol. 396, no. 6712, pp. 653–655, dec 1998. [Online]. Available: http://www.nature.com/articles/25303 (Cited on page 61.)

[124] J. Chapin, "The Planar Magnetron," *Research Development*, vol. 25, no. 1, pp. 37–40, 1974. [Online]. Available: http://ci.nii.ac.jp/naid/10025667114/en/ (Cited on page 63.)

[125] ——, "Sputtering Process and Apparatus," pp. 2–6, 1979. (Cited on page 63.)

[126] C. Boniface, L. Garrigues, G. J. M. Hagelaar, J. P. Boeuf, D. Gawron, and S. Mazouffre, "Anomalous cross field electron transport in a Hall effect thruster," *Applied Physics Letters*, vol. 89, no. 16, p. 161503, oct 2006. [Online]. Available: http://aip.scitation.org/doi/10.1063/1.2360182 (Cited on page 64.)

[127] D. Lundin, P. Larsson, E. Wallin, M. Lattemann, N. Brenning, and U. Helmersson, "Cross-field ion transport during high power impulse magnetron sputtering," *Plasma Sources Science and Technology*, vol. 17, no. 3, p. 035021, aug 2008. [Online]. Available: http://stacks.iop.org/0963-0252/17/i=3/a=035021?key=crossref.2ca07b0671dcb79b8b3592ac7ec7b457 (Cited on page 64.)

[128] J. Alami, P. O. Å. Persson, D. Music, J. T. Gudmundsson, J. Bohlmark, and U. Helmersson, "Ion-assisted physical vapor deposition for enhanced film properties on nonflat surfaces," *Journal of Vacuum Science & Technology A: Vacuum, Surfaces, and Films*, vol. 23, no. 2, pp. 278–280, mar 2005. [Online]. Available: http://avs.scitation.org/doi/10.1116/1.1861049 (Cited on page 65.)

[129] J. T. Gudmundsson, N. Brenning, D. Lundin, and U. Helmersson, "High power impulse magnetron sputtering discharge," *Journal of Vacuum Science & Technology A: Vacuum, Surfaces, and Films*, vol. 30, no. 3, p. 030801, may 2012. [Online]. Available: http://avs.scitation.org/doi/10.1116/1.3691832 (Cited on page 65.)

[130] A. Anders, "A structure zone diagram including plasma-based deposition and ion etching," *Thin Solid Films*, vol. 518, no. 15, pp. 4087–4090, 2010. [Online]. Available: http://dx.doi.org/10.1016/j.tsf.2009.10.145 (Cited on page 65.)

[131] T. E. Sheridan, M. J. Goeckner, and J. Goree, "Observation of twotemperature electrons in a sputtering magnetron plasma," *Journal of Vacuum Science & Technology A: Vacuum, Surfaces, and Films*, vol. 9, no. 3, pp. 688–690, may 1991. [Online]. Available: http://avs.scitation.org/doi/10.1116/1.577344 (Cited on pages 65, 72, and 73.)

[132] J. Bohlmark, J. Gudmundsson, J. Alami, M. Latteman, and U. Helmersson, "Spatial electron density distribution in a high-power pulsed magnetron discharge," *IEEE Transactions on Plasma Science*, vol. 33, no. 2, pp. 346–347, apr 2005. [Online]. Available: http://ieeexplore.ieee.org/document/1420469/ (Cited on page 65.)

[133] S. Tsikata, B. Vincent, T. Minea, A. Revel, and C. Ballage, "Time-resolved electron properties of a HiPIMS argon discharge via incoherent Thomson scattering," *Plasma Sources Science and Technology*, vol. 28, no. 3, p. 03LT02, mar 2019. [Online]. Available: http://stacks.iop.org/0963-0252/28/i=3/a=03LT02?key=crossref.56ae02bd7c1937aabe7307d3a4f46aeb (Cited on pages 66 and 122.)

[134] P. J. Ryan, J. W. Bradley, and M. D. Bowden, "Comparison of Langmuir probe and laser Thomson scattering for plasma density and electron temperature measurements in HiPIMS plasma," *Physics of Plasmas*, vol. 26, no. 4, p. 040702, apr 2019. [Online]. Available: https://doi.org/10.1063/1.5094602http://aip.scitation.org/doi/10.1063/1.5094602 (Cited on page 66.)

[135] ——, "Comparison of Langmuir probe and laser Thomson scattering for plasma density and electron temperature measurements in HiPIMS plasma," *Physics of Plasmas*, vol. 26, no. 4, p. 040702, apr 2019. [Online]. Available: http://aip.scitation.org/doi/10.1063/1.5094602 (Cited on page 66.)

[136] U. Balachandran and N. G. Eror, "Raman spectra of titanium dioxide," *Journal of Solid State Chemistry*, vol. 42, no. 3, pp. 276–282, 1982. (Cited on page 72.)

[137] X. Xue, W. Ji, Z. Mao, H. Mao, Y. Wang, X. Wang, W. Ruan, B. Zhao, and J. R. Lombardi, "Raman Investigation of Nanosized TiO 2 : Effect of Crystallite Size and Quantum Confinement," *The Journal of Physical Chemistry C*, vol. 116, no. 15, pp. 8792–8797, apr 2012. [Online]. Available: http://pubs.acs.org/doi/10.1021/jp2122196 (Cited on page 72.)

[138] T. E. Sheridan and J. Goree, "Lowfrequency turbulent transport in magnetron plasmas," *Journal of Vacuum Science & Technology A: Vacuum, Surfaces, and Films*, vol. 7, no. 3, pp. 1014–1018, may 1989. [Online]. Available: http://avs.scitation.org/doi/10.1116/1.576221 (Cited on page 72.)

[139] J. Emmerlich, S. Mráz, R. Snyders, K. Jiang, and J. M. Schneider, "The physical reason for the apparently low deposition rate during high-power pulsed magnetron sputtering," *Vacuum*, vol. 82, no. 8, pp. 867–870, apr 2008. [Online]. Available: https://linkinghub.elsevier.com/retrieve/pii/S0042207X07003703 (Cited on page 76.)

[140] A. Rauch and A. Anders, "Estimating electron drift velocities in magnetron discharges," *Vacuum*, vol. 89, no. 1, pp. 53–56, mar 2013. [Online]. Available: http://dx.doi.org/10.1016/j.vacuum.2012.09.002http://linkinghub.elsevier.com/retrieve/pii/S0042207X12004010 (Cited on page 76.)

[141] A. Rauch, R. J. Mendelsberg, J. M. Sanders, and A. Anders, "Plasma potential mapping of high power impulse magnetron sputtering discharges," *Journal of Applied Physics*, vol. 111, no. 8, p. 083302, apr 2012. [Online]. Available: http://aip.scitation.org/doi/10.1063/1.3700242 (Cited on page 76.)

[142] P. A. Ni, C. Hornschuch, M. Panjan, and A. Anders, "Plasma flares in high power impulse magnetron sputtering," *Applied Physics Letters*, vol. 101, no. 22, p. 224102, nov 2012. [Online]. Available: http://aip.scitation.org/doi/10.1063/1.4768925 (Cited on page 76.)

[143] A. Anders, P. Ni, and A. Rauch, "Drifting localization of ionization runaway: Unraveling the nature of anomalous transport in high power impulse magnetron sputtering," *Journal of Applied Physics*, vol. 111, no. 5, p. 053304, mar 2012. [Online]. Available: http://aip.scitation.org/doi/10.1063/1.3692978 (Cited on page 76.)

[144] O. Chapurin and A. Smolyakov, "On the electron drift velocity in plasma devices with EŒB drift," *Journal of Applied Physics*, vol. 119, no. 24, p. 243306, jun 2016. [Online]. Available: http://aip.scitation.org/doi/10.1063/1.4954994 (Cited on pages 77 and 123.)

[145] J. W. Bradley, S. Thompson, and Y. A. Gonzalvo, "Measurement of the plasma potential in a magnetron discharge and the prediction of the electron drift speeds," *Plasma Sources Science and Technology*, vol. 10, no. 3, pp. 490–501, aug 2001. [Online]. Available: http://stacks.iop.org/0963-0252/10/i=3/a=314?key=crossref.1700b17622724fd9017d03fe6581ea1d (Not cited.)

[146] E. Bultinck and A. Bogaerts, "The effect of the magnetic field strength on the sheath region of a dc magnetron discharge," *Journal of Physics D: Applied Physics*, vol. 41, no. 20, p. 202007, oct 2008. [Online]. Available: http://www.iop.org/EJ/abstract/0022-3727/41/20/202007/{%}5Cnhttp://stacks.iop.org/0022-3727/41/i=20/a=202007?key=crossref.a40b25082933e2aa0d861d319a1cddc1http://stacks.iop.org/0022-3727/41/i=20/a=202007?key=crossref.a40b25082933e2aa0d861d319a1cddc1 (Cited on page 77.)

[147] A. Hecimovic, C. Maszl, V. Schulz-von der Gathen, M. Böke, and A. von Keudell, "Spoke rotation reversal in magnetron discharges of aluminium, chromium and titanium," *Plasma Sources Science and Technology*, vol. 25, no. 3, p. 035001, jun 2016. [Online]. Available: http://stacks.iop.org/0963-0252/25/i=3/a=035001?key=crossref.955dcf12a58b09083b7b31e938b68080 (Cited on page 78.)

[148] N. Brenning, I. Axnäs, M. A. Raadu, D. Lundin, and U. Helmerson, "A bulk plasma model for dc and HiPIMS magnetrons," *Plasma Sources Science and Technology*, vol. 17, no. 4, p. 045009, nov 2008. [Online]. Available: http://stacks.iop.org/0963-0252/17/i=4/a=045009?key=crossref.d299670e9086842f128c8dd038367e0e (Cited on pages 78 and 87.)

[149] C. Huo, D. Lundin, M. A. Raadu, A. Anders, J. T. Gudmundsson, and N. Brenning, "On the road to self-sputtering in high power impulse magnetron sputtering: particle balance and discharge characteristics," *Plasma Sources Science and Technology*, vol. 23, no. 2, p. 025017, apr 2014. [Online]. Available: http://stacks.iop.org/0963-0252/23/i=2/a=025017?key=crossref.9b9d3ed0c82c13025ece0f8c9d5085b2 (Cited on page 80.)

[150] U. Helmersson, M. Lattemann, J. Bohlmark, A. P. Ehiasarian, and J. T. Gudmundsson, "Ionized physical vapor deposition (IPVD): A review of technology and applications," *Thin Solid Films*, vol. 513, no. 1-2, pp. 1–24, aug 2006. [Online]. Available: https://linkinghub.elsevier.com/retrieve/pii/S0040609006004317 (Cited on page 81.)

[151] A. Anders, "Deposition rates of high power impulse magnetron sputtering: Physics and economics," *Journal of Vacuum Science & Technology A: Vacuum, Surfaces, and Films*, vol. 28, no. 4, pp. 783–790, jul 2010. [Online]. Available: http://avs.scitation.org/doi/10.1116/1.3299267 (Cited on page 81.)

[152] T. Kubart, M. Čada, D. Lundin, and Z. Hubička, "Investigation of ionized metal flux fraction in HiPIMS discharges with Ti and Ni targets," *Surface and Coatings Technology*, vol. 238, pp. 152–157, jan 2014. [Online]. Available: https://linkinghub.elsevier.com/retrieve/pii/S0257897213009985 (Cited on page 82.)

[153] D. Lundin, M. Čada, and Z. Hubička, "Ionization of sputtered Ti, Al, and C coupled with plasma characterization in HiPIMS," *Plasma Sources Science and Technology*, vol. 24, no. 3, p. 035018, jun 2015. [Online]. Available: http://stacks.iop.org/0963-0252/24/i=3/a=035018?key=crossref.77001a90fe258ce7b1cb11200908ad62 (Cited on page 82.)

[154] H. Hajihoseini, M. Čada, Z. Hubička, S. Ünaldi, M. A. Raadu, N. Brenning, J. T. Gudmundsson, and D. Lundin, "The Effect of Magnetic Field Strength and Geometry on the Deposition Rate and Ionized Flux Fraction in the HiPIMS Discharge," *Plasma*, vol. 2, no. 2, pp. 201–221, may 2019. [Online]. Available: https://www.mdpi.com/2571-6182/2/2/15 (Cited on page 84.)

[155] J. Čapek, M. Hála, O. Zabeida, J. E. Klemberg-Sapieha, and L. Martinu, "Deposition rate enhancement in HiPIMS without compromising the ionized fraction of the deposition flux," *Journal of Physics D: Applied Physics*, vol. 46, no. 20, p. 205205, may 2013. [Online]. Available: http://stacks.iop.org/0022-3727/46/i=20/a=205205?key=crossref.4b8b3aa643d33709a62caf8b46423320 (Cited on page 85.)

[156] J. W. Bradley, A. Mishra, and P. J. Kelly, "The effect of changing the magnetic field strength on HiPIMS deposition rates," *Journal of Physics D: Applied Physics*, vol. 48, no. 21, p. 215202, jun 2015. [Online]. Available: http://dx.doi.org/10.1088/0022-3727/48/21/215202http://stacks.iop.org/0022-3727/48/i=21/a=215202?key=crossref.9a3eee5fd4b2367e5cc16eed9900ae70 (Cited on page 85.)

[157] S. H. Seo, J. H. In, and H. Y. Chang, "Temporal evolution of electron energy distribution function and plasma parameters in the afterglow of drifting magnetron plasma," *Plasma Sources Science and Technology*, vol. 14, no. 3, pp. 576–580, 2005. (Cited on page 87.)

[158] M. A. Raadu, I. Axnäs, J. T. Gudmundsson, C. Huo, and N. Brenning, "An ionization region model for high-power impulse magnetron sputtering discharges," *Plasma Sources Science and Technology*, vol. 20, no. 6, p. 065007, dec 2011. [Online]. Available: http://stacks.iop.org/0963-0252/20/i=6/a=065007?key=crossref.18debfb180b92ec7b1e5d59acf5602fc (Cited on page 87.)

[159] G. D. Stancu, N. Brenning, C. Vitelaru, D. Lundin, and T. Minea, "Argon metastables in HiPIMS: validation of the ionization region model by direct comparison to time resolved tunable diode-laser diagnostics," *Plasma Sources Science and Technology*, vol. 24, no. 4, p. 045011, jul 2015. [Online]. Available: http://dx.doi.org/10.1088/0963-0252/24/4/045011http://stacks.iop.org/0963-0252/24/i=4/a=045011?key=crossref.ffe67650bc1dd8516d9d73eb4976a581 (Cited on page 87.)

[160] R. Geller, "New high intensity ion source with very low extraction voltage," *Applied Physics Letters*, vol. 16, no. 10, pp. 401–402, 1970. (Cited on page 90.)

[161] P. Briand, R. Geller, B. Jacquot, and C. Jacquot, "Nouvelle source d'ions multicharges a hautes performances," *Nuclear Instruments and Methods*, vol. 131, no. 3, pp. 407–409, dec 1975. [Online]. Available: https://linkinghub.elsevier.com/retrieve/pii/0029554X75904255 (Cited on page 90.)

[162] I. I. Rabi, J. R. Zacharias, S. Millman, and P. Kusch, "A New Method of Measuring Nuclear Magnetic Moment," *Physical Review*, vol. 53, no. 4, pp. 318–318, feb 1938. [Online]. Available: https://link.aps.org/doi/10.1103/PhysRev.53.318 (Cited on page 90.)

[163] E. K. Zavoisky, "Paramagnetic absorption in orthogonal and parallel fields for salts, solutions and metals." Ph.D. dissertation, Kazan University, 1944. [Online]. Available: https://ci.nii.ac.jp/naid/10008591194/ (Cited on page 90.)

[164] T. I. U. NTU, *Radio Regulations*. IUT, 2016. [Online]. Available: https://linkinghub.elsevier.com/retrieve/pii/B9780750682091500103 (Cited on page 90.)

[165] I. G. Brown, *The Physics and Technology of Ion Sources*. Wiley, aug 2004. [Online]. Available: https://onlinelibrary.wiley.com/doi/book/10.1002/3527603956 (Cited on page 90.)

[166] T. Vialis, "Développement d' un propulseur plasma à résonance cyclotron électronique pour les satellites," Ph.D. dissertation, Sorbonne Université, 2018. (Cited on page 90.)

[167] T. Vialis, J. Jarrige, A. Aanesland, and D. Packan, "Direct Thrust Measurement of an Electron Cyclotron Resonance Plasma Thruster," *Journal of Propulsion and Power*, pp. 1–11, jul 2018. [Online]. Available: https://arc.aiaa.org/doi/10.2514/1.B37036 (Cited on page 90.)

[168] P. Bagryansky, A. Anikeev, G. Denisov, E. Gospodchikov, A. Ivanov, A. Lizunov, Y. Kovalenko, V. Malygin, V. Maximov, O. Korobeinikova, S. Murakhtin, E. Pinzhenin, V. Prikhodko, V. Savkin, A. Shalashov, O. Smolyakova, E. Soldatkina, A. Solomakhin, D. Yakovlev, and K. Zaytsev, "Overview of ECR plasma heating experiment in the GDT magnetic mirror," *Nuclear Fusion*, vol. 55, no. 5, p. 053009, may 2015. [Online]. Available: http://stacks.iop.org/0029-5515/55/i=5/a=053009?key=crossref.1248bed75bdf4756e5b3b550340ecb1f (Cited on page 90.)

[169] P. A. Bagryansky, A. D. Beklemishev, and V. V. Postupaev, "Encouraging Results and New Ideas for Fusion in Linear Traps," *Journal of Fusion Energy*, vol. 38, no. 1, pp. 162–181, feb 2019. [Online]. Available: https://doi.org/10.1007/s10894-018-0174-1http://link.springer.com/10.1007/s10894-018-0174-1 (Cited on page 90.)

[170] O. Tuske, O. Delferrière, R. Gobin, F. Harrault, and T. Steiner, "Results of the CEA/Saclay H electron cyclotron resonance ion source, ECRIN," *Review of Scientific Instruments*, vol. 77, no. 3, p. 03A507, mar 2006. [Online]. Available: http://aip.scitation.org/doi/10.1063/1.2163277 (Cited on page 90.)

[171] O. Tuske, G. Charruau, O. Delferriere, D. De Menezes, R. Gobin, Y. Gauthier, F. Harrault, and A. Madur, "ECRIN and MultiCusp Sources at CEA Saclay," in *AIP Conference Proceedings*, vol. 925. AIP, mar 2007, pp. 114–120. [Online]. Available: http://aip.scitation.org/doi/10.1063/1.2163277http://aip.scitation.org/doi/abs/10.1063/1.2773651 (Cited on page 90.)

[172] S. Nyckees, "Etude et développement d ' une nouvelle source ECR produisant un faisceau intense d'ions légers," Ph.D. dissertation, Université Paris-Saclay, 2013. [Online]. Available: https://tel.archives-ouvertes.fr/tel-00826838 (Cited on pages 91 and 92.)

[173] A. Dunaevsky, Y. Raitses, and N. J. Fisch, "Secondary electron emission from dielectric materials of a Hall thruster with segmented electrodes," *Physics of Plasmas*, vol. 10, no. 6, pp. 2574–2577, jun 2003. [Online]. Available: http://aip.scitation.org/doi/10.1063/1.1568344 (Cited on page 91.)

[174] Z. Xie, "State of the art of ECR ion sources," in *Proceedings of the 1997 Particle Accelerator Conference (Cat. No.97CH36167)*, vol. 3. IEEE, 2002, pp. 2662–2666. [Online]. Available: http://ieeexplore.ieee.org/document/752725/ (Cited on page 91.)

[175] J. E. Ricker and J. H. Hendricks, "Unit Conversions | NIST," 2017. [Online]. Available: https://www.nist.gov/pml/div685/grp01/unit_conversions (Cited on page 93.)

[176] O. Tarvainen, "Studies of electron cyclotron resonance ion source plasma physics," Ph.D. dissertation, University of Jyväskylä, 2005. (Cited on page 96.)

[177] J. J. Balmer, "Notiz über die Spectrallinien des Wasserstoffs," *Annalen der Physik*, vol. 261, no. 5, pp. 80–87, 1885. [Online]. Available: http://doi.wiley.com/10.1002/andp.18852610506 (Cited on page 97.)

[178] A. Campargue, S. Kassi, K. Pachucki, and J. Komasa, "The absorption spectrum of H 2 : CRDS measurements of the (2-0) band, review of the literature data and accurate ab initio line list up to 35 000 cm 1," *Phys. Chem. Chem. Phys.*, vol. 14, no. 2, pp. 802–815, 2012. [Online]. Available: http://xlink.rsc.org/?DOI=C1CP22912E (Cited on page 97.)

[179] I. Gordon, L. Rothman, C. Hill, R. Kochanov, Y. Tan, P. Bernath, M. Birk, V. Boudon, A. Campargue, K. Chance, B. Drouin, J.-M. Flaud, R. Gamache, J. Hodges, D. Jacquemart, V. Perevalov, A. Perrin, K. Shine, M.-A. Smith, J. Tennyson, G. Toon, H. Tran, V. Tyuterev, A. Barbe, A. Császár, V. Devi, T. Furtenbacher, J. Harrison, J.-M. Hartmann, A. Jolly, T. Johnson, T. Karman, I. Kleiner, A. Kyuberis, J. Loos, O. Lyulin, S. Massie, S. Mikhailenko, N. Moazzen-Ahmadi, H. Müller, O. Naumenko, A. Nikitin, O. Polyansky, M. Rey, M. Rotger, S. Sharpe, K. Sung, E. Starikova, S. Tashkun, J. V. Auwera, G. Wagner, J. Wilzewski, P. Wcisło, S. Yu, and E. Zak, "The HITRAN2016 molecular spectroscopic database," *Journal of Quantitative Spectroscopy and Radiative Transfer*, vol. 203, pp. 3–69, dec 2017. [Online]. Available: https://linkinghub.elsevier.com/retrieve/pii/S0022407317301073 (Cited on page 97.)

[180] J. R. Hiskes, "Cross sections for the vibrational excitation of the H2(X 1J+g) state via electron collisional excitation of the higher singlet states," *Journal of Applied Physics*, vol. 51, no. 9, pp. 4592–4594, 1980. (Cited on page 98.)

[181] J. Marx, A. Lebehot, and R. Campargue, "Cross sections for vibrational excitation of H2(X 1Σ +g, ν" = 0) via electronically excited singlet states populated by low energy electron impact," *Journal de Physique*, vol. 46, no. 10, pp. 1667–1670, 1985. [Online]. Available: http://www.edpsciences.org/10.1051/jphys:0198500460100166700 (Cited on page 98.)

[182] M. D. Bowden, T. Okamoto, F. Kimura, H. Muta, K. Uchino, K. Muraoka, T. Sakoda, M. Maeda, Y. Manabe, M. Kitagawa, and T. Kimura, "Thomson scattering measurements of electron temperature and density in an electron cyclotron resonance plasma," *Journal*

of Applied Physics, vol. 73, no. 6, pp. 2732–2738, mar 1993. [Online]. Available: http://aip.scitation.org/doi/10.1063/1.353046 (Cited on pages 100 and 101.)

[183] E. Y. Choueiri, "A Critical History of Electric Propulsion: The First 50 Years (1906-1956)," *Journal of Propulsion and Power*, vol. 20, no. 2, pp. 193–203, mar 2004. [Online]. Available: http://arc.aiaa.org/doi/10.2514/1.9245 (Cited on page 108.)

[184] V. Kim, K. Kozubsky, V. M. Murashko, and A. Semenkin, "History of the Hall Thrusters Development in USSR," *30th International Electric Propulsion Conference*, pp. 17–20, 2007. (Cited on page 108.)

[185] J.-p. Boeuf, "Tutorial: Physics and modeling of Hall thrusters," *Journal of Applied Physics*, vol. 121, no. 1, p. 011101, jan 2017. [Online]. Available: http://aip.scitation.org/doi/10.1063/1.4972269 (Cited on page 108.)

[186] E. Y. Choueiri, "Plasma oscillations in Hall thrusters," *Physics of Plasmas*, vol. 8, no. 4, pp. 1411–1426, 2001. (Cited on page 108.)

[187] A. Bugrova, "Electron distribution function in the channel of an electron-ring plasma accelerator.pdf," *Sov. Phys. Tech. Phys.*, vol. 32, no. 1111, 1987. (Cited on page 108.)

[188] G. Giono, J. T. Gudmundsson, N. Ivchenko, S. Mazouffre, K. Dannenmayer, D. Loubère, L. Popelier, M. Merino, and G. Olentšenko, "Non-Maxwellian electron energy probability functions in the plume of a SPT-100 Hall thruster," *Plasma Sources Science and Technology*, vol. 27, no. 1, p. 015006, dec 2018. [Online]. Available: http://stacks.iop.org/0963-0252/27/i=1/a=015006?key=crossref.3cc1b9821d68b707749e109ec7a9f5b5 (Cited on page 108.)

[189] S. Barral, K. Makowski, Z. Peradzyński, N. Gascon, and M. Dudeck, "Wall material effects in stationary plasma thrusters. II. Near-wall and in-wall conductivity," *Physics of Plasmas*, vol. 10, no. 10, pp. 4137–4152, 2003. (Cited on page 108.)

[190] D. Sydorenko, A. Smolyakov, I. Kaganovich, and Y. Raitses, "Kinetic simulation of secondary electron emission effects in Hall thrusters," *Physics of Plasmas*, vol. 13, no. 1, p. 014501, jan 2006. [Online]. Available: http://aip.scitation.org/doi/10.1063/1.2158698 (Cited on page 108.)

[191] S. Tsikata, A. Héron, and C. Honoré, "Hall thruster microturbulence under conditions of modified electron wall emission," *Physics of Plasmas*, vol. 24, no. 5, p. 053519, may 2017. [Online]. Available: http://aip.scitation.org/doi/10.1063/1.4984255 (Cited on page 108.)

[192] N. Gascon, M. Dudeck, and S. Barral, "Wall material effects in stationary plasma thrusters. I. Parametric studies of an SPT-100," *Physics of Plasmas*, vol. 10, no. 10, pp. 4123–4136, oct 2003. [Online]. Available: http://aip.scitation.org/doi/10.1063/1.1611880 (Cited on pages 109 and 110.)

[193] I. G. Mikellides, I. Katz, R. R. Hofer, D. M. Goebel, K. de Grys, and A. Mathers, "Magnetic shielding of the channel walls in a Hall plasma accelerator," *Physics of Plasmas*, vol. 18, no. 3, p. 033501, mar 2011. [Online]. Available: http://aip.scitation.org/doi/10.1063/1.3551583 (Cited on page 111.)

[194] L. Grimaud, "Magnetic shielding topology applied to low power Hall thrusters," Ph.D. dissertation, Université d'Orléans, 2018. (Cited on pages 111, 120, and 126.)

[195] R. Shastry, A. Gallimore, and R. Hofer, "Near-Wall Plasma Properties and EEDF Measurements of a 6-kW Hall Thruster," in *45th AIAA/ASME/SAE/ASEE Joint Propulsion Conference & Exhibit*, no. August. Reston, Virginia: American Institute of Aeronautics and Astronautics, aug 2009, pp. 1–15. [Online]. Available: http://arc.aiaa.org/doi/abs/10.2514/6.2009-5356 (Cited on page 111.)

[196] K. Dannenmayer, P. Kudrna, M. Tichý, and S. Mazouffre, "Time-resolved measurements of plasma properties using electrostatic probes in the cross-field discharge of a hall effect thruster," *Contributions to Plasma Physics*, vol. 53, no. 1, pp. 63–68, 2013. (Cited on page 111.)

[197] M. Tichý, A. Pétin, P. Kudrna, M. Horký, and S. Mazouffre, "Electron energy distribution function in a low-power Hall thruster discharge and near-field plume," *Physics of Plasmas*, vol. 25, no. 6, p. 061205, jun 2018. [Online]. Available: http://aip.scitation.org/doi/10.1063/1.5017578 (Cited on pages 111, 124, 137, and 139.)

[198] J. Sommerville and L. King, "An Optical Diagnostic for Xenon Hall Thrusters Including Metastable Contributions," in *42nd AIAA/ASME/SAE/ASEE Joint Propulsion Conference & Exhibit*, no. July. Reston, Virginia: American Institute of Aeronautics and Astronautics, jul 2006, pp. 1–9. [Online]. Available: http://arc.aiaa.org/doi/abs/10.2514/6.2006-4823 (Cited on page 111.)

[199] R. Spektor and E. J. Beiting, "Non-Invasive Plasma Diagnostic Inside A Hall Thruster Discharge," *IEPC-2007*, pp. 1–9, 2007. (Cited on page 111.)

[200] N. P. Brown, A. M. Steinberg, J. A. Deibel, and M. L. R. Walker, "Terahertz Time-Domain Spectroscopy as an Electric Propulsion Plasma Diagnostic," in *IEPC-2019*, 2019, pp. 1–19. (Cited on page 111.)

[201] R. L. Washeleski, "Laser Thomson scattering measurements of electron temperature and density in a Hall-effect plasma," Ph.D. dissertation, Michigan Technological University, 2012. [Online]. Available: https://digitalcommons.mtu.edu/etds/422/ (Cited on page 111.)

[202] R. L. Washeleski, E. J. Meyer, and L. B. King, "Application of maximum likelihood methods to laser Thomson scattering measurements of low density plasmas," *Review of Scientific Instruments*, vol. 84, no. 10, p. 105101, oct 2013. [Online]. Available: http://aip.scitation.org/doi/10.1063/1.4821980 (Cited on page 111.)

[203] A. Friss and A. P. Yalin, "Further Development of Cavity Enhanced Thomson Scattering for Plasma Thruster Diagnostics," in *53rd AIAA/SAE/ASEE Joint Propulsion Conference*, no. July. Reston, Virginia: American Institute of Aeronautics and Astronautics, jul 2017, pp. 2017–4972. [Online]. Available: https://arc.aiaa.org/doi/10.2514/6.2017-4972 (Cited on page 112.)

[204] ——, "Electron Temperature and Density Measurements in a Low-Power Hollow Cathode Discharge by Cavity Enhanced Thomson Scattering," in *AIAA Scitech 2019 Forum*, no. January, 2019, pp. 1–12. [Online]. Available: https://arc.aiaa.org/doi/10.2514/6.2019-0192 (Cited on page 112.)

[205] A. Lejeune, K. Dannenmayer, G. Bourgeois, S. Mazouffre, M. Guyot, and S. Denise, "Impact of the channel width on Hall thruster discharge properties and performances," in *IEPC-2011*, 2011, pp. 1–15. (Cited on page 112.)

[206] S. Mazouffre, G. Bourgeois, K. Dannenmayer, and A. Lejeune, "Ionization and acceleration processes in a small, variable channel width, permanent-magnet Hall thruster," *Journal of Physics D: Applied Physics*, vol. 45, no. 18, p. 185203, may 2012. [Online]. Available: http://stacks.iop.org/0022-3727/45/i=18/a=185203?key=crossref.d29436c21e2c63e84f66965547aee922 (Cited on page 112.)

[207] L. Grimaud and S. Mazouffre, "Ion behavior in low-power magnetically shielded and unshielded Hall thrusters," *Plasma Sources Science and Technology*, vol. 26, no. 5, p. 055020, apr 2017. [Online]. Available: http://dx.doi.org/10.1088/1361-6595/aa660d (Cited on pages 112 and 122.)

[208] ——, "Performance comparison between standard and magnetically shielded 200 W Hall thrusters with BN-SiO2 and graphite channel walls," *Vacuum*, vol. 155, no. June, pp. 514–523, sep 2018. [Online]. Available: https://linkinghub.elsevier.com/retrieve/pii/S0042207X18306821 (Cited on page 112.)

[209] R. W. Conversano, D. M. Goebel, R. R. Hofer, T. S. Matlock, and R. E. Wirz, "Development and Initial Testing of a Magnetically Shielded Miniature Hall Thruster," *IEEE Transactions on Plasma Science*, vol. 43, no. 1, pp. 103–117, jan 2015. [Online]. Available: http://ieeexplore.ieee.org/document/6823735/ (Cited on page 112.)

[210] K. de Grys, A. Mathers, B. Welander, and V. Khayms, "Demonstration of 10,400 Hours of Operation on 4.5 kW Qualification Model Hall Thruster," in *46th AIAA/ASME/SAE/ASEE Joint Propulsion Conference and Exhibit*, no. July. Reston, Virginia: American Institute of Aeronautics and Astronautics, jul 2010. [Online]. Available: http://arc.aiaa.org/doi/abs/10.2514/6.2010-6698 (Cited on page 112.)

[211] W. E. Ernst, T. P. Softley, and R. N. Zare, "Stark-effect studies in xenon autoionizing Rydberg states using a tunable extreme-ultraviolet laser source," *Physical Review A*, vol. 37, no. 11, pp. 4172–4183, jun 1988. [Online]. Available: https://link.aps.org/doi/10.1103/PhysRevA.37.4172 (Cited on page 116.)

[212] T. Jiang, M. D. Bowden, E. Wagenaars, E. Stoffels, and G. M. Kroesen, "Diagnostics of electric fields in plasma using Stark spectroscopy of krypton and xenon atoms," *New Journal of Physics*, vol. 8, 2006. (Cited on page 116.)

[213] J. P. Boeuf and L. Garrigues, "E Œ B electron drift instability in Hall thrusters: Particle-in-cell simulations vs. theory," *Physics of Plasmas*, vol. 25, no. 6, p. 061204, jun 2018. [Online]. Available: http://aip.scitation.org/doi/10.1063/1.5017033 (Cited on page 119.)

[214] G. Bourgeois, "Influence de la topologie magnétique , de la cathode et de la section du canal sur l'accélération des ions dans un propulseur à effet Hall," Ph.D. dissertation, Université d'Orléans, 2012. (Cited on page 120.)

[215] L. Garrigues, S. Santhosh, L. Grimaud, and S. Mazouffre, "Operation of a low-power Hall thruster: comparison between magnetically unshielded and shielded configuration," *Plasma Sources Science and Technology*, vol. 28, no. 3, p. 034003, mar 2019. [Online]. Available: https://doi.org/10.1088/1361-6595/ab080d (Cited on pages 122 and 128.)

[216] L. Grimaud and S. Mazouffre, "Conducting wall Hall thrusters in magnetic shielding and standard configurations," *Journal of Applied Physics*, vol. 122, no. 3, p. 033305, jul 2017. [Online]. Available: http://aip.scitation.org/doi/10.1063/1.4995285 (Cited on page 124.)

[217] D. Staack, Y. Raitses, and N. J. Fisch, "Temperature gradient in Hall thrusters," *Applied Physics Letters*, vol. 84, no. 16, pp. 3028–3030, apr 2004. [Online]. Available: http://aip.scitation.org/doi/10.1063/1.1710732 (Cited on page 124.)

[218] S. Janhunen, A. Smolyakov, D. Sydorenko, M. Jimenez, I. Kaganovich, and Y. Raitses, "Evolution of the electron cyclotron drift instability in two-dimensions," *Physics of Plasmas*, vol. 25, no. 8, p. 082308, aug 2018. [Online]. Available: http://dx.doi.org/10.1063/1.5033896 (Cited on page 124.)

[219] Y. Raitses, A. Smirnov, D. Staack, M. Keidar, and N. Fisch, "Characterization of plasma in a Hall thruster operated at high discharge voltage," in *41st AIAA/ASME/SAE/ASEE Joint Propulsion Conference & Exhibit*, no. July. Reston, Virginia: American Institute of Aeronautics and Astronautics, jul 2005, pp. 1–6. [Online]. Available: http://arc.aiaa.org/doi/abs/10.2514/6.2005-4404 (Cited on page 128.)

[220] W. A. Hargus and M. A. Cappelli, "Interior and Exterior Laser-Induced Fluorescence and Plasma Measurements within a Hall Thruster," *Journal of Propulsion and Power*, vol. 18, no. 1, pp. 159–168, jan 2002. [Online]. Available: http://arc.aiaa.org/doi/10.2514/2.5912 (Cited on pages 128 and 135.)

[221] V. H. Chaplin, B. A. Jorns, A. Lopez Ortega, I. G. Mikellides, R. W. Conversano, R. B. Lobbia, and R. R. Hofer, "Laser-induced fluorescence measurements of acceleration zone scaling in the 12.5 kW HERMeS Hall thruster," *Journal of Applied Physics*, vol. 124, no. 18, p. 183302, nov 2018. [Online]. Available: http://aip.scitation.org/doi/10.1063/1.5040388 (Cited on pages 128 and 135.)

[222] S. Mazouffre, L. Grimaud, S. Tsikata, K. Matyash, and R. Schneider, "Rotating spoke instabilities in a wall-less Hall thruster: Experiments," *Plasma Sources Science and Technology*, feb 2019. [Online]. Available: http://iopscience.iop.org/article/10.1088/1361-6595/ab07fc (Cited on page 128.)

[223] K. Matyash, R. Schneider, S. Mazouffre, S. Tsikata, and L. Grimaud, "Rotating spoke instabilities in a wall-less Hall thruster: simulations," *Plasma Sources Science and Technology*, vol. 28, no. 4, p. 044002, apr 2019. [Online]. Available: http://iopscience.iop.org/article/10.1088/1361-6595/ab1236 (Cited on page 128.)

[224] M. R. Nakles, W. A. Hargus, J. J. Delgado, and R. L. Corey, "A Performance Comparison of Xenon and Krypton Propellant on an SPT-100 Hall Thruster The 32nd International Electric Propulsion Conference," 2011. [Online]. Available: https://erps.spacegrant.org/uploads/images/images/iepc_articledownload_1988-2007/2011index/IEPC-2011-003.pdf (Cited on page 138.)

[225] S. Mazouffre, S. Tsikata, and J. Vaudolon, "Development and experimental characterization of a wall-less Hall thruster," *Journal of Applied Physics*, vol. 116, no. 24, p. 243302, dec 2014. [Online]. Available: http://aip.scitation.org/doi/10.1063/1.4904965 (Cited on page 139.)

[226] J. Vaudolon, S. Mazouffre, C. Hénaux, D. Harribey, and A. Rossi, "Optimization of a wall-less Hall thruster," *Applied Physics Letters*, vol. 107, no. 17, 2015. [Online]. Available: http://dx.doi.org/10.1063/1.4932196 (Cited on page 139.)

Benjamin VINCENT

Étude de propulseurs de Hall, de magnétrons planaires et de sources d'ions ECR par diffusion Thomson incohérente

La diffusion Thomson incohérente (DTI) est l'une des techniques les plus fiables pour sonder les propriétés électroniques d'un plasma. Des informations clés (densité, température, vitesse de dérive et FDEE) peuvent être obtenues par analyse de l'intensité et de la distribution spectrale de la lumière diffusée sur les électrons libres. Cette technique est non perturbative, permet de bonnes résolutions spatiotemporelles et peut être appliquée dans des régions magnétisées du plasma. Pourtant, l'implémentation de diagnostiques de DTI dans les plasmas bas températures pose un défi en raison des faibles densités plasma.
Cette thèse se concentre sur le développement et l'application d'un nouveau diagnostic DTI. Un nouveau type de filtre notch est utilisé pour atténuer la lumière parasite (provenant de la diffusion de Rayleigh et des réflexions laser) et faciliter la détection du signal de diffusion Thomson. Ce composant a permis le développement d'un diagnostic, nommé THETIS, à la fois sensible et compact pour étudier trois sources plasmas magnétisés basse température fonctionnant à basse pression.
Un magnétron plan a été étudié en régime continu (DCMS) et pulsé (HiPIMS), ces investigations ont permis l'extraction de profils spatiotemporels des propriétés électroniques. Cette étude s'est concentrée sur l'influence du type de gaz, du taux de répétition et de l'intensité du champ magnétique.
Une source d'ions ECR a également été étudiée en régime pulsé et continu. L'influence du type de gaz, de la pression et de la puissance a été étudiée. En plus de l'étude de la dynamique électronique en régime pulsé, l'analyse de l'émission du plasma a permis de suivre les processus d'excitation et ionisation.
Enfin, les propriétés électroniques selon les directions radiales et azimutales de propulseurs à effet Hall dans les configurations "standard" et "écrantage magnétique" ont été étudiées. L'influence du champ magnétique et des conditions de décharge ont été étudiées. Ce travail a révélé non seulement la présence d'anisotropies dans les propriétés des électroniques, mais également la présence de forte température dans les régions magnétisées du plasma du propulseur couplées à des FDEE fortement non maxwelliennes.
Les résultats des travaux de cette thèse contribuent à la meilleure compréhension de ces plasmas et ouvrent une nouvelle voie pour leur modélisation et développement.
Mots clés : diffusion Thomson incohérente, diagnostic laser, filtre notch à réseau de Bragg, magnétron planaire, source d'ion ECR, propulseur de Hall

Incoherent Thomson scattering investigations in Hall thurster, planar magnetron and ECR ion source plasmas

Incoherent Thomson Scattering (ITS) is one of the most reliable techniques for determining electron properties inside a plasma. Key information (electron density, temperature (more generally, the EEDF), and drift velocity) can be determined from the analysis of the intensity and spectral distribution of light of a laser pulse scattered by free electrons. In contrast to many conventional techniques, it is non-perturbative, gives access to spatiotemporally-resolved information, and can be applied in magnetized plasma regions. Yet ITS implementation in low-temperature plasmas poses a particular challenge due to the low plasma densities involved.
This thesis focuses on the development and application of a new ITS diagnostic.Traditional diagnostics have commonly used triple grating spectrometers to filter the stray light signal (from Rayleigh scattering and laser reflections) in order to allow detection of the Thomson-scattered signal from electrons. Instead, this work uses a recently-commercialized notch filter for stray light reduction. This approach enabled the development of a diagnostic with notable sensitivity and compactness.This diagnostic, named THETIS, was used to gain insights into three low-temperature, magnetized plasmas sources operating at low pressure.
A planar magnetron was studied in continuous (DCMS) and pulsed (HiPIMS) regimes, with these investigations allowing the extraction of spatial and temporal profiles of electron properties. This study focused on the influence of the gas type, repetition rate, and magnetic field intensity.
A ECR ion source was also studied in pulsed and continuous regimes. The influence of the gas type, pressure and power were investigated. In addition to the study of the dynamics of electron properties in pulsed operation, insights into species excitation and ionization were gained from the analysis of the plasma emission.
Lastly, electron properties along radial and azimuthal directions in Hall thrusters in "standard" and "magnetic shielding" configurations were investigated. The influence of the magnetic field intensity, configuration, and direction were investigated, as well as the discharge power and voltage. This work revealed not only the presence of anisotropies in electron properties, but also high electron temperatures in magnetized regions of the thruster plasma and the presence of strongly non-Maxwellian EEDFs in such regions.
The information on electron properties, and the accompanying physical insights obtained in this work, contribute to current understanding of these plasmas and provides a new path forward for their modeling and development.
Keywords : incoherent Thomson scattering, laser diagnostic, volume Bragg grating notch filter, planar magnetron, ECR ion source, Hall thruster.

ICARE - CNRS
1C avenue de la Recherche Scientifique
45071 Orléans Cedex 2, France